Treatment planning for tumors with residual motion in scanned ion beam therapy

Bestrahlungsplanung für restbewegte Tumoren in der gescannten Ionenstrahltherapie
Zur Erlangung des Grades eines Doktors der Naturwissenschaften (Dr. rer. nat.)
genehmigte Dissertation von Dipl.-Phys. Daniel Richter aus Aachen, Deutschland
Juli 2012 — Darmstadt — D 17

TECHNISCHE UNIVERSITÄT DARMSTADT

Fachbereich Physik
Institut für Festköperphysik

Treatment planning for tumors with residual motion in scanned ion beam therapy
Bestrahlungsplanung für restbewegte Tumoren in der gescannten Ionenstrahltherapie

Genehmigte Dissertation von Dipl.-Phys. Daniel Richter aus Aachen, Deutschland

1. Gutachten: Prof. Dr. Marco Durante
2. Gutachten: Prof. Dr. Dr. h. c. Gerhard Kraft

Tag der Einreichung: 10. April 2012
Tag der Prüfung: 6. Juni 2012

Darmstadt — D 17

Abstract

The treatment of mobile tumors with a scanned ion beam requires dedicated beam delivery and treatment planning techniques. Interference effects (interplay) between beam and tumor motion can lead to clinically unacceptable dose distributions. Motion mitigation techniques, such as beam gating or irradiation under abdominal compression, can effectively reduce tumor motion but typically do not fully compensate motion-induced dose inhomogeneities. Further mitigation therefore is desirable.

In this work, the dosimetric impact of optimized treatment plan parameters on dose heterogeneities caused by residual tumor motion was investigated. For this purpose, a 4D treatment planning system (4DTPS) for the treatment of moving tumors with a scanned ion beam was developed based on previous efforts at GSI Helmholtz Center for Heavy Ion Research (GSI). The system was validated in dedicated experiments, reaching an accuracy of $(-1 \pm 4)\,\%$ for the typical beam configuration. The new software enabled extensive experiments, simulations, and treatment planning studies for liver cancer patients. The results show that an enlarged beam spot size can considerably mitigate motion-induced dose inhomogeneities for treatments with respiratory gating and under abdominal compression. Moreover, the 4DTPS allowed 4D dose reconstructions of the first treatments of liver tumors with a scanned ion beam at the Heidelberg Ion-Beam Therapy Center (HIT), revealing a considerable degradation of the dose coverage in an exemplary case ($V_{95} = 92.8\,\%$).

The 4DTPS is currently used as a basis for further research at GSI and by international collaborators. Results of this work have contributed to the world's first treatments of moving liver tumors with a scanned carbon ion beam at HIT.

Zusammenfassung

Die Bestrahlung bewegter Tumoren mit gescannten Ionenstrahlen stellt hohe Anforderungen an Strahlapplikation und Bestrahlungsplanung. Interferenzen zwischen Tumor- und Strahlbewegung (sogenanntes Interplay) können bei dieser Therapieform zu einer klinisch inakzeptablen Beeinträchtigung der applizierten Dosis führen. Spezielle Techniken, wie die unterbrochene Bestrahlung (Gating) oder die Bestrahlung unter abdominaler Kompression, ermöglichen eine effektive Einschränkung der Tumorbewegung, jedoch in der Regel keine vollständige Kompensation der Dosisbeeinträchtigungen.

Ziel dieser Arbeit war die Durchführung von Studien zur Kompensation von Dosisinhomogenitäten mit Hilfe optimierter Bestrahlungsparameter. Hierfür war zunächst die Weiterentwicklung eines 4D-Bestrahlungsplanungsprogramms für die Bestrahlung bewegter Tumoren mit einem gescannten Ionenstrahl notwendig. Bei der experimentellen Validierung des Systems konnte für die typische Strahlkonfiguration eine Übereinstimmung der gerechneten und gemessenen Dosis von im Mittel $(-1 \pm 4)\,\%$ erreicht werden. In auf dieser Basis durchgeführten Experimenten, Simulationen und Bestrahlungsplanungsstudien für Lebertumorbehandlungen konnte gezeigt werden, dass insbesondere die Verwendung eines vergrößerten Strahlfokus in Verbindung mit Gating und abdominaler Kompression eine deutliche Verringerung der bewegungsbedingten Dosisbeeinträchtigungen erzielt. Weiterhin wurden mit Hilfe des Systems Dosisrekonstruktionen der ersten Bestrahlungen von Lebertumoren am Heidelberger Ionenstrahl-Therapiezentrum (HIT) durchgeführt und ergaben beispielhaft bewegungsinduzierte Abweichungen von rund 7 % in Bezug auf die geplante Dosisabdeckung ($V_{95} = 92.8\,\%$).

Das 4D-Bestrahlungsplanungsprogramm wird derzeit als Grundlage weiterer Forschungsarbeiten am GSI Helmholtz Center for Heavy Ion Research (GSI) und von internationalen Kollaborationspartnern genutzt. Ergebnisse aus dieser Arbeit flossen in die Vorbereitung der weltweit ersten Bestrahlungen von atembewegten Lebertumoren mit einem gescannten Kohlenstoffstrahl am HIT ein.

Publications related to this work

Peer-reviewed articles

Steidl P., **Richter D.**, Schuy C., Schubert E., Haberer Th., Durante M., and Bert C. (2012). A breathing thorax phantom with independently programmable 6D tumour motion for dosimetric measurements in radiation therapy. *Physics in Medicine & Biology*, 57(8):2235–2250.

Bert C., **Richter D.**, Durante M. and Rietzel E. (2012). Scanned carbon beam irradiation of moving films: comparison of measured and calculated response. *Radiation Oncology*. 7(1):55.

Knopf A., Bert C., Heath E., Nill S., Kraus K., **Richter D.**, Hug E., Pedroni E., Safai S., Albertini F., Zenklusen S., Boye D., Söhn M., Soukup M., Sobotta B. and Lomax A. (2010). Special report: workshop on 4D-treatment planning in actively scanned particle therapy—recommendations, technical challenges, and future research directions. *Medical Physics*, 37(9):4608–14.

Scientific reports

Richter D., Steidl P., Saito N., Härtig M., Jäkel O., Durante M. and Bert C. (2011). Simulation of uncompensated and gated treatments of a liver cancer patient with scanned carbon ions. *GSI Scientific Report 2011*, 548.

Richter D., Trautmann J., Schwarzkopf A., Krämer M., Lüchtenborg R., Eley J.G., Gemmel A., Bert C., Durante M. (2010). Status of 4D Treatment Planning Implementations for TRiP98. *GSI Scientific Report 2010*, 476.

Richter D., Trautmann J., Schwarzkopf A., Krämer M., Gemmel A., Jäkel O., Durante M., Bert C. (2009). 4D Treatment Planning Implementations for TRiP98. *GSI Scientific Report 2009*, 500.

Patent applications

Steidl P., **Richter D.**, Schuy C., Schubert E., Bert C. (2010). Bestrahlungsphantom. *Patent application*, DE 10 2010 061 121.2.

Bert, C., Lüchtenborg, R., and **Richter, D.** (2009). Bestrahlungsverfahren und Vorrichtung zur Durchführung des Verfahrens. *Patent application*, DE 10 2009 058 294.0.

Conference contributions

Richter D., Steidl P., Trautmann J., Schwarzkopf A., Krämer M., Gemmel A., Naumann J., Panse R., Saito N., Jäkel O., Durante M., and Bert C. (2010). Mitigation of residual motion effects in scanned ion beam therapy. *Radiotherapy and Oncology, 96(Supplement 1)*:S72. Oral presentation.

Richter D., Steidl P., Gemmel A., Brons S., Panse R., Jäkel O., Durante M., and Bert C. (2011). Beam Parameter Optimization for Motion Mitigation in Scanned Ion Beam Radiotherapy. *PTCOG 50*. Oral presentation.

Richter D., Trautmann J., Schwarzkopf A., Gemmel A., Krämer M., Jäkel O., Durante M. und Bert C. (2009). 4D Bestrahlungsplanung für bewegte Organe in der Radiotherapie mit einem gescannten Ionenstrahl. *DPG Frühjahrstagung*. Oral presentation.

Contents

List of Abbreviations

LBL	Lawrence Berkeley Laboratory
LLUMC	Loma Linda University Medical Center
USA	United States of America
NIRS	National Institute of Radiological Sciences
GSI	GSI Helmholtz Center for Heavy Ion Research
PSI	Paul Scherrer Institut
DKFZ	German Cancer Research Center
UCHD	University Clinic Heidelberg
FZD	Research Center Rossendorf
MGH	Massachusetts General Hospital
HIT	Heidelberg Ion-Beam Therapy Center
RPTC	Rinecker Proton Therapy Center
MDACC	MD Anderson Cancer Center
RBE	relative biological effectiveness
LET	linear energy transfer
DNA	deoxyribonucleic acid
ICRU	International Commission on Radiation Units and Measurements
LEM	local effect model
SOBP	spread-out Bragg peak
PMMA	polymethyl methacrylate
BEV	beam's-eye-view
IMPT	intensity-modulated particle therapy
IES	iso-energy slice
MWPC	multi-wire proportional chamber
TCS	treatment control system
ACS	accelerator control system
RiFi	ripple-filter
IMRT	intensity-modulated radiation therapy
SI	superior-inferior
AP	anterior-posterior
LR	left-right
4D	four-dimensional
ART	adaptive radiotherapy
KO	knock-out extraction
CT	computed tomography
GW	gating window
3DCT	three-dimensional computed tomography
MRI	magnetic resonance imaging
PET	positron emmission tomography
4DCT	time-resolved computed tomography
GTV	gross tumor volume
CTV	clinical target volume
PTV	planning target volume
OAR	organ at risk
TPS	treatment planning system
FWHM	full width at half maximum
HU	Hounsfield unit
WEPL	water-equivalent path length
4DTP	4D treatment planning

4DRT	4D radiotherapy
ROI	region of interest
ITV	internal target volume
4DTPS	4D treatment planning system
MVH	motion volume histogram
VBM	volumetric boolean mask
RDBT	real-time dose compensation combined with beam tracking
AB	amplitude-based
PB	phase-based
RB	relative-amplitude-based
BDS	beam delivery sequence
BDE	beam delivery event
MSC	motion state change
DAQ	data acquisition system
IC	ionization chamber
TTL	transistor-transistor logic
RMSE	root-mean-square error
SD	standard deviation
BED	biologically effective dose
UD	up-down
BF	back-front
FL	focus level
DVH	dose volume histogram
HI	dose homogeneity index
CI	dose conformity index
CN	conformation number
HCC	hepatocellular carcinoma
PCC	Pearson correlation coefficient

1 Introduction

1.1 Motivation

According to the German Federal Statistical Office (Destatis), in 2010, every fourth case of death in Germany—that is over 218.000—was due to cancer (2012). Today, the available treatment options for cancer include surgery, chemotherapy, radiotherapy and combinations of these. The goal of radiotherapy is the sterilization of all tumor cells, while protecting normal tissue at the highest possible level. As a promising alternative to modern x-ray therapy, ion beam therapy has been developed at several research facilities over the last twenty years. Clinical studies have shown that the physical and biological advantages of ion beams enable superior dose conformity and tumor control rates for some indications (Durante and Loeffler, 2010; Schulz-Ertner et al., 2007; Tsujii et al., 2004). At most facilities, broad beams and patient-specific absorbers are used to conform the dose to the tumor (passive beam delivery). As a promising alternative, a *beam scanning* technique has demonstrated potential for treatments with even higher precision. The technique employs a narrow beam (pencil beam) to sequentially irradiate the tumor. However, the full benefit of this technique currently can only be realized for stationary tumors. Tumors in the chest or abdomen, such as lung and liver tumors, usually are subject to respiratory-induced motion. The interaction of tumor and pencil beam motion (interplay) results in strongly inhomogeneous dose distributions, compromising the precision of the beam scanning technique. Hence, only few patients with moving tumors have so far been treated with scanned ion beams. Most of these treatments were delivered in apnea under general anesthesia which poses further clinical workload (RPTC, 2011). Several other strategies have been proposed to facilitate the safe treatment of moving tumors. One of these techniques is synchronization of the irradiation with the tumor motion, such that the tumor is only irradiated in a defined motion window, so-called *gating* (Minohara et al., 2000). An alternative approach is constriction of the tumor motion using *abdominal compression* (Hof et al., 2003). Both techniques have been used for the treatment of liver cancer at Heidelberg Ion-Beam Therapy Center (HIT) since 2011.

Patients with liver cancer have an especially poor prognosis. The five year survival rate is only ten percent (Robert Koch Institute, 2012). Historically, the application of radiotherapy for inoperable liver cancer was limited by the dose tolerance level of the normal liver tissue (Skinner et al., 2011). Although modern x-ray therapy can safely deliver these treatments, there is evidence that a further dose increase can improve the survival rate for these patients (Dawson et al., 2000; Seong et al., 2003). Clinical studies at National Institute of Radiological Sciences (NIRS) in Chiba (Japan) indicate that the treatment of liver tumors with passively delivered carbon ions is safe and effective (Kato et al., 2004). The application of scanned carbon ion beam therapy at HIT for these tumors, therefore, seems promising.

This dissertation addresses the topic of treatment planning for moving tumors in scanned ion beam therapy. In the context of the liver treatments at HIT, particular focus is given to the compensation of dose degradation caused by residual tumor motion.

1.2 Scope of this work

The scope of this dissertation can be grouped into two main objectives:

(I) A research treatment planning system for scanned carbon ion therapy is to be developed, which is suited for treatment planning of moving tumors. The developments should be based on previous work in this particular field by other authors (Krämer et al., 2000; Bert and Rietzel, 2007; Gemmel et al., 2011) and consider the current state of research in radiotherapy of moving tumors. The extension of existing functionality is to be focused on the application to a clinical environment.

(II) The safe treatment of moving liver tumors requires precautions like gating or abdominal compression. However, residual tumor motion can still cause unacceptable dose degradation. To address this issue, Bert et al. (2009) have proposed a concept of robust superposition of pencil beams. Experiments and simulation studies are to be conducted which extend this concept to complex geometries. Furthermore, treatment planning studies with patient data are required, in order to assess the clinical applicability of the concept.

The structure of this dissertation is as follows. Chapter 2 will give an overview of the physical and biological fundamentals of ion beam therapy. Furthermore, the impact of organ motion on beam delivery and the treatment planning process will be introduced. Chapter 3 will deal with the implementation and verification of a treatment planning system geared to the treatment of moving tumors with scanned ion beams. In chapter 4, the impact of a robust superposition of pencil beams on the delivered dose to moving targets is studied in experiments and simulations. In the subsequent chapter, the concept is transferred to treatment planning for carbon ion therapy of liver cancer using patient data. A discussion of the results and future directions will be given in chapter 6. Finally, the thesis will be concluded in chapter 7.

2 Research background and fundamentals

In this chapter the field of research will be introduced in which this work is embedded and the conceptions required for the understanding of the subsequent chapters will be clarified. The chapter consists of four parts. The first section will introduce the physical, biological and technical fundamentals of ion beam radiotherapy. Subsequently, the problem of organ motion in radiotherapy will be addressed. In particular, the implications for scanned ion beam therapy will be emphasized. The necessary precautions for the deployment of scanned ion beams in the presence of organ motion include a dedicated treatment planning work flow which will be introduced in the third section. Finally, a brief summary will be given.

2.1 Ion beam therapy

In the past decades ion beam therapy has developed alongside conventional x-ray therapy into a promising branch of radiation therapy that offers superior dose distributions while sparing normal tissue to a large extent (figure 2.1 on the following page). In 1946 Robert R. Wilson first recognized the potential benefits of the favorable depth-dose profile of ion beams for precision cancer therapy (Wilson, 1946). Initial research on the physical and biological properties of protons was followed by the first patient treatments with proton beams at Lawrence Berkeley Laboratory (LBL), Berkeley (USA) in the early 1950s (Tobias et al., 1958). The first proton therapy facility embedded in a clinical environment started operation in 1990 at Loma Linda University Medical Center (LLUMC) (USA), soon followed by other facilities in the United States, like the Francis H. Burr Proton Therapy Center at Massachusetts General Hospital (MGH).

In the mid-1970s for the first time also heavier ions, mainly He^{2+} and ^{20}Ne, were employed for therapy at LBL, to exploit their increased biological effectiveness. Shortly after the end of the Berkeley ion therapy project in the early 1990s the heavy ion therapy project at NIRS in Chiba (Japan) started to employ similar concepts for carbon ions like those pioneered at LBL (Hirao et al., 1992). Up to that time only passive beam delivery systems had been used for ion beam therapy (section 2.1.3.1). In parallel, more elaborate active beam delivery solutions (section 2.1.3.2) were developed at Paul Scherrer Institut (PSI), Villigen (Switzerland) for protons (Pedroni et al., 1995) and at GSI, Darmstadt (Germany) for ^{12}C ions (Haberer et al., 1993).

From 1997–2008 the first patient treatments with a scanned heavy ion beam were performed in a clinical trial at GSI in close collaboration with the German Cancer Research Center (DKFZ), the University Clinic Heidelberg (UCHD) and the Research Center Rossendorf (FZD). Most of the over 400 patients had tumors in the brain or at the base of the skull. A dedicated treatment planning system was used for treatment plan optimization, including full biological modeling of the enhanced biological effectiveness of the ^{12}C ions (Krämer et al., 2000; Krämer and Scholz, 2000). Despite the technical complexity of the system, the raster-scan technique has proven capable of sub-millimeter accuracy and stable operation. Clinical follow-up studies have shown high control rates for the treated tumor entities combined with very low side effects (Schulz-Ertner et al., 2007). These promising clinical results have encouraged the

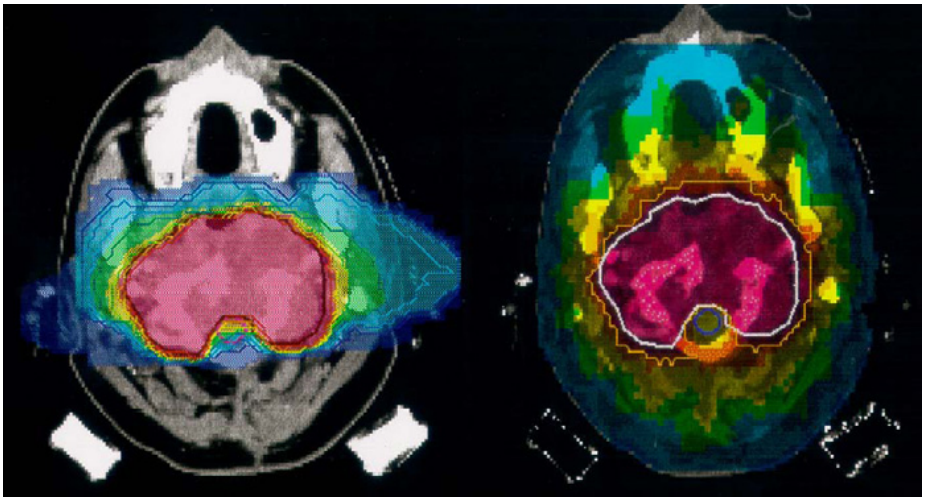

Figure 2.1.: Comparison of treatment plans for scanned carbon ions (intensity-modulated particle therapy) with 2 fields (left) and x-rays (intensity-modulated radiation therapy) with 9 fields (right). At a comparable level of dose conformity the dose to normal tissue is drastically reduced for the IMPT plan. Figure from (Amaldi and Kraft, 2005).

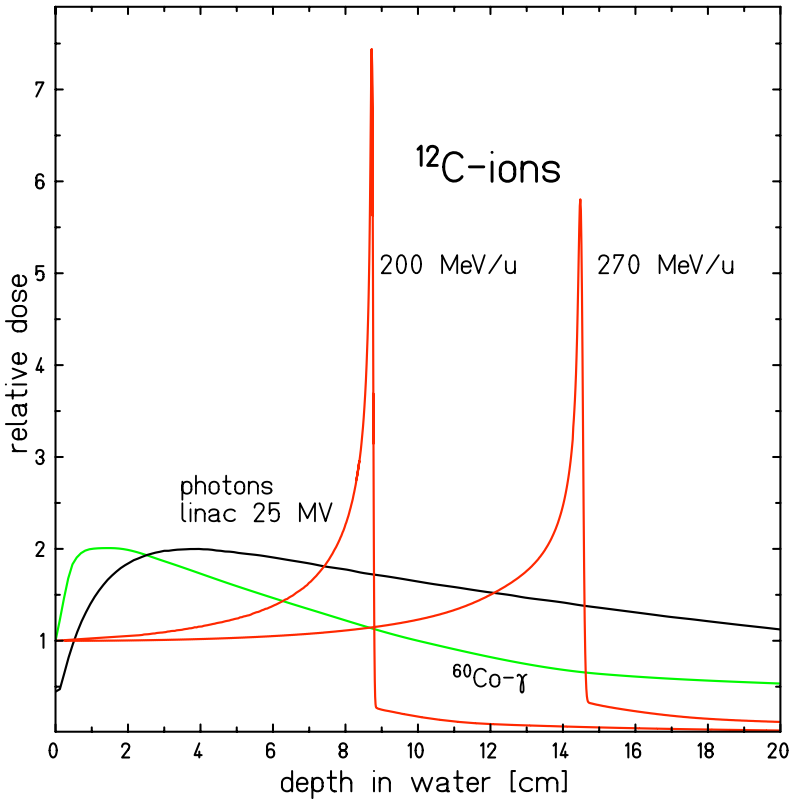

Figure 2.2.: Depth-dose profiles in water for photon and ^{12}C ion radiation at different energies. The relative dose for ^{12}C ions features a sharp maximum at the end of the finite range. The photon curve drops exponentially after reaching a maximum in the entrance channel (build-up effect). The decrease of the Bragg maximum and the increased width is caused by a larger energy loss straggling. The tail after the Bragg maximum is caused by lighter fragments due to nuclear reactions. From Schardt et al. (2010).

design and construction of several dedicated heavy ion facilities based on the scanning technique. As the first clinical center employing beam scanning, the HIT started clinical operation in 2009 (Haberer et al., 2004; Combs et al., 2010). A similar scanning system for carbon therapy was implemented at NIRS Furukawa et al. (2010b). The first centers using commercial beam scanning systems for protons were the MD Anderson Cancer Center (MDACC), Houston (USA) in 2006 and the Rinecker Proton Therapy Center (RPTC), Munich (Germany) in 2009. Several other facilities are presently under construction or in the planning phase. To date worldwide about 40 ion-beam therapy facilities are in operation, most of them using proton beams with passive beam delivery systems. About 20 facilities are in the design or construction phase, four of them are designed to use carbon ion beams (PTCOG, 2011).

The following sections will introduce the physical, biological and technical concepts of ion beam therapy. After a brief discussion of the underlying physics of ion beams the implications for radiobiology will be discussed. Since large parts of this work require a basic understanding of the technical framework of ion beam delivery, especially of the fully active scanner systems as they are used at GSI and HIT, a separate section will be dedicated to their introduction.

2.1.1 Physical properties

The main rationale for using ion beams for localized tumor therapy is their favorable depth-dose profile compared to photons. A comparison of the depth-dose curves for photons and ions with different energies is shown in figure 2.2 on the preceding page (Schardt et al., 2010). After a shallow maximum in the entrance region, caused by the dose build-up due to forward scattered Compton electrons (Alpen, 1998), the photon depth dose profile drops exponentially with the penetration depth. In contrast, the ion depth dose-curve features a distinct narrow peak with a sharp dose fall-off at the end of the particle range. This curve is called *Bragg curve* or *Bragg peak*, named after its discoverer, Sir William Henri Bragg (Bragg, 1905). The position of the Bragg peak in depth can be precisely controlled by varying the kinetic energy of the incident ions. This 'inverse' depth-dose profile, the small lateral scattering and the finite particle range evidently are particularly appealing for the treatment of deep-seated tumors, sparing normal tissue, especially behind the Bragg peak. The underlying physics will be discussed in the following sections.

2.1.1.1 Dose deposition and electronic stopping

The dose, D, deposited in the tissue is of central importance in radiotherapy and is defined by the ratio of the absorbed energy dE per mass element dm (ICRU, 1993b):

$$D = \frac{dE}{dm} \quad \left[1\,\mathrm{Gy} = 1\,\mathrm{J/kg}\right]. \tag{2.1}$$

For a parallel beam traversing a thin layer of material the absorbed dose is determined by the *specific energy loss* per unit length or *stopping power* of the particles, dE/dx, the fluence, F, and the material mass density, ρ:

$$D[\mathrm{Gy}] = 1.6 \cdot 10^{-9} \times \frac{dE}{dx}\left[\frac{\mathrm{keV}}{\mu\mathrm{m}}\right] \times F\left[\mathrm{cm}^{-2}\right] \times \frac{1}{\rho}\left[\frac{\mathrm{cm}^3}{\mathrm{g}}\right]. \tag{2.2}$$

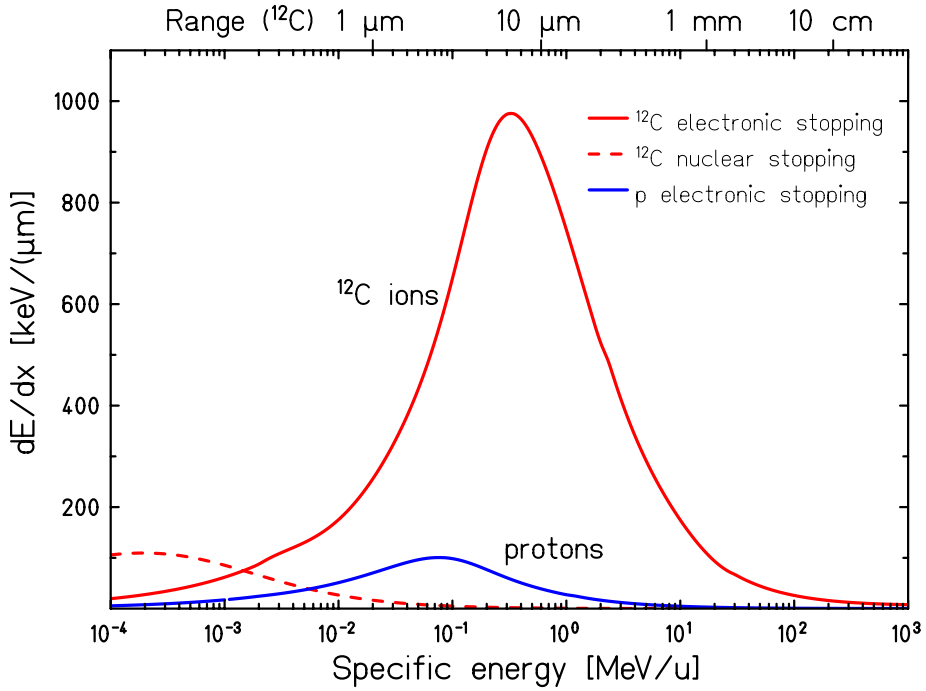

Figure 2.3.: Specific energy loss of ^{12}C and protons in water (Schardt et al., 2010).

Different energy loss processes contribute to the total stopping power, dE/dx. The required maximum penetration depth of about 30 cm in the human body corresponds to kinetic energies of protons and carbon ions of 200 and 430 MeV/u, respectively. In this medium relativistic regime the total stopping power is dominated by inelastic scattering of the ions with the target electrons. The collisions result in ionization and excitation of the target atoms. Elastic collisions with the target nuclei (nuclear stopping) only contribute significantly to the total energy loss at very small particle energies, i.e. near the end of their range. Radiative energy losses play a role in the highly relativistic regime only and therefore can be neglected as well (Nakamura and Particle Data Group, 2010). Thus, the considerations will be limited to the electronic stopping power here.

In the energy range of interest the electronic stopping power is well described by the Bethe formula (Bethe, 1930; Bloch, 1933b,a; Fano, 1963)

$$-\left\langle \frac{dE}{dx} \right\rangle = \frac{4\pi e^4 Z z^2}{m_e c^2 \beta^2} \left[\ln\left(\frac{2 m_e c^2 \beta^2}{I(1-\beta^2)} \right) - \beta^2 - \frac{C}{Z} \right] \tag{2.3}$$

Here $\beta = v/c$ is given by the velocity v of the incident particle normalized to the speed of light c. Z and z are the nuclear charges of the target and the projectile, respectively. m_e denotes the mass and e the elementary charge of the electron. The mean ionization potential, I, of the target atoms or molecules is usually obtained empirically and is around 75–78 eV for liquid water (Schardt et al., 2008; Paul, 2007; Kumazaki et al., 2007). Values for other materials are summarized in ICRU (1993, 1984). Equation (2.3) also includes the shell correction term, C/Z, which takes into account the orbital velocities of the target electrons at low particle energies. Detailed reviews on the shell correction term and other low energy corrections of the electronic stopping power are given in (ICRU, 1993; Ziegler, 1999).

Figure 2.3 shows the mean electronic stopping power for carbon ions and protons in the relevant energy regime for ion beam therapy (Schardt et al., 2010). The energy loss increases

sharply with decreasing particle velocity, due to the $1/\beta^2$ dependence in (2.3). At lower velocities recombination processes with the target electrons gradually lower the effective charge of the projectile and result into a decreasing energy loss rate after reaching a maximum at a specific energy of ≈350 keV/u in the case of ^{12}C ions. This effect can be incorporated into (2.3) by replacing z with the effective charge z_{eff}. Empirically z_{eff} can be parametrized using Barkas' formula (Barkas and Berger, 1964):

$$z_{\text{eff}} = z\left[1 - \exp(-125\beta z^{-2/3})\right]. \tag{2.4}$$

Figure 2.3 also shows the minor contribution of the elastic scattering with the target nuclei at the very end of the particle range (dashed line).

2.1.1.2 Range straggling and lateral scattering

The Bethe formula describes the *mean* electronic stopping power only. However, energy loss by inelastic Coulomb scattering is governed by large statistical fluctuations. For a beam of many slowing down particles this results in a significant broadening and a reduced peak-to-entrance dose ratio of the Bragg peak (figure 2.2). In the limit of a large number of collisions or thick layers the energy loss obeys a Gaussian probability distribution. The energy loss fluctuations directly translate into *range straggling* (Bohr, 1940; Ahlen, 1980). The ratio σ_R/R of the straggling width σ_R and the mean range R is proportional to $1/\sqrt{M}$ with M, the ion mass. Thus, the broadening of the Bragg peak is less pronounced for heavier ions. For example the ratio σ_R/R is about a factor 3.5 smaller for ^{12}C ions than for protons (Schardt et al., 2010).

On their way through the material the particles undergo small lateral deflections, due to elastic scattering off the target nuclei. This has been described analytically by Molière (1948) and is in very good agreement with measurements (Gottschalk et al., 1993). Heavier target nuclei cause a larger angular spread for the same thickness of a material layer. The angular spread also depends significantly on the particle's energy and increases towards the lower end of the particle range. Compared to a proton beam with the same range in water of about 16 cm the angular spread of a ^{12}C beam is more than three times smaller (Schardt et al., 2010). In clinical practice ion beams therefore offer significantly sharper dose gradients and better sparing of normal tissue (Weber and Kraft, 2009).

2.1.1.3 Nuclear fragmentation

The cross section for nuclear interactions is orders of magnitude smaller than for Coulomb interaction. Nuclear fragmentation reactions nevertheless play a significant role at large penetration depths. For ions heavier than protons projectile fragments contribute significantly to the absorbed dose and lead to dose tails at the distal end of the depth dose profile (figure 2.2). To a lesser extent fragments of the target nuclei also contribute. However, these have very low ranges and do not travel with the beam. For all ions except protons projectile fragmentation is the dominant process. In collisions of the projectile with a target nucleus a partial disintegration of the projectile results into excited states of the remaining projectile fragments, followed by de-excitation through the emission of nucleons, nucleon clusters and photons. Detailed reviews of the underlying fundamental processes have been published elsewhere (Goldhaber and Heckman, 1978; Hüfner, 1985; Lynch, 1987).

Nuclear fragmentation leads to a loss of primary particles and a build-up of mostly lower-Z fragments increasing with depth. For kinematical reasons these lighter fragments move with approximately the same velocity and into the same direction as the primary particles. While the rare heavier fragments are stopped rather quickly, the lighter hydrogen and helium fragments have larger ranges and produce significant dose tails behind the Bragg peak. Due to the exponential loss of primary particles, the depth dose profiles feature a gradually diminishing peak-to-entrance dose ratio (figure 2.2). Additionally the profiles are increasingly broadened by straggling (Schardt et al., 2010). These effects are more pronounced for heavier ions and become intolerable for therapy for ions heavier than ^{20}Ne (Kraft, 2000). Taking into account the dose contributions of nuclear fragments based on measured data is essential for treatment planning. This is particularly important for the inclusion of the biological efficacy of the different constituents of a mixed particle beam (section 2.1.2). For this reason, measurements have been performed at many centers to assess the magnitude of fragmentation, the relative composition of isotopes and their contribution to the absorbed dose (Maccabee and Ritter, 1974; Schimmerling et al., 1983; Llacer et al., 1984; Schall et al., 1996; Hättner et al., 2006).

2.1.1.4 Track structure and radial dose distribution

Ions lose their energy by ionization and excitation of the target electrons via inelastic Coulomb scattering. The liberated electrons undergo frequent elastic and inelastic scattering and may cause secondary ionization of the target atoms if their kinetic energy is sufficiently high. For electron energies larger than ≈50 eV ionization is the dominant process leading to large numbers of additional electrons (Kraft, 2000; Schardt et al., 2010). The energy spectrum of the electrons defines both, the radial dose profile around the track and the track diameter. Since most of the electrons only receive small energy transfers or are scattered in forward direction, the radial dose is concentrated at the track core and quickly falls off with larger radial distances r. The existing models (Chatterjee and Schaefer, 1976; Katz and Cucinotta, 1999) and Monte Carlo codes (Paretzke, 1986; Krämer, 1995) all predict an approximate $1/r^2$ dependence for the radial dose fall-off. This has been confirmed by dosimetry experiments (Varma et al., 1977). For the dose contribution at smaller radii than 10 nm a flat profile is often assumed (Scholz and Kraft, 1996). The maximum track extension, $r_{\max}$, is determined by the energy of the most energetic electrons and empirically can be related to the energy, E, of the primary particle: $r_{\max} \propto E^{1.7}$ (Kiefer and Straaten, 1986). Due to the z^2 and the $1/\beta^2$ dependence of equation (2.3), the track structure of ions is considerably dependent on the ion species and energy. Figure 2.4 on the facing page demonstrates the much more dense ionization patterns of carbon ions compared to protons at different energies obtained by a Monte Carlo simulation (Krämer and Durante, 2010). Most of the electrons have very low energies, resulting into ranges on the nanometer scale and a very localized energy deposition. For decreasing energy the increasing stopping power of the ions translates into significantly larger numbers of secondary electrons. The energy deposition of the electrons in the material is often described using the *linear energy transfer (LET)* or *restricted energy loss*. The LET is closely related to dE/dx and defines the *locally* transferred energy to the medium, excluding contributions of electrons with energies above a certain threshold (ICRU, 1984; Nakamura and Particle Data Group, 2010).

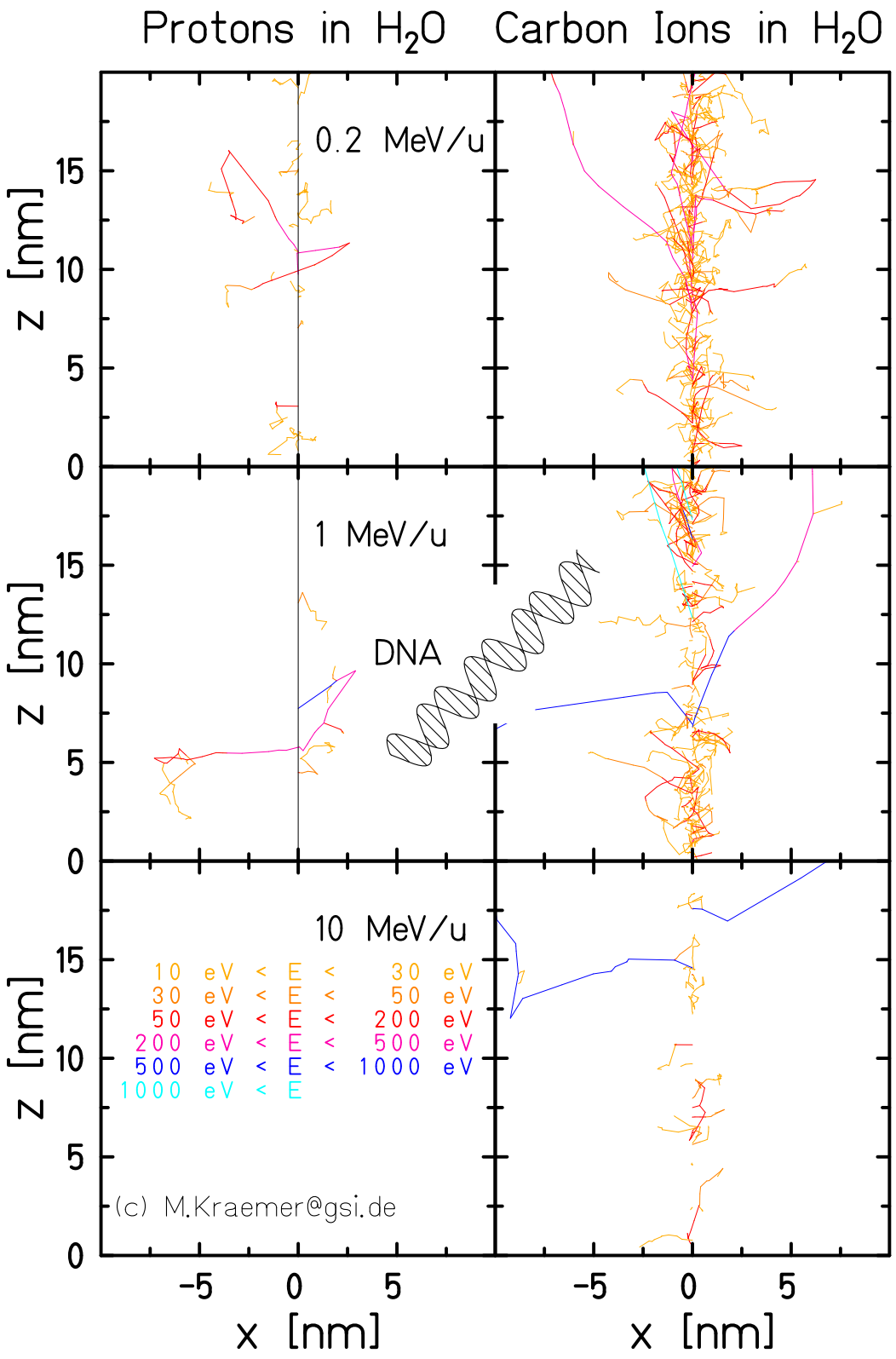

Figure 2.4.: Simulated paths of secondary electrons with different energies created by protons and carbon ions at different specific energies. The DNA molecule illustrates the geometrical dimension of the track structure. Figure courtesy of M. Krämer.

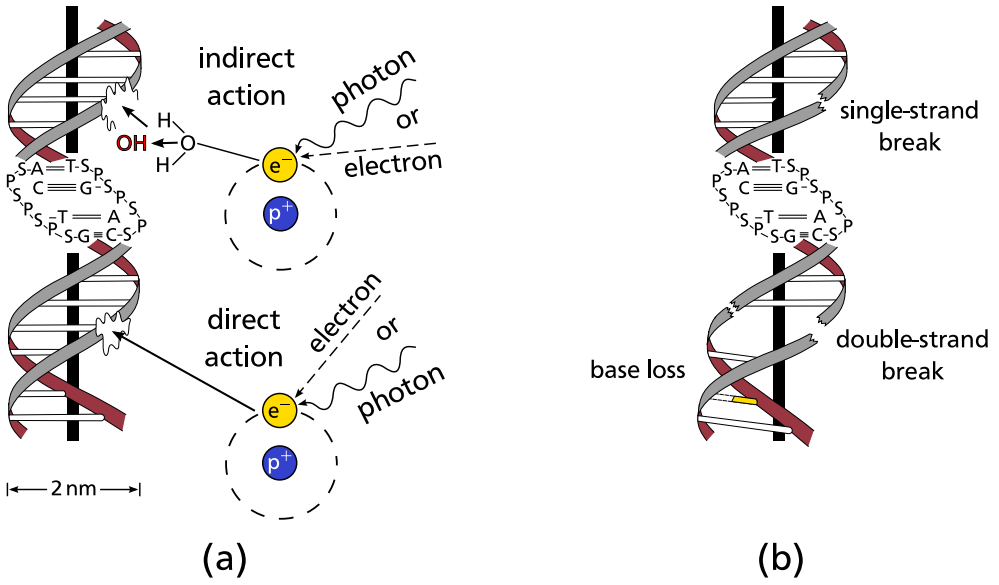

Figure 2.5.: (a) Direct and indirect radiation damage to the DNA. Direct damage is caused by energy deposition in direct hits from electrons liberated in ionization processes. Free hydroxyl radicals (OH), formed by ionization in the hydrolysis of water, can cause indirect damage to the DNA in chemical reactions. (b) Schematic illustration of selected types of radiation damage to the DNA. The effectiveness of the repair mechanisms of cells depends on the complexity of the damage.

2.1.2 Radiobiology

The goal of radiotherapy is to inactivate all tumor cells and thus prevent further cell growth and cell division. Radiation damage can be induced everywhere in the cell. However, it is commonly acknowledged that the most critical structure of a cell with respect to radiation damage is the deoxyribonucleic acid (DNA) which is located inside the cell nucleus (Munro, 1970). Although cells have a number of sophisticated repair mechanisms, the repair capacities are limited, depending on the type of damage (Sancar et al., 2004). Commonly, direct and indirect radiation-provoked effects are distinguished, as shown schematically in figure 2.5a. **Direct effects** are caused by the ionization of a DNA constituent itself. Consequently, molecular bonds can be destroyed and result in break-up of a single or both DNA strands (figure 2.5b). Furthermore, randomly created new bonds may be formed and alter the DNA structure. While single-strand breaks can be repaired rather efficiently, double-strand breaks often result in eventual cell death. In general, they are considered the critical events for lethal lesions. Direct effects are of increased importance for ion radiation. For more sparsely ionizing radiation like photons, however, the majority of the radiation-induced effects are **indirect effects**. Most notably, free and highly reactive hydroxyl-radicals (OH) are created in the radiation-induced hydrolysis of water molecules surrounding the cell nucleus. Although they have a short lifetime, they can migrate over several nanometers and are capable of damaging the DNA structure. Due to larger recombination of radicals these effects are of less importance for ion radiation. Direct and indirect radiation damage occur in parallel and can accumulate to an extent so that the repair of the DNA is no longer possible.

A key advantage of heavy ion beams in radiotherapy applications is their increased biological efficiency in the target region, compared to photon irradiation. The large ionization densities along the ion tracks at the Bragg peak can cause clustered lesions of the DNA molecule, i.e. multiple double-strand breaks, which have a small probability of being repaired, resulting into subsequent cell death. Figure 2.4 illustrates the spatial distribution of the secondary electron halo around the track of protons and ^{12}C ions in relation to the size of a DNA molecule. Most of the insight into the response of cells to radiation has been acquired for photon radiation. Hence, the biological effect of ion radiation is commonly described relative to a reference photon response, using the concept of the *relative biological effectiveness (RBE)*. The RBE is defined as the ratio of the reference photon dose to the dose level needed for a specific ion radiation in order to achieve the same biological effect (isoeffect)

$$\mathrm{RBE} = \frac{D_\gamma^{\mathrm{ref}}}{D_{\mathrm{ion}}}\bigg|_{\mathrm{isoeffect}} . \tag{2.5}$$

Comparisons of RBE values are valid only for the same effect and effect level (biological endpoint) and the same reference radiation. In ion beam tumor therapy the most relevant biological endpoints are cell survival and certain normal tissue side effects. In the following the term RBE is used synonymously with the RBE for cell survival. Figure 2.6 on the next page illustrates the calculation of RBE at the 10 % and 1 % survival level. The survival curve for ion irradiation shows a steeper fall-off in survival while the x-ray curve exhibits a characteristic shoulder. Consequently, the RBE values are dependent on the dose level. In addition to the physically absorbed dose, as defined in equation (2.1), the term of a *photon-equivalent* or *biological dose* incorporating the RBE is often convenient. The difference to the *physical dose* is marked by expressing the biological dose in units of GyE or Gy (RBE). The latter notation is recommended by the International Commission on Radiation Units and Measurements (ICRU) and will be used in the following (ICRU, 2007). The shouldered curve describing the cell survival, S, in dependence of the dose level, D, is commonly described by an exponential linear-quadratic model (LQ-model) (Fowler, 1989):

$$S(D) = \exp\left(-\alpha D - \beta D^2\right) \quad . \tag{2.6}$$

The ratio α/β is characteristic of the tissue type and radiation quality and is related to the repair capacities of the cells. A large α/β ratio indicates a small repair capacity or, equivalently, a large radiation sensitivity.

The systematics of the RBE are complex. Apart from the biological endpoint the RBE depends on other physical and biological parameters, the most important ones being the dose level, the LET, the particle species and the tissue type. The reader is referred to the reviews by Kraft (2000), Scholz (2003), Fokas et al. (2009) and Schardt et al. (2010) for detailed discussion of the various RBE systematics. It should be noted that the increased biological effectiveness of ions can only be exploited to the maximum extent if it is more pronounced in the tumor than in the normal tissue. Due to the LET dependence the RBE is elevated also in the entrance channel for relatively heavy ions, like argon. In contrast, carbon ions feature a sharp RBE maximum which coincides with the Bragg peak (Kraft, 2000). In proton therapy the assumption of a constant RBE of 1.1 over the treatment field is feasible (Paganetti et al., 2002). For carbon ions the RBE varies over a factor of ten from values close to 1.0 in the entrance channel to typical values around 5.0 in the target region. Even higher values of around 10.0 can result in the normal tissue beyond the field edges (Kraft and Kraft, 2009).

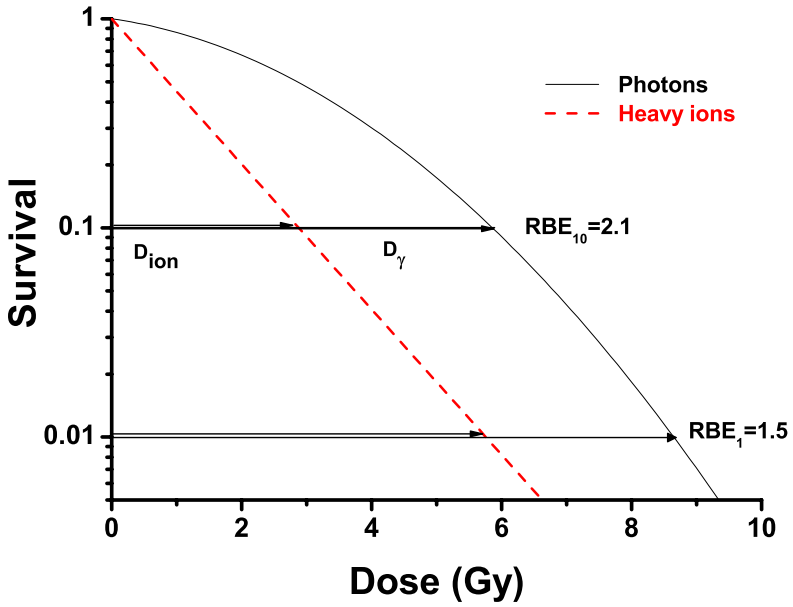

Figure 2.6.: Sketch of typical cell survival curves for photon and heavy ion irradiation. The ion curve shows a steeper decrease with dose and lacks the characteristic shouldered form of the photon curve. The RBE value depends on the survival level, or equivalently, on the dose level (Schardt et al., 2010).

The large variations in RBE facilitate the need for a biological model which is able to predict the RBE in a mixed radiation field over a wide range of atomic numbers and energies. At GSI this is done using the *local effect model (LEM)* developed by Scholz et al. (Scholz and Kraft, 1994, 1996). The model predicts the biological efficacy starting from the dose dependence of the cell inactivation by x-rays which was measured in cell experiments, the radial dose distribution around the particle track and the size of the cell nucleus. The general underlying assumption is that there is no fundamental difference in the physical dose deposited by photons or ions via secondary electrons. The different biological response solely originates from the characteristics of the dose deposition pattern. While for photons a homogeneous dose distribution over the cell nucleus can be assumed, particle irradiation leads to highly localized dose distributions at the same total dose. Assuming the x-ray response is valid also for these high local doses, the dose response for ions can then be determined according to the x-ray response at the same dose level. Improved versions of the LEM have been published over the years (Elsaesser and Scholz, 2006, 2007; Elsaesser et al., 2009) and the model has been successfully tested in numerous cell experiments (Mitaroff et al., 1998; Krämer and Scholz, 2000; Krämer et al., 2003) and is incorporated into the GSI treatment planning system which has been used in the past in clinical routine in the GSI pilot project from 1995–2008 (Krämer et al., 2000; Krämer and Scholz, 2000) as well as at HIT since 2009.

2.1.3 Beam delivery

Ion beam therapy requires complex beam delivery systems capable of accelerating ions to therapeutic energies of several hundred MeV/u, transporting the ion beams to the treatment area and guiding them onto the target with the necessary accuracy. Particle acceleration is typically realized using either cyclotron or synchrotron accelerators. **Cyclotrons** nowadays can be built

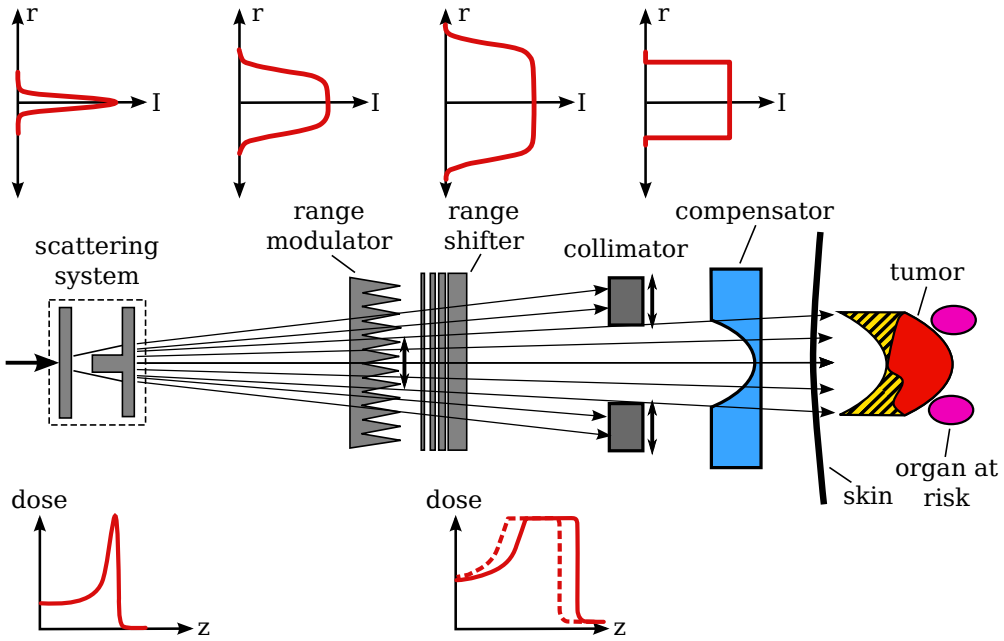

Figure 2.7.: Schematic of a passive beam delivery system. The narrow, mono-energetic beam is scattered to match the required lateral dimensions. Lateral and longitudinal adaption to the tumor is performed by different passive modulator devices. The distal edge of the tumor is conformed by an individually machined compensator. The hatched area indicates the resulting inevitable irradiation of normal tissue. Figure redrawn from (Schardt et al., 2010).

very compact and offer continuous beams with stable beam intensities. However, active energy variation is not possible with this design, therefore passive degraders have to be used at the cost of beam intensity and quality. **Synchrotrons** in contrast provide pulse-to-pulse active energy variation. The beams have to be injected into the synchrotron ring by a dedicated linear accelerator. Ion optics are used to keep the ions on track during further acceleration and storage. While cyclotrons are used in most proton facilities, to date all heavy ion centers employ the synchrotron solution.

A single Bragg peak does not adequately cover the target volume with a homogeneous dose, consequently the beams need to be shaped, once the beam has been guided to the treatment area. Two different strategies have been developed over the years and are in use today in different variations. The following section will introduce passive and active beam shaping systems, concentrating on the fully active beam delivery system at GSI and HIT which are of major interest in this work.

2.1.3.1 Passive beam shaping

Passive beam shaping systems employ different devices inserted into the beam line to manipulate the beam laterally and longitudinally. In the following, the basic concept shall be presented. More detailed overviews of passive beam shaping techniques and the specific devices can be found in Chu et al. (1993); Kraft (2000) and Gottschalk and Pedroni (2008). In figure 2.7 the concept of passive beam shaping is shown schematically. First the initial narrow beam is broadened with a scattering device to generate a broad and flat lateral beam profile. Here,

e.g., passive double scattering systems or magnetic wobbler devices are frequently used (Kraft, 2000). The mono energetic beam beam is then spread out over the required depth using a range modulator. In practice, ridge filters or rotating wheels of varying thickness are employed (Chu et al., 1993). Stacking of Bragg peaks at different depths results into a so-called *spread-out Bragg peak (SOBP)*. The SOBP is then shifted to the needed depth using a range shifter. Again, this is a passive absorber that is chosen at the required material thickness. The discussed devices are not patient-specific although, e.g., a whole library of range modulators may be needed for different longitudinal field extensions. In addition, devices machined individually for each patient are needed to tailor the beam to the respective target as much as possible. The lateral extension of the treatment field is defined by a collimator, typically made from brass, in order to yield sharp lateral field gradients. The collimator is followed by a range compensator usually made from polymethyl methacrylate (PMMA) and designed such that the SOBP is adjusted to the distal edge of the tumor in beam's-eye-view (BEV). A major deficiency of the compensator is the incapacity to form the proximal edge of the tumor. This results into parts of the SOBP dose being deposited in surrounding normal tissue, as depicted by the hatched area in figure 2.7.

For historical reasons, the vast majority of ion beam therapy centers worldwide employ passive beam delivery techniques. Although passive beam delivery techniques have been refined over the years, they carry intrinsic limitations, e.g., a restricted tumor conformity, the need for patient-specific hardware and an inflexibility in dose modulation. Many of the limitations can be overcome using active beam shaping techniques which will be introduced in the next section.

2.1.3.2 Active beam shaping

Active beam shaping systems employ beam scanning techniques to distribute the beam over the target area. The basic idea is to dissect the tumor into layers of iso-energy in beam's-eye-view (BEV). Each of these iso-energy layers or -slices is covered with a grid of target points which are irradiated sequentially using a thin pencil beam. This approach is suited to irradiate volumes of arbitrary shape without any need for additional patient-specific hardware. Since the dose can be modulated on a per-spot basis, the technique is intrinsically intensity-modulated and allows for very conformal treatments with extensive sparing of normal tissue (see also figure 2.1 on page 4). Also, variable RBE distributions can be incorporated into the planning at any point in the treatment field so that homogeneous biologically equivalent dose distributions can be realized. The amount of material in the beam is drastically reduced, yielding efficient beam usage and less neutron flux towards the patient.

Beam scanning has been developed in parallel at PSI for protons (spot scanning) and at GSI (raster scanning) for carbon ions in the 1990s. The strategy at PSI was to use a cyclotron with passive energy variation in combination with horizontal beam scanning, facilitated by magnetic deflection, and a mechanical couch displacement in the vertical direction. The reader is referred to Pedroni et al. (1995) for more details on the implementation.

In the following section the GSI concept of a fully active three-dimensional scanning system for therapy will be given attention to. For more comprehensive reviews the reader is referred to the literature (Haberer et al., 1993; Kraft, 2000; Schardt et al., 2010). A schematic of the GSI *raster-scan system*, is given in figure 2.8 on the next page. A thin pencil beam of ^{12}C ions is extracted from a synchrotron providing active energy control. The position of the Bragg peak in depth is defined by the beam energy. The dose is delivered slice-by-slice with each of the slices corresponding to a fixed beam energy (IES). The Bragg peaks are stacked in depth over the

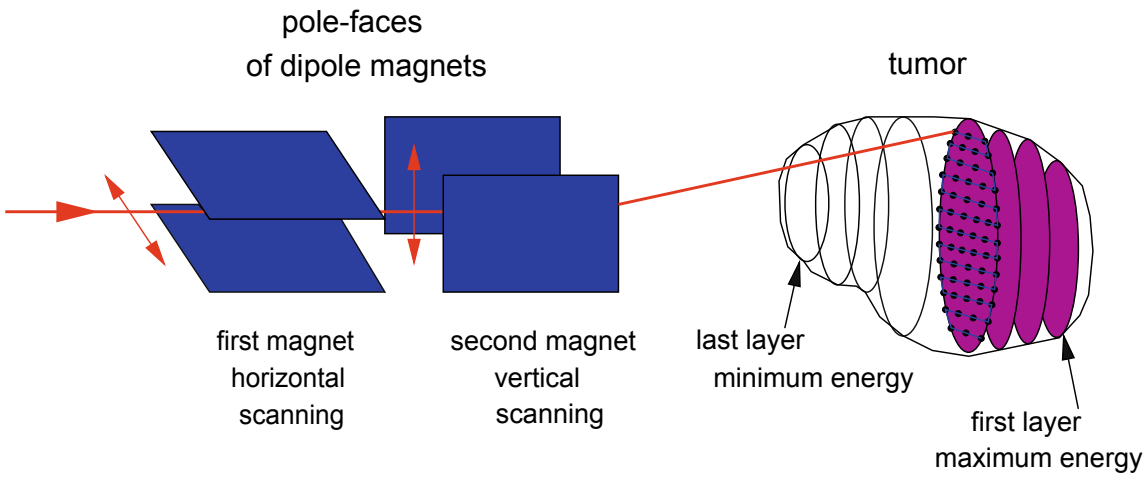

Figure 2.8.: Schematic of the GSI raster-scan system. The treatment is performed slice-by-slice by moving the beam on a meander-like path. The beam position and the delivered dose are constantly monitored and fed back into the treatment control system. Figure from Krämer (2009).

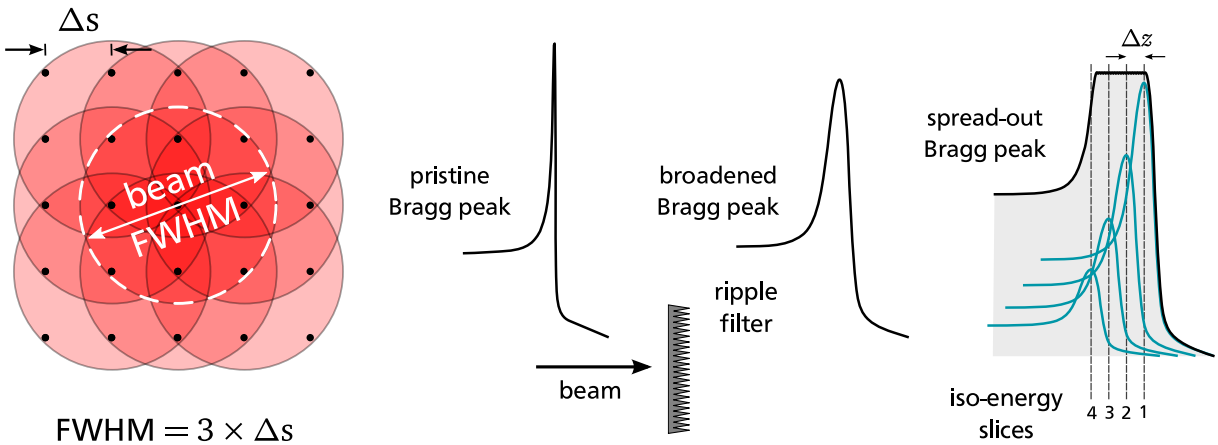

Figure 2.9.: (a) Lateral pencil beam overlap ensures adequate target dose homogeneity in the transversal direction. Commonly, the raster spacing, Δs, is adjusted to 2–3 mm and the beam's FWHM amounts to roughly three times the raster spacing. (b) The pristine Bragg peaks are broadened in depth using a ripple-filter (RiFi) and then are stacked in depth. Sufficient overlap is maintained to yield a homogeneous target dose in the longitudinal dimension (SOBP). The standard RiFi is optimized for an IES spacing, Δz, of 3 mm.

longitudinal extension of the tumor (figure 2.9b). In each IES a raster of target points, so-called raster points, is adjusted to match the tumor cross section in BEV. The beam is guided over the raster on a continuous and optimized path by two orthogonal magnetic deflection units. The dwell time of the beam at a raster point is controlled by an intensity monitoring system, moving the beam to the next position when the variable pre-defined dose of a raster point has been delivered. The stability of the beam position is ensured by using a fast feed-back loop between the magnet power supplies and two multi-wire proportional chambers (MWPCs) measuring the beam position. After the completion of an energy slice the irradiation is interrupted and the next beam energy is requested from the accelerator for the next IES of the treatment plan. The treatment control system (TCS) communicates with the accelerator control system (ACS) and requests the appropriate beam parameters and the beam intensity for each slice, namely the size of the beam spot, the beam energy and the beam intensity. For each of the available sets of beam parameters the ACS holds a data base with optimized settings for the synchrotron and all magnets in the beam line. In this way, the accelerator is capable of providing reproducible and stable conditions for each of the parameter sets. The technical design of the HIT beam delivery system in large parts is based on the GSI prototype and therefore is very similar. A major technical achievement is the transfer of the raster-scan concept to an iso-centric gantry system in one of the three treatment rooms (Haberer et al., 2004).

In raster-scanning at GSI the target dose homogeneity is assured by two means. Firstly, the lateral overlap of the thin pencil beams is chosen sufficiently large in order to compensate for the expected positioning uncertainties of the beam spots. This is illustrated in figure 2.9a for the typical configuration in which a beam FWHM of three times the lateral raster spacing is used. Secondly, the iso-energy slices spacing is chosen such that the individual Bragg peaks have enough overlap. However, the number of IESs should be kept small to reduce the treatment time. For this reason, the pristine Bragg peaks are broadened in depth by using a so-called *ripple-filter (RiFi)*—the only passive device in the beam line— similar to the ridge filters employed for passive beam delivery. The standard RiFi is optimized for an IES spacing of 3 mm and guarantees longitudinal dose homogeneity (Weber and Kraft, 1999). The concept of longitudinal beam overlap is shown in figure 2.9b. In chapter 4 the approach of achieving target dose homogeneity by lateral and longitudinal beam overlap in stationary irradiations will be extended to moving targets and constitutes one of the major research questions addressed in this thesis.

2.2 Treatment of moving tumors

Modern radiotherapy modalities like photon intensity-modulated radiation therapy (IMRT) and ion beam therapy offer high precision and superior dose conformity. The increased accuracy allows for treatment of tumors very close to critical structures sparing the normal tissue to a large extent. As a result of this development, the reduction of safety-margins and the escalation of the therapeutic dose in the tumor are of frequent clinical interest. However, at many sites of the human body the advantage of the increased conformity of these techniques is severely limited or compromised, due to organ motion. Normal tissue toxicity puts constraints on the therapeutic tumor dose, even though higher dose levels yield better local control and would be desirable for some entities (Rengan et al., 2004; Rosenzweig et al., 2005; Kong et al., 2005). Consequently, motion management constitutes a major contemporary research field in radiotherapy. This section will clarify the different manifestations of organ motion, their implications for ion beam therapy and the existing techniques proposed to mitigate motion effects.

2.2.1 Origin and extent of organ motion

The following section will briefly introduce the different types of organ motion or anatomy changes and their characteristics. Extensive reviews on the topic have been published elsewhere (Langen and Jones, 2001). Organ motion is commonly divided into patient motion, inter-fractional and intra-fractional motion.

Patient motion comprises position-related uncertainties during or in-between fractions or imaging sessions. The application of patient immobilization prior to each fraction is common clinical practice. Depending on the time-scale of patient motion it can impact inter- or intra-fractional motion.

Inter-fractional organ motion refers to changes in the anatomy in-between fractions on a typical time-scale of minutes to days. The sources of inter-fractional motion and anatomy changes are diverse. Lung tumor shrinkage and lung density changes over a treatment course were, e.g., observed by Mori et al. (2009). Changes in the base line of respiratory breathing patterns were i.a. reported by Sonke et al. (2008). Prostate tumors are frequently subject to position changes due to varying bladder or gut filling (Fokdal et al., 2004).

Intra-fractional organ motion occurs on a time-scale of seconds, i.e. during treatment, mainly as a result of respiration or heart beat. In this work, respiration-induced intra-fractional organ motion will be focused on.[1] Intra-fractional tumor motion shows a large variation depending on the individual conditions. However, respiration-induced tumor motion is consistently found to be more pronounced in the superior-inferior (SI) direction than in the anterior-posterior (AP) and left-right (LR) directions (Seppenwoolde et al., 2002; Britton et al., 2007; Liu et al., 2007; Case et al., 2010). Liu et al. (2007) report lung tumor motion amplitudes in SI direction larger than 5 mm in approximately 40 % of their patients. They also found correlations with respect to tumor size and T-staging. Liver tumor motion was assessed, e.g., by Case et al. (2010). They measured a mean amplitude in SI direction of 8 mm. A detailed overview on intra-fractional motion in lung and liver was published by Shirato et al. (2004).

2.2.2 Implications of organ motion

Organ motion generally leads to the spatial deformation of the dose distribution and a blurring of the dose gradients in ion beam therapy similarly to photon therapy, since the tumor centroid is partially moving in and out of the field (Bortfeld et al., 2004). Typically, this also leads to increased exposure of the surrounding normal tissue. The additional sources of dose deterioration for ion beams will be briefly discussed in the following.

2.2.2.1 Changes in the radiological path length

The radiological path length is defined as the geometrical depth traversed in a given material multiplied by its mass density (Alpen, 1998). For x-ray photons the changes in absorbed dose with the radiological depth are small, except for the small build-up region in the entrance channel, as shown in figure 2.2 on page 4 for the depth in water. Variations in material density, therefore, have little effect on the dose. It can also be seen from the figure that ions, in contrast,

[1] In the following, the term *organ motion* will be used synonymously with intra-fractional motion, unless stated otherwise.

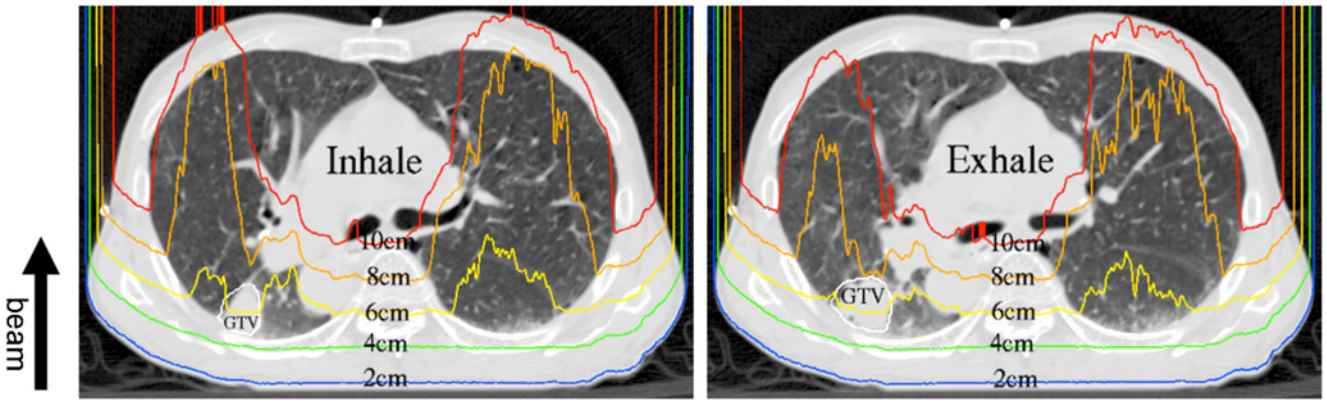

Figure 2.10.: Changes in the radiological depth induced by lung tumor motion. The variations are visualized by iso-range lines for posterior-anterior incidence of the ion beam. As the tumor (GTV) moves in and out of the displayed axial slice the radiological depth is modified, due to the higher density of the tumor with respect to the lung tissue. The induced range changes also affect the dose to normal tissue, e.g., the chest wall. Figure from Bert and Durante (2011).

are much more sensitive to density changes along their path through the patient. As the density changes translate directly into a modulation of the ion range in the tissue, structures near the Bragg peak can be subject to large deviations in absorbed dose w.r.t. the planned dose. This effect is independent from the beam delivery technique. Range changes may result, e.g., from varying lung density, bony structures moving in and out of the beam, or small patient positioning errors. Figure 2.10 visualizes the significant changes in radiological depth induced by a moving lung tumor, due to its higher density with respect to the lung (Bert and Durante, 2011).

2.2.2.2 Interference of beam and target motion

In contrast to passive beam delivery techniques beam scanning delivers the dose to the target volume in a sequential way using thin pencil beams (section 2.1.3.2). Delivery times per field typically are on the order of minutes, i.e. much longer than a typical breathing cycle. In this case, interference between the dynamic beam delivery and the target motion can compromise the dose uniformity and conformity, leading to significant over- and underdose (Phillips et al., 1992) as well as unintended exposure of normal tissue. This so-called *interplay effect* (figure 2.11) among other parameters strongly depends on the motion amplitude, the relative direction between target and beam motion and the extraction rate of the accelerator (Lambert et al., 2005; Groezinger et al., 2006; Bert et al., 2008). The modeling of the interplay effect and the determining parameters is of great interest for treatment planning and will be discussed in detail later in chapter 3. The inherent sensitivity of beam scanning to dose distortions in the presence of organ motion so far severely limits the clinical application of scanned ion beams for moving tumors.

2.2.3 Motion mitigation techniques

The impact of inter- and intra-fractional organ motion on the target dose distribution and the dose in the surrounding normal tissue is a general problem in radiotherapy, therefore, many of

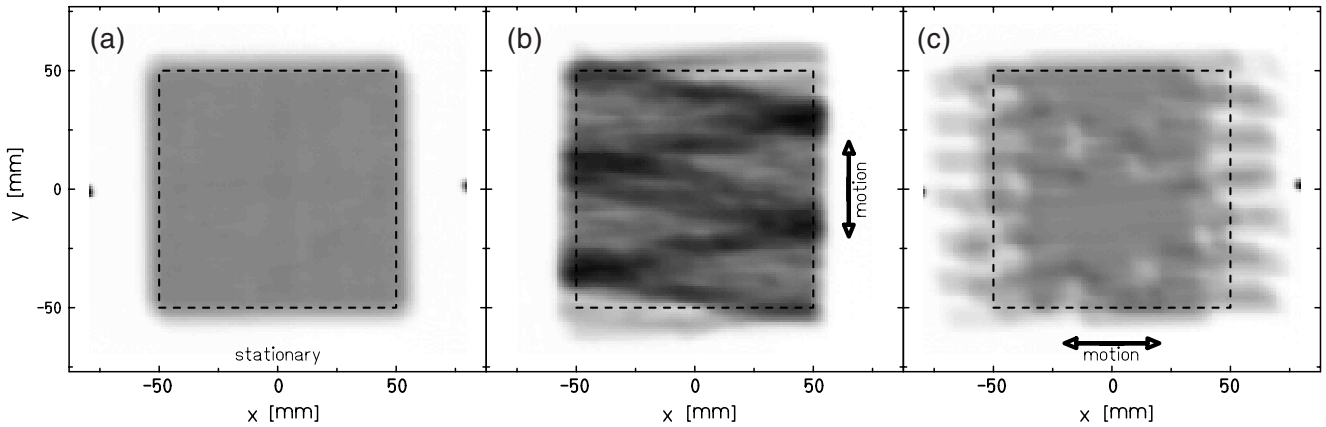

Figure 2.11.: Impact of the interplay effect on the dose response of radiographic films. (a) static dose distribution, (b)–(c) show the heterogeneous optical density distributions obtained for films moving in up-down and left-right direction w.r.t. the beam incidence. Figure from Bert et al. (2008).

the employed concepts are of relevance also in photon therapy. The mitigation of inter-fractional organ motion on the basis of repeated imaging, re-planning and adapted treatment delivery is a separate field of research, usually called adaptive radiotherapy (ART), and will not be discussed in further detail here. Reviews for adaptive treatment of prostate and liver tumors have, e.g., been published by Ghilezan et al. (2010) and Brock and Dawson (2010).

Various different strategies have been developed to face the problem of intra-fractional organ motion. The following section will introduce these strategies with a focus on scanned beam delivery. A more detailed discussion of motion management has been published by Bert and Durante (2011). It should be emphasized that most of the discussed strategies require dedicated treatment planning. Treatment planning for moving targets in ion beam therapy will be introduced separately in section 2.3.

2.2.3.1 Organ motion reduction

A common approach is aimed on the reduction of organ motion. For instance, abdominal compression has successfully been used in liver and lung treatment with photons to reduce the mean motion below 10 mm (Negoro et al., 2001; Hof et al., 2003). The compression is usually applied mechanically via an adjustable plate on a frame (Eccles et al., 2011). The technique is also employed for scanned carbon therapy of hepatocellular cancer at HIT. The partial or complete suppression of respiration can, e.g., be achieved by using jet-ventilation (Hof et al., 2003) or apneic oxygenation (RPTC, 2011). All these approaches, however, increase the clinical workload with respect to technical requirements and patient setup time.

2.2.3.2 Treatment margins and plan adaption

The adaption of the treatment plan in practice is often used in conjunction with additional motion mitigation techniques. Optimization of safety margins is done during treatment planning which will be introduced later in this chapter. For reasons of clarity, the common definitions of

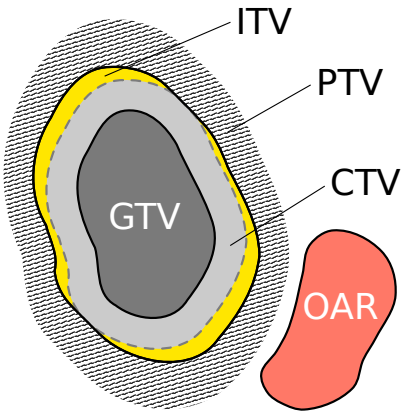

Figure 2.12: The clinical target volume (CTV) encompasses the gross tumor volume (GTV), including possible microscopic tumor spread. The internal target volume (ITV) is formed from the union of CTV contours throughout the full motion cycle. PTV margins take into account geometrical uncertainties and avoidance of organs at risk (OARs).

treatment margins shall be given here already. The ICRU recommends the definition of a number of volumes for treatment planning (ICRU, 1993a, 1999):

Gross Tumor volume: *'The GTV is the gross palpable or visible/demonstrable extent and location of malignant growth.'*

Clinical Target Volume: *'The CTV is a tissue volume that contains a demonstrable GTV and/or subclinical microscopic malignant disease, which has to be eliminated. This volume thus has to be treated adequately in order to achieve the aim of therapy, cure or palliation.'*

Planning Target Volume: *'The PTV is a geometrical concept, and it is defined to select an appropriate beam size and beam arrangements, taking into consideration the net effect of all the possible geometrical variations, in order to ensure that the prescribed dose is actually absorbed in the CTV.'*

Internal Target Volume: *This is the margin that must be added to the CTV to compensate for expected physio-logical movements and variations in size, shape, and position of the CTV during therapy.'*

Organs at risk: *'Organs at risk (OAR) are normal tissues whose radiation sensitivity may significantly influence treatment planning and/or prescribed dose.'*

A usual configuration of treatment volumes is shown in figure 2.12. For passive beam delivery the sole enlargement of the treatment margins, such that the tumor is in the treatment field at all times, can be an option and has successfully been used at NIRS (Nihei et al., 2006). Due to the interplay effect the mere adaption of the margins is usually not feasible for scanned beam delivery and has to be accompanied, e.g., by the adaption of the beam delivery, as discussed in the following section.

Apart from the adaption of treatment margins a dedicated optimization of other treatment plan parameters is possible. The optimization of treatment plan and beam parameters to mitigate small residual motion under abdominal compression or in comparable scenarios with reduced tumor motion will be a major focus of this work in the chapters 4–5.

2.2.3.3 Beam gating

Beam gating is the irradiation in a selected part of the breathing cycle only, the *gating window (GW)* (Minohara et al., 2000; Lu et al., 2006a). Typically, the rather stable and reproducible

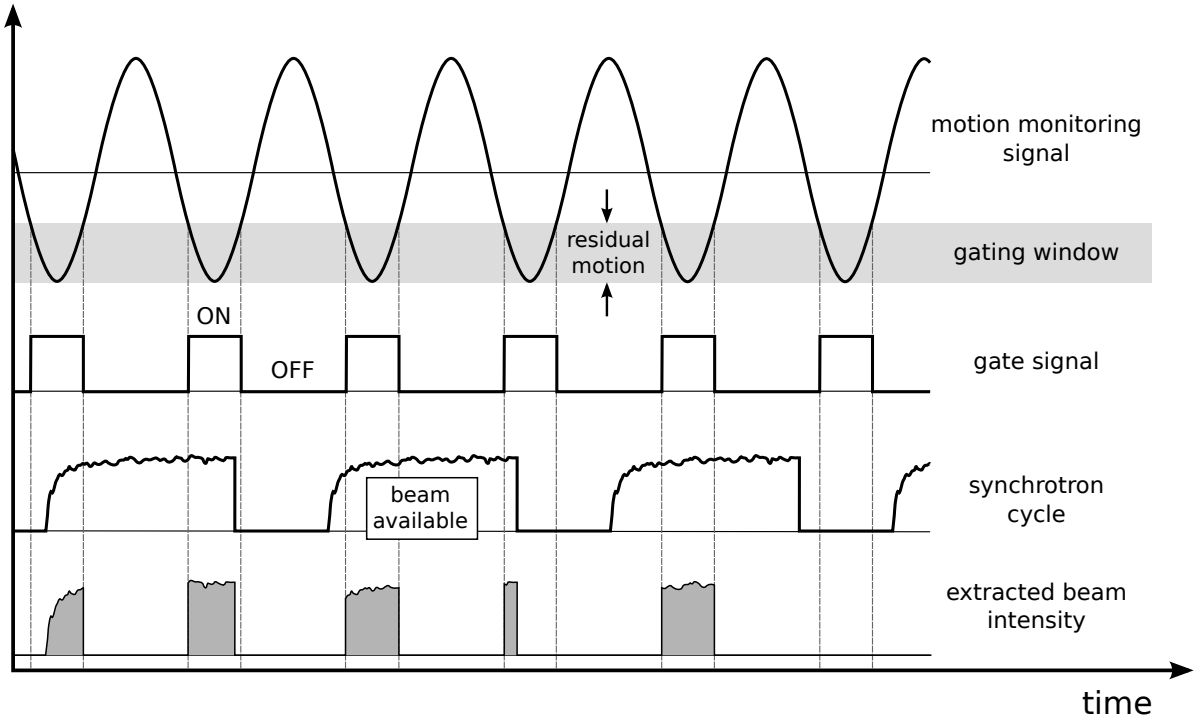

Figure 2.13.: Simplified diagram of the gating delivery mode with a synchrotron accelerator. The logical gate signal is generated by applying the gating window (GW) to the motion monitoring signal. Irradiation is only possible if the gate signal is active during beam availability. The amount of residual tumor motion depends on the GW size.

exhale position is chosen as the center of the gating window. The extraction of the beam is controlled using a motion monitoring signal (section 2.2.4). A major disadvantage of this technique is the prolonged treatment time due to the frequent interruptions of the beam. In figure 2.13 the principle of gating is shown schematically for a synchrotron accelerator. As depicted, the additional folding of the gate signal with the accelerator's duty cycle results into even longer treatment times. However, it has been shown that optimization of the synchrotron cycle is possible and can considerably limit the increase in treatment time (Tsunashima et al., 2008). The efficiency can be further improved by the extraction of multiple beam gates per synchrotron pulse (spill). For that purpose, so-called *knock-out extraction (KO)* has been implemented at a number of facilities, including HIT (Noda et al., 1996; Heeg et al., 2004).

Gating has successfully been used for the treatment of lung and liver cancer at several centers with passive beam delivery systems (Iwata et al., 2010; Hashimoto et al., 2006). Since the GW has a finite size, a corresponding residual motion inevitably remains. For beam scanning this can result into dose inhomogeneities due to the interplay effect. For this reason to date only few gated treatments have been performed using beam scanning. The amount of residual motion depends on the GW and is typically on the order of few millimeters and therefore comparable to the situation of abdominal compression for liver and lung tumors. The optimization of treatment plan parameters to mitigate residual motion effects has been proposed by Bert et al. (2009). This is the central research topic of this work and will be dealt with in chapters 4–5. An alternative approach is pursued by NIRS and PSI, in which additional plan robustness can be gained by combining gating with the rescanning technique (Furukawa et al., 2007; Zenklusen et al., 2010).

2.2.3.4 Rescanning/Repainting

The rescanning technique is a specific approach for scanned beam delivery. It aims at a statistical leveling of the dose inhomogeneities originating from beam interference effects by performing repeated fractional irradiation of the same volume (Phillips et al., 1992). A number of rescan options have been proposed so far, all having their specific characteristics (Furukawa et al., 2007; Rietzel and Bert, 2010; Zenklusen et al., 2010). The major discussed options are *slice-by-slice* rescanning and *volumetric* rescanning. A number of groups have proposed strategies to additionally ensure the statistical leveling of the dose after a number of rescans, namely *random-delay rescanning* (Seco et al., 2009; Rietzel and Bert, 2010) and *phase-controlled rescanning* or *breath-sampled rescanning*. In the latter two the rescans are performed equally distributed over the respiratory cycle, resulting into fewer required rescans and increased robustness. (Furukawa et al., 2010a; Seco et al., 2009).

In contrast to gating, rescanning requires to enlarge the treated volume to at least the envelope of the tumor in all motion states. This may result in considerable dose to normal tissue and constitutes a major disadvantage of the technique. Despite the breath-sampled options, the delivery of rescanning is technically simple and does not require real-time motion monitoring (section 2.2.4). So far, rescanning has not yet been established in patient treatments but is planned for the future, e.g., at NIRS (Furukawa et al., 2007) and PSI (Zenklusen et al., 2010).

2.2.3.5 Beam tracking

Beam tracking was originally proposed for photon IMRT (Keall et al., 2001). The underlying concept is to adjust the treatment beam with respect to the tumor and to establish the full compensation of the target motion such that no additional margins will be required. Beam tracking is clinically used in x-ray radiosurgery in the robotic Cyberknife Synchrony system (Accuray Inc., Sunnyvale, Ca., USA) (Brown et al., 2007; Kilby et al., 2010).

A full tracking system for scanned beam delivery has been implemented at GSI. Lateral compensation is performed with the two scanner magnets, while longitudinal range adjustment requires fast energy modulation via a linear motor-driven double wedge system (Weber et al., 2000). The correction of the beam position is performed based on a motion monitoring signal and pre-calculated look-up tables for the compensation parameters. The system has been fully integrated into the GSI treatment control system. Dosimetric and technical tests have proven high precision of the system (Bert and Rietzel, 2007; Bert et al., 2010; Saito et al., 2009). Reliable clinical use of the system, however, requires accurate four-dimensional (4D) imaging data and fast and precise real-time internal motion monitoring to ensure proper functioning of the motion compensation. This is currently not feasible.

2.2.4 Motion monitoring

The application of motion monitoring in radiotherapy is manifold, ranging from passive monitoring over interlock generation during treatment delivery to active beam delivery control as in the beam gating or beam tracking techniques discussed above. Motion monitoring techniques can be grouped into those directly measuring the tumor position, as in fluoroscopic imaging (Shirato et al., 2000; Berbeco et al., 2004) or with electromagnetic transponders (Balter et al.,

2005), and motion surrogates utilizing body surface expansion, air flow or other secondary signals. Commercially available system, e.g., are the Varian RPM system (Varian Medical Systems, Inc.) using infrared reflective markers in combination with a camera tracking system and the ANZAI AZ-773V system (ANZAI MEDICAL CO., LTD) employing either laser distance or pressure sensors attached to a waist belt (Li et al., 2006). Surrogate motion monitoring systems do not allow for absolute measurement of organ motion. Instead, they are used to detect the motion state of the patient relative to the respiratory cycle.

2.3 Treatment planning

Modern three-dimensional treatment planning is based on a computed tomography (CT) of the volume of interest. The volumetric dataset is the basis for the delineation of the target volume, nearby organs and critical structures by a physician. Other fused volumetric data sets like magnetic resonance imaging (MRI) or positron emmission tomography (PET) can be used in support during the delineation process. The common definitions of the different treatment volumes have been introduced in the last section (cf. figure 2.12 on page 20). The core task of treatment planning is the dose optimization process. That is the determination of the machine-dependent delivery parameters needed to yield the prescribed—usually homogeneous—PTV dose coverage for a chosen beam configuration while minimizing the dose to normal tissue. According to recommendations by the ICRU, 100 % of the PTV volume should receive between 95 % and 107 % of the planned dose (ICRU, 1993a). The dose optimization is normally performed in an iterative computational way using a treatment planning system (TPS). Treatment planning strongly depends on the employed radiation type and the beam delivery technique. The following section will concentrate on the specifics for scanned ion beam therapy.

2.3.1 Treatment planning for scanned ion beams

In treatment planning for scanned ion beams the characteristics of the active beam delivery system and the physical interactions of the ion radiation in the tissue have to be considered. For heavier ions than protons the modeling of the biological effectiveness adds additional complexity, due to the multiple dependencies of the RBE (section 2.1.2). Several treatment planning systems have been developed at the different centers employing beam scanning, e.g., at PSI (Scheib, 1993) and at NIRS (Inaniwa et al., 2008). In the following, the fundamental steps in treatment planning with the GSI treatment planning system, TRiP98, will be briefly introduced, as they are of further interest later in this work. A detailed description of the program and the underlying concepts can be found elsewhere (Krämer et al., 2000; Krämer and Scholz, 2000).

The treatment planning process is aimed at the optimization of a treatment plan which is applicable with the raster-scanner system (section 2.1.3.2) and yields a prescribed (biologically effective) dose distribution. The plan consists of raster points in a defined order (scan path). They are organized in slices of specific energy and beam FWHM. The optimization task is to determine the required energies, positions and particle numbers of all superimposed pencil beams, so that the optimal target dose distribution is obtained. The employed physical beam model uses a pencil beam approach with a Gaussian beam profile in combination with measured depth-dose curves in water. Lateral scattering is included based on Molière's theory (Molière, 1948). Ion transport model calculations take into account nuclear fragmentation and yield

secondary particle spectra in energy and atomic number. Tissue inhomogeneities are accounted for using the planning CT dataset. The Hounsfield units (HUs) (representing x-ray attenuation, thus, essentially the electron density) are voxel-wise[2] related to a water-equivalent path length (WEPL) using a piece-wise linear calibration curve which has been determined in dedicated measurements with tissue-equivalent materials (Geiss et al., 1999; Jäkel et al., 2001a; Rietzel et al., 2007). Calculation of the biological effectiveness in TRiP98 is performed using the local effect model (section 2.1.2). Starting from the secondary particle spectra in energy and atomic number the model is able to relate local ionization densities to a biological effectiveness at any point in the treatment field. Dose optimization is performed iteratively and takes into account the RBE for each target voxel. The algorithm initially distributes raster points according to the requested raster spacing in each of the energy layers covering the target in water-equivalent space. The subsequent least square minimization algorithm determines the required particle fluences per raster point. The physical and biological beam models are used to calculate the dose contributions from all raster points to each individual target voxel.

It should be noted that the modeling of the beam delivery in TRiP98 does not include any time structure, i.e. it neglects the subsequent nature of the beam scanning process and any target motion. The tumors treated in the GSI pilot project were mostly tumors of the brain and pelvis which could be well immobilized. Thus, they were considered static on the time-scale of the treatment delivery and no interference with the beam scanning had to be taken into account. Per definition this is no longer the case for intra-fractionally moving tumors. For treatment of this kind of tumors 4D treatment planning (4DTP) is essential.

2.3.2 4D treatment planning

It has been shown by several studies that higher tumor dose, e.g., in lung cancer, can significantly improve local tumor control rates (Rosenzweig et al., 2005; Kong et al., 2005). It is also observed that radiation-induced complications depend significantly on the normal tissue dose. For instance, Belderbos et al. report that the probability of acute esophagus toxicity in treatment of lung cancer is significantly correlated with the volume receiving a dose of at least 35 Gy (Belderbos et al., 2005). The objective of 4D radiotherapy (4DRT) is to increase the dose to the moving tumor while sparing the normal tissue and can be defined as *"the explicit inclusion of the temporal changes in anatomy during the imaging, planning and delivery of radiotherapy"* (Keall, 2004). This section will concentrate on the planning aspect of 4DRT. In the following, the technical prerequisites for 4D treatment planning will be described. Emphasis will be put on 4DTP for ion beams. Further details on 4DTP aspects will then follow in the subsequent chapter which focuses on the development of a 4DTPS for ion beams.

2.3.2.1 Time-resolved computed tomography

The basis for 4DTP is *time-resolved computed tomography (4DCT)* which was developed at several centers in the past decade and is now readily available (Ford et al., 2003; Keall, 2004; Rietzel et al., 2005a) in clinical routine. 4DCT data acquisition is performed in dedicated protocols which ensure that projection data of the rotating x-ray tubes are taken over a full respiratory cycle at each couch position. The projections are assigned retrospectively to the respective state

[2] A voxel is a volume element and the 3D analogon of a pixel.

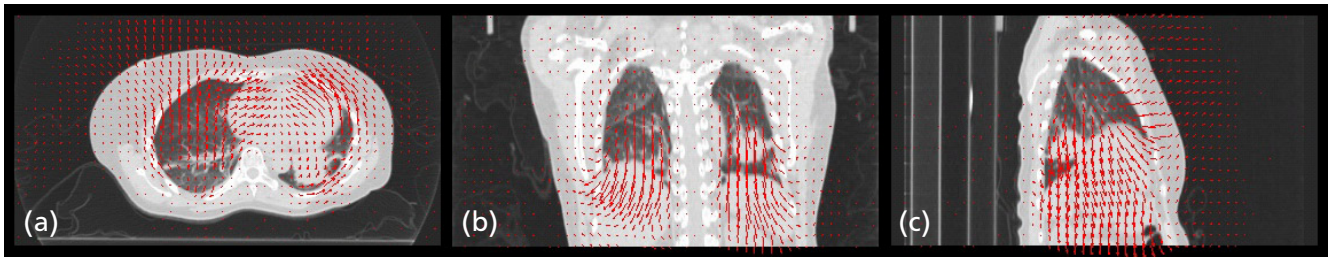

Figure 2.14.: Axial (a), coronal (b) and sagittal (c) view of the reference 4DCT phase (end-exhale) of a lung cancer patient. The deformation field transforming it to the end-inhale phase is visualized by the overlayed vector field. The predominant motion in SI direction is characteristic of respiration-induced motion.

of motion. Time correlation between the patient motion and the time stamp of the projections is established using a surrogate motion monitoring device (section 2.2.4). The reconstruction process yields a time series of three-dimensional computed tomographys (3DCTs) capturing the change of anatomy over time. Typically, on the order of ten respiratory states are acquired. The distribution of these so-called *4DCT phases*[3] over the respiratory cycle depends on the employed protocol. The 4DCT phases can, for instance, be defined using the amplitude (amplitude-based), or the phase (phase-based) of the surrogate signal (Lu et al., 2006c).

2.3.2.2 Image registration and contour propagation

The information provided by 4DCT on the temporal changes of the anatomy can only be used to the full extent if a spatial correlation between the individual 4DCT phases is established, i.e. image registration is performed. Image registration establishes a voxel-to-voxel mapping from a reference phase to any other phase of the breathing cycle. In figure 2.14 the end-exhale phase of a the 4DCT of a lung cancer patient is shown, including the deformation fields matching it with the end inhale phase. Usually rigid registration and deformable registration methods are distinguished. Various registration algorithms have been published in the literature (Hill et al., 2001; Brock et al., 2006; Rietzel and Chen, 2006b). The performance and accuracy of some of the available algorithms has been evaluated recently in a dedicated multi-institutional study (Brock, 2010). Brock et al. found that the registration accuracy for the majority of the algorithms is on the order of the CT voxel size, i.e. millimeters. However, their findings also indicate that image registration accuracy is dependent on the image contrast. It should be noted that registration inaccuracies translate directly into further treatment planning steps, such as 4D image segmentation.

Ideally, delineated structures on all 4DCT phases are available for the subsequent steps in 4DTP. The amount of image data in 4D imaging is increased roughly by one order of magnitude compared to 3D imaging. Thus, manual contouring, as in a conventional work flow, is time-consumptive and in general not feasible. Therefore, contour propagation methods are often used to automate this procedure. An overview of the available techniques can be found in (Xing et al., 2007). One approach is to propagate the manually contoured region of interest (ROI)

[3] The terms *motion phase* and *motion state* are also used frequently in the literature and will be used synonymously here.

on the reference phase to all other phases by using the deformation maps obtained by image registration (Lu et al., 2006b). Alternatively, elastic deformable models can be employed which locally adjust the reference phase contours to the test image by physical modeling of image forces (McInerney and Terzopoulos, 1996).

2.3.2.3 Target volume definition and motion mitigation

As already introduced in section 2.2.3, a widely used approach to include organ motion into the planning process is the generation of an *internal target volume (ITV)* which is formed by the union of the CTV in all relevant motion phases (ICRU, 1999). Different options of this geometrical concept have been reported for photon therapy (Rietzel et al., 2006; de Orban et al., 2007; Wolthaus et al., 2008). For ion beams this geometrical approach is not sufficient (Moyers et al., 2001; ICRU, 2007) and needs to be modified, taking into account range variations of the beam. An overview of the techniques currently used for passively delivered ion beams was published recently by Bert and Durante (Bert and Durante, 2011). For scanned ion beam therapy an approach based on 4DCT has been proposed (Bert and Rietzel, 2007; Rietzel and Bert, 2010). In the most recent version the full target dimensions in water-equivalent space in the respective motion phases are considered for the design of the ITV. It should be noted that the formation of the ITV depends on the employed motion mitigation technique. For beam gating, for instance, ITV generation needs to be performed using the 4DCT phases in the gating window only.

Bert and Rietzel (2007) have incorporated 4DTP functionality for gating, rescanning and tracking into the GSI treatment planning system TRiP98. Apart from the ITV generation for rescanning and gating, optimization of compensation parameters for beam tracking are supported. The basic planning strategy in TRiP98 is to optimize a treatment plan on a reference 4DCT phase and to ensure adequate dose coverage of the target volume in the other phases either by optimization of compensation parameters in beam tracking or by the use of an appropriate ITV in combination with gating or rescanning. However, as introduced in section 2.2.3, the mere use of enlarged margins, i.e. an ITV, is not sufficient for scanned beams. Even in the case of gating or small uncompensated target motion—as in treatments under abdominal compression—residual motion will induce interplay effects. Bert et al. have proposed to optimize the beam's FWHM and the distance of iso-energy slices to mitigate the resulting dose inhomogeneities (Bert et al., 2009). The research questions addressed in this dissertation are tying up to these investigations.

2.3.2.4 4D dose calculation and optimization

Complementary to the treatment plan optimization step 4D dose calculation is an important tool in 4DTP. For ion beams it allows to quantify dose heterogeneities caused by interplay effects. 4D dose calculation algorithms exploiting deformable image registration have been developed by several groups. Depending on the 4DCT sampling technique, weighting of the individual dose distributions is needed for photons and passive ion beam delivery (Rietzel et al., 2005a). For scanned beams the time-structure of the sequential plan delivery has to be considered (Bert and Rietzel, 2007; Paganetti et al., 2004). Summation of the individual dose contributions is either done by transforming dose contributions in each phase to a common reference frame (Bert and Rietzel, 2007) or by deforming the dose grid (Knopf et al., 2010b). The latter approach has the

advantage that it also enables for biological dose calculation, which is particularly important for heavy ion therapy. Based on this principle, Gemmel et al. have implemented a 4D dose algorithm into the GSI TPS which is capable of biological and physical dose calculations (Gemmel et al., 2011). The algorithm was validated in cell survival measurements using a dedicated phantom. The implementation and validation of 4D dose calculation and the modelling of interplay effects will be dealt with in further detail in the next chapter.

In contrast to the strategy of planning on a reference phase only, the full incorporation of the complete 4DCT information into the dose optimization process seems promising. At the time of writing no full 4D optimization has been reported for particle beams. However, several attempts have been made for x-ray therapy. Unkelbach et al. (2009), e.g., have studied robust treatment plan optimization based on probability distributions of patient geometries. Suh et al. (2009) and Nohadani et al. (2010) have developed robust inverse planning techniques for IMRT motion tracking that incorporate possible variations in the patient's breathing cycle.

2.4 Summary

In this chapter the rationale for the clinical application of ion beam radiation has been defined and the physical and biological properties of ions have been introduced. Their specific advantages and characteristics have been described and the different existing techniques to deliver ion beams to the tumor volume were discussed. Emphasis was put on the beam scanning technique. Furthermore, the problem of organ motion in modern radiotherapy has been illuminated and the different existing techniques to manage organ motion effects have been introduced. In particular, the mitigation of interplay effects for scanned beams and of the induced changes in radiological depth has been motivated. In the last section the requirement of dedicated 4DTP for scanned ion beams was clarified and an overview of the current state of research in the field was given. To address the subject of this dissertation—the mitigation of residual tumor motion—a functional 4DTPS is indispensable. The posed problem required a substantial revision of the existing GSI 4D treatment planning functionality and its integration into a new software. The implementation of this system will be described in the subsequent chapter.

3 Development of a 4D treatment planning system for scanned ion beam therapy

In the preceding chapter the principal steps required in treatment planning for static targets were discussed for the GSI in-house treatment planning system, TRiP98 (Krämer et al., 2000; Krämer and Scholz, 2000; Jäkel et al., 2001a). Its original design was geared to treatment planning for head and neck tumors, thus, any effects of organ motion could safely be neglected. The treatment of moving organs with a scanned beam introduces additional complexity in a two-fold way. Firstly, the individual intra-fractional changes of the patient's anatomy over time and their impact on the relative beam position need to be considered, in order to avoid geometric miss. Secondly, the temporal structure of the dynamic beam delivery process, its interaction with the target motion and the negative impact on the dose coverage (interplay effect) has to be taken into account (Bert and Durante, 2011).

This chapter will present the development of a 4DTPS, based on the TRiP98 program, named **TRiP4D** in the following. The first section will review the previous efforts made in the development of 4DTP functionality at GSI and will define the design requirements for the new software. The second section focuses on the implementation of the respective functionality into TRiP4D. The validation of the 4DTPS is presented in the third section. Finally, the last section discusses the results of the software implementation and validation.

3.1 Introduction

The initial attempts made at GSI with respect to irradiation of moving tumors were focused on the implementation of a beam tracking solution (section 2.2.3). Li et al. established a simulation environment based on TRiP98 concentrating on 4D dose calculation for beam tracking and uncompensated irradiation of moving targets (Li et al., 2004). Target motion was modeled rigidly only, i.e. translational and rotational. Simulation of the dynamic beam delivery was based on single measured beam intensity profiles which were applied cyclically and took into account spill pauses of the synchrotron accelerator. The program was capable of 4D dose calculation with variable time resolution for artificial and experimental water phantom setups (Groezinger et al., 2006). The program was successfully validated in film measurements (Li et al., 2004). However, the program's design was not compatible with the upcoming 4DCT and deformable registration workflows and, therefore, was not suitable for simulation of time-resolved dose delivery in a realistic patient environment.

In a more general approach, Bert and Rietzel implemented 4DTP functionality for ion beams in a newly developed descendant of TRiP98 (Bert and Rietzel, 2007). The design was primarily led by 4DTP workflows based on 4DCT and deformable image registration, as proposed for 4D photon therapy (Keall, 2004; Rietzel et al., 2005a). The temporal changes of the anatomy during beam delivery, i.e. the transitions through the CT phases, were determined from motion monitoring traces. Sub-treatment plans for each 4DCT phase, containing all raster points irradiated in a particular phase, were generated on the basis of the time-correlated motion trace and a

time-resolved beam delivery sequence. 4D physical dose calculation was established by sequential 3D dose calculation for each sub-treatment plan on the respective CT phase and subsequent transformation of the sub-distributions to the reference phase. Apart from beam tracking and uncompensated irradiation the program also was capable of simulating rescanned and gated beam delivery. Compared to Li et al., the time structure of the irradiation was incorporated in a more realistic way using beam intensity courses simulated or measured over the entire delivery time. Also, 4D optimization functionality was developed comprising the calculation of motion compensation parameters for beam tracking and the design of ITVs in water-equivalent space for realistic patient geometries. An improved version of beam tracking takes into account real-time adaption of the particle numbers per raster point, in order to compensate for dose changes caused by target rotation or deformation. Validation of the 4DTPS was performed in numerous experiments (Bert et al., 2010; Bert, Richter et al., 2012).

The sequential nature of the TPS and the 4D dose calculation algorithm developed by Bert and Rietzel has proven incompatible with the calculation of biologically effective dose. Since the RBE value depends non-linearly on the full spectrum of energies and particles contributing to the total physical dose at each point in the treatment field, it can not be determined from the constituent physical dose distributions per CT phase. Therefore, Gemmel et al. (2011) developed a complementary program based on TRiP98. It featured a dedicated 4DCT structure for full access during run-time and a new biological dose calculation concept considering particle spectra and dose contributions from all CT phases to the total dose at each point in the treatment field. Furthermore, the algorithm also was capable of calculating 4D physical dose distributions. The code has been successfully verified in cell survival measurements in the presence of target motion (Gemmel et al., 2011). It should be emphasized that the program relied on functionality and intermediate results from the TPS of Bert and Rietzel and did not constitute a full replacement of the latter.

Although well tested and established in experiments, the 4DTPS codes previously available at GSI carry substantial limitations with respect to 4D treatment planning for realistic patient geometries. The existing approaches also suffer from decentralized functionality and cumbersome workflows. Against the background that the treatment of abdominal-compressed hepatocellular tumors at HIT has been commenced recently and other tumor sites subject to intra- and inter-fractional motion are planned for the near future, an integrated and efficient 4DTPS is strongly required. Considering the experiences made and the current state of research in the field of 4D radiotherapy the following central requirements were defined for the new treatment planning system, TRiP4D:

(1) TRiP4D is based on TRiP98 for efficient use of the well established 3D treatment planning functionality, as well as the physical and biological beam model. New functionality is to be integrated using existing conventions and must not impair existing core functionality.

(2) The existing functionality of the predecessor programs should be fully integrated. This particularly includes 4D (biological) dose and detector response calculation as well as the generation of quasi-static sub-treatment plans based on temporal correlation of a time-resolved beam delivery sequence and motion traces.

(3) New structures are to be integrated as flexibly and efficiently as possible to meet the requirements of future research, such as 4D dose optimization tasks. This specifically requires

run-time access to all 4D structures and rules out sequential calculation procedures in separate sessions and remote access to external software as employed by Bert and Rietzel.

(4) 4D optimization and beam delivery for multiple treatment fields, as needed for typical clinical treatment plans, have not been available with the previous planning systems and should be incorporated in compliance with TRiP98's 3D design concepts for multiple fields (Gemmel et al., 2008).

(5) Previous GSI planning systems were lacking dedicated structures and functionality for 4D segmentation and deformable image registration support. Key requirements are the flexible integration of deformation maps of various registration software packages, the propagation of contours from a reference CT phase and their efficient handling throughout the 4D planning process. Similarly, support for 4DCT data as introduced by Gemmel et al. needs to be significantly extended.

(6) Full compatibility of the program to the clinical treatment planning workflow at HIT and similar facilities needs to be established. Specifically, this includes the 4DCT protocol and motion monitoring data. In earlier implementations the integration of realistic patient motion traces was restricted to amplitude-based motion state identification (section 2.3.2). In clinical practice motion state identification and the corresponding signal processing routines have to be integrated into the TPS in accordance with the 4DCT protocol.

(7) The design of TRiP98 is compatible with scanned beam delivery systems similar to the one used at GSI. Modelling of 4D beam delivery using time-resolved beam delivery sequence data therefore should be flexible enough to ensure compatibility to the respective systems, in particular the one used at HIT.

3.2 Implementation

The TRiP98 mother program is a command-line-based software without graphical user interface. It is written in C programming language using a pseudo object-oriented structure and natively runs on an IBM AIX operating system. The development of TRiP4D has been performed in a development branch of TRiP98. The inherent complexity and scope of operation of the program involves constant evolution and refinement. The information given here represents the state of TRiP4D and its mother program TRiP98 at the time of writing and may be subject to changes in the future. The author was the main person responsible for the development of TRiP4D. However, the work of collaborators significantly contributed to the functionality. Their contributions will be indicated in the respective places.

In the following, the implementation of the 4D treatment planning functionality of TRiP4D will be discussed. The first section will concentrate on the modeling of patient anatomy changes in TRiP4D. Subsequently, the currently pursued four-dimensional optimization strategy will be discussed. In the last section TRiP4D's 4D treatment simulation capabilities and the required components are dealt with.

3.2.1 Moving patient geometry

The modeling of the moving patient geometry in the 4DTPS involves integration of 4DCT imaging, motion monitoring and of 4D segmentation of anatomic structures as well as interpretation

of deformation maps obtained by deformable image registration. This section will discuss the development and implementation of the required modules in TRiP4D.

3.2.1.1 4D computed tomography

Imaging, characterization and quantification of the moving patient geometry can be considered the first step in 4D treatment planning (Keall, 2004; Chen et al., 2007). Time-resolved computed tomography (4DCT) has proven essential for the assessment of patient motion and 4D treatment planning tasks, such as the design of safety margins and 4D dose calculation (Rietzel et al., 2005b). Dedicated 4DCT structures and functionality have been implemented in TRiP4D, in order to fully exploit its potential for treatment planning.[1] Since 3DCT datasets are the starting point for any 3D treatment planning workflow in TRiP98, corresponding structures and extensive functionality were well established and served as a basis for the integration of 4DCT. The 4DCT structure was implemented as a sequence of 3DCTs, mapping its real representation as a time-correlated series of individual 4DCT phases, i.e. 3DCTs, with a distinguished reference state CT. Individual 4DCT phases are characterized and indexed by their position in the respiratory cycle. The mapping of an external surrogate motion trace to the corresponding 4DCT state at a certain time is essential for the simulation of 4D treatments and will be discussed in the subsequent section. The reference state CT of the 4DCT structure supersedes the original CT of the 3D workflow, e.g., for dose optimization tasks. The comprehensive and already established 3DCT functionality, such as the computation of water-equivalent path lengths, could be re-used efficiently for the constituent 4DCT phases. The current integration of 4DCT in TRiP4D enables elaborate planning tasks like biological 4D dose calculation, as it provides access to the full 4DCT information at run-time of the program. It should be noted that the data volume for 4DCT is increased by about one order of magnitude with respect to 3DCT datasets with a typical 4DCT consuming on the order of 0.5 GB of memory. The existing memory-mapping approach for 3DCTs in TRiP98 therefore has been extended to the 4DCT structures. TRiP98 supports the native data format of the VOXELPLAN planning system developed at DKFZ (Schlegel et al., 1992) for any data input and output. The corresponding routines in TRiP4D have been extended for compatibility with 4DCTs datasets. The usability of DICOM standard CT data is guaranteed by a dedicated in-house DICOM converter software (appendix A.1).

3.2.1.2 Motion monitoring data

Retrospective reconstruction of 4DCT requires a surrogate motion signal to determine the respiratory state of the patient throughout data acquisition (Ford et al., 2003; Rietzel et al., 2005a). Similarly, for simulation of a 4D treatment delivery the transition of the patient through the 4DCT states over time has to be known. The latter will be discussed in detail in section 3.2.3.1.

Signal handling and processing of realistic patient motion trajectories has been integrated into TRiP4D. Compatibility of the TPS to the ANZAI AZ-733 system (ANZAI MEDICAL CO., LTD) has been established, including the implementation of an interface for the acquired motion traces. The ANZAI system provides a one-dimensional surrogate signal from either a pressure sensor in a waist belt or a laser distance measurement. The system is used clinically for motion

[1] The 4DCT functionality has been implemented in close collaboration with two master students, A. Schwarzkopf and J. Trautmann, which were supervised by the author.

monitoring and 4DCT acquisition at HIT and UCHD and is the designated control device for gated treatments.

Additionally, a general motion trace format has been established supporting 3D position measurements for multiple markers. It is expected that general compatibility to the format can be easily facilitated for other commercial monitoring systems by data conversion or adaption. The format also is compliant with the information provided by the ANZAI system. Dedicated routines are available for automatic generation of regular sinusoidal motion traces or traces according to Lujan et al. (1999) for experimental purposes. Additional routines for motion trace manipulation and signal processing, such as signal-smoothing have been implemented.

In TRiP4D two different kinds of motion signals can be used in parallel, i.e. the surrogate signal and the internal motion signal. The latter holds the *true* motion data to be used for 4D dose reconstruction while the former represents the *observed* motion signal and may, for instance, include phase shifts or base-line drifts w.r.t. the internal motion. In this way real-time decisions based on motion monitoring and affecting the beam delivery course, such as motion state identification for beam tracking, can be modeled correctly.

3.2.1.3 Image registration and deformation maps

The implicit information of 4DCT data on the spatial and temporal changes of the patient's anatomy can be extracted with image registration which establishes the alignment between a fixed reference state CT and a test 4DCT state. The resulting deformation maps represent voxel-to-voxel displacements between the registered CTs and are a key prerequisite for quantitative incorporation of 4DCT information into the treatment planning process. Various algorithms have been published in the literature (Rietzel and Chen, 2006a; Kessler, 2006; Yang et al., 2008). Their individual characteristics and performance is beyond the scope of this work.

The output of the registration process of a 4DCT with N states can be characterized by $N-1$ transformation maps, $\boldsymbol{T}_{ri}(\boldsymbol{x})$, relating a distinguished reference state r and a state $i \neq r$. The map relates the position of a point $\boldsymbol{x}'$ in state i to its position $\boldsymbol{x}$ in the reference state:

$$\boldsymbol{x}' = \boldsymbol{x} + \boldsymbol{u}_{ri}(\boldsymbol{x}) \quad . \tag{3.1}$$

In its simplest form the vector displacement $\boldsymbol{u}_{ri}(\boldsymbol{x})$ is directly given by a vector field representation of $\boldsymbol{T}_{ri}(\boldsymbol{x})$, however, depending on the registration software the vector field may have to be reconstructed first from the registration output data, as in the case of a B-spline parameter representation.

Integration of deformation maps

At the time of writing the design of TRiP4D did not include native image registration functionality. Since various reliable external registration software packages are available, it is sufficient and more flexible to only integrate the interfaces to the respective programs in TRiP4D, i.e. the input and processing of image registration output. A separate module has been implemented in TRiP4D which supports reading and processing of deformation maps of the open source software packages Plastimatch (Sharp et al., 2007), VTK CISG (Hartkens, 1993) and of a commercial Siemens prototype software.[2] VTK CISG provides binary B-spline-based parameter sets

[2] The work of two master students, A. Schwarzkopf and J. Trautmann, has contributed to the discussed implementation.

from deformable image registration while Plastimatch and the Siemens prototype deliver CT-like volume datasets in vector field representation. Compatibility to the B-spline representation also provided by Plastimatch has not been established so far. Priority was given to the integration of deformation maps in volume dataset representation featuring one CT-like structure per displacement vector component and state transition $r \rightarrow i$:

$$\boldsymbol{T}_{ri}(\boldsymbol{x}) = \left(T_{ri}^{x}(\boldsymbol{x}), T_{ri}^{y}(\boldsymbol{x}), T_{ri}^{z}(\boldsymbol{x})\right) \quad . \tag{3.2}$$

This representation is compatible with both the registration output of Plastimatch and the Siemens prototype and requires only minor pre-processing for TRiP4D. The approach of a general implementation of CT-like deformation maps seems promising for three reasons.

(1) All registration software packages should, at least in principle, be able to deliver the registration output in this basic form, although minor differences in the data format are to be expected. Hence, compatibility to other registration software packages can easily be established in the future.

(2) The interpretation of the volume dataset deformation maps is simple and does not require extensive, software-specific algorithms and calculations as, e.g., the evaluation of B-spline parameters.

(3) The CT-like structure enables efficient use of existing and well tested basic functionality for similar volume datasets in TRiP4D.

It should be emphasized that memory consumption of deformable registration maps in the form of volume datasets is substantial and easily amounts to more than 1 GB of memory for a complete set of deformation maps, depending on the number of 4DCT states and the resolution of the volume datasets. Specific steps of 4D treatment planning, e.g., contour propagation (section 3.2.1.4), also require the inverse deformation maps, $\boldsymbol{T}_{ir}(\boldsymbol{x})$. In general, these have to be obtained from a separate registration process. In order to improve memory efficiency, subsets of the deformation maps can be selected for the respective planning tasks via the command-line interface. Additionally, the program can handle volume dataset deformation maps at any spatial resolution and independent from the original CT voxel spacing. Consequently, also lower resolution deformation maps can be employed, further limiting the memory consumption.

Apart from deformable registration, rigid registration is of frequent interest in treatment planning, e.g., when modeling experimental setups. Rigid transformation maps in TRiP4D have been implemented employing the commonly used 4×4 matrix representation and formalism (Veblen and Young, 2005). TRiP4D supports affine deformation maps provided by VTK CISG and a native deformation map format expected to be generally compatible with other registration software packages delivering matrix-based rigid deformation maps. Dedicated routines have been added for fast and convenient generation of rigid deformation maps based on regular motion trajectories or specified parameters to suit experimental needs.

Coordinate transformation

Interpretation and evaluation of the deformation field is required in various steps throughout 4D treatment planning and involves calculation of displacement vectors for a given source vector and destination state. In general, the coordinate systems of TRiP4D and the respective

registration software have to be aligned before the actual transformation. This has been implemented by additional rigid transformation of the source and displacement vectors such that (3.1) translates into:

$$\boldsymbol{x}' = \boldsymbol{x} + \boldsymbol{P}^{-1}\tilde{\boldsymbol{u}}_{ri}(\boldsymbol{P}\cdot\boldsymbol{x}) \quad . \tag{3.3}$$

Here $\boldsymbol{P}$ and its inverse, $\boldsymbol{P}^{-1}$, denote the 4×4 matrices transforming the respective coordinate systems of TRiP4D and of the registration software into each other. $\tilde{\boldsymbol{u}}_{ri}$ is the displacement vector in the extrinsic coordinate system. The matrices $\boldsymbol{P}$ and $\boldsymbol{P}^{-1}$ usually depend on the employed registration software only. However, they also can flexibly be defined by the user, if required.

Calculation of the displacement vectors, $\boldsymbol{u}_{ri}(\boldsymbol{x}) = \boldsymbol{P}^{-1}\tilde{\boldsymbol{u}}_{ri}(\boldsymbol{P}\cdot\boldsymbol{x})$, is carried out depending on the deformation map modality. For B-spline maps the corresponding parameters are employed to reconstruct the deformation field $\tilde{\boldsymbol{u}}_{ri}$ at the requested position using a software-specific algorithm. For volume dataset maps $\tilde{\boldsymbol{u}}_{ri}$ is directly given on a discrete voxel grid. To determine the deformation vector at an arbitrary position, trilinear interpolation of $\tilde{\boldsymbol{u}}_{ri}$ is performed among the neighboring voxel centers. Finally, the evaluation of rigid deformation maps at a certain position $\boldsymbol{x}$ involves matrix multiplication with the matrix representation of the map, $\boldsymbol{M}_{ri}$:

$$\boldsymbol{x}' = \boldsymbol{x} + \boldsymbol{P}^{-1}\boldsymbol{M}_{ri}\boldsymbol{P}\,\boldsymbol{x} \quad . \tag{3.4}$$

Motion assessment

Patient motion analysis is an important aspect of 4DTP. Hence, specific commands and routines have been implemented in TRiP4D to conveniently assess the extent and distribution of patient motion on the basis of the available deformation maps. Specifically, patient motion of certain volumes often is of interest. Therefore, the functionality is coupled to the segmentation functionality discussed in the next section. The export of volumetric cuts of the displacement fields has been implemented, similar to those generally used for dose distributions or CT visualization. Selected ROIs can be overlayed on demand to ease interpretation. Additionally, differential and cumulative motion volume histograms (MVHs) of displacement vectors in selected ROIs can be exported. Basic statistical parameters such as mean and median values or standard deviations are calculated from the distributions. Figure 3.1 on the following page illustrates the functionality in the example of a liver tumor and the displacement field between the end exhale and end inhale 4DCT phases.

3.2.1.4 4D segmentation

Elaborate 4D treatment planning requires information on the spatial and temporal changes of target volumes and organs at risk. The automatic propagation of a manually delineated reference contour is a promising and efficient approach to obtain contours on all 4DCT states (Lu et al., 2006b; Gaede et al., 2011). The design of ITVs and other steps in the 4D treatment planning workflow can benefit from a full integration of 4D segmentation into the treatment planning system. Therefore, TRiP4D's existing module for handling 3D segmentation has been enhanced with respect to 4D treatment planning functionality. This comprises a novel 4D contour data model, a contour propagation algorithm and contour manipulation functionality.[3]

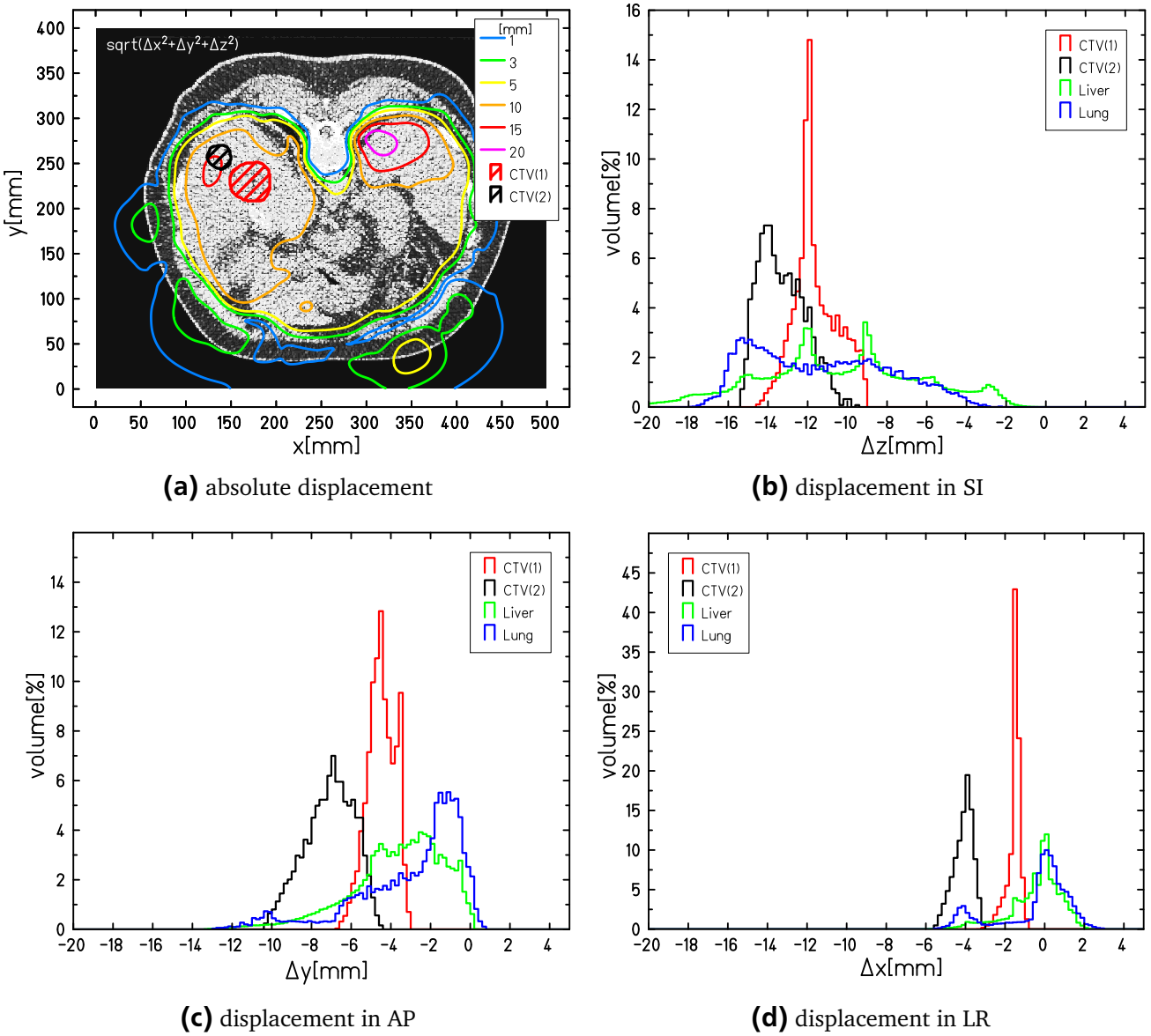

(a) absolute displacement

(b) displacement in SI

(c) displacement in AP

(d) displacement in LR

Figure 3.1.: Visualization and assessment of organ motion using deformation maps from deformable image registration in TRiP4D. **(a)** Axial cut of the reference state CT (end exhale) and the overlayed displacement field between the extreme states, end exhale and end inhale are shown. The absolute values of the displacement vectors are shown as a contour plot, CTV contours of a liver tumor are also indicated. **(b–d)** Histograms of the displacement vector components for the two CTV volumes, liver and lung in the SI, AP and LR direction, respectively. Organ motion is most pronounced in the SI direction and is significantly larger in CTV(2) than in CTV(1) volume for all vector components.

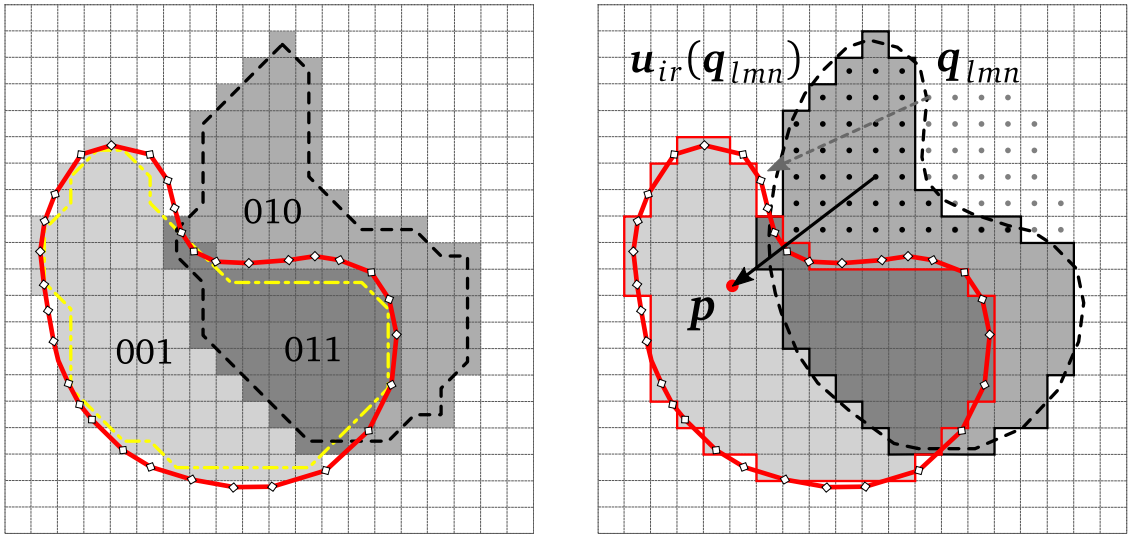

Figure 3.2.: (a) ROI conversion from a polygon contour (red solid line) into volumetric boolean masks (VBMs) (gray areas) and re-converted polygon contours (dashed lines). Resulting Boolean masks are indicated for the two ROI areas and the overlap region. **(b)** Contour propagation by inverse transformation from a regular grid. The propagated ROI (dark gray) is formed from voxels with source points inside the polygon contour (red solid line). Transformation vectors are indicated for two voxels (arrows).

4D contour data model

The segmentation module of TRiP98 relies on contour data given in the form of co-planar polygons usually originating from the delineation process on axial CT slices. Complementary to the CT data the VOXELPLAN format of DKFZ is supported (Schlegel et al., 1992). Compatibility to the DICOM standard additionally has been established in the context of this work through an external conversion software (appendix A.1). The new implementation of 4D segmentation in TRiP4D extends the 3D functionality by integration of 4DROIs in the form of Boolean masks held in a volume dataset structure as a single entity. This approach is based on several arguments. Firstly, a major focus was on the design of an integrated 4D structure capable of handling ROIs in all CT states. Flexible combination of the individual volumes should also be supported and is particularly simple in the approach of Boolean masks. Secondly, volume datasets are well established structures in TRiP4D and the existing functionality can be efficiently re-used. And thirdly, contour propagation involves deformation of the ROI. In this context, a volume dataset model offers advantages over polygonal contours.

Generation of the volumetric boolean mask (VBM) ROIs from the polygon contours is performed as follows:

(1) One volume dataset per ROI is created. Usually the CT voxel spacing is sufficient to map the polygon contour adequately, otherwise a finer lateral voxel spacing is used. The longitudinal resolution corresponds to the CT slice spacing. For reasons of memory efficiency the

[3] The discussed 4D segmentation functionality has been implemented by two master students supervised by the author, A. Schwarzkopf and J. Trautmann.

volume dimensions are determined from the spatial extension of the polygon ROI, taking into account necessary margins due to motion.

(2) Each voxel center is tested for its position w.r.t. the polygon ROI. A point-in-polygon ray-casting algorithm on the basis of the Jordan curve theorem is used to determine whether the respective voxel is inside the polygon ROI (Glassner, 1989; Hales, 2007).

(3) Each voxel inside the polygon ROI is marked in the volume dataset using a bit mask. A single bit per ROI representation and voxel is required. Consequently, different ROI states can be held on individual bits in a single volume dataset.[4]

Figure 3.2a illustrates the conversion of the polygon contour into a VBM and the resulting bit patterns for the different ROI states. In order to ensure compatibility with other software packages, e.g., external visualization tools, the VBM datasets can be re-converted into polygon contours. Contour detection routines have been implemented based on a Freeman code chain algorithm (Freeman and Davis, 1977). The enveloping polygons of the ROI volume are reconstructed in each axial slice of the volume dataset (dashed lines in figure 3.2a) taking into account potential separation of sub-ROIs. Further manipulation of the 4DROIs can be performed conveniently using the VBM datasets. For instance, the formation of geometrical unions or intersections among different ROI states involves bit mask operations only and has been implemented in TRiP4D for further 4DTP tasks (cf. section 3.2.2.1).

Contour propagation

Different methods of contour propagation have been published in the literature and are commonly divided into deformable registration-based (Ragan et al., 2005; Lu et al., 2006b; Shekhar et al., 2007) and deformable model-based methods (McInerney and Terzopoulos, 1996; Montagnat and Delingette, 2005). Contour propagation in TRiP4D employs a deformable registration-based approach taking advantage of the already discussed infrastructure for deformable registration maps. The underlying concept is to guide the transformation of the reference state ROIs with the deformation fields obtained from registration of the underlying CT geometry. The use of co-planar polygons alone poses problems in contour propagation, since the co-planar character is in general lost under spatial transformation. For this reason triangular mesh surfaces are used by some groups to model the transformation of the ROIs (Lu et al., 2006b; Faggiano et al., 2011). The alternative approach in TRiP4D of employing VBM dataset structures for contour propagation will be introduced in the following section.

The initial step of the transformation procedure of a polygonal ROI from the reference state r to all states $i \neq r$ starts with the conversion of the reference state contour into a VBM dataset as described in the previous section. Let $\boldsymbol{q}_{lmn} = (x_l, y_m, z_n)$ denote the position of the voxel centers. Propagation of the reference state ROI to state i is performed by inverse transformation of each voxel center $\boldsymbol{q}_{lmn}$ to the reference state

$$\boldsymbol{p} = \boldsymbol{q}_{lmn} + \boldsymbol{u}_{ir}(\boldsymbol{q}_{lmn}) \quad . \tag{3.5}$$

Here, $\boldsymbol{p}$ denotes the reference state position of $\boldsymbol{q}_{lmn}$. The displacement vectors, $\boldsymbol{u}_{ir}(\boldsymbol{q}_{lmn})$, are obtained from the inverse deformation maps, $\boldsymbol{T}_{ir}(\boldsymbol{x})$, as discussed earlier in section 3.2.1.3.

[4] The maximum number of ROI states depends on the size of the data type used, e.g., 32 states for a 32 bit integer per voxel.

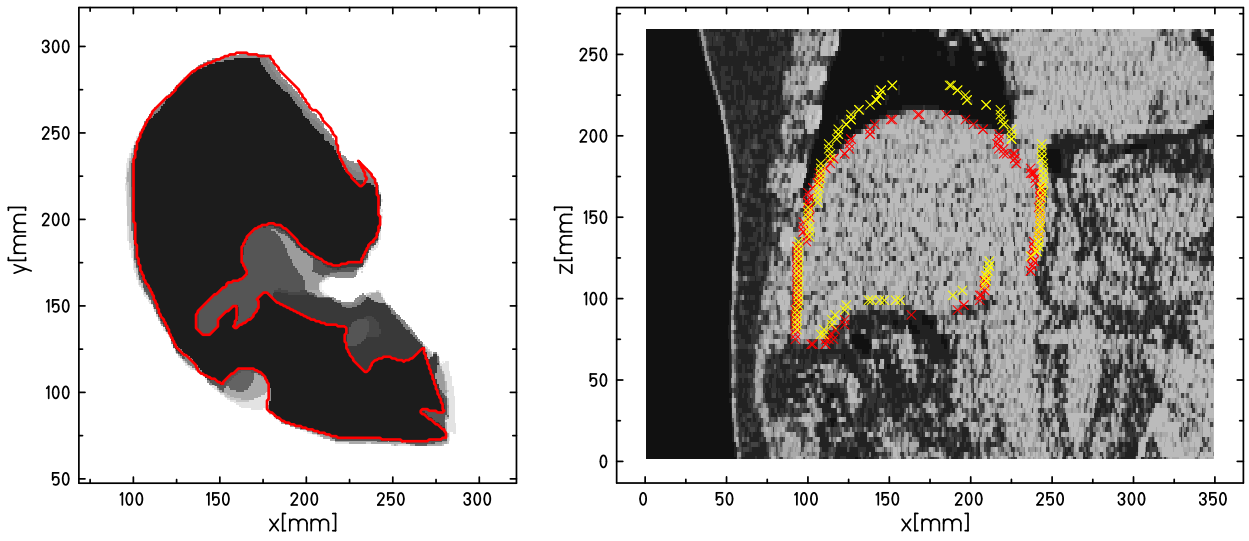

Figure 3.3.: (a) View of an axial slice of a VBM dataset for a liver ROI. The different ROI states are indicated by a gray shading, the red solid line is the overlayed polygon contour of the reference state. **(b)** Coronal cut of liver contours for the reference state (exhale, yellow markers) and the propagated inhale state (red markers). The contours are overlayed on the inhale CT phase.

The procedure is illustrated in figure 3.2b. The position of $\boldsymbol{p}$ w.r.t. the reference state contour is tested using the point-in-polygon ray-casting algorithm described in the last section. The voxel positions having a source point inside the polygonal reference contour are marked in the volume dataset as a Boolean mask using separate bits for the different states (figure 3.2a). After repetition of the procedure for each state i and each $\boldsymbol{q}_{lmn}$ the VBMs for all ROI states are contained within a single dataset (figure 3.3a). It should be noted that the described propagation algorithm does not require transformation of the reference state VBM-ROI. Instead, it makes direct use of the polygonal reference state contour to obtain the VBM-ROIs in all states.

The performance of the contour propagation algorithm has been assessed by visual inspection. Figure 3.3b shows the result of a liver contour propagation driven by the deformation maps obtained from image registration of a 4DCT. The liver contour was propagated from the reference end exhale state (yellow markers) to the end inhale state (red markers) and shows good agreement with the underlying anatomy depicted in the inhale CT phase.

3.2.2 4D treatment plan optimization strategy

Common 4D treatment planning strategies for ion beams have been introduced in section 2.3.2. At the time of writing treatment plan optimization for all motion mitigation techniques in TRiP4D is performed on a reference 4DCT state only, as reported by Bert and Rietzel (Bert and Rietzel, 2007).

Depending on the employed motion mitigation technique (section 2.2.3) optimization of the target volume, i.e. ITV generation, and technique-specific parameters are required to ensure adequate dose coverage. These parameters, for instance, comprise the optimization of motion compensation parameters in the case of beam tracking or the gating window size in beam gating.

This section briefly introduces the design of ITVs and the optimization of beam tracking and dose compensation parameters in TRiP4D. The functionality predominantly has been implemented by colleagues and is mentioned here for the sake of completeness. The optimization of beam parameters for the compensation of residual motion will be discussed later in chapter 4, since it does not require specifically implemented functionality.

3.2.2.1 Internal target volume design

ITVs are formed from the CTVs in all relevant 4DCT phases (ICRU, 1999). Rescanning, for instance, requires the formation of an ITV over all respiratory states, while for gating only the states inside the gating window are relevant. In ion beam therapy the mere use of a geometrical union is not sufficient for the design of ITVs, since range variations in the beam path need to be considered (ICRU, 2007). For scanned ion beam therapy a water-equivalent approach has been proposed by Rietzel and Bert (Rietzel and Bert, 2010) and has been implemented into TRiP4D (Graeff et al., 2012). The method makes use of the 4D segmentation functionality of TRiP4D to form the geometric union of the target volume as a first step. For a specific beam incidence the composite target volume in water equivalent space is then calculated laterally and longitudinally, taking into account motion-induced density variations. Further treatment planning is then performed on the water-equivalent ITV. The latter also can be re-converted to geometrical space, if needed. It shall be emphasized again that due to the density variations in the beam path the ITV is port-specific. Consequently, the unique geometric target volume required for dose optimization on multiple-field ITVs has to be related to multiple water equivalent representations, depending on the beam port.

3.2.2.2 Optimization of real-time beam adaption parameters

In beam tracking the beam position is adjusted to the tumor motion in real-time (Groezinger et al., 2006). During beam delivery pre-calculated correction vectors are applied to the planned beam position according to the current motion state of the patient. A more elaborate version of beam tracking additionally compensates for potential dose changes of tumor areas with respect to the reference treatment plan, caused , e.g., by target rotations, and is called *real-time dose compensation combined with beam tracking (RDBT)* (Bert and Rietzel, 2007; Lüchtenborg et al., 2011). The optimization of position and dose compensation parameters has been integrated into TRiP4D by Lüchtenborg et al. (Lüchtenborg et al., 2011). In brief, the deformation maps obtained from image registration (section 3.2.1.3) are used to calculate lateral and longitudinal correction parameters for each raster point and in all motion states relative to the planned position in the reference state. The correction parameters are stored in a look-up table. During beam delivery the lateral position adaptation is realized via the scanner magnets. The longitudinal correction corresponds to a modulation of the water-equivalent range via the beam energy using a fast double-wedge system (Weber et al., 2000). For real-time dose compensation the look-up table of correction vectors is extended by the motion state-dependent dose contributions of each raster point to all other raster points. The dose compensation parameters enable correction of the applied particle numbers in real-time, in order to compensate for motion-induced dose changes.

3.2.3 Simulation of 4D treatment delivery

Dose deposition for moving targets in scanned ion beam therapy is determined by the double-dynamic nature of the system, also representing the origin of the interplay effect. Firstly, the beam delivery process itself is time-dependent, since the beam is scanned over the target. Secondly, the effective beam position is affected by the target motion. Both contributing aspects have to be modeled adequately in the TPS, in order to enable simulation of 4D treatments. It has been shown with earlier versions of the GSI 4DTPS that simulation of dose delivery subsequent to treatment is well feasible for experimental setups (Li et al., 2004; Gemmel et al., 2011; Bert, Richter et al., 2012).

TRiP4D has been extended for simulation of clinical 4D treatment delivery in realistic patient environments. This particularly includes irregular surrogate motion trajectories, 4D dose calculation using transformation maps obtained from deformable image registration and time-resolved beam delivery sequence data compatible with clinically used accelerators, e.g., HIT. In the following sections the integration of clinical motion monitoring data and the time structure of the beam delivery process into TRiP4D are described. Temporal correlation of these two components finally enables simulation of physical and biological 4D dose deposition which considers the specific motion characteristics at treatment delivery time. The implementation of these aspects will be discussed in the last section.

3.2.3.1 Motion state identification

In section 3.2.1.2 the principal incorporation of motion monitoring data into TRiP4D was discussed. The simulation of 4D treatments in TRiP4D requires information on the transition of the patient through the 4DCT phases over time. Surrogate motion monitoring data acquired concurrently to beam delivery can provide this information, given that the identification of the motion state is performed in agreement with the 4DCT reconstruction process (Ford et al., 2003; Rietzel et al., 2005a).

Motion state identification is a central functionality of TRiP4D's motion trajectory module. Different methods are available based on: (i) the absolute signal amplitude, (ii) the signal phase and (iii) the relative signal amplitude. The latter is needed in particular for use in conjunction with the ANZAI system. In contrast to **amplitude-based (AB)** motion state identification, the methods (ii)–(iii) require dedicated signal pre-processing prior to motion state identification. For **phase-based (PB)** identification the signal phase is computed using the Hilbert transform of the original signal (Lyons, 2010). The Hilbert transform is obtained by external fast Fourier transform routines (Frigo and Johnson, 2005). Figure 3.4 shows an original patient trajectory and the corresponding Hilbertian phase component. For **relative-amplitude-based (RB)** identification the original signal is converted into a normalized trajectory with a fixed amplitude range. This is done based on a search for the maximum and minimum position in each respiratory cycle and subsequent normalization of the signal to the amplitude range in each exhale (negative slope) and inhale branch, respectively (figure 3.4).

After signal pre-processing, motion state identification at a specific time along the trajectory is performed as follows:

(i) The limits on the pre-processed signal for the respective motion states are configured either automatically or by the user. The limits should be in agreement with the distribution of the

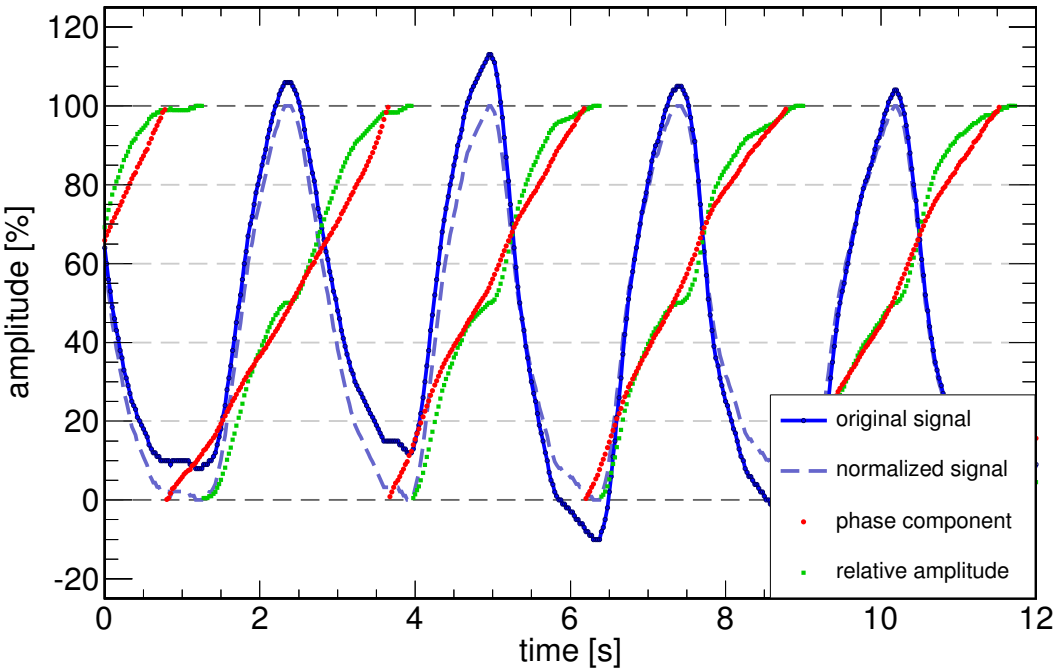

Figure 3.4.: Motion state identification in TRiP4D. Depending on the employed method the original signal (AB), its Hilbertian phase component (PB) or the relative amplitude (RB) is discriminated against motion state limits (gray dashed lines). The relative amplitude is obtained from the normalized signal by flipping over the exhale branches at each maximum and normalizing to 100 %.

motion states over the respiratory cycle as defined during reconstruction of the 4DCT. This step is independent from the input time and usually done only once during a treatment planning session.

(ii) If necessary, the pre-processed signal is interpolated linearly between the neighbouring supporting points.

(iii) The motion state is determined by discrimination of the interpolated signal value against the motion state limits. In contrast to AB identification the inhale/exhale status is also considered for the RB and PB methods.

3.2.3.2 Beam delivery sequence and time structure

In raster scanning the individual dwell time per raster point depends on the requested particle fluence and the intensity delivered by the accelerator. Due to the complexity of the system, the a priori modeling of the time structure of beam delivery is challenging, especially if beam pauses caused by gating or by the synchrotron are to be considered. However, the time structure, called beam delivery sequence (BDS) in the following, can be measured during irradiation. The procedure to obtain the BDS can be considered highly facility dependent. Nevertheless, several general beam delivery events (BDEs) can be expected to be accessible at any scanning facility. Table 3.1 summarizes the types of BDEs and the possible transitions between them.

TRiP4D provides the interface to a generally defined table format for BDS input files describing the chronology of BDEs. The tables have to be compiled externally according to the specific

event type	characterization	possible transition to
BON	beam on	BOF, NXP
NXP	end of a raster point	NXP, EOP, BOF
EOP	end of iso-energy slice	BOF
BOF	beam off	BON

Table 3.1.: Types of general beam delivery events (BDEs). The chronology of BDEs defines the beam delivery sequence (BDS).

conditions of the respective machine and the data acquisition system used. In contrast to the data model used in previous 4D versions of TRiP98, only the basic information needed for simulation of 4D dose deposition is integrated into the TPS in an efficient way. No measured beam intensity profiles or memory-consumptive intensity courses are needed. The automatic generation of simulated BDS tables for 4D treatment simulation purposes has not been integrated into the TPS, since this is a highly facility dependent task. External software is used to model the beam delivery time structure at GSI and HIT. An example of a simulated beam delivery sequence is shown in figure 3.5.

3.2.3.3 4D dose deposition

4D dose deposition is fully determined by the treatment plan, the time structure of the beam delivery and the patient motion. In order to account for dose contributions to each dose voxel in consideration of target motion, knowledge is required on which raster points were fully or partly irradiated in a certain motion state. This information is obtained from the combined time courses of the BDS and the surrogate motion trajectory. This section will discuss the necessary steps to model the dose deposition in 4D treatment simulations based on measured or simulated surrogate motion traces and beam delivery sequences.

Time correlation

The treatment control system and the motion monitoring device are usually independent medical products of different manufacturers, hence, beam delivery and motion monitoring naturally do not share the same data acquisition and system clock. At the time of writing, the integration of motion monitoring into the HIT treatment control system is not sufficient to allow full base data acquisition for 4D treatment simulation.[5] Similar situations are to be expected for other facilities. Therefore, temporal alignment of the BDS and the surrogate motion trace, i.e. the identification of the time offsets between the different acquisition systems, is mandatory. Figure 3.5 illustrates the time-correlated motion trajectory and the respective BDS. Temporal correlation is performed with external tools and the determined time offsets then are communicated to TRiP4D. For this purpose, user-specified offset values for both the native BDS and motion trace input files are supported. Time stamps are handled with micro-second precision and any time resolution larger than one micro-second is supported for the surrogate monitoring and BDS input files.

[5] Nevertheless, a dedicated interface for gated beam delivery with the ANZAI AZ-733 system exists.

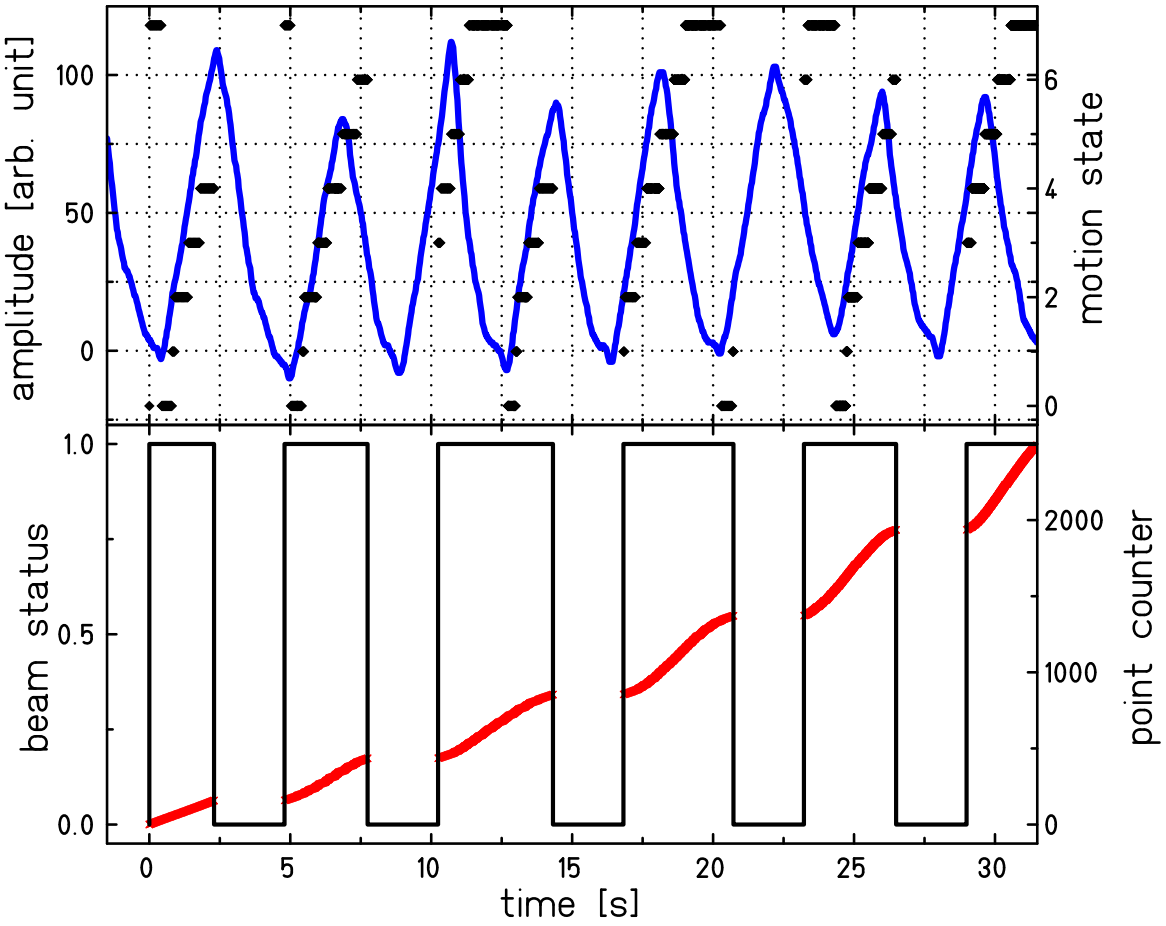

Figure 3.5.: Visualization of an example 4D beam delivery course. The lower graph visualizes the beam delivery sequence comprising the beam status (BON/BOF events, cf. table 3.1) shown as a logical signal (black line) and the irradiated raster points (NXP events) as red markers. Due to their temporal clustering, the single raster points can not be resolved in this graphical representation. The upper graph depicts the time-correlated motion trajectory (blue line) and the distribution of motion states as they were detected for the irradiation of each raster point (black diamonds) according to RB motion state identification. The motion states are encoded as integer numbers with '0' marking the end exhale position (minimum). The presented kind of graphical visualization of 4D beam delivery courses is part of the TRiP4D functionality.

Generation of quasi-static sub-treatment plans

Temporal correlation of the motion surrogate with the beam delivery sequence enables identification of the motion state in which each of the treatment plan's raster points was irradiated. The original treatment plan is split into quasi-static sub-treatment plans, according to Bert and Rietzel (2007). Each plan comprises all raster points fully or partly irradiated in the respective 4DCT phase. Sorting of the points into the associated sub-treatment plans is performed using either amplitude-based, phase-based or relative-amplitude-based motion state identification, as discussed above. Let it be emphasized again, that the motion state identification method ideally should match the one used for 4DCT reconstruction.

The generation of sub-treatment plans has been fully re-implemented to integrate the functionality developed by Bert and Rietzel (2007), RDBT according to Lüchtenborg et al. (2011) and new functionality developed within the scope of this thesis. The implemented algorithm will be described in the following.[6]

The temporal sequence of beam delivery events first is complemented by identification of the valid motion state for each event. The different types of BDEs and their valid transitions are recalled in table 3.1. Additional events which mark a change of the 4DCT phase, so-called *motion state change (MSC)* events, are then generated and inserted into the BDS at the respective times. Determination of the temporal position of the MSC events is performed by nested temporal interval searches in-between subsequent BDEs using the functionality provided by TRiP4D's motion trace module. The extended BDS constitutes the basis for sub-treatment plan generation. Note that any temporal misalignment of the motion trajectory and the BDS will result into an entirely different mapping of the motion states to the respective BDEs (see also figure 3.5).

Generation of the sub-treatment plans is performed by sequential processing of the linked list of BDEs. A flow chart of the algorithm is given in figure 3.6. In contrast to earlier implementations, the algorithm employs a state machine approach to more effectively handle transitions between BDEs and reliably intercept invalid event transitions being inconsistent with table 3.1, e.g., if resulting from defective data. The irradiation of each raster point is traced over time and the nominal fluence is sub-divided and allocated to the respective sub-treatment plans. For this purpose specific actions are triggered upon detection of the different BDE types, as illustrated in the flow chart. Start of irradiation for a raster point is triggered by the BON event in the case of the first point of an iso-energy slice and by the NXP event otherwise. Stop of irradiation of a point is communicated via the subsequent NXP event. After the start of irradiation of a point has been triggered, the subsequent motion state changes are buffered in a temporal list of MSC events. Beam pauses occurring during irradiation of the point are also registered. At stop of irradiation the coordinates and particle fluence of the respective point are obtained from the 3D treatment plan, maintaining the irradiation order. If simulation of beam tracking has been requested, the raster point coordinates are adapted according to the provided tracking look-up table (Bert and Rietzel, 2007). In the case of RDBT the particle fluences are adapted according to Lüchtenborg et al. (2011).[7] In order to maintain consistency between the simulation and the actual beam delivery, the same routines are also used in the treatment control system. Beam tracking and RDBT both rely on motion monitoring for real-time calculations. Miscorrelation of the true tumor motion and the monitored motion, such as phase shifts, can be simulated using a dedicated motion monitoring trajectory for all real-time tasks. The subsequent evaluation of the fractional particle fluences is independent from the motion mitigation modality

[6] The integration of RDBT predominantly has been carried out by R. Lüchtenborg (Lüchtenborg et al., 2011).

[7] The dose compensation functionality can also be used stand-alone and independent from beam tracking.

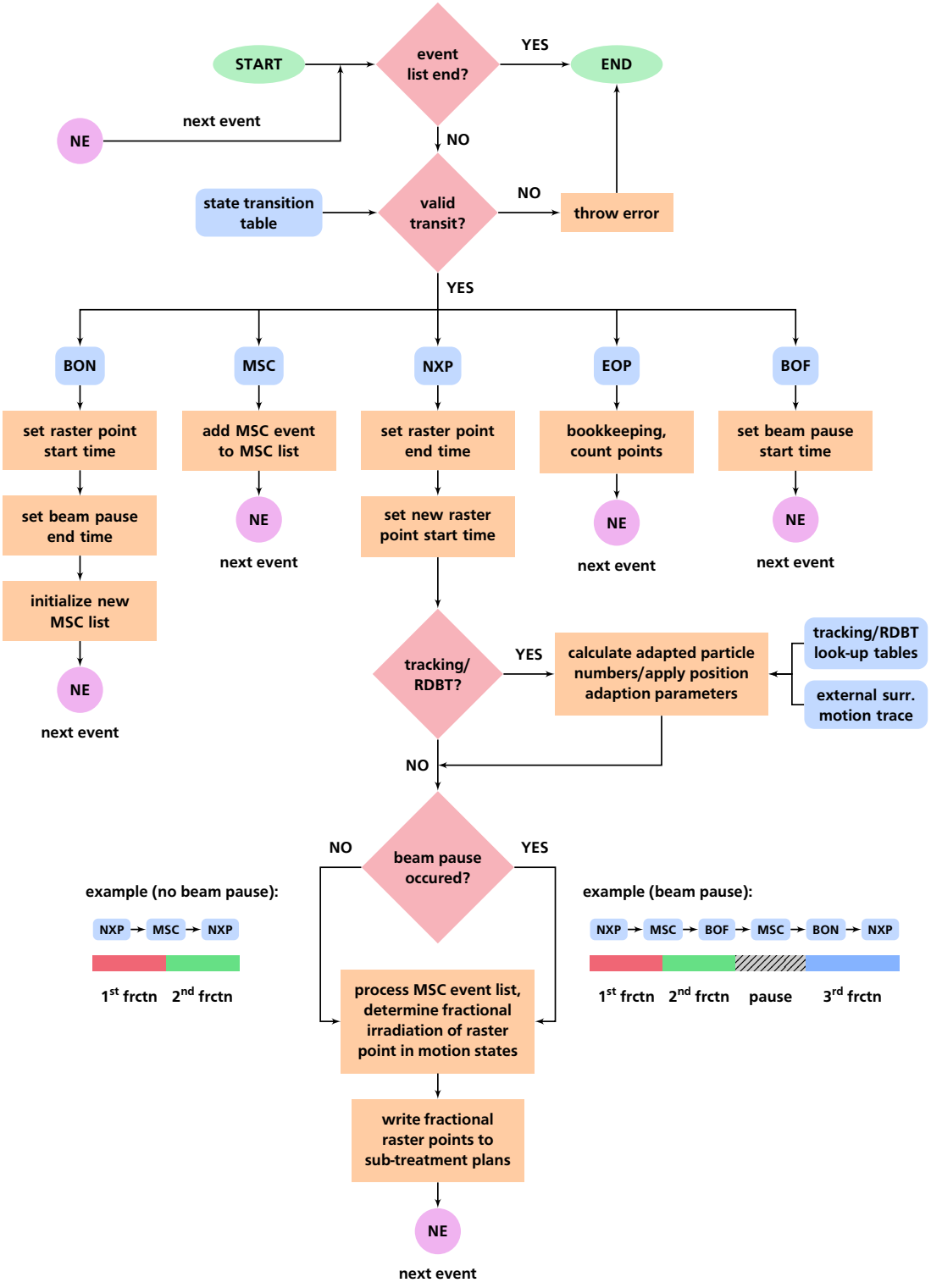

Figure 3.6.: Flow chart of the generation of quasi-static sub-treatment plans after temporal correlation of BDS and motion surrogate. The linked list of BDEs (cf. table 3.1) is processed event by event keeping track of all MSC events during irradiation of a raster point. Particle fluences are linearly sub-divided and allocated to the sub-treatment plans according to the relative time spent in the respective motion state during irradiation. The examples show typical configurations for the irradiation history of raster points with and without beam pause.

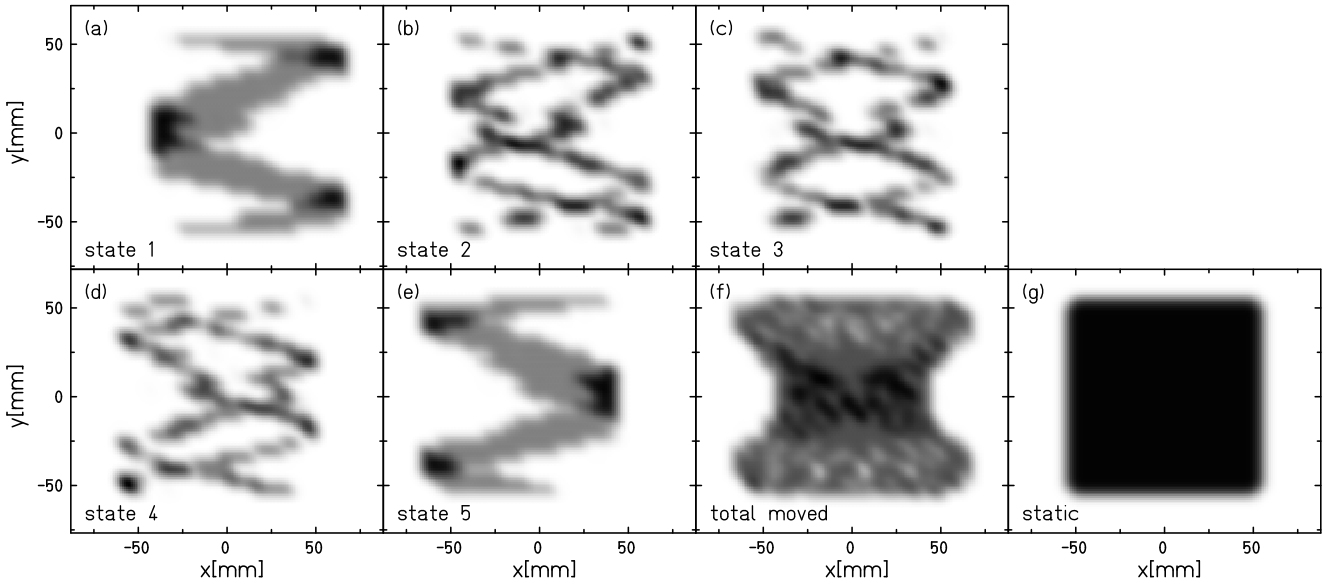

Figure 3.7.: Example of 4D dose and film response calculation with TRiP4D for a sinusoidally moved film along the x axis in free air. Figures **(a–e)** break down the total 4D film response **(f)** to the individual dose contributions in each of the five motion states. All distributions are shown in the reference state coordinate system and are normalized to their individual maximum in optical density. The 3D treatment plan covers a homogeneous square on the stationary film **(g)**.

and also applies for uncompensated irradiation. The fractional particle fluences are determined using the buffered list of MSC events. The beam intensity is assumed to be constant over the time-scale of a raster point irradiation (several milliseconds). This is a valid approximation for treatment conditions at HIT and GSI. The nominal particle fluence then is sub-divided according to the relative weight of the irradiation time span in the respective motion state, taking potential beam pauses into account. Two typical configurations of fractional raster point irradiation and the resulting fluence sub-division are illustrated in figure 3.6. The procedure is repeated until all raster points of the 3D treatment plan have been processed. Note that solely for beam tracking and RDBT specific steps need to be taken. In all other cases the treatment modality characteristics of the beam delivery are communicated by the BDS only.

4D dose calculation

The quasi-static sub-treatment plans discussed in the last section are the starting point for 4D dose calculation. The dose calculation algorithm of Gemmel et al. was implemented in TRiP4D and is capable of both biological and physical dose calculation. For details the reader is referred to the respective publication (Gemmel et al., 2011). In brief, the dose contributions of all raster points of the respective sub-treatment plan to each dose voxel are collected in every motion state. For this purpose, the voxel position is transformed accordingly, using TRiP4D's deformation map module (section 3.2.1.3) and taking into account the radiological density distribution of the respective 4DCT phase. The algorithm therefore is fully compatible with transformation maps obtained from deformable image registration of patient 4DCTs. The total physical dose is computed by summation of the dose contributions from all motion states in the reference state (figure 3.7). For biological dose calculation the particle spectra in energy and atomic number

are also accumulated over all motion states in consideration of the transforming dose grid. The total spectra finally are used as the input for the calculation of the relative biological effectiveness and the resulting biologically effective dose using the LEM (Krämer and Scholz, 2000). Accordingly, TRiP98's capabilities to calculate non-linear dose response of radiographic films in dependence of the local particle and energy spectra using a model similar to the LEM (Spielberger et al., 2003) have been extended to 4D. Additionally, calculation and output of dose and detector response distributions in individual motion states is supported. An example of a 4D film response simulation including the state-resolved sub-distributions is given in figure 3.7. Finally, TRiP4D provides calculation of dose volume histograms for ROIs in all motion states in conjunction with the 4D segmentation module (section 3.2.1.4).

3.3 Verification

TRiP4D is a newly designed 4DTP extension to the established GSI treatment planning system TRiP98. The integration of the 4D functionality required substantial changes of the existing program structure and source code. Systematic testing is required to assure that core functionality of TRiP98 is not impaired. Moreover, the 4D planning functionality combines newly implemented features and re-implementations based on earlier programs. Both demand elaborate validation, especially considering the program's possible future application in clinical routine. The consistency of TRiP98's core functionality in TRiP4D has been verified successfully using the comprehensive test suit delivered with the mother program and will not be discussed here. The predecessors of TRiP4D were repeatedly tested in various dedicated experiments (Li et al., 2004; Gemmel et al., 2011; Bert, Richter et al., 2012). Within the scope of this thesis selected tests were re-iterated and TRiP4D's performance was benchmarked against the experimental results and the predecessor programs. Additionally, new water phantom experiments were designed and conducted, in order to test the program's combined functionality at a high level of complexity.

3.3.1 Radiographic film response simulations

The 4D treatment simulation capabilities of TRiP4D were tested in simulations of the dose response of radiographic films moved during irradiation. The simulations were verified against the experimental results obtained by Bert, Richter et al. (2012) and were compared to previous simulations of the 4D detector response by the same authors.

3.3.1.1 Materials and methods

The experimental setup of the radiographic film measurements is summarized here in brief. For a detailed description the reader is referred to the original publication by Bert, Richter et al. (2012). Irradiation was performed at GSI with a carbon ion beam and a single-slice treatment plan. The plan was designed to cover a $110 \times 110\,\mathrm{mm}^2$ field with a homogeneous dose. Radiographic films were used as detectors and mounted on a motorized sliding table in free air. The films were moved sinusoidally during irradiation in left-right direction w.r.t. BEV. Different motion amplitudes, periods and initial phases were chosen and adjusted via the sliding table. The radiographic films were developed and digitized according to Spielberger

et al. (2003). The film trajectories were measured with sub-millimeter precision and recorded during irradiation with a calibrated camera system tracking an infrared LED at an acquisition rate of 40 Hz. The beam delivery sequence, i.e. the irradiation times of all raster points and the start and stop times of the beam extraction, were measured in a separate data acquisition system (DAQ) via TTL pulses generated from the control system. In order to establish temporal correlation between target motion and the beam delivery sequence, the beam status signals were additionally recorded with the motion monitoring DAQ.

The simulations of the optical film density were carried out using the 4D extensions to the TRiP98 program by Bert and Rietzel (TRiPB) on the one hand and those of TRiP4D on the other. According to section 3.2.3.3 the simulations were divided into two steps: (i) the generation of sub-treatment plans and (ii) the calculation of the 4D detector response on the basis of the sub-treatment plans. The two simulations steps were performed with either of the two programs and in all possible combinations to assess the origin of possibly differing performance. Due to the different working principles of the programs rigid transformation maps (cf. section 3.2.1.3) were created on the basis of the measured film trajectories for TRiP4D, while for TRiPB the displacement vectors were determined directly from the trajectories. Simulations were performed for 20 motion states and amplitude-based motion state identification. Calculation of the expected optical density of the films in response to the local deposited dose for both programs is based on the model of Spielberger et al. and the resulting particle-specific film responses (Spielberger et al., 2003). The same set of depth-dose and particle spectra base data was used in all simulations to guarantee comparability (Krämer et al., 2000).

The agreement of the simulations with the respective measurement for each of the motion parameter sets was assessed by statistical analysis of the differential optical density distributions. The rigid registration of the coordinate systems of the measured films and the simulations was used as determined by Bert, Richter et al. (2012). The analysis was restricted to a region of interest of $155 \times 135\,\mathrm{mm}^2$ and pixels with optical densities $S > 0.01$. These criteria establish an individually adjusted analysis mask for each case to prevent domination of the background outside the irradiated area. The relative mean deviation in optical density and its standard deviation were computed and chosen as a figure of merit to evaluate the agreement.

3.3.1.2 Results

Table 3.2 lists the results of the statistical analysis for the 14 measured parameter combinations. Peak-to-peak motion amplitudes range from 8–20 mm for motion periods between 3 and 7 s. The initial phases were 0°, 90°, 180° and 270°, depending on the case. In the table, the analyzed simulation combinations are denoted by the identifiers for the programs used in each of the two simulation steps, TRiPB (B) and TRiP4D (R), respectively. The comparison of the results for the unmixed configurations RR and BB reveals that the mean relative deviation μ of simulated and measured optical densities is closer to zero for all 14 cases in the full TRiP4D simulations. The largest differences are obtained for cases (a)–(d) with a 20 mm peak-to-peak amplitude ($> 2\,\%$). For case (d) the absolute decrease in μ exceeds 7 % and amounts to about 2 % for the other 13 cases. Similarly, the standard deviation σ is reduced for all cases except case (j). The largest decrease for σ is observed for the 20 mm amplitude cases (a)–(d). For case (d) the absolute decrease is larger than 50 % and larger than 7 % for cases (a)–(c). An absolute decrease of around 6 % is yielded for cases (l)–(n), only minor decreases are observed for cases (e)–(i) and (k) ($< 1\,\%$) and a negligible increase for case (j) ($< 0.1\,\%$).

motion parameters				BB		RR		BR		RB	
case	A[mm]	T[s]	ϕ[°]	μ[%]	σ[%]	μ[%]	σ[%]	μ[%]	σ[%]	μ[%]	σ[%]
(a)	20	5	90	−5.03	20.64	−2.14	12.98	−4.76	20.35	−2.42	13.66
(b)	20	5	0	−7.32	21.52	−3.73	13.23	−7.28	21.66	−3.88	13.35
(c)	20	7	0	−4.80	21.76	−1.46	9.72	−4.76	21.92	−1.59	9.66
(d)	20	7	90	−9.84	68.98	−2.19	12.68	−8.96	56.94	−2.24	12.21
(e)	15	3	0	−1.85	10.78	−0.55	10.48	−1.70	10.71	−0.68	10.54
(f)	15	3	90	−0.89	11.53	0.37	10.84	−0.77	11.50	0.24	10.92
(g)	15	4	0	−3.50	12.06	−2.13	11.68	−3.36	11.96	−2.24	11.68
(h)	15	4	90	−4.39	11.19	−2.89	10.73	−4.21	11.04	−3.06	10.87
(i)	15	5	0	−5.40	14.99	−4.06	14.55	−5.19	14.66	−4.17	14.66
(j)	15	5	180	−5.74	12.74	−4.43	12.78	−5.65	12.86	−4.53	12.65
(k)	15	5	270	−6.46	16.09	−5.11	16.01	−6.38	16.31	−5.21	15.82
(l)	8	5	0	−2.24	18.53	0.12	12.78	−1.04	12.94	−1.02	18.11
(m)	8	4	0	−2.83	15.56	−0.88	9.43	−2.69	15.53	−1.00	9.47
(n)	8	3	0	−2.98	16.92	−1.11	10.93	−2.75	15.71	−1.21	10.89

Table 3.2.: Results of the statistical analysis of the agreement between simulated and measured optical film densities for all 14 motion parameter sets (A = amplitude, T = period, ϕ = initial phase). In the four columns the mean relative deviation μ of the simulated from the measured densities and its standard deviation σ are reported for all studied program combinations in the two successive simulation steps: generation of sub-treatment plans and 4D detector response calculation. B and R denote the used program for each step, TRiPB and TRiP4D, respectively. The red highlighted column indicates the results of the full TRiP4D simulation (RR).

Results for the mean optical density and standard deviation for the mixed simulation RB are comparable to those obtained for simulation RR in most cases. Absolute differences for mean and standard deviation values between RB and RR are below 1 %. Only for case (l) differences of about 1 and 5 % are observed for the mean and standard deviation, respectively.

Comparing simulations BR and BB, both using TRiPB to generate the sub-treatment plans, the changes in the mean and standard deviation w.r.t. BB are much less pronounced than those between simulations RB and RR. Only cases (d) and (l) show significant improvements in the mean value (> 0.8 %) and the standard deviation (> 5 %).

3.3.1.3 Discussion

The data in table 3.2 show that the major improvement in simulation accuracy results from the new algorithm for the generation of sub-treatment plans in TRiP4D. These improvements could be traced back to the more consistent handling of beam delivery sequences in TRiP4D compared to TRiPB. The state machine approach discussed in section 3.2.3.3 proves less error-prone, in particular in the case of corrupted beam delivery sequence data. For the cases (a)–(d) the defective data resulted from timing issues of the data acquisition at the time of the experiments and could be resolved retrospectively. Using TRiP4D for the 4D dose calculation step instead of

TRiPB had a small impact on the agreement of the simulated optical density distributions with the measurements. The small improvements gained over TRiPB for mean value and standard deviation predominantly result from additional interpolation steps needed for the summation of individually transformed state dose cubes in the reference state for TRiPB. The larger deviations obtained for cases (d) and (l) result from high sensitivity of these cases w.r.t. minor differences in the applied displacements vectors. Specifically, small film displacements (<2 mm) orthogonal to the motion direction, i.e. up-down BEV, have been neglected for TRiP4D calculations, as they are affected by large relative errors of the position measurement. On average, the measured optical density distributions are reproduced by the full TRiP4D simulations RR to about (-2 ± 12) %. Hence, the calculated optical densities in general are slightly overestimated by TRiP4D. Regarding the accuracy of around 10 % to be expected from film response calculations for ion beams (Spielberger et al., 2003), the simulations otherwise are in good agreement with the measurements.

3.3.2 Water phantom experiments and simulations

Predecessor versions of the GSI 4D treatment planning system have been tested repeatedly in experiments. So far, 2D target motion, with and without range changes introduced by absorbers were studied (Li et al., 2004; Bert, 2006; Bert and Rietzel, 2007; Bert et al., 2009). In preparation of extensive patient treatment planning studies and future clinical application, more elaborate tests of TRiP4D were carried out in water phantom experiments at the Heidelberg Ion-Beam Therapy Center using a robotic setup with 3D target motion and gated beam delivery. TRiP4D simulations were compared to absolute 4D dose measurements.

3.3.2.1 Materials and methods

The experiments were part of a measurement series with and without gated beam delivery. The details given here on the experimental setup will focus on the specifics for gated beam delivery. Further details on the data acquisition and instrumentation will be given later in chapter 4 in the context of residual motion experiments using a largely identical setup.

An ellipsoidal target volume of 82 cm^3 was irradiated in a static water phantom with gated beam delivery. The absorbed dose was measured with an array of 24 pinpoint ionization chambers (ICs), as reported by Karger et al. (1999). 3D sinusoidal motion of the IC array was facilitated using a robotic arm (Steidl, Richter et al. 2012). Peak-to-peak motion amplitudes of 20 mm in left-right BEV and 10 mm in the remaining dimensions were chosen. Additionally, non-gated static reference irradiations were performed. Beam control and the adjustment of the gating window were established using the ANZAI AZ-773V system (ANZAI MEDICAL CO., LTD). The gating window (GW) was configured based on the signal of a laser distance sensor which monitored the LR projection of the IC array motion. The GWs were adjusted to result in residual motion amplitudes of 2–10 mm around the maximum amplitude in LR BEV. Target motion, raster point irradiation times and beam status signals were acquired with a dedicated data acquisition system (section 4.2.1).

Treatment plans were optimized with the GSI reference 3D treatment planning system TRiP98. 18 different combinations of lateral grid spacing (2 and 3 mm), iso-energy slice spacing (1, 2, 3 and 4 mm water-equivalent), beam FWHM (6, 8 and 10 mm) and two different ripple-filters (section 2.1.3.2) were chosen. Apart from the standard ripple-filter (RiFi) with 3 mm

effective Bragg-peak width (RiFi3), two orthogonally crossed 3 mm RiFis were used, approximately corresponding to a 4 mm RiFi (RiFi4). The plans were optimized for a homogeneous target dose of 2 Gy.

Simulations were performed based on the nominal 3D target trajectory as the motion surrogate, the reference treatment plan and the respective BDS according to section 3.2.3.3. The BDS was obtained by combined evaluation of the measured signals from the treatment and accelerator control systems over time. The temporal alignment procedure will be explained in detail in section 4.2.3.1. Generation of the sub-treatment plans (cf. section 3.2.3.3) was based on the nominal target motion trajectory generated by TRiP4D. The individual initial phases for each measurement due to the gated beam delivery were taken into account (section 4.2.3.2). 4D physical dose calculations were performed for 22 phases of a computer-generated 4DCT and phase-based motion state identification (section 3.2.3.1). The transformation maps for rigid target motion were generated with TRiP4D based on the target motion trajectory.

The agreement of the simulations with the respective measurements was assessed by statistical analysis of measured and calculated dose values at the ionization chamber positions. A dedicated program has been developed within the scope of this thesis to extract dose values from calculated dose distributions for a given ionization chamber array geometry (appendix A.2). Dose extraction is based on trilinear interpolation among neighbouring dose voxel centers. For the analysis of the individual measurements the mean relative difference

$$\overline{\Delta D} = \sum_{i}^{N} \left(D_i^{\text{calc}} - D_i^{\text{meas}} \right) / D_i^{\text{meas}} \tag{3.6}$$

of measured (D^{meas}) and calculated (D^{calc}) dose values and its standard deviation, σ^D, has been calculated for $N = 22$ of the 24 ionization chamber positions per measurement. The remaining two ionization chambers were neglected for analysis, since they were located close to the target volume boundary (figure 3.8). Additionally, a bivariate linear regression model was fitted to the ensemble of measured and simulated dose values for the individual ICs using JMP (version 9.0, SAS Institute Inc., Cary, NC, USA):

$$D^{\text{meas}} \approx \alpha \cdot D^{\text{calc}} + \beta \cdot \begin{pmatrix} R_3 \\ R_4 \end{pmatrix} \tag{3.7}$$

The model assumes a linear relationship between the measured and simulated dose and additionally allows for individual systematic and dose-independent contributions $R_{3,4}$, of the employed RiFi3 and RiFi4 ripple filters. α and β are free parameters. The results of the bivariate regression are reported as the coefficient of variation, R^2, and the root-mean-square error (RMSE) of the model.

3.3.2.2 Results

For each plan three to four irradiations with different motion amplitudes, distributed in the range of 2–10 mm, and one static measurement were performed, resulting in a total of 82 measurements, 64 of them with gated beam delivery. 4D simulations were performed for 52 of the gated irradiations. The remaining 12 cases were removed from the analysis because of gross measurement errors, predominantly due to missing or deficient beam delivery sequence

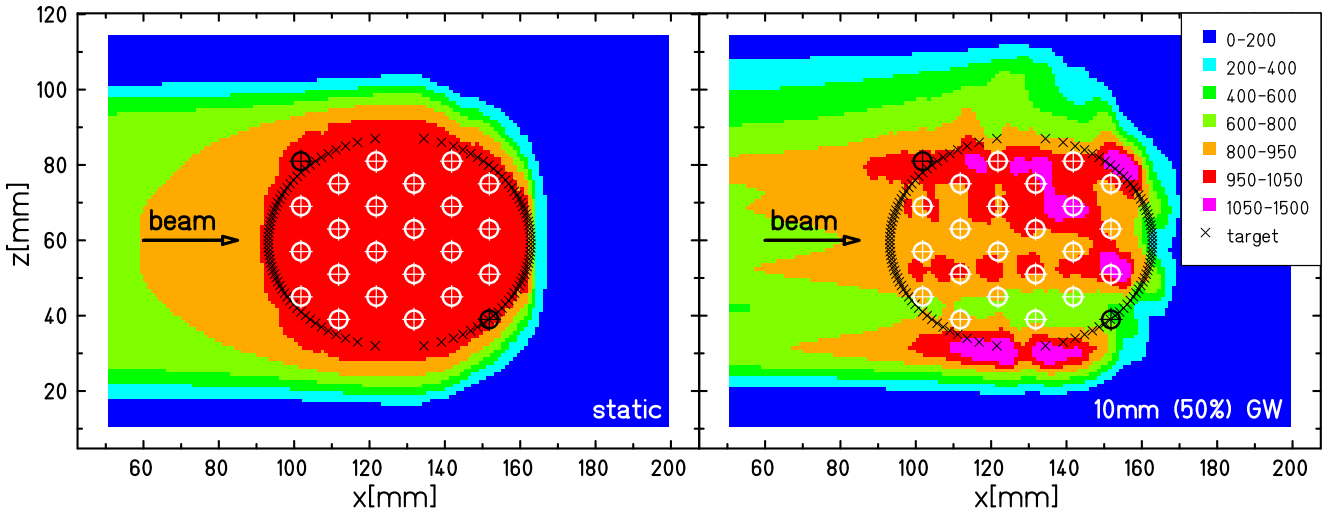

Figure 3.8.: Bird's eye view section of simulated dose distributions through the center of the target volume for static (left) and gated (right) irradiation with the same treatment plan (lateral grid spacing: 2 mm, iso-energy slice spacing: 3 mm, beam FWHM: 10 mm, 3 mm RiFi. The 4D dose distribution was transformed to the reference phase (scale in mGy). The IC positions used for dose extraction are indicated by the white and black (neglected for analysis) crosses.

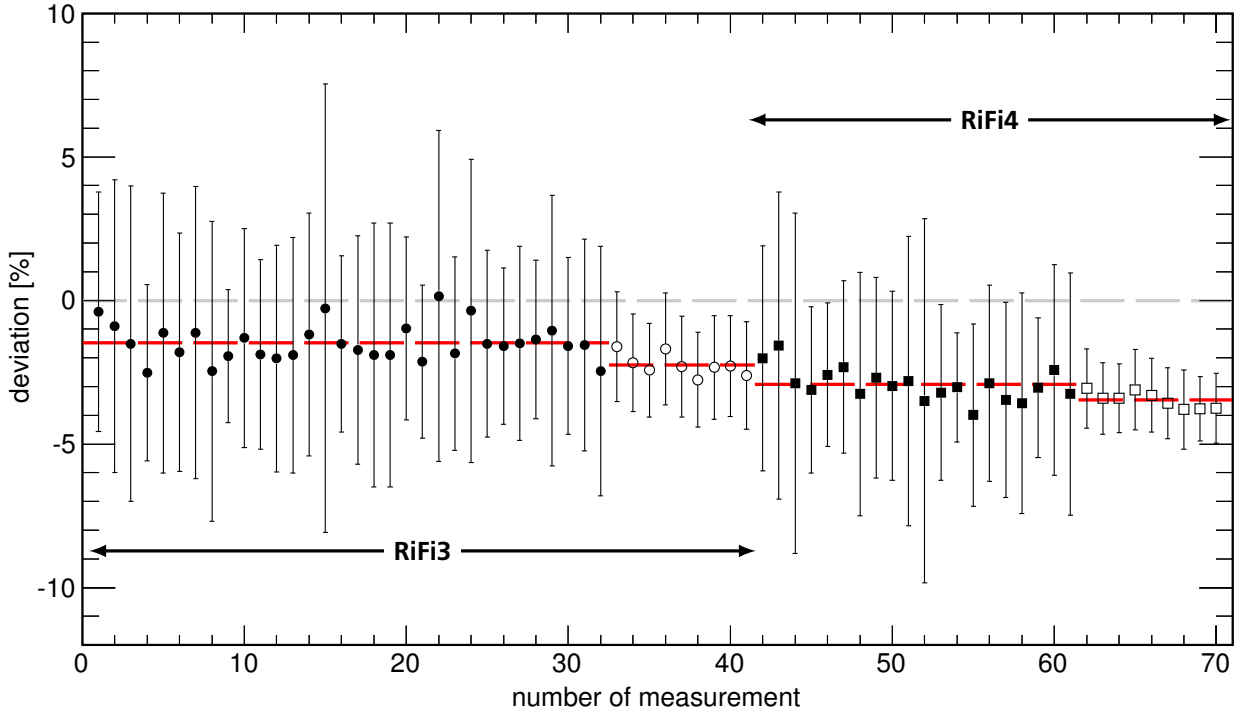

Figure 3.9.: Agreement of simulated and measured 4D dose distributions for the 52 gated and the 18 static cases (open symbols). Mean and standard deviation of the relative difference between simulated and measured dose values of the 22 ionization chambers are drawn versus the measurement index. The RiFi3 (circles) and RiFi4 (squares) measurements exhibit a different systematic deviation from zero, indicated by the respective fits (red dashed lines).

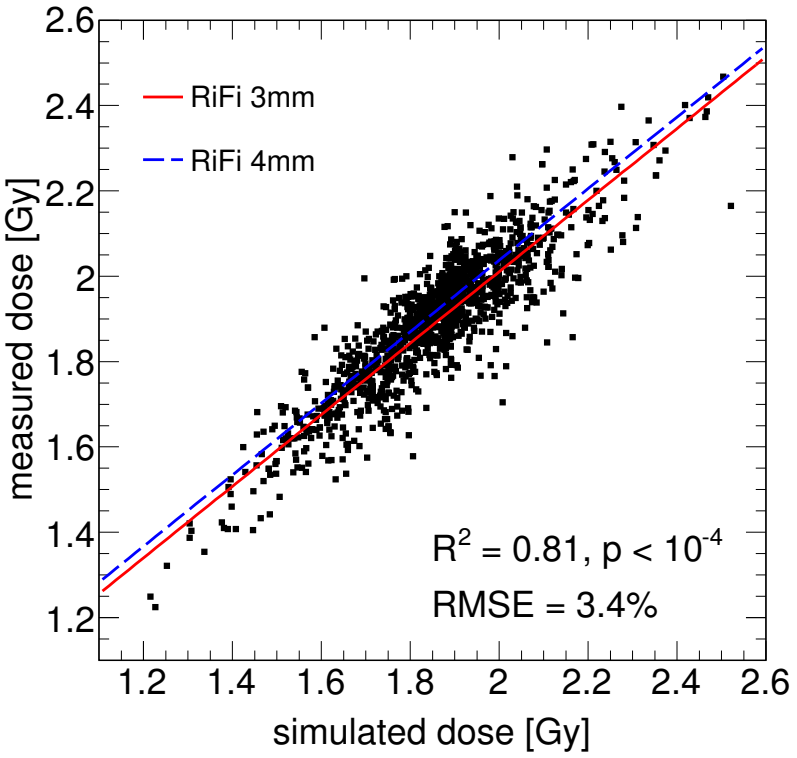

Figure 3.10: Scatter plot of the measured (D^{meas}) versus the simulated dose values (D^{calc}) at the individual IC positions for all stationary and gated irradiations. The linear fits determined with the regression model in equation (3.7) are overlayed for RiFi3 (red solid line) and RiFi4 (blue dashed line).

data. Figure 3.8 shows a section through the simulated dose distributions for the static and a representative gated irradiation using the same treatment plan. A gating window of 50 % was used in this case, corresponding to 10 mm peak-to-peak residual motion for the major (LR) motion component. The IC positions used for dose extraction and comparison with the measured data are also indicated in the figure. As expected, the dose distribution for the gated irradiation exhibits significant dose inhomogeneities due to interplay effects. Figure 3.9 reports the mean relative dose difference and standard deviation between simulated and measured dose values at the 22 IC positions for all 52 gated measurements, drawn versus the measurement number. The graph is split for 3 and 4 mm effective Bragg-peak width, i.e. RiFi3 and RiFi4, respectively. Two separate fits for the average agreement of all respective measurements are given. The simulations for RiFi3 and RiFi4 on average agree with the measurements within about (-1 ± 4) % and (-3 ± 4) %, respectively. A detailed overview of the mean and standard deviation for all 52 gated and 18 static cases is given in table B.1 in the appendix. For both RiFi configurations all cases had standard deviations smaller than 8 %, for about 80 % of the cases values smaller than 5 % were found. Simulations of the static reference irradiations on average reproduced the measurements within (-2 ± 2) % for the RiFi3 and (-3 ± 1) % for the RiFi4 treatment plans. Figure 3.10 summarizes the results of the linear regression according to the model in equation (3.7). By construction, depending on the RiFi two different linear fits are obtained. Measured and simulated dose values exhibit an explained variance of $R^2 = 0.81$ with a RMSE of the model of 3.4 % ($p < 10^{-4}$). The systematic difference in the intercept for the two RiFis also was statistically significant at the $p < 10^{-4}$ level.

3.3.2.3 Discussion

In summary, good overall agreement of the measurements and the 4D simulations was found for both the analysis for the group of 22 ICs per case and the linear regression for the individual ICs over all cases. The RiFi4 data showed a slight systematic deviation in the mean relative dose difference relative to the RiFi3 data of about 1.5 %. This is consistent among gated and stationary experiments and was also reproduced in the fits of the linear regression model. The additional systematics found for the RiFi4 data can most likely be attributed to larger uncertainties in the depth-dose base data (Krämer et al., 2000) in these cases. Furthermore, very small mean deviations of the static from the moving cases of below 1 % were observed (figure 3.9) which possibly originate from small setup errors which have less impact on the stationary results, due to the smaller gradients. The residual deviations of about 1–2 % observed for the RiFi3 cases are well within the expected systematic uncertainties of 3–3.4 % in absolute ionization chamber dosimetry for heavy ion radiation (Karger et al., 2010). With standard deviations of less than 5 % for most cases the simulations agree well with the measured dose distributions. The increase of about 2 % in standard deviation for the moving relative to the static cases can be attributed to the much higher complexity of the simulations which are subject to numerous influencing factors. For instance, additional uncertainties for the employed setup can be expected from the measured beam status signals, since, for technical reasons, these were not coupled to the beam monitoring system and feature minor unknown and systematic temporal shifts. Also, signal fluctuations were an issue during data taking. Although most measurements exhibiting the problem were disregarded, residual degradation of the beam delivery sequence data could, for instance, have an impact on the calibration of the initial motion phase.

3.3.3 Biological dose calculation

Biological 4D dose calculation is indispensable for realistic 4D treatment planning in heavy ion therapy. Cell survival experiments have been conducted by Gemmel et al. (2011) using a dedicated phantom to validate the 4D dose calculation algorithm implemented in a predecessor version of the 4DTPS. This algorithm has been integrated into TRiP4D and cell survival and biologically effective dose (BED) calculations have been re-iterated for one particular experiment (experiment 1 in the original publication). The results were compared to the measurement and the simulation results reported by Gemmel et al.

3.3.3.1 Materials and methods

The experimental setup, data acquisition and cell processing are introduced here in brief. The reader is referred to the original publication for a detailed description (Gemmel et al., 2011). A biological phantom with Chinese hamster ovary cells (CHO-K1) in a medium was positioned on a sliding table and irradiated with a carbon ion beam. The treatment plan was optimized for a homogeneous BED of 6 Gy (RBE) in a cuboid volume of $(28 \times 23 \times 45)\,\mathrm{mm}^3$. During irradiation the table was moved sinusoidally with a 40 mm peak-to-peak amplitude in left-right BEV to induce interplay effects. Changes of the radiological depth were introduced by a stationary ramp-shaped absorber in front of the phantom. Motion monitoring, acquisition of the beam delivery sequence and temporal correlation of table motion and irradiation progress were

performed as described for the radiographic film experiments discussed in the previous section. After irradiation, 10 cell samples were chosen for further analysis. Absolute cell survival was determined according to Puck and Markus (Puck and Marcus, 1955) and was converted to BED.

The 4D BED and cell survival calculations were performed based on the recorded beam delivery sequence and the motion monitoring data using both the program of Gemmel et al. (TRiPG) and TRiP4D. Simulations were performed in two steps, similar to the radiographic film response simulations in the previous section: (i) generation of sub-treatment plans and (ii) calculation of the 4D biological dose on the basis of the sub-treatment plans. Since TRiPG relies on the TPS of Bert and Rietzel, TRiPB, for the generation of sub-treatment plans, step (i) was performed with the latter and TRiP4D, respectively. The resulting sub-treatment plans then were used as input to either TRiPG's and TRiP4D's BED calculation in step (ii). The same computer-generated 4DCT with 11 motion states as used by Gemmel et al. were employed for all calculations. Biological dose calculation was carried out according to section 3.2.3.3 and (Gemmel et al., 2011). The physical dose was computed with either a standard pencil beam algorithm and an advanced algorithm including multiple scattering effects. The rigid deformation maps for TRiP4D and TRiPG were created based on the acquired motion monitoring data. Additional 4D pseudo-static simulations were performed with both programs using identity deformation maps. These serve to decouple the deformation of the dose grid and the accumulation of the particle spectra over all motion states from each other. In this way 3D dose calculation is mimicked. The resulting pseudo-static dose distributions were compared to the static dose distribution obtained for the treatment plan with the TRiP98 mother program. The same set of depth-dose and particle spectra data (Krämer et al., 2000) as well as the same LEM version (Elsaesser et al., 2008) was used in all 3D and 4D simulations to guarantee comparability. The measured BED from Gemmel et al. was compared to the corresponding simulated BED for the cell samples. The difference in BED was calculated for each sample i: $\Delta D_i = D_i^{\text{meas}} - D_i^{\text{calc}}$. The mean difference $\overline{\Delta D}$ and its standard deviation $\overline{\sigma}^D$ were determined to assess the agreement of the different simulations with the measurement.

3.3.3.2 Results

Table 3.3 lists the results of the statistical analysis of the differences in measured and simulated BED. The simulation results for the pencil beam dose algorithm (PB) are consistent for all three simulations and independent from the program used for generation of the sub-treatment plans. For the multiple scattering algorithm (MS) and simulation BG the results published by Gemmel et al. were reproduced. Simulations BR and RR using TRiP4D's BED calculation, however, show a significant systematic discrepancy of about 310 mGy (RBE) for the mean difference in BED w.r.t. simulation BG. Table 3.4 summarizes the observed maximum dose differences between the 4D pseudo-static and the static reference dose distribution. Here, for the MS algorithm the comparison of the pseudo-static dose distribution attained with configuration BG and the static TRiP98 dose distribution reveal maximum absolute dose differences per voxel, $|\Delta D_{\text{max}}|$, of more than 750 mGy (RBE). In contrast, for simulation BR, differences of less than 10^{-2} mGy (RBE) were found. Moreover, visual inspection of the MS pseudo-static dose distributions revealed less dose contributions lateral to the target volume for the BG compared to the BR simulation, indicating a different impact of multiple scattering. For algorithm PB, however, the respective dose distributions agreed within less than 10^{-2} mGy (RBE) for both the BG and BR simulations. Finally, the comparison of the static reference dose distributions for algorithms PB and MS on

	algorithm PB	algorithm MS
simulation	$\overline{\Delta D} \pm \overline{\sigma}^D$ [mGy (RBE)]	$\overline{\Delta D} \pm \overline{\sigma}^D$ [mGy (RBE)]
BG	-676 ± 642	$-298 \pm 500^*$
BR	-676 ± 641	-614 ± 533
RR	-679 ± 647	-617 ± 538

Table 3.3.: Mean difference $\overline{\Delta D}$ and standard deviation $\overline{\sigma}^D$ of measured and calculated BED for the cell samples. B, R and G denote the programs TRiPB, TRiP4D and TRiPG used for generation of sub-treatment plans or 4D biological dose calculation, respectively. For each configuration a standard pencil beam (PB) and a multiple scattering (MS) algorithm were tested for physical dose calculation. The red highlighted row indicates the results for the full TRiP4D simulations (RR). The starred result was originally published by Gemmel et al. (2011).

	algorithm PB	algorithm MS
simulation	$\lvert\Delta D_{\max}\rvert$ [mGy (RBE)]	$\lvert\Delta D_{\max}\rvert$ [mGy (RBE)]
BG	$1.67 \cdot 10^{-3}$	757
BR	$1.67 \cdot 10^{-3}$	$1.43 \cdot 10^{-3}$

Table 3.4.: Maximum deviations in BED, $\lvert\Delta D_{\max}\rvert$, of the 4D pseudo-static dose distributions from the static reference dose distribution for the two dose algorithms, PB and MS. Identity transformation maps were used to mimic 3D dose calculation. The static reference dose distributions were obtained with TRiP98.

average showed about 70 mGy (RBE) ($\approx 1\,\%$) less dose in the target region in the case of MS, due to lateral scattering. The differences in dose of around 60 mGy (RBE) found between the two algorithms in the BR simulations (cf. table 3.3) are in agreement with this fact. For the target dose of 6 Gy (RBE) the mean deviation of (617 ± 538) mGy (RBE) from the measurement for the TRiP4D simulation translates into a relative deviation of $(10 \pm 9)\,\%$. The average BED error propagated from the cell survival measurement error was estimated to about 24 %. Thus, the simulation results are well compatible with the measurement.

3.3.3.3 Discussion

Even though the agreement with the measurement is better for configuration BG, the performed tests indicate that TRiPG's dose calculation algorithm is inaccurate when using the multiple scattering physical dose calculation algorithm. The 4D pseudo-static dose calculations provide the possibility to assess the performance of the 4D dose calculation independent from the dose grid transformation and allow for comparison with the static reference dose distributions. In these simulations the static dose distributions could be reproduced by TRiP4D to a high level of precision with both the PB and MS algorithm. Since the implementation of biological dose calculation is decoupled from the implementation of the PB and MS physical dose calculation algorithms and only used downstream of these calculations, the issues observed for the MS algorithm most likely do not originate from the specific calculations performed to determine the BED. This is

supported by the fact that for the PB dose algorithm the results are comparable to those obtained with TRiPG. In contrast to the radiographic film experiments no significant improvement could be achieved using TRiP4D for the generation of sub-treatment plans (configuration RR). The reason for this is that the BDS in this case was not affected by any data acquisition issues, thus, TRiP4D's more robust algorithms did not yield an advantage over TRiPB w.r.t. simulation accuracy.

3.4 Summary and discussion

This chapter has presented the development and implementation of TRiP4D, a 4D treatment planning system for scanned ion beams. The program is based on the GSI in-house treatment planning system TRiP98 which has been used successfully for clinical treatment planning during the GSI pilot project (Krämer et al., 2000; Jäkel et al., 2001b). The main objective of this work was the integration of previous 4DTP efforts and developments made at GSI and the further advancement of the program towards a clinically serviceable 4DTPS. Previous treatment planning developments of Bert and Rietzel (2007) and Gemmel et al. (2011) in parts have served as prototypes. The new TPS enables realistic clinical treatment planning with multiple fields and is compatible with the treatment planning workflow used at HIT and UCHD.

4D treatment planning in TRiP4D is based on 4DCT, deformable image registration and 4D segmentation to model the moving patient anatomy. These tools have become well established over the past years not only in 4DTP for photon therapy (Keall et al., 2005; Rietzel et al., 2005a) but also for particle therapy (Engelsman et al., 2006; Kang et al., 2007; Zhang et al., 2008). Hence, emphasis was put on a flexible integration of these instruments to explicitly allow for realistic patient treatment planning. Interfaces to several image registration software packages have been implemented and permit quantitative assessment of 4DCT data based on the resulting deformation maps. The corresponding structures were developed with a focus on principal compatibility with a wide range of registration algorithms and programs. The use of additional registration software packages in the future, thus, is expected to be manageable with a minimum effort. Furthermore, 4D segmentation functionality has been newly implemented. A novel 4D contour data model has been introduced which employs the representation of contours as volumetric boolean masks, i.e. the ROIs are stored in a bit-wise fashion using a CT-like structure. This enables to store 4D segmentation data as a single entity and avoids the use of multiple incoherent sets of polygonal contours. Additionally, a 4D contour propagation algorithm based on deformable image registration has been implemented which is capable of creating a full 4D segmentation dataset, starting from a manually contoured reference phase. Many other groups have made efforts on the implementation of 4D contour propagation algorithms. Commonly, the approaches are divided into registration-driven (Lu et al., 2006a; Rietzel et al., 2005a) and deformable model-driven (McInerney and Terzopoulos, 1996; Montagnat and Delingette, 2005) techniques. In the first the deformation field gives guidance to the contour deformation while in the second a physical model is used to iteratively match the contours to the image features. TRiP4D relies on the former approach, since the available deformation maps can be efficiently re-used. As described in section 3.2.1.4, the contour propagation algorithm employs the inverse deformation maps and the reference phase contour to establish the ROIs in each 4DCT phase as VBMs. An alternative strategy has, for instance, been published by Lu et al. (2006a). They have used triangular meshes to model the surface of the ROIs. After surface deformation the polygon-based contours for all 4DCT phases are generated by performing sections of the surface model

with the image plane of interest. A drawback of TRiP4D's propagation algorithm is the necessity to generate both, the original (needed for 4D dose calculation) and the inverse deformation maps. Since the registration process can be sufficiently automated, this does not constitute a major limiting factor. It can be anticipated that the use of VBMs is more memory consumptive compared to, e.g., triangular meshes. Whilst the VBM contour model has the advantage that contours can be easily combined and manipulated, e.g., for ITV generation, the resolution of the contours is forced to the regular CT grid, causing a loss of precision. However, since the usual lateral CT voxel spacing as well as the expected registration accuracy are on the order of millimeters (Brock, 2010), no significant impact is expected. Nevertheless, also up-sampled VBM datasets can be used in TRiP4D at the expense of memory consumption.

4D treatment plan optimization in TRiP4D implies the appropriate design of a target volume, depending on the beam delivery technique, and the dose optimization on the CT reference phase. In the case of beam tracking or RDBT additional optimization of position or dose compensation parameters is performed (Lüchtenborg et al., 2011). Water-equivalent ITV optimization has been incorporated into TRiP4D (Graeff et al., 2012) based on the 4DCT and 4D segmentation functionality and the concept proposed by Rietzel and Bert (2010). For scanned ion beams so far no alternative concept has been proposed. Similar approaches were made in the literature for passively delivered ion beams. Engelsman et al. have studied the design of ITVs for proton therapy. They optimized treatment plans on the individual CT phases and combined the respective compensators to account for motion-induced range changes (Engelsman et al., 2006). In a simpler approach Koto et al. have investigated the formation of effective ITVs for passive carbon ion therapy of lung tumors by manipulation of the CT HU values. They combined a lateral margin with the extension of the tumor volume in the SI direction by replacing lung tissue with GTV HU values (Koto et al., 2004). Apart from the mere optimization on a reference phase CT more elaborate techniques can be thought of. At the time of writing initial implementations of 4D optimization algorithms in TRiP4D by colleagues already take into account more than one CT phase for dose optimization. These developments benefit decisively from TRiP4D's newly implemented 4DCT and 4D segmentation infrastructure. Similar 4D dose optimization concepts have been investigated for IMRT, e.g., by Nohadani et al. (2010). Unkelbach et al. (2009) have investigated 4D treatment planning incorporating robustness considerations. 4D dose optimization techniques, however, are significantly more memory and time consumptive and can quickly deplete the available computing resources. It can be expected, however, that the rapid development in the computing sector will compensate for this in the future.

In this chapter particular emphasis was put on TRiP4D's 4D treatment simulation functionality. The 4D dose deposition is modeled in two steps. First, sub-treatment plans are generated according to Bert and Rietzel (2007). The procedure is based on beam delivery sequence tables, which carry the time-structure of the beam delivery, and its correlation with the patient motion via surrogate motion traces. A general and flexible implementation of the beam delivery time structure via externally compiled tables was introduced. The implementation allows to model all commonly proposed motion mitigation techniques, including rescanning, gating, tracking and possible combinations of these. A module has been designed which is capable of handling patient breathing trajectories acquired with motion monitoring devices. Based on the motion trace, amplitude and phase-based identification of the patient's respiratory state are supported and can be performed in compliance with the 4DCT data acquisition used at HIT and UCHD. After sub-treatment plan generation 4D dose calculation is carried out, taking into account the 4DCT and the deformation maps. The 4D (biological) dose calculation algorithm developed

by Gemmel et al. (2011) has been incorporated into TRiP4D and permits to perform detailed 4D dose calculation for realistic patient motion using TRiP4D's deformable registration module. The dose algorithm additionally was extended to 4D detector response calculation. To determine the non-linear biological effect, the algorithm accumulates all dose contributions to a dose voxel over all CT phases under consideration of the deformation field. That is, the dose grid is deformed instead of the the raster grid. This concept has been used for physical dose calculation and proton beam scanning by other groups as well (Paganetti et al., 2005; Knopf et al., 2010a). Inaniwa et al. (2010) have integrated a biological dose calculation algorithm into their treatment planning system for scanned ion therapy. So far, they did not report a 4D version of the algorithm. 4D treatment simulation for scanned beams was investigated by few other groups. Furukawa et al. from NIRS have performed 2D simulations to study the mitigation of interplay effects using gating and rescanning. However, they did not attempt direct comparisons of their simulations with the measured dose distributions (Furukawa et al., 2010a). Knopf et al. (2011) have performed treatment planning studies at PSI for scanned proton treatments of liver tumors using rescanning. Apart from 4D dose calculation (van de Water et al., 2009) they also included a model of the temporal structure of the pencil beam scanning. So far, they have considered liver tumors and rigid patient motion only, hence, neglecting all density changes. For passive ion therapy and photon therapy 4D dose calculation usually is realized by time-weighted averaging of the dose distributions in each phase, taking into account their distribution over the respiratory cycle(Rietzel et al., 2005b; Kang et al., 2007). 4D treatment planning including 4D dose optimization and calculation is already commercially available for photon therapy with the Cyberknife Synchrony system (Accuray Inc., Sunnyvale, Ca., USA) (Sarfaraz et al., 2009; Accuray, 2011). The treatment planning strategy is based on 4DCT and deformable image registration.

TRiP4D's 4D simulation functionality has been extensively tested in verification experiments. The preceding sections have presented results of the verification of the full 4D treatment simulation chain, including 4D dose and detector response. Where applicable, the performance of TRiP4D was compared to the respective predecessor programs. The simulation of 4D film response showed a significant improvement w.r.t. the planning system of Bert and Rietzel in those cases where BDS data was defective and the more robust algorithms of TRiP4D could handle these issues appropriately. The measured optical film densities could be reproduced with an accuracy of around 10 %. This corresponds to the expected level of accuracy as reported by Spielberger et al. (2003). The results of the biological dose calculation tests revealed good agreement with the planning system of Gemmel et al. for one of the two tested algorithms used for the physical dose calculation part. Significant discrepancies were found for the second algorithm which takes into account multiple scattering. Comparisons with TRiP98, however, suggest that the observed differences solely originate from defective calculation of multiple scattering contributions in the predecessor program and are not caused by differences in the biological dose calculation. Reasonable agreement with the measured dose values was found for the TRiP4D calculations. Moreover, new elaborate water phantom experiments were conducted to test TRiP4D's simulation capabilities for 3D target motion, gated beam delivery and a large number of plan parameters and motion configurations. The comparison of measured and simulated dose values showed good agreement with standard deviations smaller than 5 % in most cases. It can be concluded that 4D simulations subsequent to treatment delivery are well feasible in experimental setups, provided all necessary parameters are known, i.e. in particular the time structure of the beam delivery process and the target motion during delivery. However, simulation prior to treatment delivery is very challenging even for simple setups and well

known target motion. Synchrotron accelerator systems like those used at GSI and HIT are subject to significant variability of beam availability and to the delivered intensity on a sub-second time-scale (Haberer et al., 1993). These parameters significantly affect the 4D dose deposition, while being difficult to model. Intensity-controlled beam extraction for synchrotrons is a promising development to reduce this kind of uncertainty (Furukawa et al., 2005). For patient treatments additional complexity is introduced, since prediction of the target motion in general is not feasible on a time-scale beyond several hundred milliseconds (Sharp et al., 2004; Ruan and Keall, 2010). Hence, a reliable prediction of the delivered dose prior to treatment is difficult to achieve. Nevertheless, 4D treatment simulation offers great potential for 4DTP and quality assurance. It may, for instance, provide the opportunity to monitor the success of the plan delivery, provided the beam delivery time structure and the patient motion during treatment are measured. Furthermore, in-advance treatment planning simulations can be performed for many different scenarios. Even though the patient motion and the time structure of the beam delivery are not known, simulations of a wide range of parameter settings, such as different breathing patterns or beam delivery schemes, can be performed and yield a spectrum of possible treatment outcomes. These simulations also can be used to assess plan robustness or define parameters needed as input for the respective treatment delivery technique, such as the number of required rescans or the gating window size. Simulation studies of this nature will be the subject of the following chapters, using experimental and realistic patient setups. It should be emphasized that from a technical point of view there is no principal difference between in-advance simulations in TRiP4D and those performed subsequent to treatment. The uncertainty and value of 4D treatment simulations solely depends on the reliability of the input data. It is important to realize that the accuracy of any 4D treatment planning attempt based on 4DCT and deformable image registration depends decisively on the validity and reproducibility of the input data, in particular between the time of imaging and treatment delivery (von M. Siebenthal et al., 2007; Mori et al., 2009; Case et al., 2010). The variability and accuracy of these are a separate field of study and beyond the scope of this thesis.

4 Beam parameter optimization for the mitigation of residual motion

4.1 Introduction

The preceding chapters have repeatedly highlighted the challenges of organ motion for treatment planning and beam delivery of scanned ion beams. The interference between the moving beam and the tumor motion can lead to clinically unacceptable under- and overdosage and to an increased exposure of surrounding normal tissue (section 2.2.2). These shortcomings so far have prevented the application of beam scanning for moving tumors in clinical routine. Gating (Minohara et al., 2000) and irradiation under abdominal compression (Wunderink et al., 2008) are promising candidates to reduce the effective tumor motion for lung and liver tumors to few (<10) millimeters (Berbeco et al., 2005, 2006; Eccles et al., 2011). Gating has been used successfully for treatment of lung and liver tumors with passively delivered ion beams (Iwata et al., 2010; Chiba et al., 2005). Abdominal compression and beam gating lately have been brought to clinical application for scanned beams at HIT. However, even when using these mitigation techniques, residual tumor motion can induce a degradation of the dose homogeneity.

Bert et al. (2009) have proposed to use an increased lateral and longitudinal overlap of pencil beams, in order to gain robustness w.r.t. organ motion. The basic concept is depicted in figures 4.1 and 4.2. In the lateral dimension the static configuration of overlapping pencil beams to achieve a homogeneous dose is extended either by increasing the beam's full width at half maximum (FWHM) or by decreasing the lateral raster spacing. The dose at each target point is, thus, determined by a larger number of pencil beams and a relative displacement between pencil beams will have a smaller effect on the dose homogeneity. The **lateral overlap factor** shall be introduced as:

$$f_{\mathrm{lat}} = \frac{\text{beam FWHM}}{\Delta s} \quad , \tag{4.1}$$

Δs denoting the lateral raster spacing (figure 4.2). The standard parameters used for stationary irradiation at GSI and HIT are $\Delta s = 2\,\mathrm{mm}$ and a beam FWHM of 6 mm, i.e. a lateral overlap factor of $f_{\mathrm{lat}} = 3$. While the lateral raster spacing can be set as desired in the treatment planning system, the beam FWHM is restricted to the energy-dependent beam focus settings available in the accelerator library (Schardt et al., 2010).

In the longitudinal direction an increased pencil beam overlap can be obtained either by a decreased iso-energy slice spacing, Δz, or by an increased effective Bragg peak width using dedicated ripple-filters (section 2.1.3.2).[1] The **longitudinal overlap factor** shall be defined as:

$$f_{\mathrm{lng}} = \frac{\text{effective Bragg peak width}}{\Delta z} \quad . \tag{4.2}$$

[1] The effective Bragg peak width corresponds to the sigma of the Gaussian depth-dose profile that the ripple-filter is optimized for (Weber and Kraft, 1999).

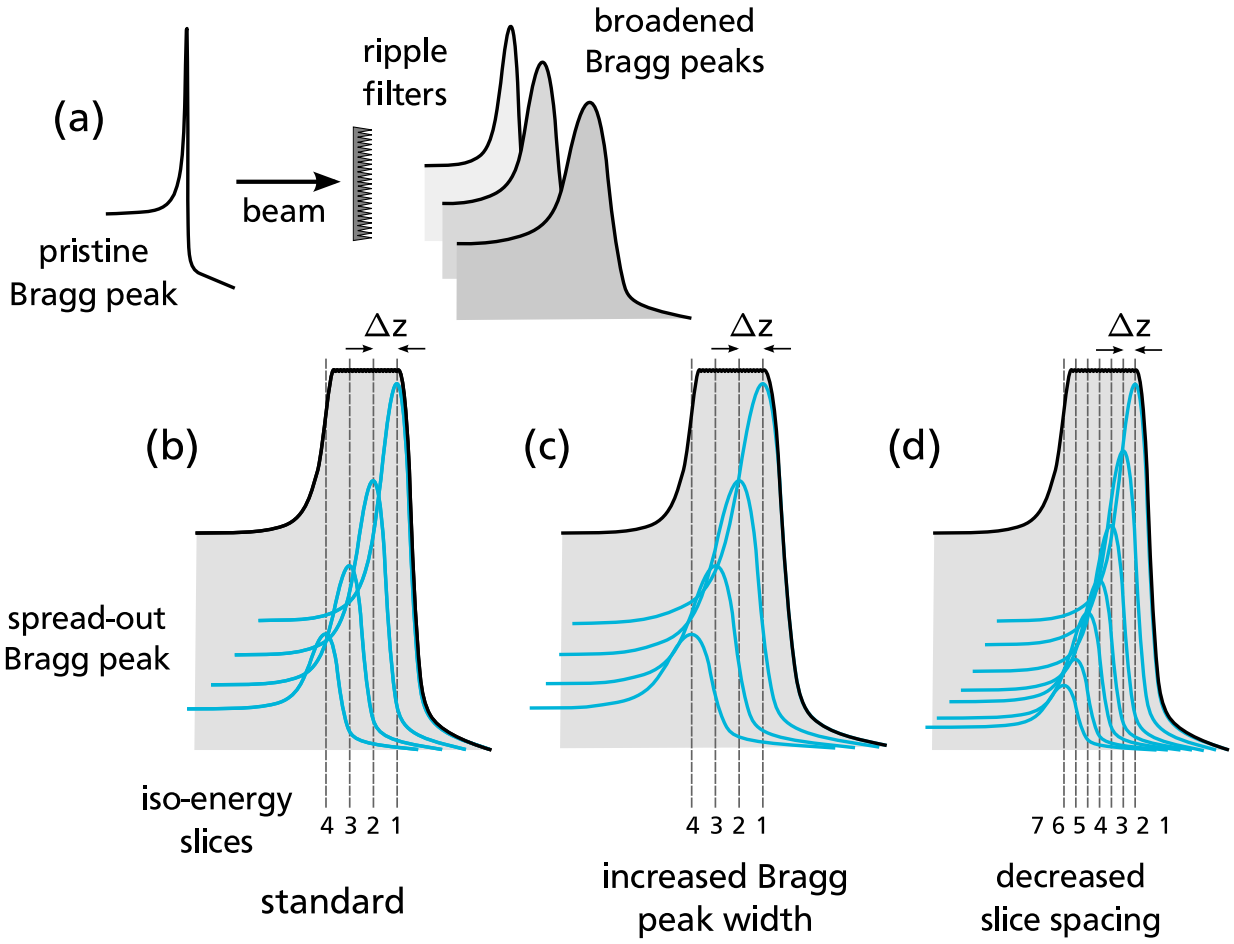

Figure 4.1.: (a) The pristine Bragg peaks are broadened in depth by the use of ripple-filters. **(b)** Standard longitudinal beam overlap as used for treatment of stationary targets at GSI and HIT. Increased longitudinal beam overlap is facilitated by a larger Bragg peak width **(c)**, or by a decreased IES spacing **(d)**.

Typically, a 3 mm RiFi and a $\Delta z = 3$ mm is used for stationary targets at GSI and HIT, thus, $f_{\mathrm{lng}} = 1$. In analogy to the lateral beam overlap an increased longitudinal overlap results in a larger number of pencil beams contributing to the dose at a certain point. This should provide enhanced robustness w.r.t. residual range variations introduced by target motion. In practice, Δz and the effective Bragg peak width can only be varied within limits. The former is determined by the energy steps available from the accelerator (1 mm steps in water at HIT) and the latter is defined by the mechanical design of the RiFi.

Bert et al. have studied increased lateral and longitudinal pencil beam overlap in separate experiments and simulations using radiographic films and gated irradiation (Bert et al., 2009). Their results indicate that motion-induced interplay effects can be effectively reduced by both increased lateral and longitudinal overlap. The portability of the concept to a more complex and realistic setup with 3D target motion has been studied at GSI for both gated and ungated irradiation. The investigations with regard to gating were carried out by Steidl (2011). The presented complementary study addresses the mitigation of residual motion for ungated irradiation.

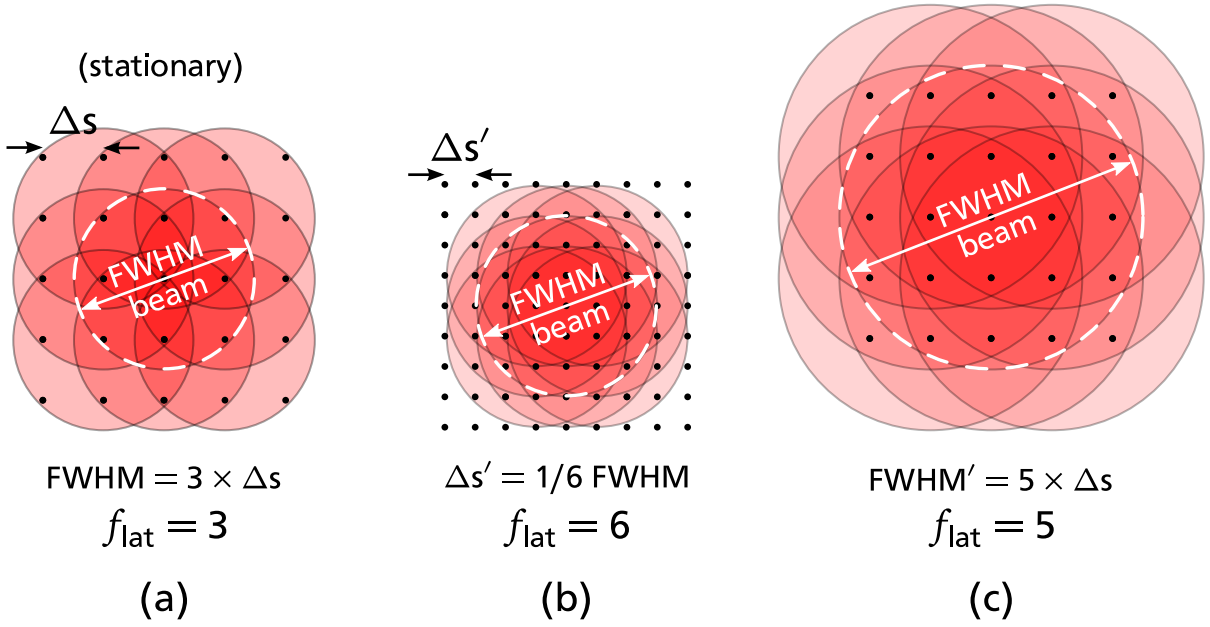

Figure 4.2.: (a) Lateral beam overlap as used for stationary targets at GSI and HIT. **(b)** Increased lateral beam overlap by a decreased raster spacing (Δs). **(c)** Increased lateral beam overlap using an increased beam FWHM.

Interplay patterns are very sensitive to the motion characteristics, including the motion amplitude and the initial motion phase. Considering that all beam parameters may also be varied independently, the parameter space of interest is highly multi-dimensional. Due to the vast amount of beam time needed, a purely experimental approach is impractical. Instead, a subspace of the parameter space has been investigated experimentally and the data were used to validate the 4D treatment simulation capabilities of TRiP4D which were discussed in detail in the last chapter. As the interplay patterns are very unique to the specific motion configuration and beam delivery sequence at the time of the 4D dose measurements, the agreement between sparsely sampled simulations and the respective measurements strongly suggests the general validity of the simulation environment. Starting from this premise, TRiP4D can be used to expand the parameter space in large-scale simulations.

4.2 Materials and methods

4.2.1 Experimental setup and conduct

The experiments for the dosimetric parameter study were conducted on three different days at the quality assurance cave at HIT. The first two measurement series were accomplished on two subsequent days. The third series constituted a repetition of the original experiment for a subset of the parameters several months thereafter. Due to other measurements occupying the cave, the setup had to be re-positioned each day. The figures 4.3a and 4.3b show a photograph and a schematic illustration of the experimental setup, respectively. An array of 24 pinpoint ionization chambers (ICs) was attached to a robotic arm and was positioned inside a water

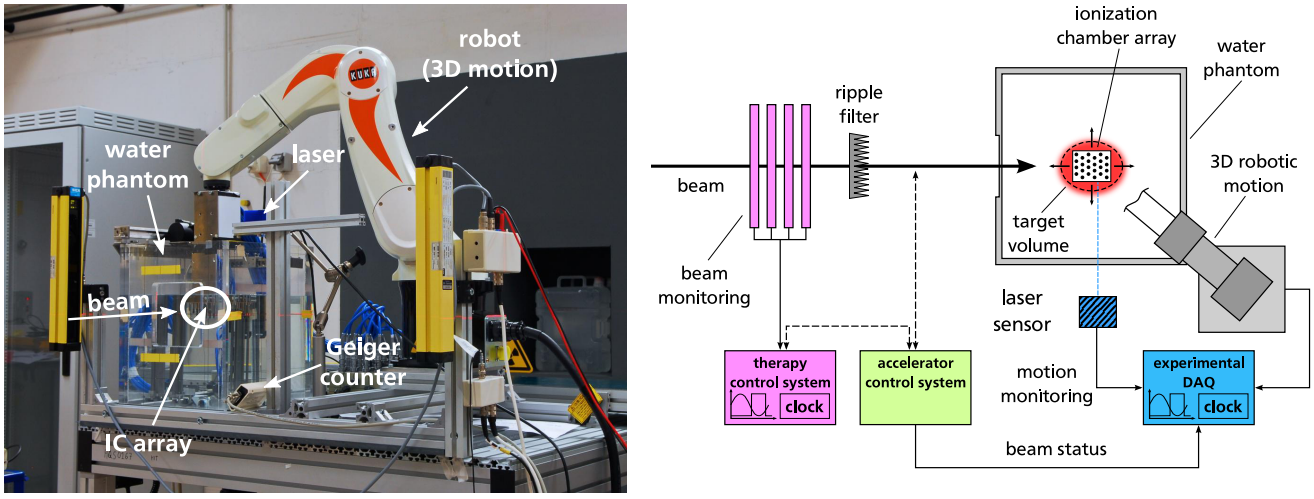

(a) (b)

Figure 4.3.: Photograph and sketch of the experimental setup. In the sketch on the right the data acquisition and the data communication between the systems is illustrated. As indicated, data on the scanner progress (point irradiation times) and on the beam status are acquired separately with the TCS and the experimental DAQ.

phantom (MP3 phantom, PTW, Freiburg, Germany). The setup is similar to the one routinely used for quality assurance measurements (Karger et al., 1999), but was extended by robotic motion. The implementation of the robotic motion is described in detail in (Steidl, Richter et al. 2012). The IC array moved sinusoidally in all three dimensions:

$$\begin{aligned} a_{\mathrm{LR}}(t) &= 0.50 \cdot A_{\mathrm{LR}} \cdot \sin\left(\frac{2\pi}{T}t\right) \\ a_{\mathrm{UD}}(t) &= 0.25 \cdot A_{\mathrm{LR}} \cdot \sin\left(\frac{2\pi}{T}t + \frac{\pi}{2}\right) \\ a_{\mathrm{BF}}(t) &= 0.25 \cdot A_{\mathrm{LR}} \cdot \sin\left(\frac{2\pi}{T}t + \frac{\pi}{2}\right). \end{aligned} \tag{4.3}$$

Here a_{LR} denotes the motion direction in LR and a_{UD} and a_{BF} are the motion components in the up-down (UD) and back-front (BF) direction w.r.t. BEV, respectively. A motion period of $T = 3\,\mathrm{s}$ was used for all measurements and the peak-to-peak amplitude A_{LR} was varied from 0 to 10 mm to mimic residual tumor motion. As shown in equations (4.3), the major motion component was set along the LR direction. In the remaining dimensions the motion amplitudes were set to 50 % of the LR amplitude. Additionally, a 90° phase shift was applied to both components w.r.t. to the LR motion, such that the array moved along the path of a tilted ellipse. The start of the IC array motion was triggered on the irradiation start with an initial motion phase of $\phi_0 = 0°$. The LR motion component was monitored using a laser distance sensor (figure 4.3). The beam status signal was acquired via a transistor-transistor logic (TTL) signal provided from the accelerator control system. Additionally, a Geiger counter was used to acquire a second and independent beam status signal. Motion monitoring data and the two beam status signals were recorded with the same experimental data acquisition system (DAQ) at a temporal resolution of 1 ms with a Beckhoff EtherCAT system (Beckhoff Automation GmbH, Frankfurt, Germany). In parallel, the

raster point irradiation times were logged via the routinely provided beam records of the TCS with a resolution of 1 μs. The 6D robotic motion was monitored and logged with dedicated software. The absorbed dose in the ICs was measured with two multi channel dosemeters with 12 channels each (MULTIDOS, PTW, Freiburg, Germany).

Daily calibration of the beam monitoring chambers controlling the delivered particle numbers per raster point (cf. figure 4.3) and of the dosimeters was performed. Specifically air density corrections were taken into account. The corrections involved calibration measurements with a reference ionization chamber at a defined position (iso-center) according to Karger et al. (2010). Due to the large setup, these calibration measurements could not be performed at the iso-center but 38 mm closer to the beam exit window. As a result, subsequent correction of the measured dose needed to be performed, taking into account the geometric divergence of the beam. Details on the correction procedure were reported by Steidl (2011).

In order to assess the beam quality, a radiographic film was irradiated with single beam spots at representative beam energies and a homogeneous field prior to each measurement series. Similarly, the treatment records were analyzed with respect to the stability of the beam position and beam spot size.

4.2.2 Treatment plan parameters and optimization

An ellipsoidal internal target volume (ITV) of 82 cm^3 and half axes of 28 mm in LR BEV, 35 mm in BF and 20 mm in UD direction was irradiated in the water phantom at a depth of 125 mm with a carbon ion beam. The treatment plans were optimized and conformed to the ellipsoidal target volume using the GSI reference 3D treatment planning system TRiP98. 18 combinations of lateral raster spacing (2 and 3 mm), iso-energy slice spacing (1, 2, 3 and 4 mm water-equivalent), beam FWHM (6, 8 and 10 mm) and RiFis were selected. Apart from the standard RiFi optimized for a 3 mm IES spacing, an additional combination of two orthogonally crossed 3 mm ripple-filter was used. At the beam energies used in the experiment the latter produces an effective Bragg peak width of about 4 mm. The FWHM of the beam spot at each focus level remained approximately constant over the selected energy range of the experiment ($\approx$216–298 MeV/u) .[2] Thus, a single focus level could be requested for each treatment plan. The plans for all 18 combinations were optimized for a homogeneous target dose of 2 Gy. Table 4.1 gives an overview of the beam parameter combinations used for the treatment plans.

4.2.3 4D dose reconstructions

To assess TRiP4D's ability to simulate the time-dependent dose delivery for the described experimental setup and the different combinations of beam parameters, dose reconstructions were performed according to section 3.2.3 and compared to dosimetric measurements. The validation of the simulation environment constitutes the prerequisite for further simulations with TRiP4D using a larger parameter space. 4D dose reconstructions were accomplished based on the measured beam status signal, the treatment records provided from the TCS, the nominal surrogate motion trajectories of the LR target motion component and a computer generated 4DCT of the water phantom with 22 phases. Dose calculations were performed on an isotropic 1 mm

[2] By trend the FWHM of the beam spot increases for decreasing beam energy, due to scattering in the beam line.

plan parameters [mm]					peak-to-peak amplitude A_{LR} [mm]								
RiFi	Δs	Δz	$\overline{\text{FWHM}}$	FL	static	2	3	4	5	6	7	8	10
series/day one													
3.0	2.0	2.0	6.1	2	×	×	–	×	–	×	–	×	×
3.0	2.0	2.0	8.3	3	×	–	×	–	×	–	×	–	×
3.0	2.0	2.0	10.1	4	×	–	×	–	×	–	×	–	×
3.0	2.0	3.0	6.1	2	×	×	–	×	–	×	–	×	×
3.0	2.0	3.0	8.3	3	×	–	×	–	×	–	×	–	×
3.0	2.0	3.0	10.1	4	×	–	×	–	×	–	×	–	×
3.0	3.0	1.0	10.1	4	×	–	×	–	×	–	×	–	×
3.0	3.0	2.0	10.1	4	×	–	×	–	×	–	×	–	×
3.0	3.0	3.0	10.1	4	×	–	×	–	×	–	×	–	×
series/day two													
4.0	2.0	2.0	6.1	2	×	×	–	×	–	×	–	–	×
4.0	2.0	2.0	8.2	3	×	–	×	–	×	–	×	–	×
4.0	2.0	2.0	10.1	4	×	–	×	–	×	–	×	–	×
4.0	2.0	3.0	6.1	2	×	×	–	×	–	×	–	–	×
4.0	2.0	3.0	8.2	3	×	–	×	–	×	–	×	–	×
4.0	2.0	3.0	10.1	4	×	–	×	–	×	×	–	–	×
4.0	2.0	4.0	10.1	4	×	–	×	–	×	–	×	–	×
4.0	3.0	2.0	10.1	4	×	–	×	–	×	–	×	–	×
4.0	3.0	3.0	10.1	4	×	–	×	–	×	–	×	–	×
series/day three													
3.0	2.0	2.0	6.1	2	×	–	–	–	×	–	–	–	×
3.0	2.0	2.0	8.3	3	×	–	–	–	×	–	–	–	×
3.0	2.0	2.0	10.1	4	×	–	–	–	×	–	–	–	×
3.0	2.0	3.0	6.1	2	×	–	–	–	×	–	–	–	×
3.0	2.0	3.0	8.3	3	×	–	–	–	×	–	–	–	×
3.0	2.0	3.0	10.1	4	×	–	–	–	×	–	–	–	×
3.0	3.0	2.0	10.1	4	×	–	–	–	×	–	–	–	×
3.0	3.0	3.0	10.1	4	×	–	–	–	×	–	–	–	×
4.0	2.0	2.0	10.1	4	×	–	–	–	×	–	–	–	×
4.0	2.0	3.0	10.1	4	×	–	–	–	×	–	–	–	×

Table 4.1.: Table of the measured beam parameter combinations and motion amplitudes. A_{LR} denotes the peak-to-peak amplitude of the major motion component (left-right in BEV). The motion amplitudes for the remaining components were: $A_{\perp} = 0.5 \times A_{LR}$. Each treatment plan was optimized for a combination of ripple-filter (RiFi), lateral raster spacing (Δs), IES spacing (Δz) and beam focus level (FL). The corresponding average FWHM of the beam spot for each FL is also given.

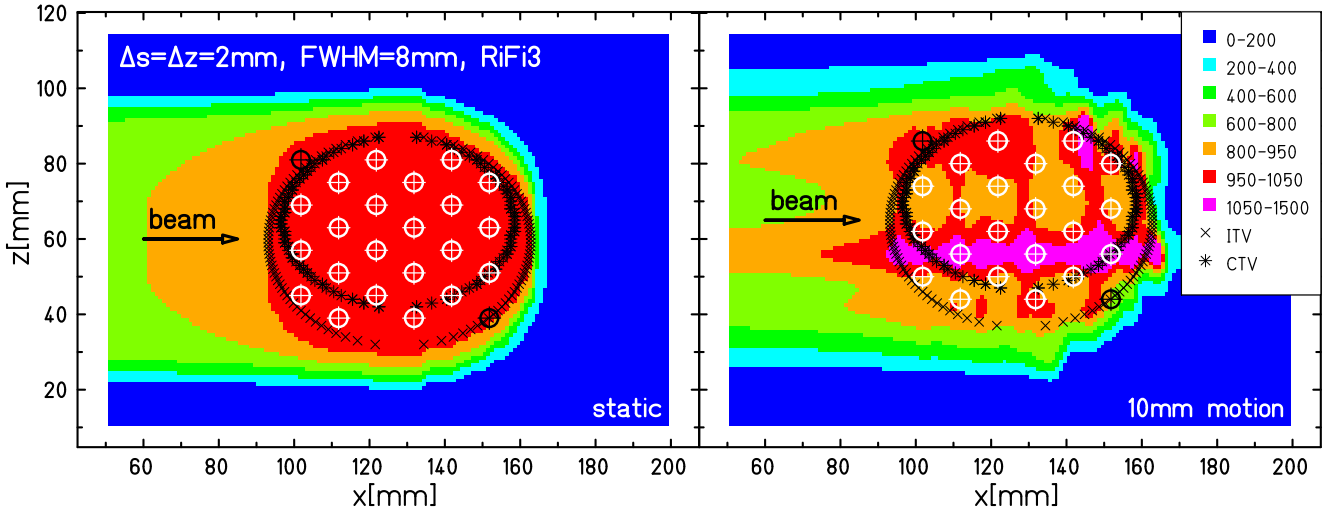

Figure 4.4.: Bird's eye view section of simulated dose distributions for the static (left) and a moving target (right) and a representative beam parameter combination (dose in mGy. The 4D dose is mapped to the reference phase (extreme left position in BEV). The IC positions are indicated by the white and black crosses (neglected for analysis).

voxel grid. The robotic target motion was modeled using rigid deformation maps generated with TRiP4D, based on the nominal 3D target motion trajectories (cf. section 3.2.1.3).

4.2.3.1 Beam delivery sequence data

As discussed in section 3.2.3.2, 4D dose calculations in TRiP4D require beam delivery sequence (BDS) input tables. The measured data of the beam status signals and of the raster point irradiation times were used to generate BDS tables reflecting the individual characteristics of the beam delivery at the time of each of the measurements. For technical reasons, raster point irradiation times and beam status signals were not acquired with the same DAQ (cf. figure 4.3). As a consequence, temporal correlation of the two systems and combination of the data into BDS tables for TRiP4D was needed. For this purpose, dedicated software was used which was developed within the scope of this thesis (appendix A.3). The inputs to the program are the measured beam status signals from the experimental DAQ and the TCS treatment records. The underlying principle of the calibration procedure is as follows. The beam is switched off rapidly ($\ll 1$ ms) by the control system at the end of a beam gate or spill (BOF event, using the nomenclature introduced in section 3.2.3.2) or after completion of the last raster point of an IES (EOP event). Temporal alignment is established by mapping the BOF events, as defined by the beam status signal, to the matching EOP events from the treatment records:

(1) Beam-on (BON event) and BOF events are generated by discrimination of the analog beam status signal against suitable thresholds. The EOP events are obtained from the treatment records using the completion time of the last raster point in each IES.

(2) A rough initial alignment is established by mapping the last EOP event to the last BOF event. Subsequently, corresponding pairs of BOF and EOP events are determined in a regional search in time around each EOP event.

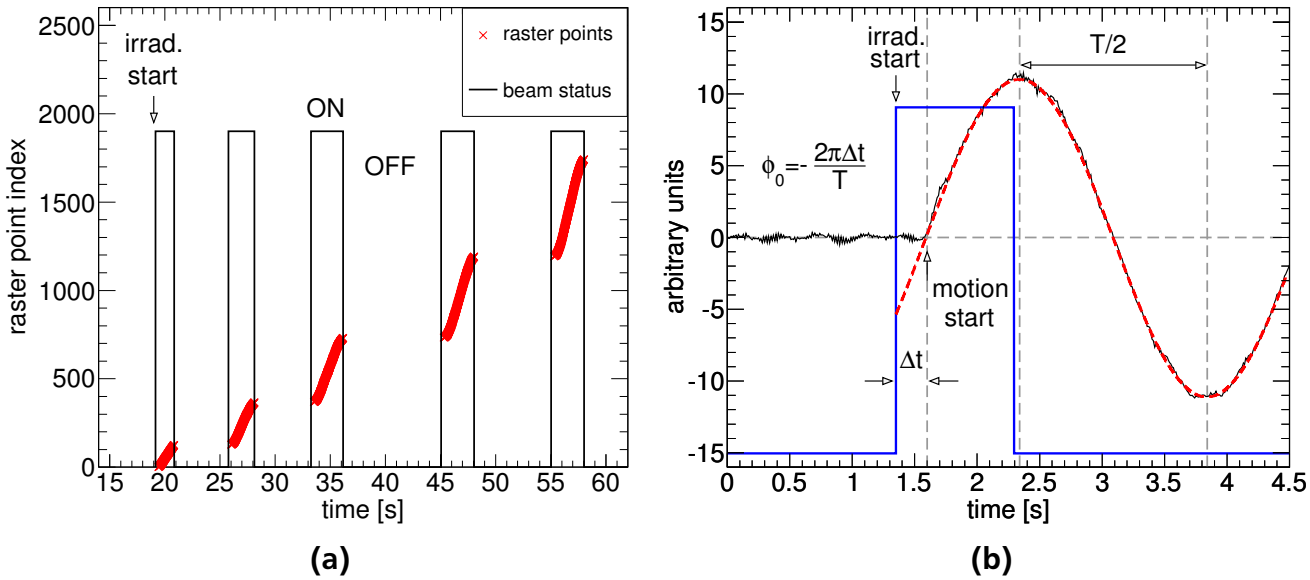

Figure 4.5.: (a) Visualization of a BDS after temporal alignment. The raster point index is drawn vs. the respective irradiation time. The falling edges of the aligned beam status match the completion time of the last raster point in each IES. **(b)** Correction of the initial phase shift originating from the starting delay (Δt). The initial phase (ϕ_0) is determined via a fit of a sinusoid to the motion trajectory (red dashed curve).

(3) Due to the lower sampling resolution of the beam status signal (1 ms), the initial alignment may lead to raster points located outside beam gates. To maintain causality, a fine-tuning of the temporal alignment is performed by relative shifting of the time axes of the two systems such that all raster points are located within spills.

A graphical visualization of an example BDS table resulting from the alignment procedure is depicted in figure 4.5a. Note, that the accuracy of the alignment depends on the number of supporting points available for calibration, i.e. the number of iso-energy slices, and is on the order of few milliseconds in the presented case.

4.2.3.2 Correction of the initial motion phase

Instead of the measured motion trajectories, the nominal sinusoidal trajectories were generated using TRiP4D's motion trace module (cf. section 3.2.1.2) and were used in the 4D simulations. Due to technical limitations, the robotic motion exhibits a significant starting delay w.r.t. the trigger at irradiation start (Steidl, Richter et al. 2012). This delay effectively corresponds to a non-negligible initial phase shift of the measured motion trajectory relative to the planned initial motion phase. In order to ensure adequate agreement of the dose reconstructions with the measurements, this phase shift was determined in a signal analysis of the measured motion trajectory and the beam status signal. For each measurement a sinusoid was fitted to the measured motion trajectory. The initial motion phase then was obtained as the phase of the sinusoid at irradiation start and was considered for generation of the sinusoidal motion trajectory with TRiP4D. The correction procedure is illustrated in figure 4.5b showing the relation of the initial

phase, ϕ_0, to the starting delay, Δt, and the resulting sinusoidal motion trajectory used in the simulations (dashed red line).

4.2.3.3 Analysis of measured and reconstructed dose distributions

The accuracy of the 4D dose reconstructions with TRiP4D was assessed by a statistical analysis of simulated and measured dose values at the respective geometrical positions of the ionization chambers. A software was developed which is capable of extracting dose values from a 3D dose distribution using a given geometry of pinpoint ICs (appendix A.2). The mean relative difference of measured and simulated dose values

$$\overline{\Delta D} = \sum_{i}^{N} \left(D_i^{\text{calc}} - D_i^{\text{meas}} \right) / D_i^{\text{meas}} \tag{4.4}$$

and the standard deviation, σ^D, was calculated for $N = 22$ ICs. The remaining two ICs were neglected for analysis because they were positioned close to the target volume boundary (figure 4.4) and exhibited significantly larger dose fluctuations compared to the other detectors.

Furthermore, the agreement between measured and simulated dose at the individual IC positions was assessed using bivariate linear regression. The same regression model as given in equation (3.7) was used (see section 3.3.2 for details). This model assumes a linear relationship between measured and calculated dose, modified by a systematic and dose-independent contribution of the two different ripple-filters. The analysis was carried out using JMP (version 9.0, SAS Institute Inc., Cary, NC, USA). The results of the bivariate regression are reported as the coefficient of variation R^2 and the root-mean-square error (RMSE) of the model.

4.2.4 4D dose simulations

4.2.4.1 Parameter space expansion

The validation of the simulation environment using the dose reconstructions discussed in the previous section was the basis for additional 4D simulations in the same setup. The sparse sampling of the motion parameter space in the experiments was extended by a finer graduated scan of the parameter space, including the initial motion phase and amplitude. Furthermore, the impact of the beam delivery sequence (BDS) on residual motion interplay effects was studied. To assess the full spectrum of the expected dose inhomogeneities for the given target geometry and the selected beam parameter combinations, the initial target motion phase was varied from 0° to 360° in 12 steps of 30°. Four motion amplitudes of 0.5, 3, 5 and 10 mm were chosen for the major motion component in the LR direction. In analogy to the experimental configuration, the amplitudes for the remaining dimensions were reduced to 50 % of the LR value. For practical reasons a motion period of three seconds was used for all simulations.

To study the impact of the temporal structure of the beam delivery on the interplay effects, the BDS data measured during the experiments were used as input to the 4D simulations. They were assumed to represent a realistic spectrum of the HIT beam delivery characteristics over time. Since the BDS is specific to a particular treatment plan, between one and ten different

BDS tables (93 in total) were available for each of the beam parameter combinations listed in table 4.1. For every sequence the full spectrum of four amplitudes and 12 starting phases was simulated, amounting to a total of 4464 dose distributions. The simulation workflow and infrastructure is identical to the one used for the dose reconstructions, including the 4DCT and target geometry. The motion parameters were used as input to TRiP4D to generate 3D target motion trajectories and the associated rigid deformation maps (section 3.2.1.3). Initial motion phase correction, as described above, did not apply.

4.2.4.2 Analysis of simulated dose distributions

The analysis of the simulated dose distributions was based on a statistical evaluation of the dose inside a CTV. It is common practice to obtain the ITV from the CTV by an appropriate definition of margins (section 2.2.3.2). In the presented case the limited amount of beam time only allowed for a single treatment plan to an ITV per beam parameter combination. Therefore, the CTV was constructed from the ITV using TRiP4D's 4D segmentation functionality (section 3.2.1.4). In brief, the ITV was transformed to all 4DCT phases based on the inverse rigid deformation maps for the respective target motion. The CTV was obtained by subsequent formation of the intersection volume over all ITV phase representations. For reasons of simplicity and comparability, only the smallest possible CTV, i.e. for the 10 mm motion amplitude, was constructed and selected for analysis of all dose distributions. In figure 4.4 the reference phase CTV and ITV are depicted as cross sections through the ITV center.

To assess the dose homogeneity inside the CTV as a function of the beam parameters and the motion amplitude, the mean dose and standard deviation, $\overline{D}$ and σ^D, and the minimum and maximum dose, D_{min} and D_{max}, were computed. Furthermore, the differential dose distributions to the static case were computed, including the mean dose and standard deviation, the minimum and the maximum dose inside the CTV. Also, dose volume histograms (DVHs) were calculated and analyzed for all dose distributions. A dose homogeneity index (HI) was defined as:

$$\text{HI} = \frac{D_5 - D_{95}}{D_p} \quad . \tag{4.5}$$

Here, D_5 and D_{95} denote the dose covering 5 % and 95 % of the CTV, respectively. D_p is the prescribed dose. The conformity of the dose to the ITV was measured using two different dose conformity indices. The so-called conformation number (CN) was adopted from van't Riet et al. (1997) and Feuvret et al. (2006) and is defined as:

$$\text{CN} = \left(\frac{V_{95}^T}{V_T}\right) \times \left(\frac{V_{95}^T}{V_{95}}\right), \quad 0 \leq \text{CN} \leq 1 \quad . \tag{4.6}$$

Here, V_T is the volume of the ITV and V_{95}^T is the ITV volume receiving at least 95 % of the prescribed dose. Finally, V_{95} denotes the overall volume receiving at least 95 % of the prescribed dose. Hence, the target coverage is balanced with the exposure of the surrounding volume. As a second figure of merit the dose conformity index (CI) according to Steidl (2011) was used:

$$\text{CI} = \frac{\int_{\text{ITV}} D(x,y,z)\,dV}{\int D(x,y,z)\,dV}, \quad 0 < \text{CI} < 1 \quad . \tag{4.7}$$

That is, the fraction of the integral dose deposited in the ITV.

	focus level 2		focus level 3		focus level 4	
series/ day	$\overline{\text{FWHM}}_x$ $\mu \pm \sigma$[mm]	$\overline{\text{FWHM}}_y$ $\mu \pm \sigma$[mm]	$\overline{\text{FWHM}}_x$ $\mu \pm \sigma$[mm]	$\overline{\text{FWHM}}_y$ $\mu \pm \sigma$[mm]	$\overline{\text{FWHM}}_x$ $\mu \pm \sigma$[mm]	$\overline{\text{FWHM}}_y$ $\mu \pm \sigma$[mm]
1	6.0 ± 0.4	5.7 ± 0.3	8.2 ± 0.7	8.0 ± 0.3	10.3 ± 1.0	10.4 ± 0.3
2	5.6 ± 0.2	5.8 ± 0.2	7.5 ± 0.1	8.1 ± 0.2	9.2 ± 0.2	10.4 ± 0.3

Table 4.2.: Mean measured FWHM of the beam spot and standard deviation for the lateral dimensions (x,y) at the different focus levels. The data were extracted from the TCS treatment records of the first two measurement series. Differences between days originate from an accelerator hardware failure.

4.3 Results

A total of 99 measurements with target motion were performed. Between two and five motion amplitudes per treatment plan were driven with the robot, some of them were measured multiple times. Additionally, 29 static reference irradiations were performed. An overview of the amplitudes measured per beam parameter combination is given in table 4.1. Due to a hardware failure on day one, beam conditions were not stable over the first two measurement series. Table 4.2 summarizes the results of the statistical analysis of the TCS treatment records regarding the FWHM of the beam. Compared to day two, beam spots on day one had a larger mean diameter in the x dimension ($\approx$10 %) and also exhibited larger fluctuations on the same order of magnitude in this dimension. The planned values of beam FWHM are given in table 4.1 for each treatment plan. Deviations of the measured beam FWHM from these values are smaller than 10 % on both days. Apart from the beam FWHM, beam positions were also less stable on day one. The standard deviation of the mean difference to the planned beam position was determined to 0.9 mm and 0.2 mm in x and y, respectively. This compares to 0.2 mm and $<$0.1 mm for x and y on day two, respectively.

Since all measurement with RiFi3 were performed on day one (cf. table 4.1) and were affected by the fluctuation in the beam spot size and position, the respective parameter combinations were repeated in the third measurement series. A smaller number of RiFi4 combinations was also measured for comparison. Beam conditions were stable during these measurements.

4.3.1 4D dose reconstructions

4D dose reconstructions were carried out using the nominal target trajectories with an individual initial phase determined from the measured motion trajectory and the acquired beam status data, as discussed above. Six of the measurements were disregarded for dose reconstruction, due to missing or deficient BDS data. On the first two measurement days the robot showed an average starting delay w.r.t. the trigger on the first beam-on of $\approx$1160 ms. For the selected motion period of 3 s this translates into an initial motion phase shift of $\approx -139°$. After improvements in the start-up behaviour of the robot for the third measurement series, the initial motion phase shift was reduced to $-29°$, corresponding to a delay of $\approx$240 ms. However, for all cases correction of the initial phase shift turned out to be necessary, in order to satisfactorily reproduce the measured IC doses in the simulations.

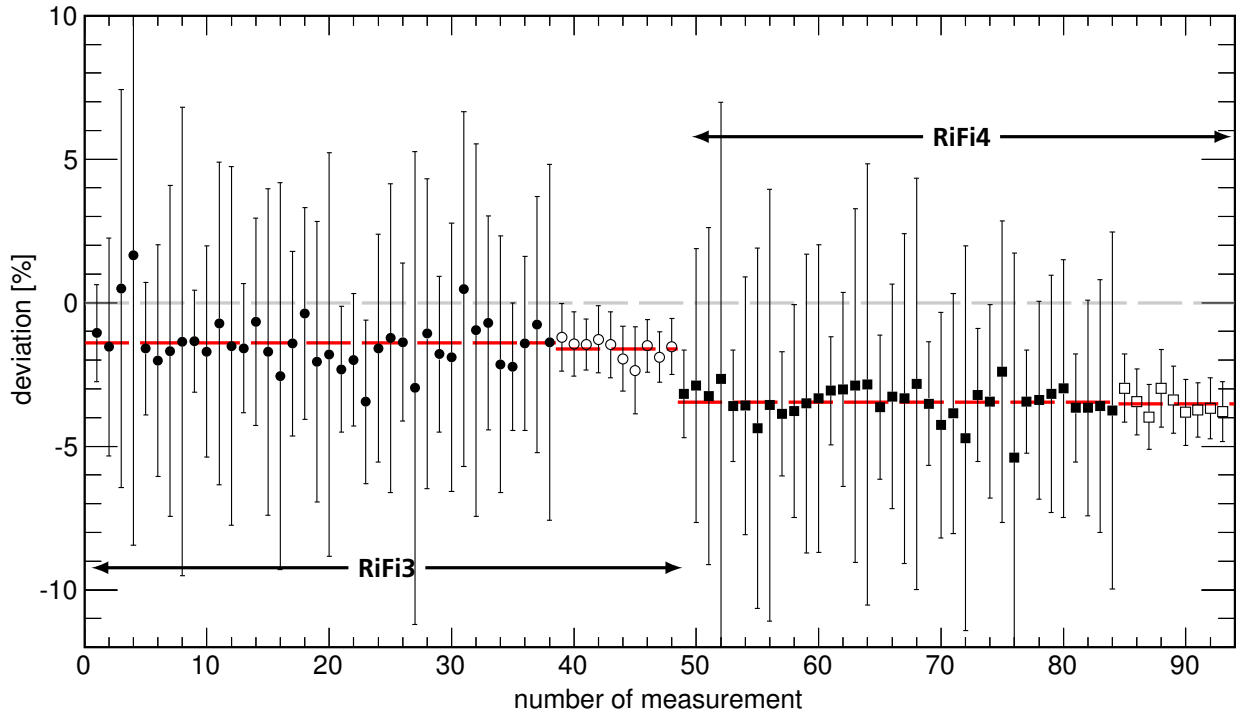

(a)

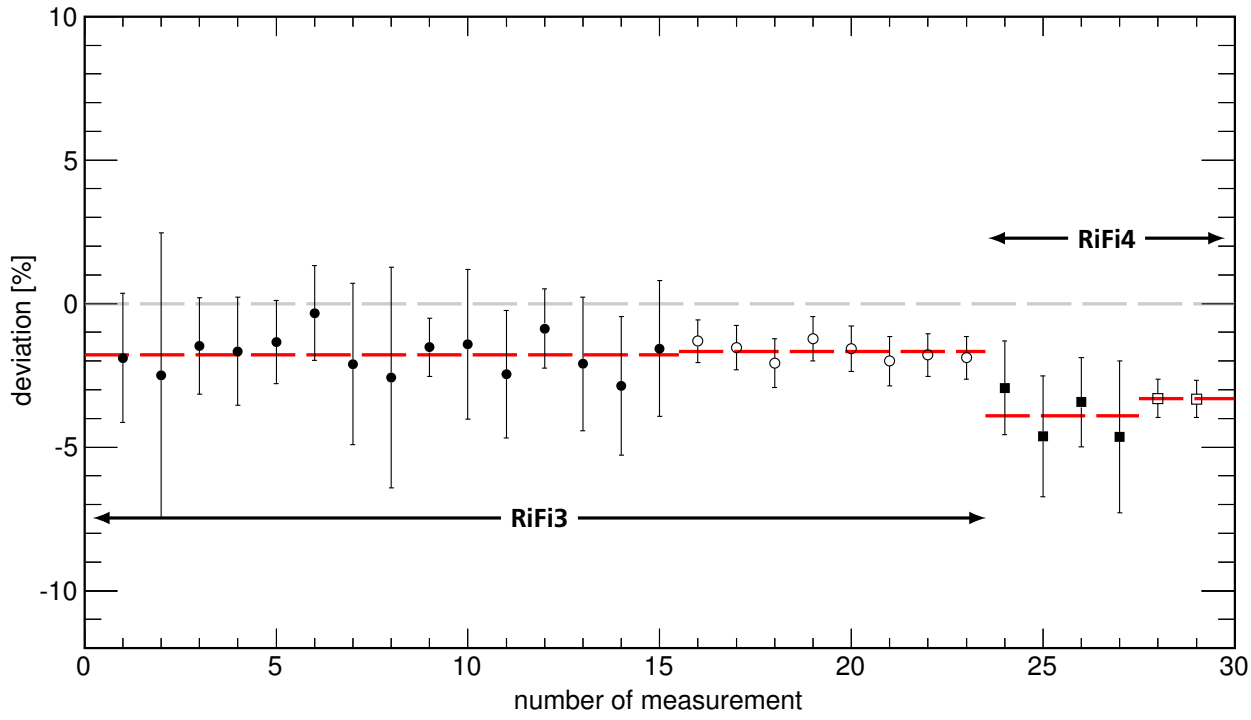

(b)

Figure 4.6.: Agreement of simulated and measured dose values for the first two **(a)** and the third measurement series **(b)**. The mean relative dose difference over the 22 IC positions and standard deviation is drawn vs. the measurement number. Static reference irradiations are indicated with open symbols. Separate fits are given for the RiFi3 and RiFi4 cases.

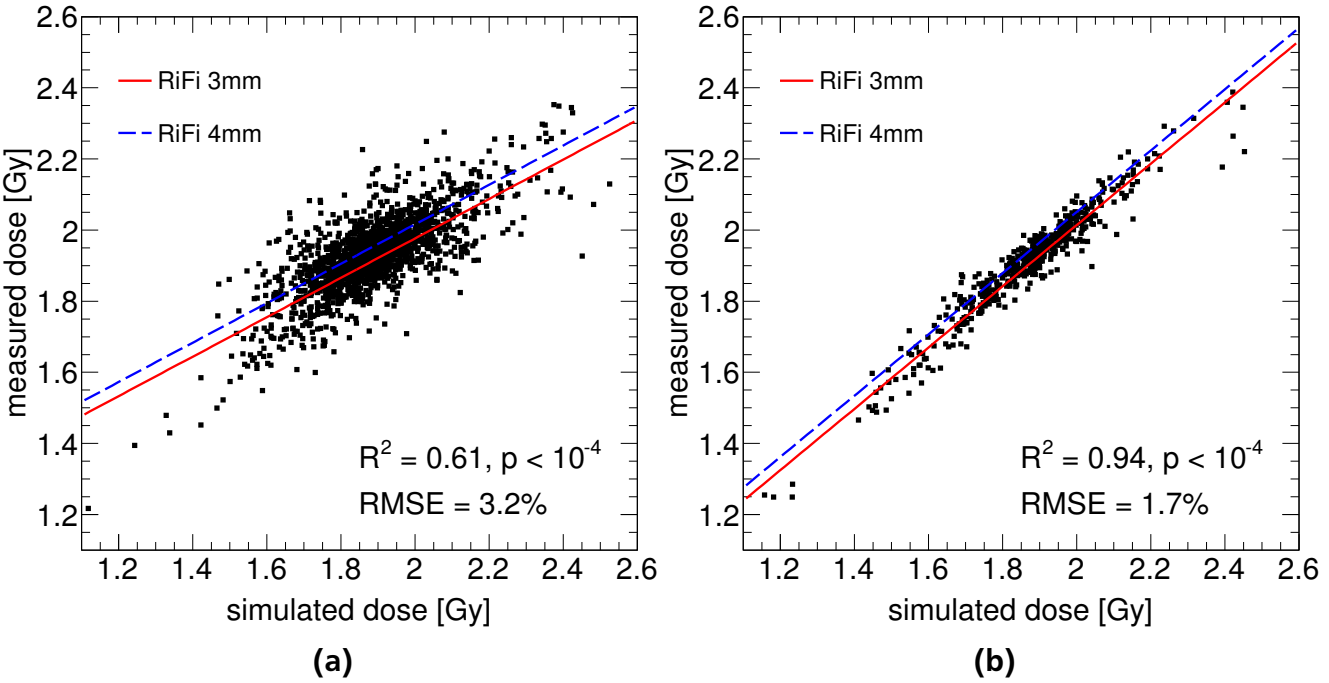

Figure 4.7.: Scatter plot of measured (D^{meas}) versus simulated dose values (D^{calc}) for the individual ICs in all moving and stationary cases of series one and two **(a)**, and series three **(b)**. The fits determined by bivariate linear regression for RiFi3 and RiFi4 are indicated for each ensemble, including the R^2 and RMSE.

In figure 4.6a and 4.6b the results for the comparison of reconstructed and measured dose values at the IC positions are given for all measured cases, including the static reference irradiations. Separate graphs are shown for the first two and the third measurement series, comprising 47(19) and 21(19) irradiations with(without) target motion, respectively. The graphs are split for the RiFi3 and RiFi4 combinations, including separate fits to the data. The average agreement of the 4D simulations with the measurements for the first two series is $(-1 \pm 5)\,\%$ and $(-3 \pm 5)\,\%$ for RiFi3 and RiFi4 cases, respectively. Standard deviations are below 8 % for more than 90 % and below 5 % for about 60 % of the cases. For the third measurement series the average agreement is $(-2 \pm 2)\,\%$ and $(-4 \pm 2)\,\%$ for the RiFi3 and RiFi4 cases, respectively. Standard deviations are below 3 % for all cases. For the static reference irradiations the simulations agree with the measurements of the first two series within $(-2 \pm 1)\,\%$ and $(-4 \pm 1)\,\%$ for RiFi3 and RiFi4 cases. Similar values of $(-2 \pm 1)\,\%$ and $(-3 \pm 1)\,\%$ were obtained for the third series. A systematic difference in the mean value of about 2 % was consistently observed between RiFi3 and RiFi4 treatment plans over all measurement series. Detailed results of the dose reconstructions for all cases are listed in tables B.2 and B.3 in the appendix.

The results of the bivariate linear regression using the model in equation (3.7) are summarized in figures 4.7a and 4.7b. The analysis was performed separately for the first two and the third measurement cohort and the respective simulations. The scatter plots show the correlation of measured and simulated dose values at the individual IC positions for all considered cases with and without target motion. The linear fits for the two ripple-filters are drawn on top. The resulting coefficient of variation, R^2, and RMSE for the model are given for both data ensembles. Compared to the first two series (figure 4.7a), the third cohort of measured and

simulated dose values exhibits a 50 % larger explained variance R^2 and a significantly smaller RMSE (figure 4.7b). The systematic dosimetric difference between RiFi3 and RiFi4 cases was statistically significant at the $p < 10^{-4}$ level.

4.3.2 4D simulation results

The following sections will present the results of the 4D simulations concentrating on the influence of the various beam parameters on the target dose homogeneity and the dose conformity. Since several of the investigated parameters turned out to be strongly correlated, only a subset of the parameters is considered here, namely the standard deviation of the mean dose in the CTV, σ^D, and the conformity indices, CI and CN. σ^D exhibited a large sample correlation coefficient, r, w.r.t. the homogeneity index, HI ($r \approx 0.99$, $p < 0.05$), and $D_{\max} - D_{\min}$ ($r \approx 0.96$, $p < 0.05$). Since variations of the static dose inside the CTV were negligible, the mean differential dose and standard deviation were strongly correlated to the respective non-differential parameters ($r \approx 1.0$, $p < 0.05$). Thus, they were not investigated any further.

4.3.2.1 Dose homogeneity

Variation of the beam spot size

In figure 4.8 bird's eye view cross sections of two 4D dose distributions for 6 and 10 mm beam FWHM, a medium LR motion amplitude of 5 mm and a selected initial motion phase are shown. On the right hand side the corresponding DVH bands for the CTV are given for three motion amplitudes. The bands represent the spread of one standard deviation around the average DVH characteristic. Both were determined using all simulations of the respective beam parameter combination, i.e. initial phases and several beam delivery sequences.[3] In the presented case the overdose to the CTV (pink areas in figures 4.8a,c) is reduced for the 10 mm beam spot size. The corresponding DVH bands feature a narrower shape and steeper slope. Target coverage is gradually improved for smaller motion amplitudes.

Figure 4.9 on page 78 shows the amplitude dependence of the target dose homogeneity (standard deviation relative to the planned dose) for the four beam parameter combinations with $\Delta s = 2$ mm in which different beam FWHM of 6, 8 and 10 mm were used. The indicated markers and error bars represent mean values and standard deviation calculated over all simulations at the respective amplitude, i.e. the 12 initial motion phases per beam delivery sequence (grey markers). The curves represent linear fits to the data, including the stationary irradiations. Median values are also shown (open symbols) to visualize the asymmetry of the distribution of standard deviation values, where applicable. A linear dependence of the dose homogeneity on the motion amplitude is observed at all beam spot sizes. Likewise, the spread increases approximately linear with amplitude and becomes increasingly asymmetric towards large values of relative standard deviation. For all combinations but ($\Delta z = 2$ mm, RiFi3) the dose homogeneity on average increases with a larger beam FWHM, in particular for the ($\Delta z = 3$ mm, RiFi3) combinations. However, the error bars for the different beam spot sizes overlap to a large extent at all amplitudes.

[3] Potentially resulting band ranges overshooting 100 % or undershooting 0 % of the volume were clipped to 100 % and 0 %, respectively.

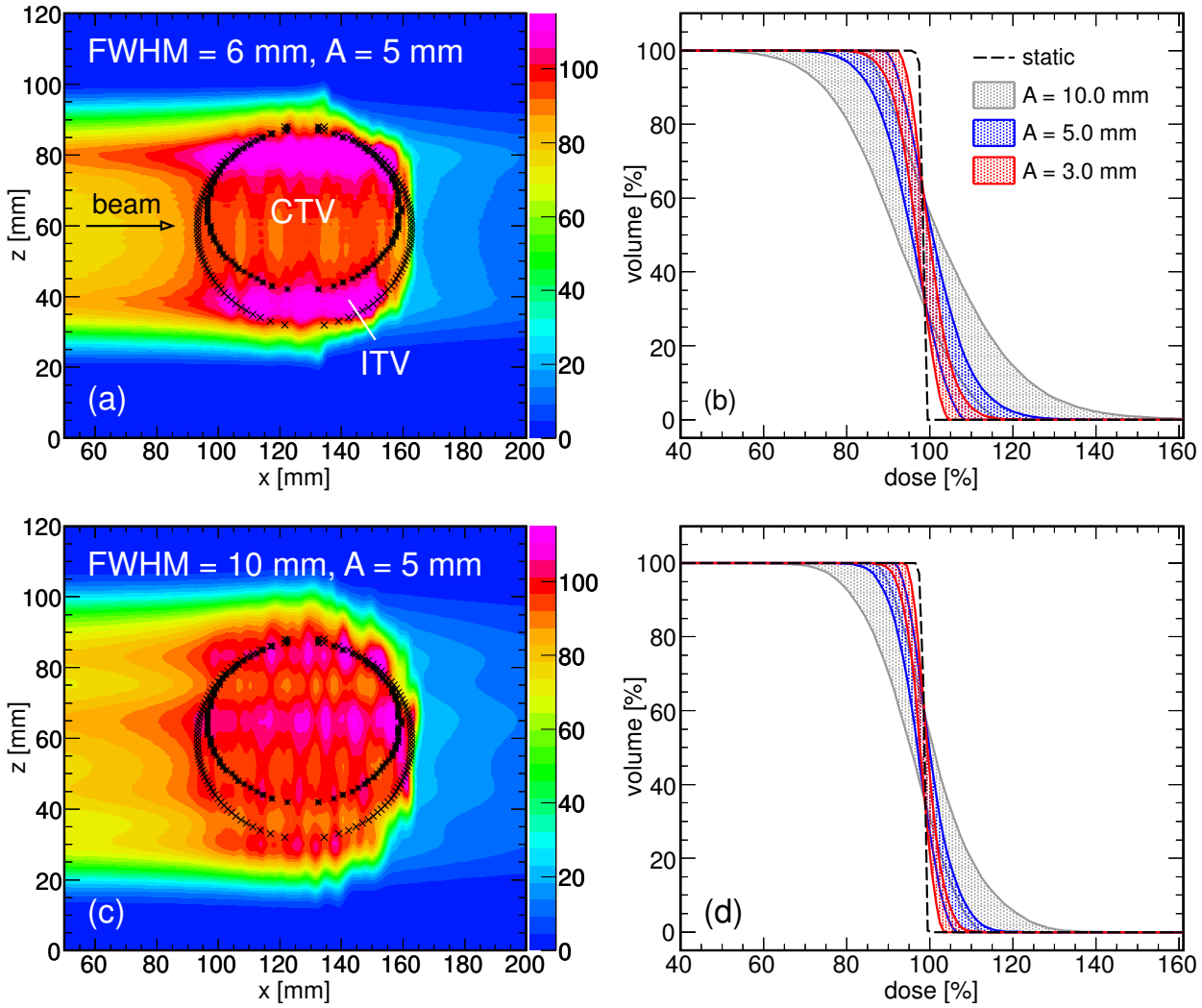

Figure 4.8.: Horizontal dose cuts and DVH bands for 6 mm **(a-b)** and 10 mm **(c-d)** beam FWHM, $\Delta s = 2\,\text{mm}$, $\Delta z = 3\,\text{mm}$ and RiFi3. Dose scale is in percent of the planned dose.

Variation of the lateral raster spacing

A varying lateral raster spacing could be studied at a beam FWHM of 10 mm only, as smaller beam spots were not combined with a Δs of 3 mm in the treatment plans (see table 4.1). The relative standard deviation versus the motion amplitude is depicted in figure 4.10 on page 79 for varying Δs of 2 and 3 mm and four combinations of Δz and RiFi. The presentation is identical to figure 4.9. The linear fits exhibit a slightly shallower slope for $\Delta s = 3\,\text{mm}$ and RiFi3. For RiFi4 the larger homogeneity of $\Delta s = 3$ is diminished at a $\Delta z = 3\,\text{mm}$ (figure 4.10d) and for $\Delta z = 2\,\text{mm}$ the situation is inverted w.r.t. to RiFi3. The error bars for different parameter combinations overlap with each other at most amplitudes.

Variation of the iso-energy slice spacing

The variation in target dose homogeneity with the IES spacing is depicted in figure 4.11 on page 80 for six combinations of beam FWHM, Δs and RiFi. For RiFi3 and $\Delta z = 2\,\text{mm}$ (figures 4.11a,c) dose homogeneity on average is improved compared to $\Delta z = 3\,\text{mm}$ at a beam FWHM of 6 mm and 8 mm (the latter is not included in the figure). No difference between 2 and

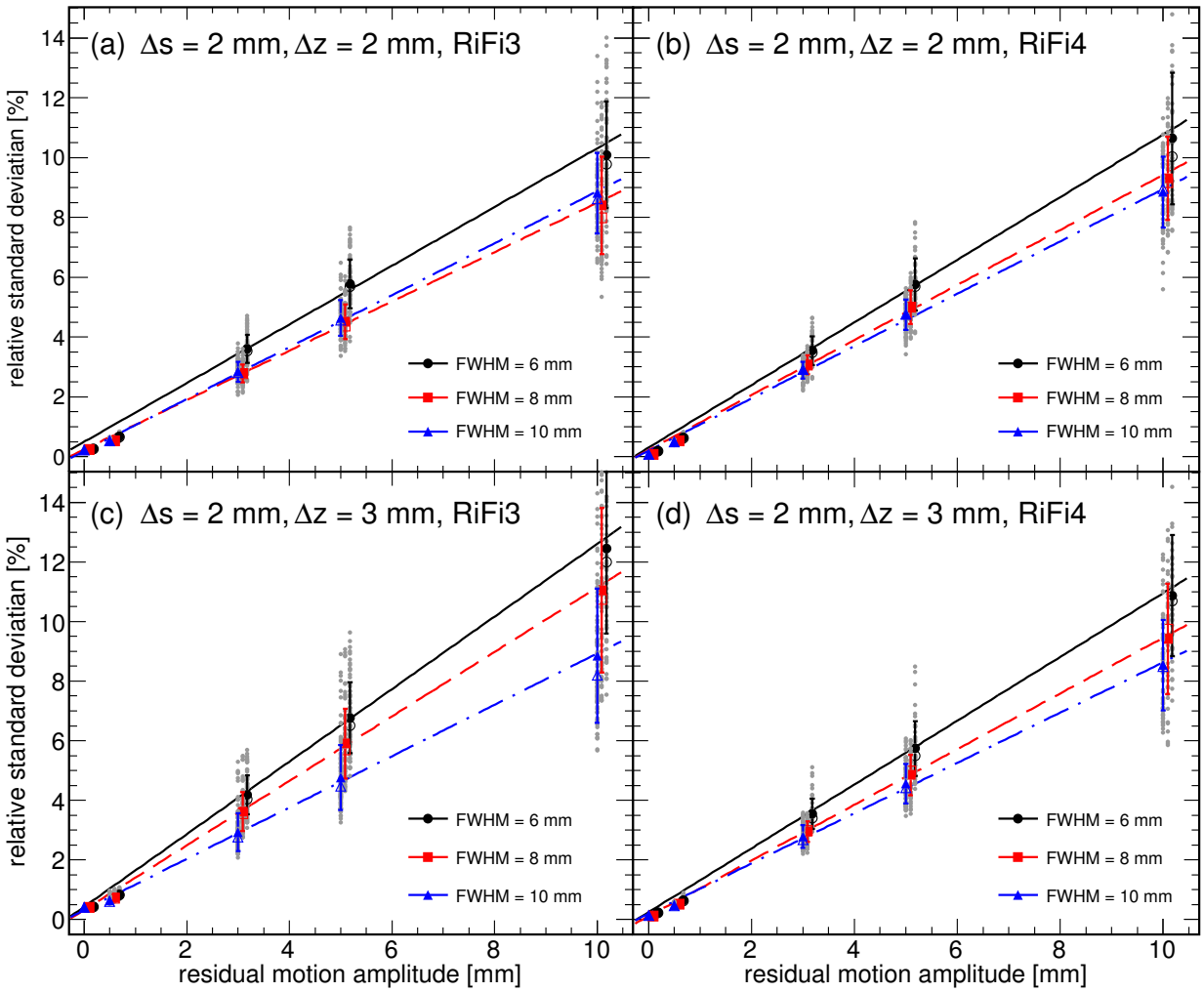

Figure 4.9.: Relative standard deviation of the CTV dose versus the residual motion peak-to-peak amplitude for varying beam FWHM and several combinations of lateral raster spacing (Δs), IES spacing (Δz) and RiFis. The grey markers indicate different initial motion phases. For clarity, markers are drawn with a horizontal offset.

3 mm slice spacing is observed for a beam FWHM of 10 mm, the same holds for $\Delta s = 2$ mm and RiFi4 (figures 4.11b,d). The curve for $\Delta z = 4$ mm shows a significantly decreased homogeneity compared to the other IES spacings (figure 4.11d). For $\Delta s = 3$ mm and RiFi3 differences are small between all IES spacings, including $\Delta z = 1$ mm (figure 4.11e). The respective RiFi4 combination on average exhibits a smaller slope for the larger IES spacing.

Variation of the ripple filter

In figure 4.12 on page 81 the relative standard deviation is drawn versus the motion amplitude for varying ripple-filters. For $\Delta s = 2$ mm and $\Delta z = 2$ mm differences between RiFis are small at all beam spot sizes (figures 4.12a,c). For $\Delta z = 3$ mm the RiFi4 curves tend to have smaller slopes than the respective RiFi3 curves, in particular for a beam FWHM of 6 and 8 mm. The graphs for a beam FWHM = 8 mm were omitted in the figure. At $\Delta s = 3$ mm only for $\Delta z = 2$ mm a significant difference (separation by more than one standard deviation) in the average characteristic is found (figure 4.12e). In this case the RiFi4 curve features larger dose homogeneity w.r.t. RiFi3.

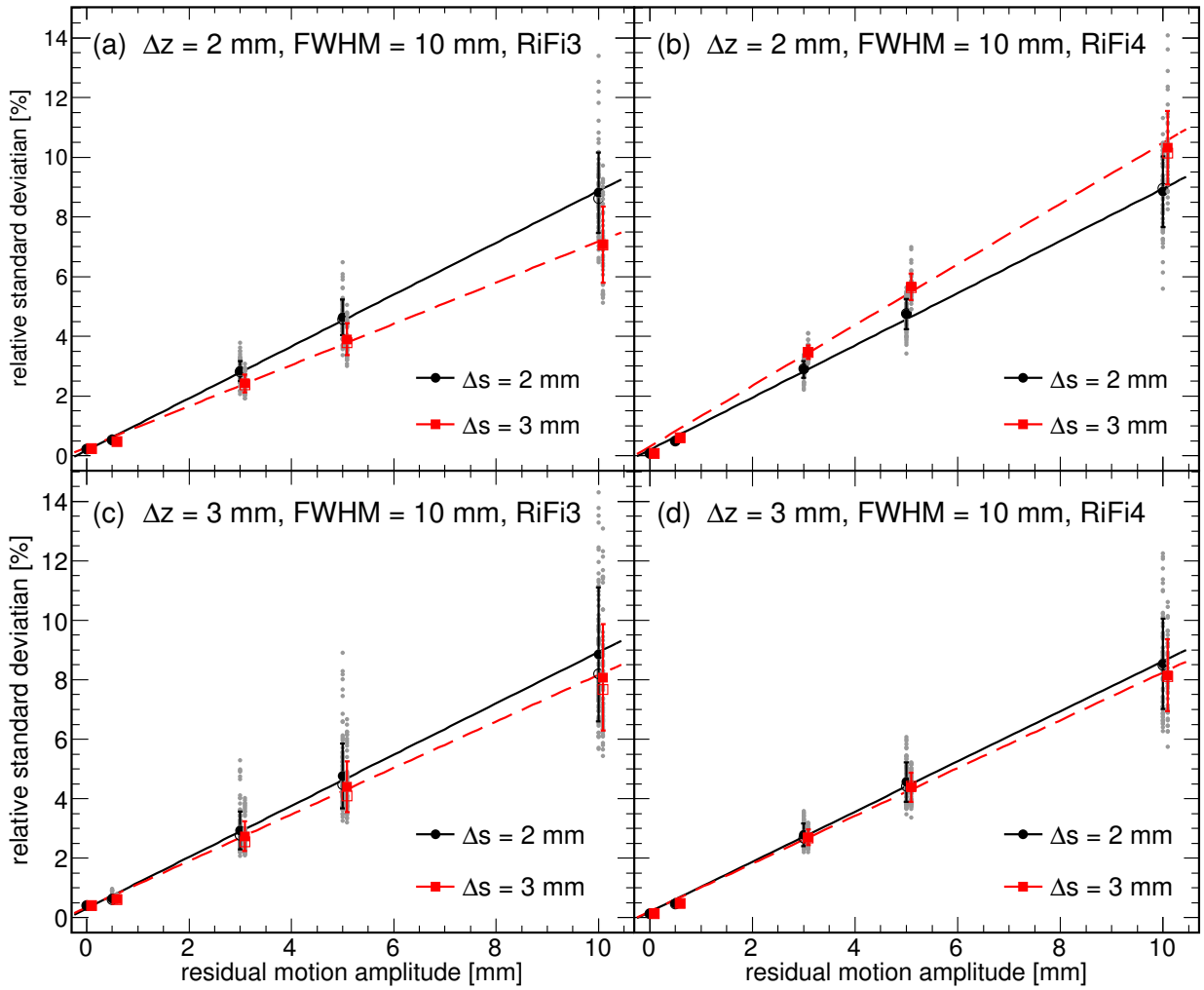

Figure 4.10.: Relative standard deviation of the CTV dose versus the residual peak-to-peak motion amplitude for varying lateral raster spacing (Δs) and several combinations of IES spacing (Δz) and RiFis.

Variation of the beam delivery sequence

The results in the previous sections were reported for simulations based on the full spectrum of BDSs. The variations observed in target dose homogeneity as a function of the BDS are illustrated for a representative beam parameter combination ($\Delta s = 2\,\text{mm}$, $\Delta z = 3\,\text{mm}$, FWHM $= 8\,\text{mm}$, RiFi3) in figure 4.13. Comparable results were obtained for most of the other combinations. On the right hand side of figure 4.13, the relative standard deviation is shown as a function of the residual motion amplitude for different BDSs. On the left hand side the DVH bands for the corresponding ensemble of dose distributions are given. For clarity, only three BDSs are depicted. These represent the worst (BDS 1), best (BDS 2) and a medium (BDS 3) case example w.r.t. to dose homogeneity at the particular parameter combination. The relative standard deviation for the best and worst case BDS differ from the overall fit (black solid line) by about $\pm 30\,\%$. The green solid line constitutes the overall fit obtained for a smaller Δz of 2 mm instead, i.e. a larger longitudinal overlap factor. For the parameter combination in question the largest improvement in dose homogeneity using a decreased IES spacing was found (cf. figure 4.11). Hence, the best case BDS for $\Delta z = 3\,\text{mm}$ and the average curve for $\Delta z = 2\,\text{mm}$

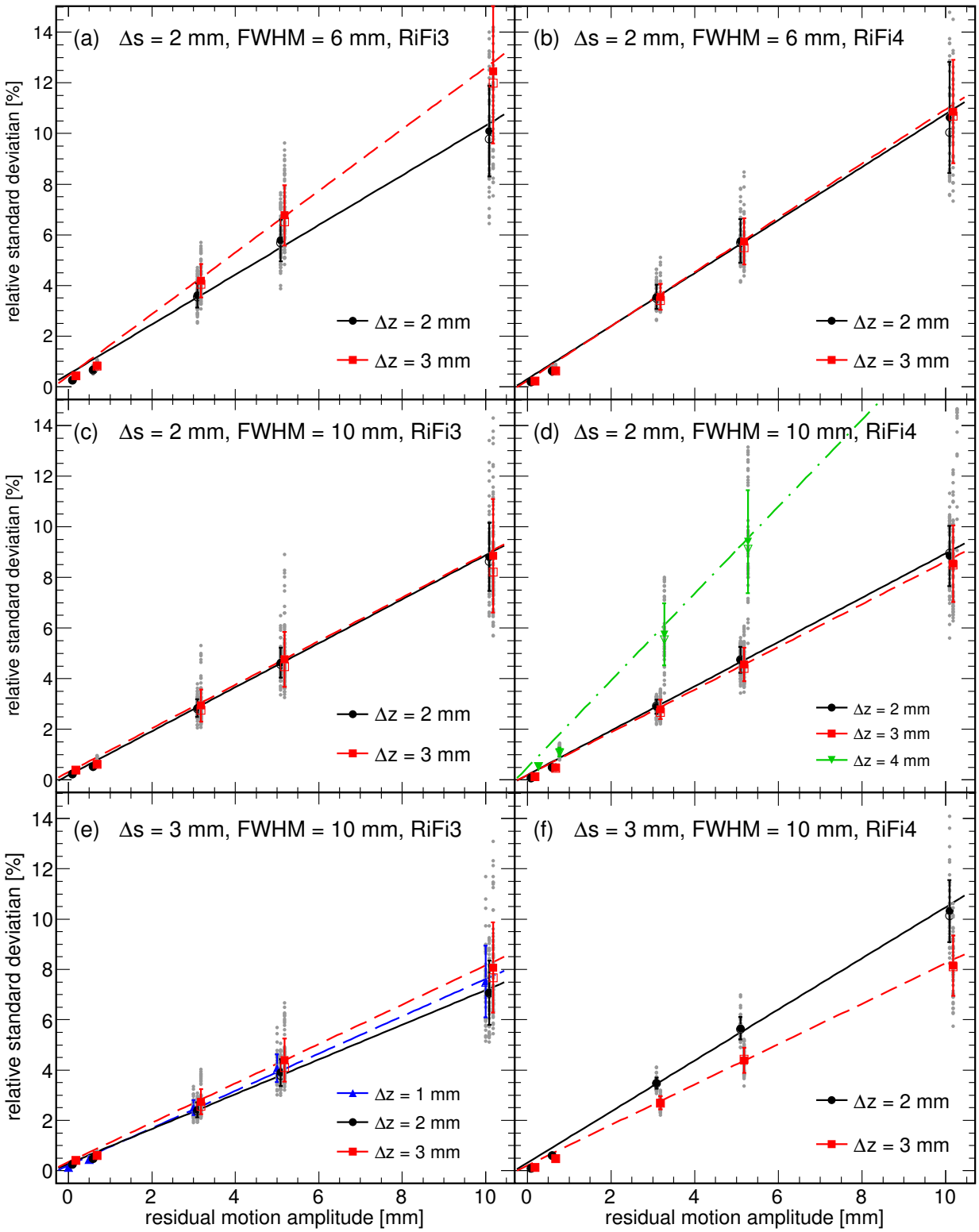

Figure 4.11.: Relative standard deviation of the CTV dose versus the residual peak-to-peak motion amplitude for varying IES spacing (Δz) and several combinations of beam FWHM, lateral raster spacing (Δs) and RiFis.

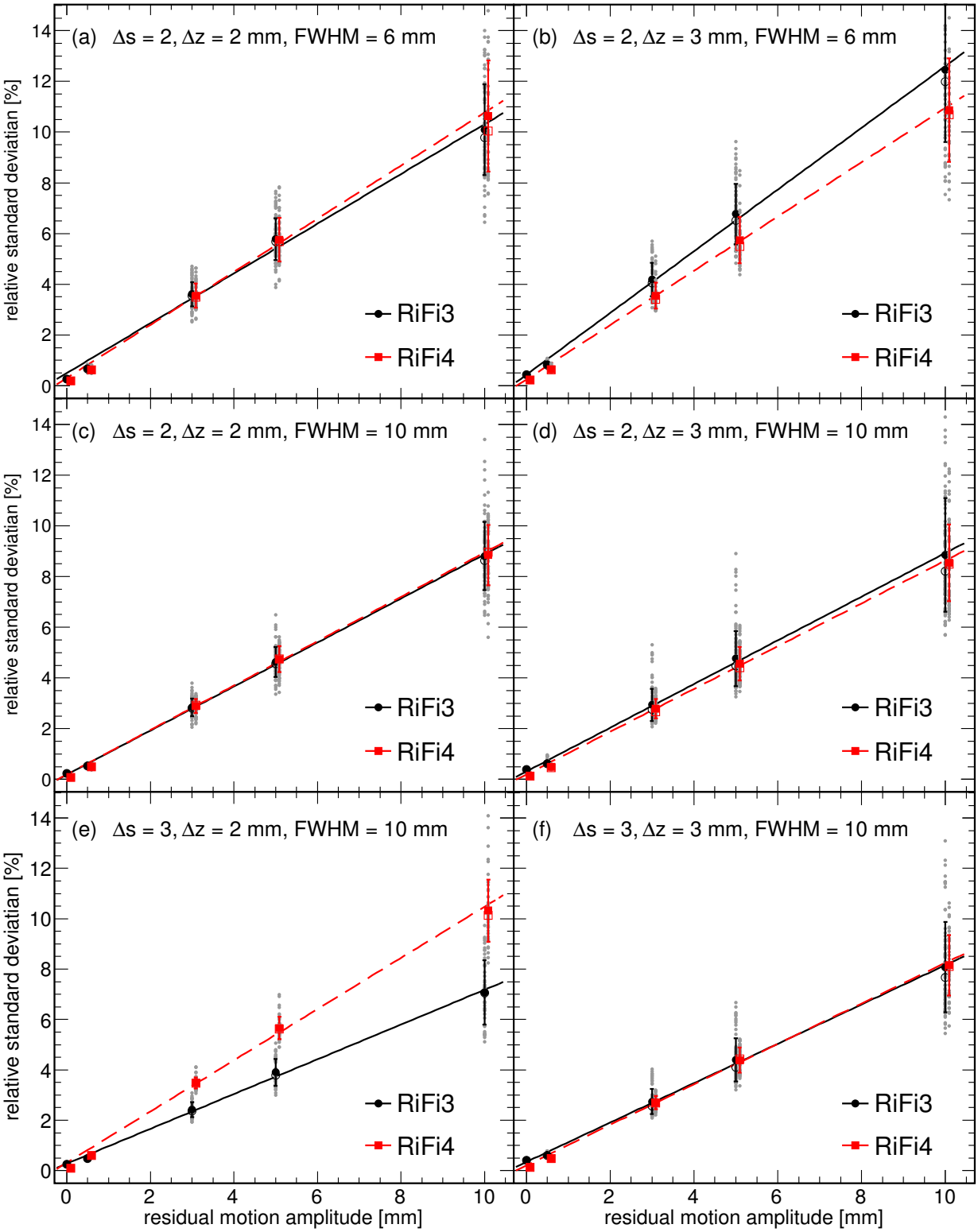

Figure 4.12.: Relative standard deviation of the CTV dose versus the residual peak-to-peak motion amplitude for varying RiFi and several combinations of beam FWHM, lateral raster spacing (Δs) and IES spacing (Δz).

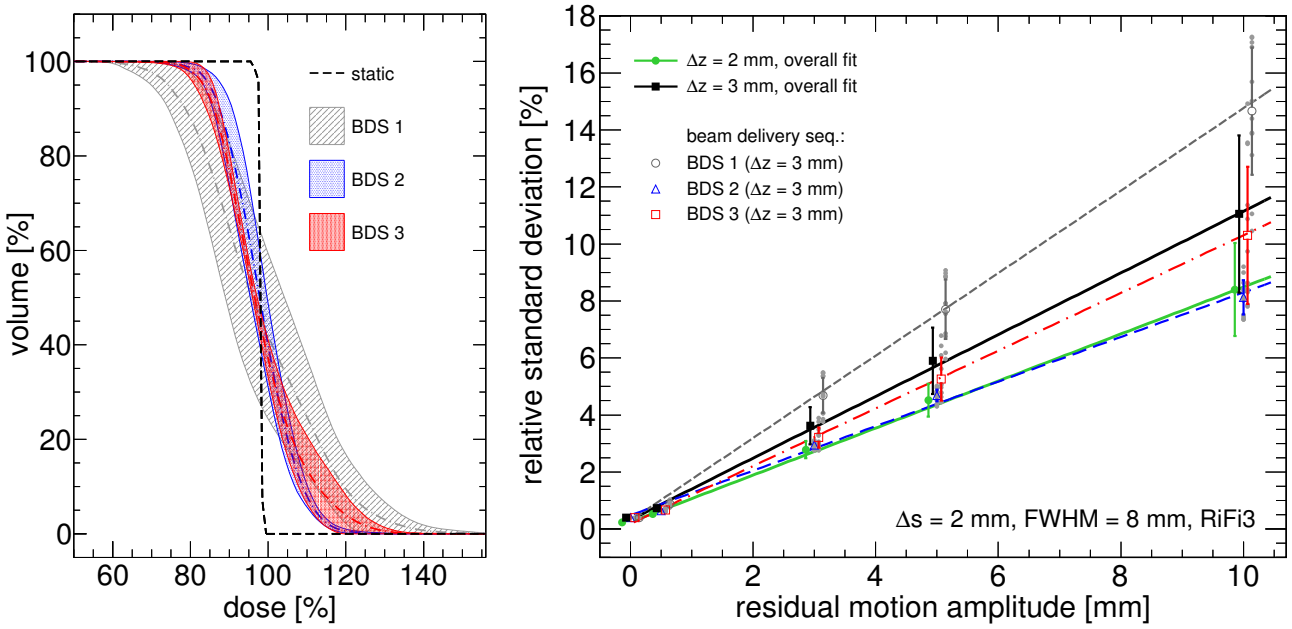

Figure 4.13.: Relative standard deviation versus the residual motion amplitude (right) and corresponding DVH bands (left) for three different beam delivery sequences (BDSs) at a selected beam parameter combination ($\Delta s = 2\,\text{mm}$, $\Delta z = 3\,\text{mm}$, FWHM $= 8\,\text{mm}$, RiFi3). The overall fits for $\Delta z = 3\,\text{mm}$ and $\Delta z = 2\,\text{mm}$ on the basis of all BDSs are shown for comparison (black and green solid lines). DVH bands are drawn for a 10 mm motion amplitude.

exhibit a comparable dose homogeneity. The different beam delivery sequence also show significant differences w.r.t. the spread in relative standard deviation (note, for instance, the grey and blue error bars). The DVH bands shown on the left of figure 4.13 represent the spread of one standard deviation around the average characteristic (dash-dotted lines) at a 10 mm motion amplitude. The three shown BDSs exhibit differences in the general shape and width of the bands, also asymmetries are observed (BDS 3). The widths and average characteristics of the DVH bands qualitatively correspond to the mean values and spreads found for the relative standard deviation.

4.3.2.2 Dose conformity

The results for the conformity indices CI and CN are presented here for a representative beam parameter combination only ($\Delta s = 2\,\text{mm}$, $\Delta z = 3\,\text{mm}$, FWHM $= 6\,\text{mm}$ and RiFi3), since very similar results were obtained for the other combinations. Figures 4.14a–c summarize the results for the dose conformity index (CI). The CI did not show dependencies on any of the beam parameters with exception of the beam FWHM. The horizontal dose cuts in figures 4.14a–b illustrate the lateral increase of dose deposition outside the ITV for a beam FWHM of 10 mm compared to a FWHM of 6 mm for a static target. In figure 4.14c the CI is drawn versus the motion amplitude. While mean values are independent of the amplitude, the standard deviation increases approximately linearly.

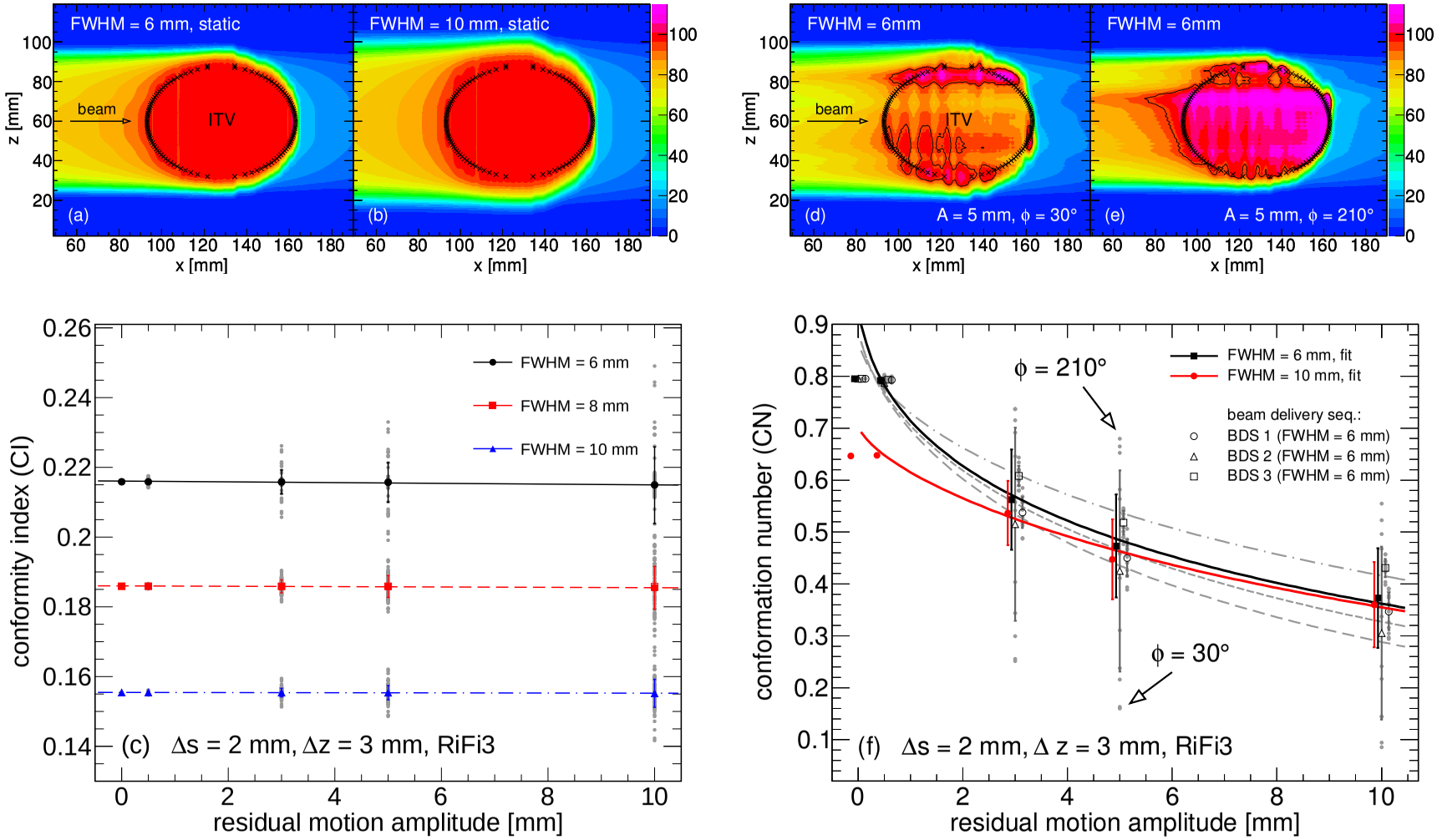

Figure 4.14.: Conformity index **(a–c)** and conformation number **(d–f)** for a representative beam parameter combination. Horizontal dose cross sections for two initial phases with extreme values for CN are shown in figures **(d–e)**, including the respective 95 % iso-dose areas (black solid line). Dose scales are given in percent of the planned dose.

Results for the conformation number (CN) are presented in figures 4.14d–f for the same beam parameter combination. In analogy to figure 4.13, curves for three different BDSs are shown. All BDSs on average exhibit an exponential decay of the CN with the motion amplitude, accompanied by an increasing standard deviation. Depending on the BDS the CN fluctuates by up to 50 % around the mean value. For a medium motion amplitude of 5 mm representative cross sections of the dose distributions for the initial phases, ϕ, with the best ($\phi = 210$) and worst ($\phi = 30$) CN and BDS 2 are depicted in figures 4.14d,e. The 95 % iso-dose areas entering into equation (4.6) for the CN are framed with a solid black line and show large differences w.r.t. to target coverage. To compare this with the dependence of the CN on the beam FWHM, the average CN characteristic for a 10 mm FWHM has been included in figure 4.14f (red solid line). It can be seen that the CN is dominated by the fluctuations due to interplay effects for amplitudes $\gtrsim$ 3 mm. Comparable results were also obtained for the other beam parameter combinations.

4.4 Summary and discussion

The purpose of the experimental and simulation studies presented in this chapter was to assess the impact of an increased beam overlap on residual motion interplay effects, in particular with respect to the target dose homogeneity and dose conformity. Experiments and simulations were performed in a water phantom setup with 3D target motion.

Measurements and 4D dose reconstructions

Several series of 4D dose measurements were conducted at HIT with a robotically moved IC array. The results of the absolute 4D dosimetry were compared to the subsequently executed 4D reconstructions with TRiP4D. Although beam positions and beam FWHM were not fully stable on the first two days of the measurements (cf. table 4.2), a good agreement of the 4D simulations with the respective measurement was found in most cases. The mean relative dose difference and standard deviation over all ICs (equation 4.4) was used to evaluate the simulation accuracy. For about 50 % of the more than 40 cases the standard deviation was smaller than 5 %. This is to be compared to standard deviations of less than 3 % determined for the static dose. Standard deviations of less than 3 % for all moving and less than 2 % for all static cases were obtained for measurements performed on the third day. A systematic offset of -2 % of the calculations w.r.t. the measurements was found for the cases using the standard 3 mm RiFi. This is within the expected level of systematic uncertainty in absolute dosimetry of ion radiation (Karger et al., 2010). An additional systematic deviation of around -2 % in the mean value was found for the cases with two crossed ripple-filters (see, e.g., figure 4.6), including the static measurements. This difference may be attributed to inaccurate beam base data employed for dose optimization and calculation with TRiP4D. These data are not as well tested as those for the standard RiFi optimized for a 3 mm IES spacing. The agreement of the simulations with the measurements has additionally been tested with a bivariate linear regression model. For the third measurement series the introduced model is capable of explaining 94 % of the observed variance at a RMSE of 1.7 % ($p < 10^{-4}$). A smaller R^2 of 0.61 was obtained for the measured and simulated data of the other two series (cf. figure 4.7a). Furthermore, the slope of the obtained fit which relates measured and simulated dose values is considerably smaller than the expected bisecting line. Differences are likely to have been introduced in the measurements rather than the simulations, since the simulation environment was the same for all considered cases. For

example, uncertainties were introduced by the varying beam conditions on the first two days (see table 4.2). The beam FWHM in one dimension showed average deviations of ≈10 % between days one and two and deviations in the beam position had standard deviations of about 1 mm. Also, since the setup had to be re-positioned each day, systematic position uncertainties on the order of 1–2 mm may have been introduced. These affect the required location of dose extraction points in the simulated dose distributions. While for the static dose distributions only a minor impact is expected, this is critical for 4D dose distributions which often exhibit strong dose gradients. Thus, even small shifts may lead to significantly different dose values. Further improvement of the agreement with the measurements might be gained by an analysis of simulated dose values near the nominal dose extraction point, to compensate for the unknown setup shift. However, considering the static agreement as a limit, the average improvements will probably not exceed 1–2 %. Additional uncertainties are to be expected from the measured beam status signals, since, for technical reasons, these could not be directly related to the time the beam reached the cave but may be slightly shifted in time. In some cases also signal fluctuations compromised the simulation accuracy. Although most measurements exhibiting these kind of problems were disregarded, residual degradation of the beam delivery sequence data must be expected and may have a particular impact on the calibration of the initial motion phase (section 4.2.3.2). From the experiences made, the ideal solution for the acquisition of beam delivery sequence data is the combination of beam status and point completion signals into a single DAQ with a sampling time of less than a millisecond, i.e. well below typical point irradiation times. This configuration inherently provides temporally correlated data without the need for major post-processing introducing additional uncertainties. At the time of the presented experiments such a solution was not available.

Simulation studies

The validated simulation environment enabled extensive 4D simulations using the same water phantom setup. In more than 4400 simulations with various motion amplitudes and initial phases the impact of a varying lateral raster spacing, IES spacing, beam FWHM, RiFi and beam delivery sequence was investigated. The target dose homogeneity in the CTV and the dose conformity inside the ITV were determined for all dose distributions. Among other parameters, the relative standard deviation and two conformity indices were considered. With regard to target dose homogeneity in the CTV the motion amplitude had the strongest influence. The mean relative standard deviation of the average CTV dose exhibited a linear increase with the amplitude for all studied beam parameters. Furthermore, the standard deviation of the homogeneity increases approximately linearly with the amplitude, as well. For a particular treatment plan the relative order of the initial phases with respect to the homogeneity remains the same at all amplitudes, i.e. the modulation of the interplay pattern by the initial phase is the same. This can be understood when considering the fact that at a fixed motion period the target travels a larger distance in the same span of time and the same relative relation of target motion and beam scanning is maintained. Thus, interplay patterns and the related standard deviation are scaled as the amplitude increases. It can be deduced from the results that the principal interplay pattern is decisively determined by the particular BDS and drives the standard deviation significantly. In the example given in figure 4.13 differences in the spread of the relative standard deviation of more than 400 % have been found between different BDSs, independent of the motion amplitude. Similarly, variations in the mean value of ±30 % were found. Although the effect was less pronounced for some of the analyzed treatment plans, variations in the average

value and the spread of the relative standard deviation exceeded 20 % in most cases. Against this background, the results obtained for the various plan parameters have to be interpreted. These have been obtained taking into account all beam delivery sequences for the respective treatment plan. The average characteristics for the beam parameters in question were compared. Due to the large number of measurements, the standard errors on the mean values are very small in most cases, such that trends in the average homogeneity may be deduced. However, due to the substantial spread of the homogeneity distributions—even considering a single BDS only—exploiting these trends for a general improvement of the target dose homogeneity is difficult. Although the increase of the beam FWHM from 6–10 mm yielded an average decrease in the relative standard deviation by up to 30 %, an inappropriately chosen initial phase can invalidate this advantage. Apart from the effect of the beam spot size, which can be attributed to the gained robustness at an increased lateral beam overlap, results for the other beam parameters are difficult to interpret, as trends are not consistent. For instance, the use of a decreased IES spacing, i.e. an increased longitudinal overlap, on average did either increase or decrease the dose homogeneity, depending on the employed RiFi. For a RiFi3 and $\Delta s = 2$ mm reductions of the relative standard deviation by 20 % and 30 % were found for a beam FWHM of 6 and 8 mm, respectively. In contrast, for RiFi4 and a $\Delta s = 3$ mm the larger IES spacing showed a 30 % improvement (compare e.g. figures 4.11a,f). Similarly, results for the lateral raster spacing obviously can not be understood with the overlap concept alone, since a 3 mm spacing showed better homogeneity at a beam FWHM of 10 mm compared to the smaller spacing in three out of four cases (see e.g. figures 4.10a,c). However, the differences were smaller—a maximum decrease in relative standard deviation by 20 % for $\Delta z = 2$ mm and RiFi3.

Apart from the dose homogeneity, the dose conformity has been investigated as a function of the target motion amplitude and various beam parameters for the ITV. The dose conformity index (CI) on average did not show a dependence on the residual motion amplitude and only exhibited differences with respect to the beam spot size. By construction, the inhomogeneous distribution of interplay patterns is neglected. The spread of the CI is dependent on the amplitude and the beam spot size. The spread is most likely caused by dose transferred outward or inward w.r.t. the ITV, due to target motion. In contrast, the conformation number (CN) considers both the target coverage and the exposure of the surrounding volume (van't Riet et al., 1997). As the 95 % iso-dose volume of the ITV enters geometrically into expression (4.6), the CN is strongly interplay-dependent. As has been shown in figure 4.13f, even for beam delivery sequences which generate a small spread in CN (e.g. BDS 1 , open circles), the fluctuations predominate the effect of a decreased dose conformity due to a larger beam FWHM at motion amplitudes larger than 3 mm.

In the presented study, the ITV volume has been used for calculation of the CN, in order to be more sensitive to dose deposition outside the treated volume. If the CTV volume had been used instead, the CN would have been dominated by the dose deposited inside the ITV. However, from a clinical point of view, this dose was accepted by the therapist and it can therefore be argued that it should not enter into the CN calculations. On the other hand, the ITV is not designed to receive the full treatment dose but to ensure adequate CTV coverage. Thus, to assess the target dose conformity, the CTV is the relevant volume. To incorporate both of these aspects, a modified conformation number is proposed here:

$$\mathrm{CN}' = \left(\frac{V_{95}^{\mathrm{CTV}}}{V_{\mathrm{CTV}}}\right) \times \left(\frac{V_{95}^{\mathrm{ITV}}}{V_{95}}\right), \quad 0 \leq \mathrm{CN}' \leq 1 \quad . \tag{4.8}$$

V_{95}^{ITV} denotes the volume of the 95 % iso-dose volume inside the ITV. An analogous definition holds for the PTV, if used.

A possible explanation for the heterogeneous results obtained for the different beam parameter combinations is that lateral and longitudinal beam overlap effects are not entirely independent, as it was assumed in the presented study. The reduced impact of the IES spacing w.r.t. the dose homogeneity for an increasing beam spot size may be an indication that an increased longitudinal overlap can not improve the dose homogeneity beyond a certain level, if a large lateral overlap has already been applied. Against the background of the findings reported here w.r.t. the large variations in dose homogeneity and conformity introduced by varying BDSs, it also seems likely that the BDS may have a systematic impact on the target dose homogeneity for certain combinations of beam parameters. An increased lateral or longitudinal raster spacing, for instance, involves larger particle numbers per raster point in order to yield the same dose. This may have an impact on both the scan speed and the choice of intensity levels by the control system. Depending on the specific correlation between target and beam motion, resonance effects with large variations of the homogeneity as a function of the initial motion phase could be more or less likely. To improve the understanding of these aspects, further studies in this area are proposed by the author. For several of the studied BDSs with a tendency towards large relative standard deviations a comparably inhomogeneous distribution of particles over the CT phases has been observed, presumably driving the dose homogeneity accordingly. Also, the distribution of the ratio of the delivered particle number and the respective irradiation time—being a measure for the beam intensity—in some cases varied significantly between BDSs. Above that, considerable differences between treatment plans were observed. Furthermore, variations in the accelerator cycle, i.e. the pattern of the beam pauses in relation to the target motion, could have an impact on the correlation between scanning and target motion.

Very similar simulation studies to the presented one were carried out by Steidl (2011) with regard to residual motion in a gating window. The same setup and simulation environment was used. However, Steidl employed simulated BDSs as opposed to measured ones. He reports qualitatively similar results for an increased lateral overlap using a larger beam FWHM. However, a larger reduction of the relative standard deviation of 60–80 % from the smallest to the largest focus was observed. With respect to a smaller IES spacing, Steidl reports a similar behaviour for beam FWHM of 6 and 8 mm and a RiFi3 in the same order of 20–30 % improvement of the homogeneity for the smaller slice spacing. For most other combinations of FWHM and RiFi a similar behaviour was found, in contrast to the findings here. Similar to the results in this work he also observed slightly improved dose homogeneity for the 3 mm lateral raster spacing compared to the 2 mm spacing. Finally, the impact of the RiFi on the target dose homogeneity, as reported here, in most cases is comparable to the results of Steidl with regard to the magnitude of the effect of about 0–10 %. However, for some combinations the effect was observed in the opposite direction. The differences observed between the two simulations can be due to several reasons. The principal structure of the BDS for gating differs significantly from the one of uncompensated delivery. For gating more beam pauses are introduced and irradiation is performed in a part of the motion cycle only. As a result, the impact of the initial motion phase and resonance effects between target and beam motion is likely to be suppressed and variations in dose homogeneity and conformity will be reduced. Finally, the accelerator constitutes a complex system which is challenging to simulate. Resulting BDSs therefore may be subject to additional uncertainties which can have an impact on the simulation results.

Bert et al. (2009) have studied lateral and longitudinal beam overlap in separate experiments using radiographic films. They found a linear dependence of the acceptable motion amplitude on the beam FWHM. For a 10 mm beam spot they report a maximum tolerable motion amplitude of 2 mm at an acceptable level of 5 % deviation from the static dose and a lateral raster spacing of 2 mm. When using an 8 mm beam spot, the accepted amount of motion is reduced to about 0.5 mm. These values can be compared to figure 4.9, assuming an acceptable relative standard deviation of 5 %. This results into acceptable motion amplitudes of 4 and 5.5 mm at a Δz of 3 mm, a Δs of 2 mm, RiFi3 and a beam FWHM of 10 and 8 mm, respectively. Steidl (2011) have stated accepted motion amplitudes of 2.5 and 4 mm for the same parameter combinations, respectively. Hence, in both cases the robustness w.r.t. residual motion is larger compared to the results of Bert et al. However, in general, a direct comparison between absolute dose and film response can not be made (Spielberger et al., 2003) but it can be concluded that the same overall trend is observed in all studies.

It should be emphasized that the results of the 4D simulations presented in this chapter are not directly transferable to patient geometries. The observed large impact of the initial motion phase, as well as possible resonance effects between target motion and beam scanning are likely to be diminished for more irregular target geometries and motion patterns, since relative correlations between the two will not exist over a longer period of time. For this reason, the next chapter will focus on systematic treatment planning studies on patient data.

Apart from the concept of increased beam overlap, other approaches have been published. Furukawa et al. (2007) have proposed to use rescanning in combination with gating to reduce the residual motion interplay effects, PSI plans to use the same approach (Zenklusen et al., 2010). Above that, a combined approach of both techniques seems promising.

5 4D treatment planning studies

5.1 Introduction

In the previous chapter the concept of increased beam overlap to mitigate dose inhomogeneities due to residual motion interplay effects has been studied in a simplified geometry. However, treatment planning studies with patient data are essential to explore the dosimetric effects in a more realistic scenario. The studies will also be indispensable if conclusions shall be drawn for the clinical applicability of the concept. At the time of writing, HIT has already commenced to use scanned carbon ions for the treatment of hepatocellular carcinoma (HCC). Tumors of the liver can be subject to a significant amount of respiratory-induced motion. For instance, Case et al. (2010), have reported an average liver motion amplitude of 8 mm in the superior-inferior (SI) direction, however, with a large range of up to 18.8 mm. Adequate motion management for these tumors is of great importance, especially for treatments using scanned ion beams. Two possible strategies to effectively reduce tumor motion in the liver are abdominal compression (figure 5.1a) and beam gating (section 2.2.3.3). For abdominal compression, Eccles et al. (2011) report an average reduction of the motion amplitude of 2.4 mm in the SI direction. Abdominal compression is in clinical use at HIT since summer 2011. Using beam gating, respiratory-induced motion can effectively be reduced to few millimeters, depending on the gating window (GW) size (Berbeco et al., 2005; Fuji et al., 2009). Several centers have successfully employed gating in combination with passive beam delivery (section 2.1.3.1) for the treatment of lung and liver tumors (Minohara et al., 2000; Lu et al., 2007). The world's first patient treatment with gating and scanned carbon ions was conducted in December 2011 at HIT. Other tumor sites subject to organ motion are planned for treatment in the future. The use of enhanced beam overlap is a promising candidate to complement both abdominal compression and gated beam delivery by further mitigating residual motion effects.

In this chapter the results of a treatment planning study will be presented in which the concept of enhanced lateral and longitudinal beam overlap has been used for realistic patient geometries. For this purpose, the data of the first patients treated under abdominal compression and with beam gating at HIT were used. Based on the results discussed in the last chapter, particular emphasis was put on the analysis of the dosimetric consequences when using an enlarged beam spot size. In addition to these treatment simulations, 4D dosimetric reconstructions of the original patient treatments have been performed for two of the patients. These reconstructions are based on motion monitoring data and beam delivery sequence (BDS) data acquired during treatment delivery and utilize the 4D treatment simulation functionality of TRiP4D, as introduced in chapter 3.

5.2 Materials and methods

5.2.1 Patient cohort

For the treatment planning study eight patients with hepatocellular carcinoma (HCC) were selected. Six of these patients were treated with scanned carbon ions at HIT. For the remaining two patients the treatment was planned but was finally cancelled for medical reasons. One of the patients was irradiated using gated beam delivery. Another four patients were irradiated under abdominal compression and one patient was treated without any motion mitigation technique. Table 5.1 lists the 11 clinical target volumes volumes in the eight patients, including the average CTV motion amplitudes. Tumor motion is most pronounced in the superior-inferior (SI) direction with SI amplitudes ranging between 0.1 mm and 13.3 mm. The tumor motion amplitudes were estimated using deformable image registration. Further details on the analysis and supplementary results are given in section C.1 in the appendix. In the context of the presented study all eight patients were re-planned with TRiP4D.

While patients A1–A4 were planned for treatment under abdominal compression, patients G1–G4 were considered for gated treatment. For patients A2 and G2, 4D dose reconstructions of the original treatments at HIT were carried out based on measured data and the clinical treatment plans.

5.2.2 Treatment planning

In the presented study two different treatment planning procedures were used. Clinical treatment planning was performed with a commercial TPS in preparation of the actual treatment. Also 4D dose reconstructions were carried out based on the clinical treatment plans. The simulation study w.r.t. enhanced beam overlap involved re-planning with TRiP4D for all patients. The agreement of the two planning systems was assessed by comparison of static dose calculations for the clinical treatment plans. Physical and biologically effective dose calculations were in very good agreement of on average $(0 \pm 1)\,\%$. Details are given in section C.2 in the appendix.

5.2.2.1 Clinical treatment planning

For each patient a 4DCT and a free-breathing planning CT scan were acquired. For three of the gating candidate patients (G2–G4) an additional breath-hold CT scan was performed in the end-exhale position. According to the HIT protocol, the ANZAI waist belt motion monitoring system (AZ-773V, ANZAI MEDICAL CO., LTD) was interfaced to the CT scanner to facilitate reconstruction of eight 4DCT phases. For patients G2 and G3 additional 4DCT phases were reconstructed to cover the respiratory cycle around the end-exhale position in 10 % steps of the relative motion amplitude (cf. figure 3.4 on page 42). Figure 5.1b illustrates the distribution of the eight and 14 4DCT phases over the breathing cycle, respectively. All patients were immobilized prior to the CT scans using a vacuum mattress. For patients A1–A4 abdominal compression was applied using a compression plate mounted to a carbon frame (figure 5.1a). The target volumes and organs at risk (OARs) were delineated by a physician, either on the free-breathing CT or the breath-hold CT (patients G2–G4). The clinical treatment plans were created by a medical

	patient	CTV	$V\,[\mathrm{cm}^3]$	mean motion amplitude and SD [mm] $\lvert\mathbf{A}\rvert$	**SI**	**AP**	**LR**
abdominal compression	**A1**	TA1	9.3	9.3 ± 1.1	-9.1 ± 1.1	-2.2 ± 0.3	0.2 ± 0.1
		TA2	62.5	1.8 ± 0.9	-1.8 ± 0.9	-0.3 ± 0.2	0.0 ± 0.1
	A2	TA3	81.1	11.4 ± 3.2	-10.9 ± 3.6	-2.5 ± 1.4	-0.9 ± 0.7
	A3	TA4	39.2	0.9 ± 0.4	0.1 ± 0.5	-0.7 ± 0.2	0.2 ± 0.3
	A4	TA5	118.2	10.1 ± 3.5	-9.4 ± 3.7	-3.2 ± 1.2	-1.2 ± 0.6
gating		TG1	6.8	9.7 ± 0.5	-9.2 ± 0.5	-3.0 ± 0.4	-0.8 ± 0.2
	G1	TG2	65.0	12.5 ± 1.2	-11.6 ± 1.1	-4.5 ± 0.7	-1.5 ± 0.3
		TG3	14.2	15.6 ± 1.6	-13.3 ± 1.1	-7.1 ± 1.2	-4.1 ± 0.5
	G2	TG4	75.5	8.2 ± 2.0	-7.4 ± 1.9	-3.4 ± 0.8	-0.4 ± 0.5
	G3	TG5	46.2	8.9 ± 1.1	-8.6 ± 1.1	-2.1 ± 0.3	0.0 ± 0.4
	G4	TG6	17.7	8.9 ± 1.1	-8.0 ± 1.2	-3.9 ± 0.3	0.0 ± 0.1

Table 5.1.: Volumes and motion amplitudes determined for the 11 CTVs in the eight selected patients. Mean motion amplitudes and standard deviation (SD) are given for the superior-inferior (SI), anterior-posterior (AP) and left-right (LR) direction, respectively. $|A|$ denotes the length of the motion vector. The values were determined from deformable registration of the end-inhale and end-exhale phases of the 4DCT.

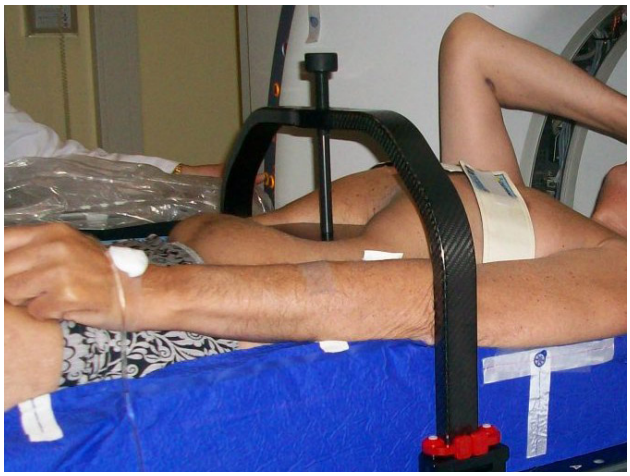

(a)

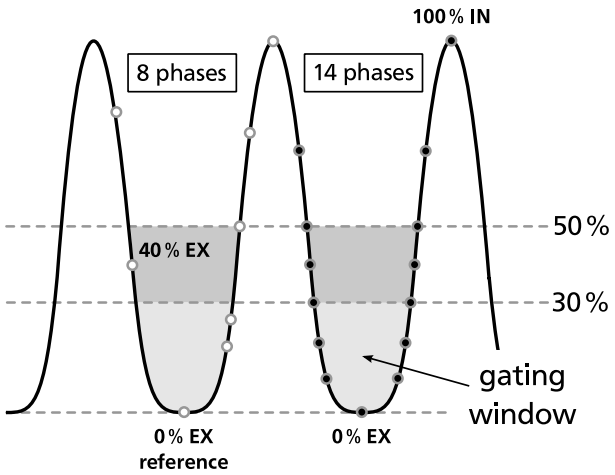

(b)

Figure 5.1.: (a) Patient immobilization for liver treatments under abdominal compression at HIT. Abdominal pressure is applied via a plate mounted to a carbon frame and an adjustable screw. **(b)** Schematic illustration of the 4DCT phase distribution over the breathing cycle for the 4DCT with eight (HIT standard) and 14 phases.

physicist using a commercial TPS. A single left-lateral carbon ion field was employed. For treatment of HCC at HIT a lateral overlap factor (section 4.1) of $f_{\text{lat}} \approx 4$ is routinely applied, using a 10 mm beam spot combined with the standard lateral and longitudinal raster spacings of 2 and 3 mm, respectively. ITV margins were estimated on a patient-specific basis in 3D, using the 4DCT. Planning target volume (PTV) margins of 5 mm in the lateral and 7 mm in the longitudinal direction were added to the ITV. The PTV was planned to receive a biologically effective dose of 32.4 Gy (RBE) in four fractions of 8.1 Gy (RBE). The fractionation scheme is based on a protocol for treatment of HCC at NIRS (Tsujii et al., 2007, 2008).

5.2.2.2 Treatment planning with TRiP4D

For re-planning with TRiP4D, non-rigid registration with the Plastimatch software package (Sharp et al., 2007) was used to match the free-breathing planning CT and the end-exhale phase of the 4DCT. In a second step, non-rigid registration of all 4DCT phases was established, using the end-exhale phase as the reference phase. The contours were propagated to the 4DCT phases using TRiP4D and the resulting deformation maps (section 3.2.1.4).[1] For patients G2 and G3, registration and contour propagation were performed for both 4DCT sets with eight and 14 phases, respectively. ITVs including range changes were optimized with TRiP4D based on the 4D contours of the CTV and the eight phase 4DCT according to section 3.2.2.1. For abdominal compression the ITVs were generated using the full respiratory cycle. For gating, only the CT phases around end-exhale were taken into account, approximately corresponding to a 50 % gating window (GW) (cf. figure 5.1b). For reasons of comparability the ITV optimized for the 50 % GW was also used for the 30 % GW. Since no setup uncertainties were considered in the simulations, no additional PTV margins were added to the ITVs. Dose optimization was performed on the ITV in the reference phase (end-exhale). According to recommendations of the ICRU, 100 % of the ITV volume was required to receive between 95 % and 107 % of the planned dose (ICRU, 1993a). The beam port configuration and the fractionation scheme (8.1 Gy (RBE) per fraction) of the clinical liver treatments at HIT were adopted for all patients. At HIT the LEM-I model (section 2.1.2) and corresponding RBE tables are used in combination with a commercial treatment planning system. The respective RBE tables were adopted for dose calculation in TRiP4D. Depth-dose tables and any other required beam base data (Krämer et al., 2000) were employed in accordance with the data used clinically at HIT.

12 different treatment plans per patient were optimized using various combinations of lateral raster spacing (2 and 3 mm), iso-energy slice spacing (2 and 3 mm water-equivalent) and beam spot FWHM (6, 8, 10 and 15 mm).[2] The combinations of beam FWHM and lateral raster spacing resulted in lateral overlap factors (section 4.1) of $3 \lesssim f_{\text{lat}} \lesssim 7.5$. A lateral overlap factor of $f_{\text{lat}} \approx 3$ is typically used for stationary targets at HIT. A RiFi optimized for 3 mm IES spacing was considered for all treatment plans. Other RiFis could not be used because the required particle spectra data needed for biological dose calculation with TRiP4D were not available.

[1] Deformable registration and contour propagation was kindly provided by N. Saito.

[2] Note, that the precise values for the beam FWHM depend on the requested beam energy and by trend are larger for smaller energies, i.e. shorter penetration depths.

5.2.3 4D treatment reconstructions

4D treatment reconstructions were carried out for patients A2 (abdominal compression) and G2 (gating). Motion monitoring data were acquired with the ANZAI waist belt motion monitoring system during treatment delivery. For patient G2 the ANZAI system was also employed to define the gating window and communicate the beam requests to the TCS. The gating window was adjusted asymmetrically around the end-exhale position, covering 30 % of the amplitude range in exhale and 70 % in inhale, respectively. Raster point irradiation times were recorded via the treatment records routinely provided from the TCS. The beam status was logged using the ANZAI system. Data analysis revealed unexpected timing inaccuracies of the ANZAI system, increasing proportionally with the acquisition time. For the patient treatments temporal discrepancies of up to 500 ms were observed. For this reason, the ANZAI beam status data could not be used to generate the required BDS input data for TRiP4D (section 3.2.3.2). Instead, manual temporal correlation between the TCS treatment records and the ANZAI motion data had to be performed. For patient A2 the global time offset between the two systems was extracted from a synchronous read-out of the respective system clocks after irradiation. For patient G2 the system time stamps marking the end of the first beam gate were used for temporal correlation. The beam delivery sequence (BDS) input data for TRiP4D were generated based on the TCS treatment records only. The missing beam status data was incorporated as follows: To a good approximation beam-off signals could be assumed to coincide with the completion of the last raster point in each beam gate. Beam-on signals were established by using a fixed irradiation time of the first raster point in each beam gate. A constant irradiation time of 15 ms was estimated from the treatment records.

The treatment reconstructions were performed based on the BDS data, the clinical treatment plans, the patient's 4DCT and related deformation maps, as well as the motion monitoring data recorded during treatment (section 3.2.3). The target point for the clinical treatment plan was mapped from the free-breathing planning CT to the 4DCT reference phase, using the transformation maps resulting from deformable registration. Motion state identification was based on the relative amplitude of the ANZAI motion trace and was performed in correspondence with the 4DCT data acquisition (see section 3.2.3.1), thus, taking into account the irregular respiration of the patient. 4D dose calculations were based on eight 4DCT phases for patient A2 and on 14 phases for patient G2.[3] To assess the robustness of the delivered 4D dose and to incorporate the uncertainties of the ANZAI system timing and the temporal alignment procedure, two additional reconstructions were performed for each fraction, considering temporal displacements Δt of -250 ms and $+250$ ms between the motion trajectory and the BDS. For patient A2 all four fractions were reconstructed. As a possible treatment outcome, a total dose distribution has exemplarily been calculated for patient A2 by direct summation of the nominal constituent dose distributions ($\Delta t = 0$ ms). For technical reasons, only three fractions could be reconstructed for patient G2. Therefore, no total dose distribution could be calculated.

[3] For all calculations TRiP4D's APDB pencil beam algorithm was used. The algorithm includes geometrical beam divergence effects and neglects multiple scattering effects.

5.2.4 4D treatment simulations

4D treatment simulations were performed for all patients based on the optimized treatment plans for varying lateral and longitudinal beam overlap, the 4DCT data and the related deformation maps. Since the major purpose of this study was to assess the effect of optimized beam parameters on the 4D dose distribution, variations in the patient breathing patterns were not considered. Regular patient motion according to Lujan et al. (1999) was assumed. Two representative breathing periods of 3.6 and 5.4 seconds were used. The fractional numbers were chosen for technical reasons. Additionally, a spectrum of initial motion phases was considered. For patients A1–A4 (abdominal compression) six equally distributed initial phases (60° steps) were chosen. For gated treatment, two gating windows covering 30 % and 50 % of the relative amplitude range around the end-exhale position were defined, as illustrated in figure 5.1b. Due to the synchronization of BDSs for gating at HIT after few beam gates, the initial motion phase is expected to have less impact on the 4D dose distribution. Therefore, six initial phases were simulated for patient G2 only. For the remaining three patients two initial phases were selected (center and start of the GW). Simulations were based on the standard 4DCT with eight phases for all patients. Additional simulations for the same treatment plans and a 4DCT with 14 phases were performed for patients G2 and G3. BDS data were generated using a dedicated software developed within the scope of this work. Assuming a rectangular beam extraction profile, the program is able to generate BDS data for a gated or ungated treatment course. The simulation is based on the treatment plan, the motion trajectory and realistic HIT accelerator timing including an appropriate choice of intensity levels (Naumann, 2011). 4D treatment simulations were performed according to section 3.2.3. Motion state identification was carried out based on the relative motion amplitude (section 3.2.3.1).

5.2.5 Data analysis

Dose parameters

For both treatment reconstructions and simulations the dose delivered to the CTV was assessed for each dose distribution by calculating dose volume histograms (DVHs) and the volumes receiving 95 % (V_{95}) and 107 % (V_{107}) of the prescribed dose. Additionally, the dose homogeneity index (HI), as defined in equation (4.5), was used to evaluate the dose homogeneity. The dose conformity to the CTV was analyzed using the conformation number (CN), as introduced in equation (4.6). Mean and standard deviation of V_{95}, V_{107}, HI and CN over all initial motion phases and motion periods were analyzed as a function of the beam FWHM and the various raster spacing combinations. The correlation of V_{95} and HI with the CTV motion amplitude was investigated using the Pearson correlation coefficient (PCC), r. The exposure to lung and liver was assessed for all patients by calculation of DVHs and of the maximum and the mean dose deposited in the respective organ.

Statistical analysis

In the context of the beam overlap parameter study a statistical analysis of the dose homogeneity as a function of the beam and tumor motion parameters was performed using univariate and multivariate linear regression. The investigated influencing variables were the beam FWHM, the median CTV motion amplitude components A_{xx} in left-right (xx=LR), anterior-posterior (AP),

and superior-inferior (SI), the median length of the CTV motion vector, $|A|$, the longitudinal and the lateral raster spacings, Δz and Δs, and the CTV volume, V. The analysis was performed separately for abdominal compression and each of the two gating windows. Due to the non-normal distribution of V_{95} and V_{107}, the variables were tested against HI only. All variables were screened in univariate regression, and if found significant at the $p < 0.05$ level were also entered in a multivariate regression model:

$$\mathrm{HI}(v_1, \ldots, v_N) \approx \sum_{i}^{N} \alpha_i \cdot v_i + \sum_{ij}^{i \neq j} \beta_{ij}\, v_i \cdot v_j + \gamma \quad . \tag{5.1}$$

That is, a multilinear superposition of the influencing variables v_i was used in combination with non-linear cross terms (coefficients β_{ij}). γ denotes a constant term. The multivariate model was identified through step-wise regression. The results of this multivariate regression are reported as the coefficient of variation R^2. To judge the contributions of the single variables to the overall regression, a series of regression models were computed, starting with the strongest single contributor and subsequently entering more variables until the complete model as resulting from the step-wise regression was reached. Finally, also the cross-terms of all entered variables were considered ($\beta_{ij} \neq 0$). All analyses were carried out using JMP (version 9.0.3, SAS Institute Inc., Cary, NC, USA).

5.3 Results

5.3.1 4D treatment reconstructions

A total of 12 dose reconstructions were performed for patient A2 and the four treatment fractions. Additionally, the static dose and an exemplary total dose distribution were calculated (direct sum). Resulting dose distributions and DVH bands are given in figure 5.2. Dose cross sections through the CTV are shown for the static dose, total dose and a selected fractional dose distribution in the CT reference phase. The displayed slice and fractional dose were chosen as a worst case example of the obtained dose distributions. The DVH for the total dose is drawn on top of the DVH bands (red dash-dotted line). The total dose exhibits improved target coverage (V_{95}) and overdose (V_{107}) compared to the majority of single fraction dose distributions, visible in the steeper DVH. Table 5.2 lists the resulting dose parameters of all 12 simulated treatments. While the mean dose to the CTV is stable ($\approx \pm 1\,\%$), V_{95} and V_{107} show larger variability between 76–97 % and 2–27 %, respectively. Within the same fraction, differences of up to $\approx$10 % for the V_{95} and of up to 20 % for the V_{107} occur for different temporal shifts. The analysis of the dose to normal tissue showed that the mean lung dose increased by about 25 % w.r.t. to the static dose distribution (see also the blue band in figure 5.2d). 4D dose delivery had no impact on the mean liver dose. Details on the values for individual fractions are given in table C.3 in the appendix. For both lung and liver the maximum dose to the respective organ in a single fraction increased by about 1–2 Gy (RBE), compared to the static case. The average exposure of liver and lung for the exemplary full treatment increased by about 3 and 0.5 Gy (RBE), respectively.

A worst case dose distribution (lowest V_{95}) and the DVH bands, based on the nine single fraction dose distributions for patient G2, are shown in figure 5.3. The detailed results for the analyzed dose parameters for each fraction are listed in table 5.3. The original treatment has

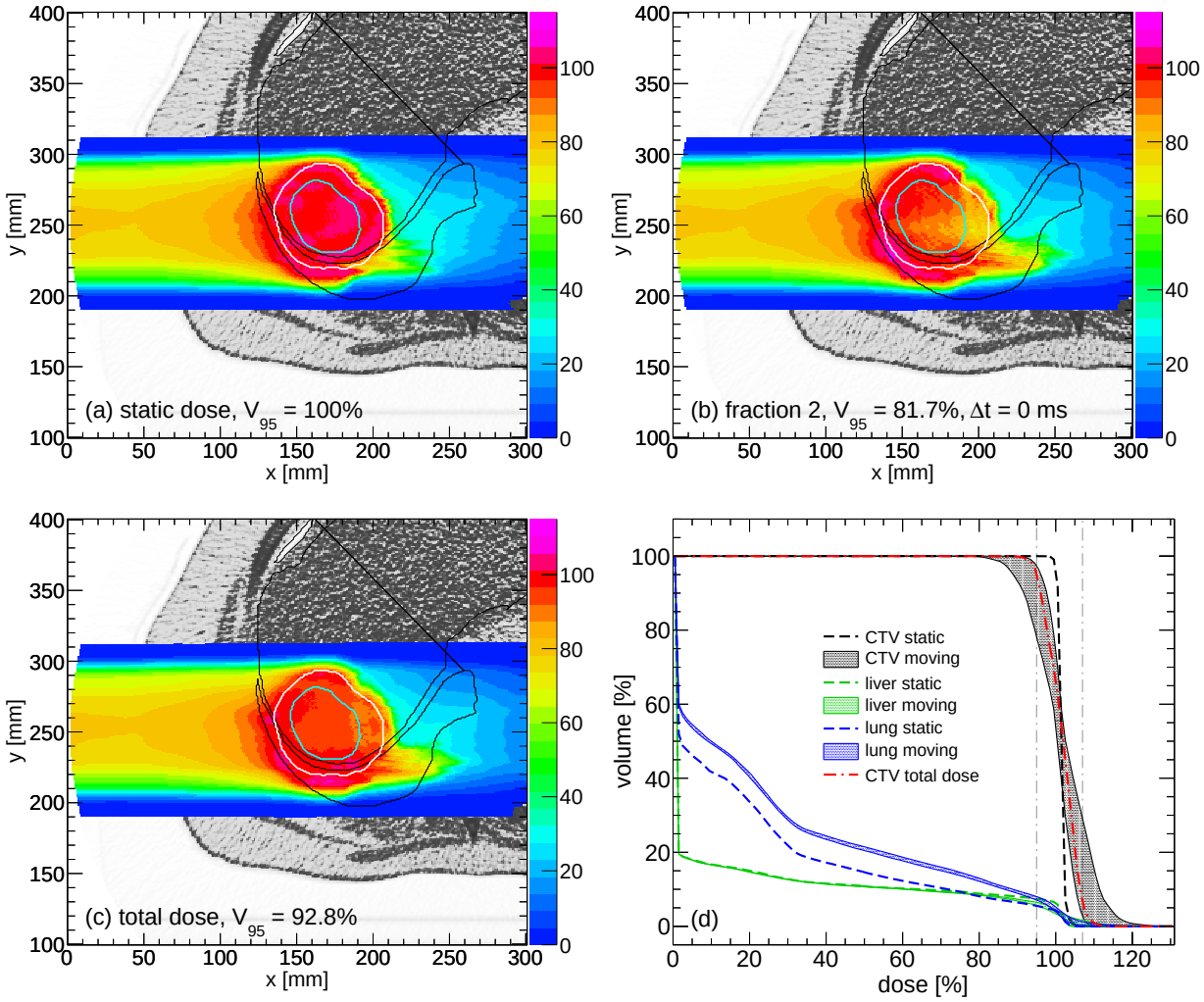

Figure 5.2.: Results of dose reconstructions for patient A2. Axial cross sections of the static dose **(a)**, a single fraction dose **(b)**, and the exemplary total dose distribution **(c)** are shown. Contours are overlayed for the PTV (white), the CTV (cyan) as well as lung and liver (black). The DVH bands encompass all 12 single dose distributions.

dose distr.	Δt [ms]	dose in % prescribed dose				volume in %		
		mean ± SD	HI	min	max	V_{95}	V_{107}	CN
static	—	101.0 ± 0.8	2.8	94.7	106.0	100.0	0.0	0.30
fraction 1	−250	101.0 ± 4.6	15.2	83.5	117.7	90.9	8.5	0.28
	+0	101.2 ± 6.8	22.2	80.4	121.0	80.4	21.3	0.24
	+250	101.3 ± 7.7	24.5	76.1	123.9	76.8	27.0	0.22
fraction 2	−250	101.4 ± 7.5	24.3	74.7	127.9	78.1	23.7	0.22
	+0	101.1 ± 6.6	22.0	75.9	123.0	81.7	18.0	0.24
	+250	100.2 ± 4.2	13.8	83.1	120.5	88.0	5.0	0.27
fraction 3	−250	101.2 ± 7.4	22.8	79.6	128.0	76.1	23.3	0.22
	+0	100.3 ± 6.5	21.3	81.6	120.9	77.8	16.0	0.22
	+250	99.7 ± 3.9	12.8	81.7	112.8	87.6	1.6	0.27
fraction 4	−250	102.0 ± 4.7	15.2	83.8	119.1	95.8	16.1	0.31
	+0	101.7 ± 4.3	14.4	82.4	116.5	93.8	10.3	0.30
	+250	101.6 ± 3.6	12.1	83.6	119.0	96.5	6.4	0.31
total	—	101.1 ± 3.9	12.4	88.3	114.1	92.8	4.6	0.29

Table 5.2.: Results of the treatment reconstructions for patient A2. Three dose distributions for varying time offsets , Δt, between BDS and motion monitoring data were calculated. The total dose was calculated by direct summation of the distributions for $\Delta t = 0$ ms.

dose distr.	Δt [ms]	dose in % prescribed dose				volume in %		
		mean ± SD	HI	min	max	V_{95}	V_{107}	CN
static	—	100.2 ± 1.2	3.9	95.4	104.4	100.0	0.0	0.19
fraction 2	−250	100.1 ± 4.3	14.2	84.8	113.7	88.2	5.9	0.17
	+0	99.7 ± 4.8	15.9	82.9	114.4	83.4	6.9	0.15
	+250	100.1 ± 3.9	12.9	84.8	113.5	91.5	4.8	0.18
fraction 3	−250	100.8 ± 4.3	14.4	86.8	117.6	92.6	8.6	0.17
	+0	100.7 ± 4.0	13.1	87.9	114.2	94.0	7.1	0.17
	+250	100.5 ± 3.1	10.4	88.7	113.6	97.0	2.9	0.18
fraction 4	−250	100.9 ± 2.5	8.4	89.3	111.0	98.8	0.9	0.18
	+0	100.5 ± 2.7	8.9	89.2	111.9	97.2	0.5	0.18
	+250	100.5 ± 4.0	13.3	87.8	121.5	92.9	5.7	0.18

Table 5.3.: Results of the treatment reconstructions for patient G2. Three dose distributions for varying time offsets , Δt, between BDS and motion monitoring data were calculated. For technical reasons, the data of the missing first fraction could not be analyzed.

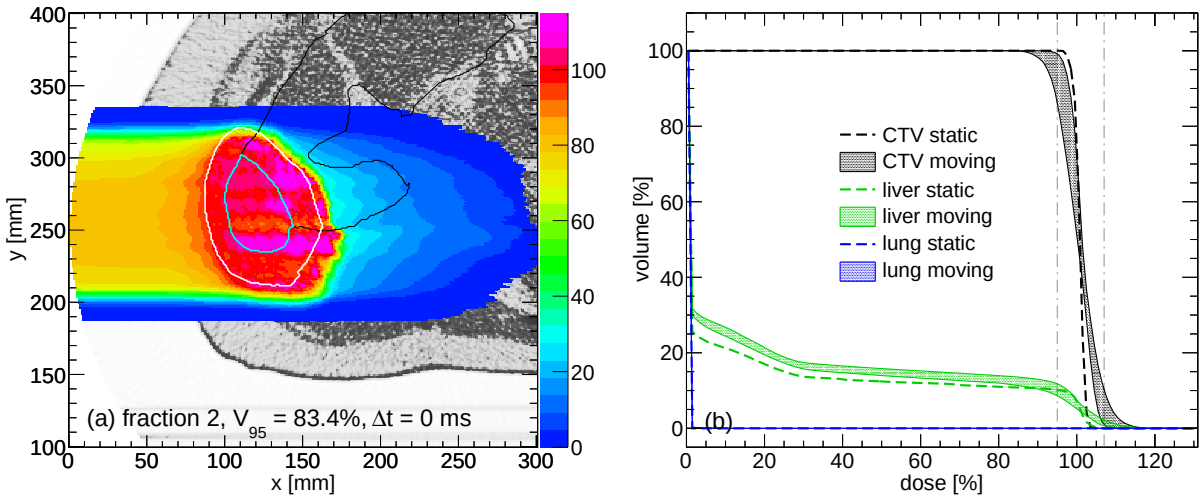

Figure 5.3.: Results of dose reconstructions for patient G2. **(a)** Axial cross section of the worst case single fraction dose distribution. Contours are overlayed for the PTV (white), the CTV (cyan) and the liver (black). **(b)** DVH bands encompass all nine calculated single dose distributions.

been performed with a gating window ranging from 30 % of the relative amplitude in exhale to 70 % in inhale. V_{95} values are above 90 % for all but two dose distributions and V_{107} values remain below 10 %. The mean lung dose remains small and comparable to the static case (+0.2 to +0.3 Gy (RBE)). A small increase < 0.8 Gy (RBE) in the maximum liver dose is also observed. The mean liver dose exhibits a slight increase by about 0.2 Gy (RBE). This is also indicated in figure 5.3b (green band). Compared to the static simulation, the maximum liver dose is on average about 1 Gy (RBE) smaller. Detailed results on the normal tissue exposure are given in table C.4 in the appendix.

5.3.2 4D treatment simulations

5.3.2.1 Dose coverage and homogeneity

Impact of beam parameters on the dose coverage

The CTV dose coverage was assessed using the V_{95} of the simulated dose distributions. In figures 5.4 and 5.5 the V_{95} is shown as a function of the beam spot FWHM for abdominal compression and gating, respectively. The data for different lateral raster and IES spacings are visualized with different colors and markers. The markers represent the mean and standard deviation of V_{95}, resulting from the various initial motion phases and periods. For clarity, markers for different raster spacing combinations are drawn with a horizontal offset to each other (0.2 mm). For the gated cases the colored markers represent mean and standard deviation of V_{95} for simulations with a 50 % GW. Data for the 30 % GW are drawn as black triangles with a second smaller horizontal offset (0.08 mm). With respect to the 50 % GW, an approximately linear increase in the average V_{95} with the beam FWHM is found for all CTVs and both mitigation techniques. The overall trend is indicated by the gray dash-dotted lines which have been determined by linear fits to the data. The increase in V_{95} on average amounts to about 6–10 %

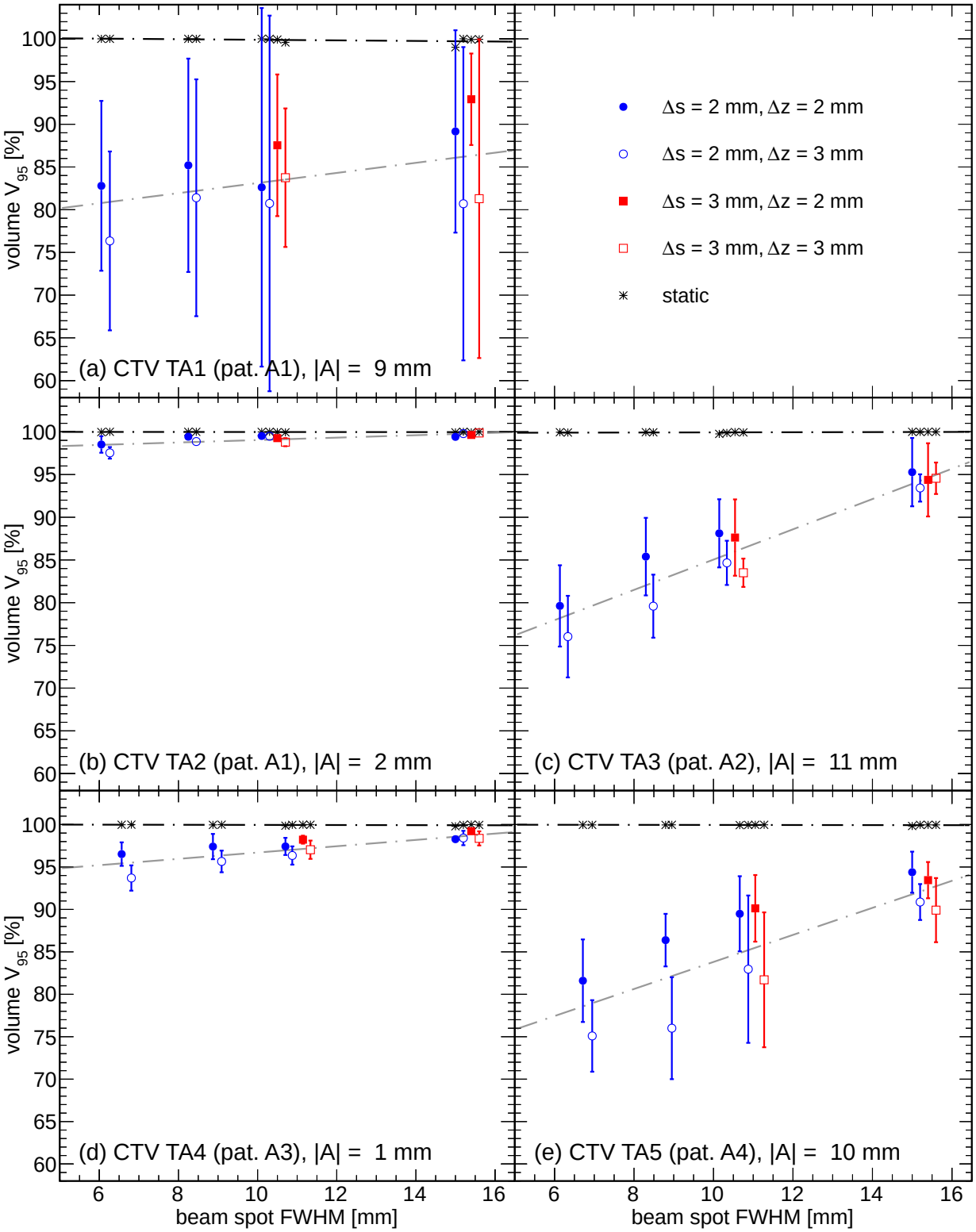

Figure 5.4.: V_{95} as a function of the beam spot FWHM for the five CTVs in patients A1–A4 with abdominal compression. $|A|$ denotes the motion amplitude for each CTV volume. The dash-dotted lines are linear fits to the data.

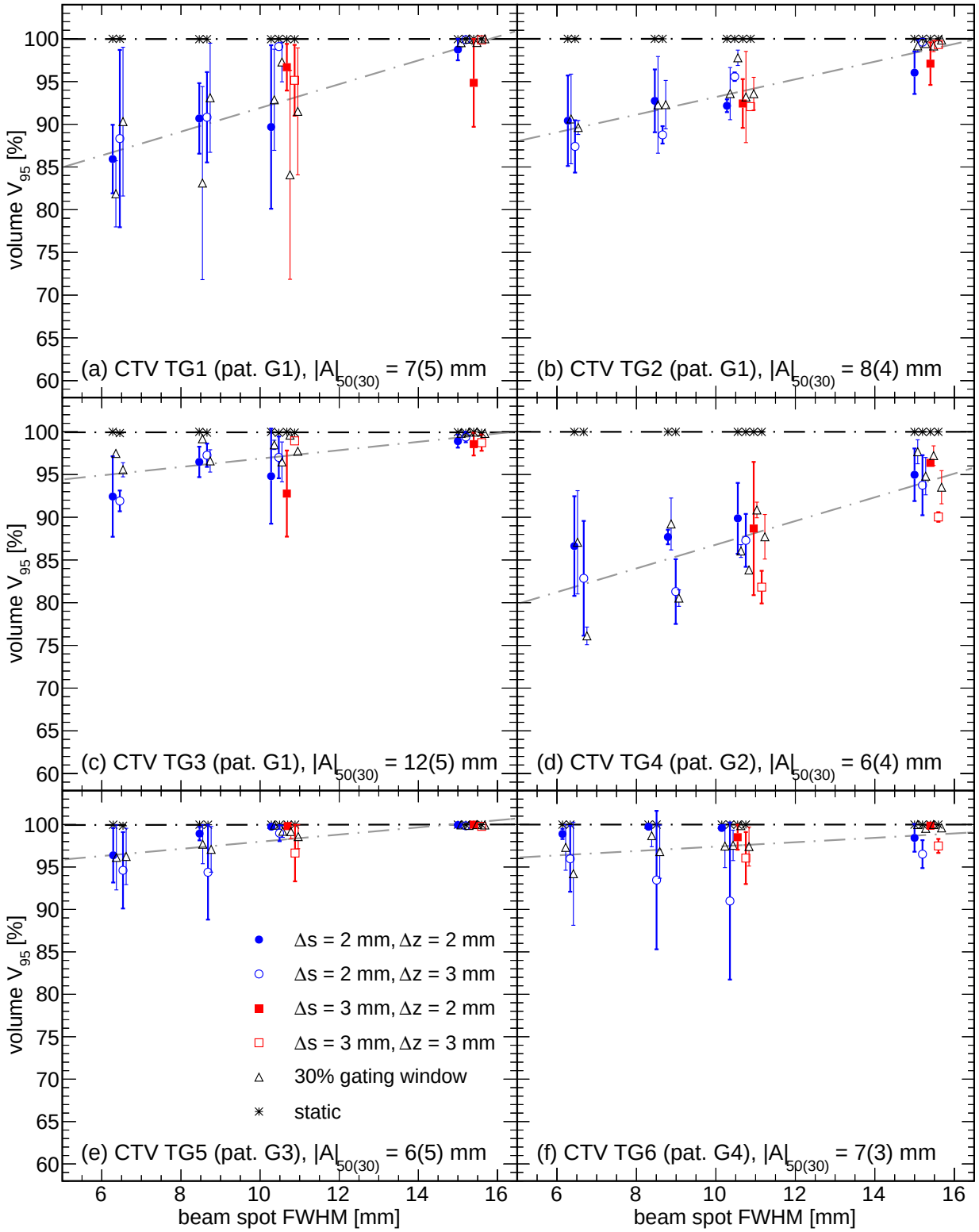

Figure 5.5.: V_{95} as a function of the beam spot FWHM for the six CTVs in patients G1–G4 with gating. $|A|_{50(30)}$ denotes the motion amplitude in the 50 % and the 30 % GW, respectively.

per millimeter beam FWHM, relative to the initial difference in V_{95} w.r.t. the static case at a 6 mm beam spot.

Four out of five CTVs with abdominal compression exhibit mean V_{95} values larger than 90 % for all raster spacing combinations and a beam FWHM of 15 mm. At the same beam spot size five out of six gated CTVs have average V_{95} values larger than 95 %. Two of them reach values comparable to the static level (TG3 and TG5) at all raster spacing combinations. For abdominal compression CTVs TA2 and TA4 (figures 5.4b,d) show similarly large values at the largest beam spot size. The two volumes, however, have only very small tumor motion amplitudes (<2 mm). For the gated CTVs a direct relation between the motion amplitude and the magnitude of V_{95} is not observed. Considering, for instance, the volumes TG3 and TG4, it can be seen that TG3 has a 6 mm larger tumor motion amplitude at a 50 % GW, but V_{95} values are consistently smaller than for TG4 (see figures 5.5c,d). For abdominal compression similar motion amplitudes on average seem to yield comparable V_{95} values, as can be seen in figures 5.4a,c,e. On the basis of figure 5.5 no systematic differences in the mean V_{95} are observed between the two gating windows. Only for CTV TG3 consistently larger V_{95} values are obtained for the 30 % GW (figure 5.5c). In few cases significant differences in V_{95} are observed between the two IES spacings of 2 and 3 mm, in particular for TA5 and TG4, where data points are separated by more than one standard deviation at a FWHM of 8 mm. Based on the presented data no difference in the V_{95} for different lateral raster spacings is found.

V_{107} values have also been studied and show a linear decrease with the beam spot FWHM. The average decrease in V_{107} amounts to about 8–12 % per millimeter beam FWHM, relative to the initial difference to the static V_{107} at 6 mm FWHM. At a FWHM of 15 mm, mean V_{107} values are below 5 % for all gated CTVs and four out of five CTVs with abdominal compression. Significant differences (separation of more than one standard deviation) in V_{107} for different IES spacings are observed in one case (TA5). For the lateral raster spacing no effect is observed. For one gated case (TG3) systematically lower values of the mean V_{107} and small standard deviations were found for the 30 % GW compared to the 50 % GW. Detailed results are given in figures C.3 and C.4 in the appendix.

Impact of beam parameters on the dose homogeneity

Figure 5.6 displays axial cross sections of examplary dose distributions for a fixed lateral and longitudinal raster spacing and beam spots of 6 and 15 mm FWHM. On the right hand side the corresponding DVH bands are depicted. The bands encompass all single DVHs for the varying initial motion phases and the two motion periods. Dose distributions were calculated for patient A2 with abdominal compression. DVH bands for the CTV at the 15 mm beam spot are narrower in shape, i.e. less variability is observed among the respective dose distributions. Furthermore, they feature an increased steepness, indicating improved dose homogeneity compared to the 6 mm beam spot. The thresholds of 95 % and 107 % of the prescribed dose, as recommended by the ICRU, are drawn as dash-dotted lines for comparison. The illustrated effect was also observed at FWHM of 8 and 10 mm and showed a gradual increase with the beam spot size.

In figures 5.7 and 5.8 the dose homogeneity index (HI) is shown as a function of the beam FWHM for abdominal compression and gating, respectively. The data presentation is identical to figures 5.4 and 5.5. For all CTVs a linear decrease of the HI with the beam FWHM is observed which is equivalent to an increase of the dose homogeneity. The gray dash-dotted lines have been fitted to the data to indicate the trend. On average the homogeneity index decreases by

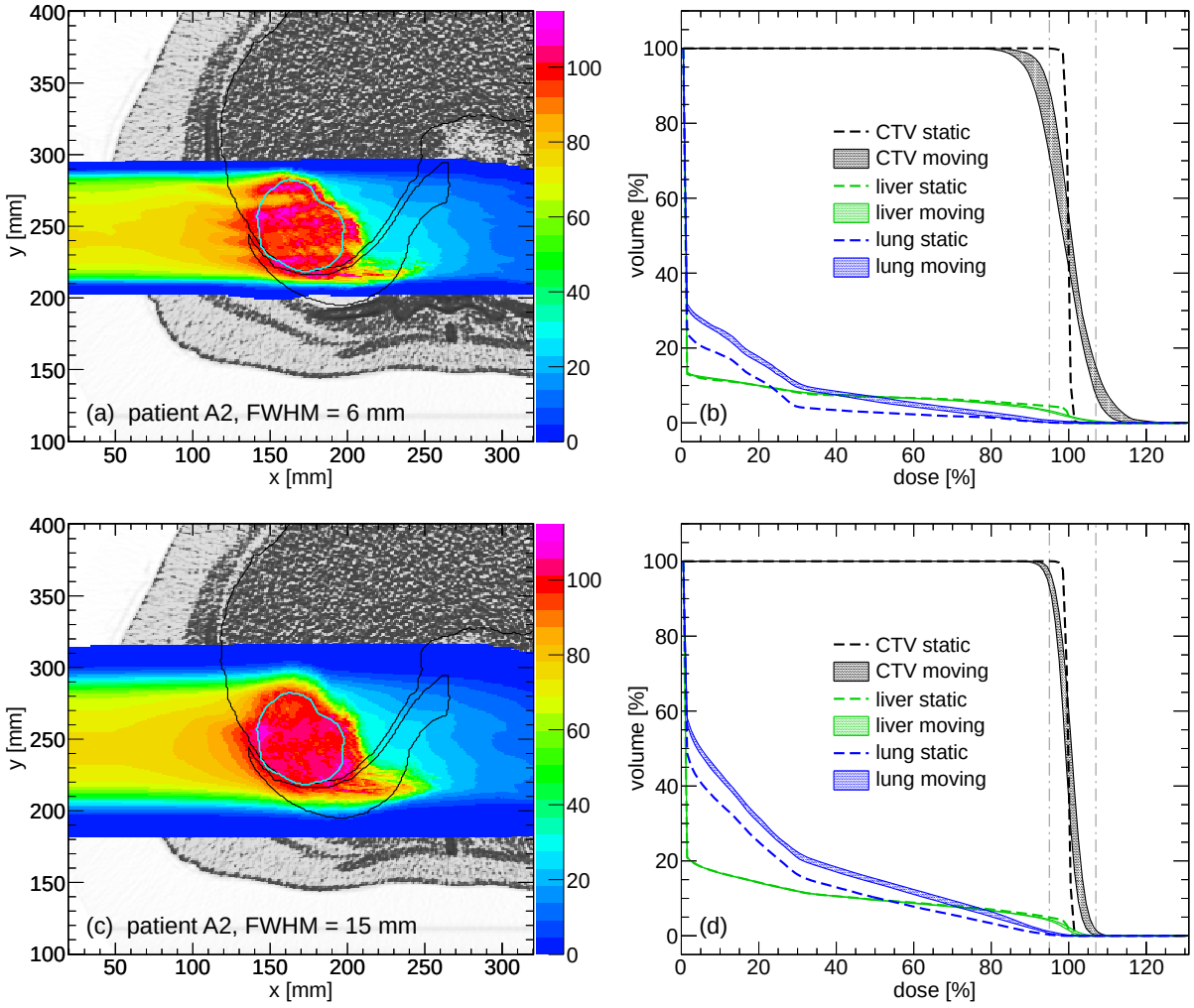

Figure 5.6.: Axial dose cuts through the CTV and DVH bands for varying beam FWHM at a fixed lateral ($\Delta s = 2\,\text{mm}$) and longitudinal ($\Delta z = 3\,\text{mm}$) raster spacing (dose in percent of the prescribed dose). DVH bands are the envelope to all single DVHs.

about 5–7 % per millimeter beam FWHM, relative to the initial difference to the static case at a 6 mm beam spot. Standard deviations also decrease for increasing beam spot size. Data points for CTV TG3 show systematically smaller mean HI values for the 30 % than for the 50 % GW (separation larger than one standard deviation). For all other CTVs no systematic difference between the two gating windows is observed. From figure 5.7 it can be seen that for most of the CTVs there is a general trend of the larger 3 mm IES spacing (open markers) towards larger HI values, compared to the 2 mm spacing (see e.g. figures 5.7a,e). Differences are on the order of 10–30 %. The effect is particularly pronounced for CTV TA5 (≈50 %). For the gated CTV TG4 differences of ≈20 % in the mean HI are found between the two IES spacings. However, error bars overlap in most cases, so a clear advantage of a smaller IES spacing can not be ascertained. From figures 5.7 and 5.8 no difference in the HI is observed w.r.t. the lateral raster spacing.

Impact of the CTV motion amplitude

In figure 5.9 the dependence of the HI on the CTV motion amplitude in the superior-inferior (SI) and the anterior-posterior (AP) direction is shown for a fixed combination of beam param-

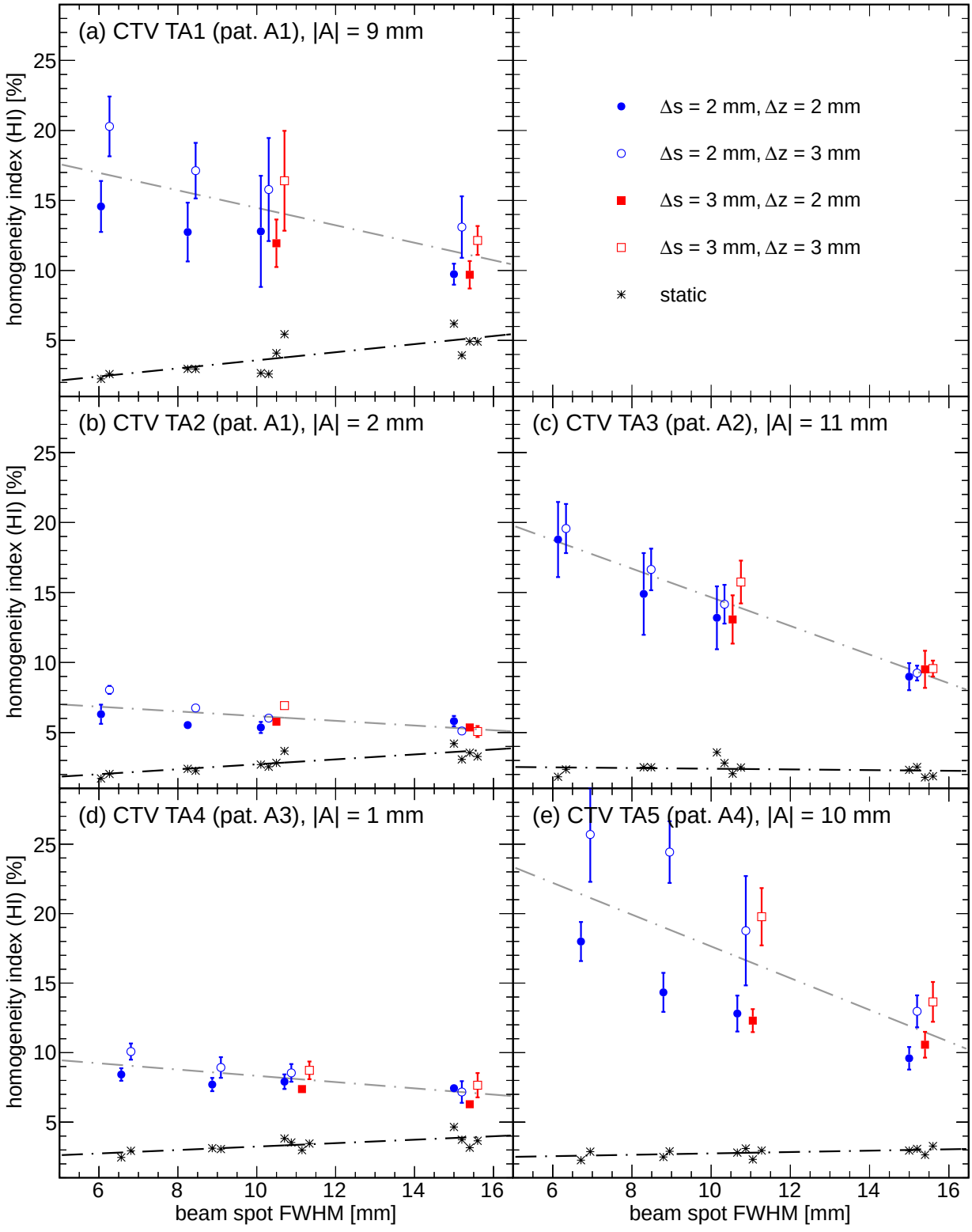

Figure 5.7.: Homogeneity index as a function of the beam spot FWHM for the five CTVs in patients A1–A4 with abdominal compression. $|A|$ denotes the motion amplitude for each CTV volume. For clarity, data points are shifted against each other in the abscissa.

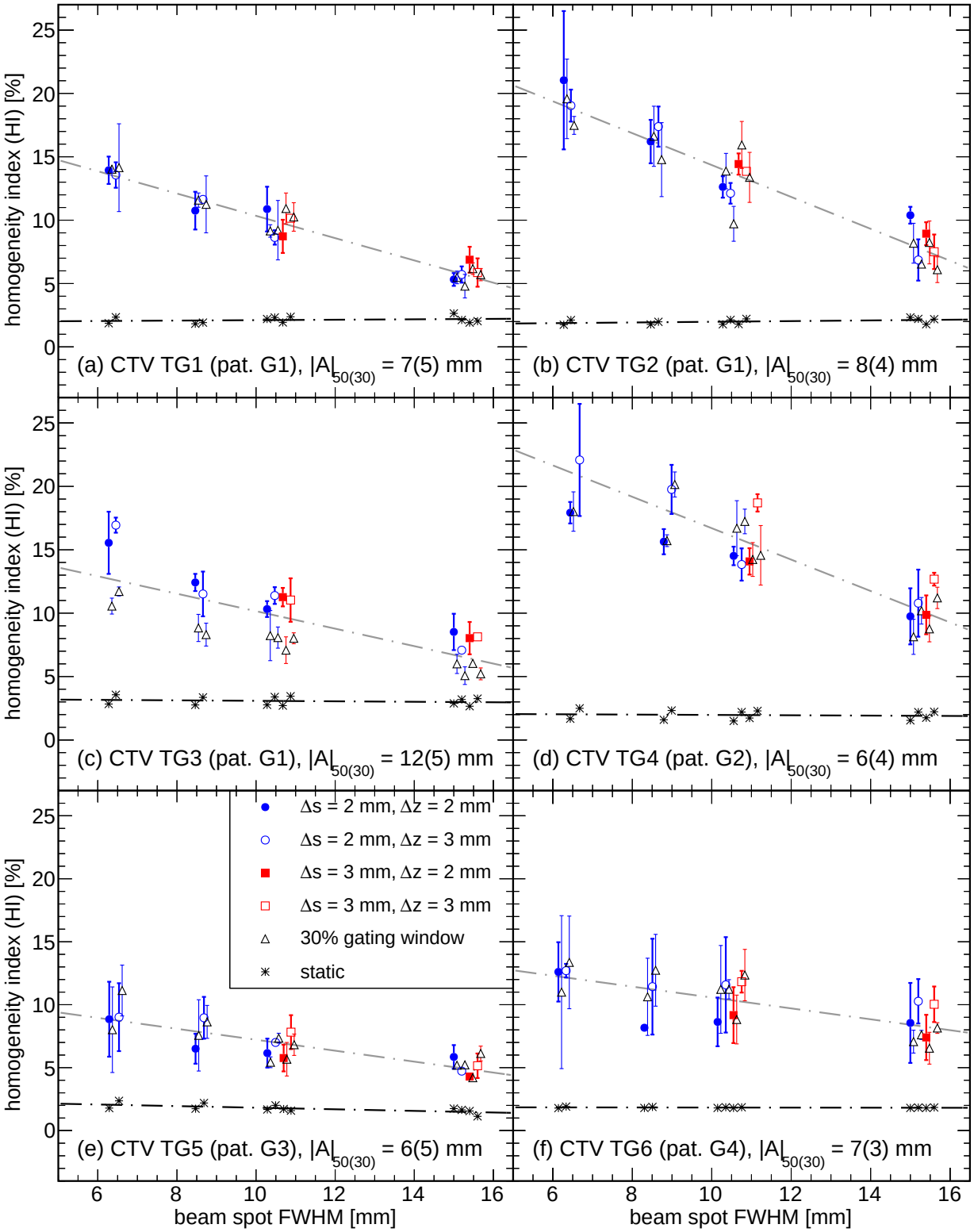

Figure 5.8.: Homogeneity index as a function of the beam spot FWHM for the six CTVs in patients G1–G4 with gating. $|A|_{50(30)}$ denote the motion amplitude in the 50 % and 30 % GW, respectively.

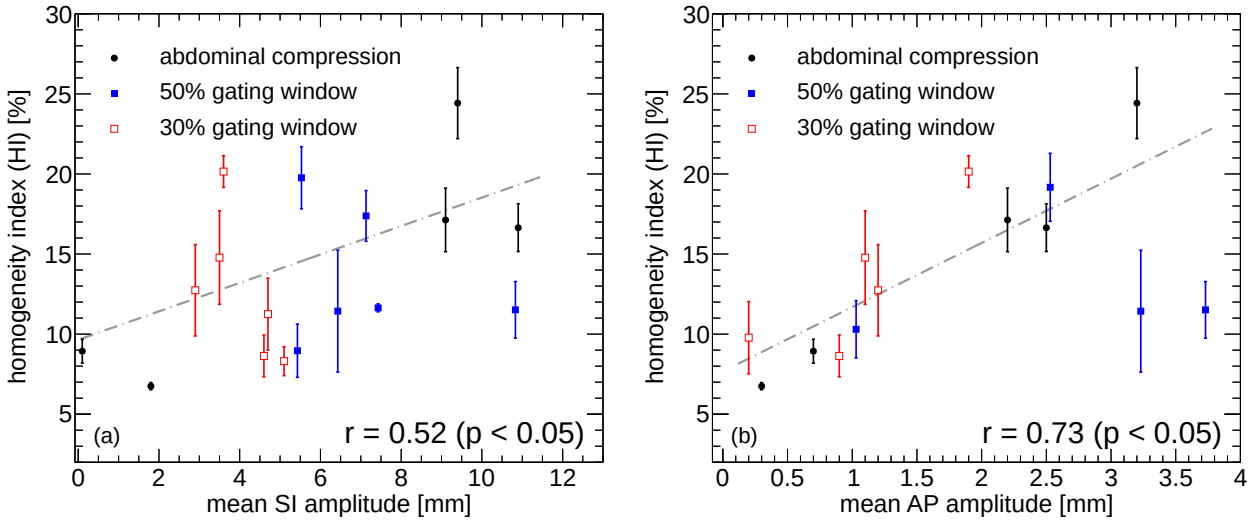

Figure 5.9.: Homogeneity index as a function of the motion amplitudes in **(a)** superior-inferior (SI) and **(b)** anterior-posterior (AP) direction for $\Delta z = 2\,\text{mm}$, $\Delta z = 3\,\text{mm}$ and a beam FWHM of 8 mm. Markers and error bars represent mean and standard deviation of the HI and r denotes the Pearson correlation coefficient (PCC).

eters. The gray dash-dotted line has been determined by a linear fit to the data. An average increase of the HI with the motion amplitude is observed. The HI exhibits a stronger correlation with the mean AP motion amplitude than with the SI component, although AP motion amplitudes are significantly smaller (<4 mm). The Pearson correlation coefficients (PCCs), r, calculated in both cases are given in the figures for comparison. Similar correlation has consistently been found for all studied beam parameter combinations. The average r and standard deviations for the SI and AP motion components were 0.50 ± 0.06 and 0.68 ± 0.06, respectively. Hence, the overall correlation found between the HI and the motion amplitude is low and about 0.18 larger for the AP motion component.

The same analysis was also performed with regard to the V_{95}, showing an average decrease with the motion amplitude. A low level of overall correlation and no significant differences w.r.t. the two motion components were found. The average r and standard deviations were -0.46 ± 0.08 and -0.45 ± 0.09 for the SI and AP directions, respectively. The detailed results for all beam parameter combinations are given in table C.5 in the appendix. CTV motion amplitudes for abdominal compression and in the two gating windows were determined from the 4DCT using deformable registration. Details on the method and the results are given in section C.1 in the appendix.

Statistical analysis

Of the investigated variables, the amplitude components, the amplitude vector length $|A|$, the beam FWHM, the CTV volume V, and Δz showed a significant contribution to HI (all $p<0.01$). Only for the 50 % gating window, $|A|$ was not significant. The volume V showed a high correlation to the motion variables and was thus excluded from the model to avoid statistical artifacts. In step-wise regression, the A_{AP} component, the beam FWHM and Δz were identified as mutually independent contributors to HI and remained highly significant also in the multivariate model. All multivariate models showed considerably increased explained variance R^2 in comparison to the strongest univariate predictor (A_{AP} for abdominal compression, the beam FWHM

model	variables/terms	R^2 ($p < 0.05$)		
		abdominal compr.	**50 % GW**	**30 % GW**
1	$\|A\|$	0.49	n.s.	0.04
2	A_{AP}	0.54	0.08	0.27
3	FWHM	0.16	0.33	0.35
4	Δz	0.06	0.02	0.01
5	$A_{\mathrm{AP}} + \mathrm{FWHM}$	0.7	0.41	0.64
6	$A_{\mathrm{AP}} + \mathrm{FWHM} + \Delta z$	0.76	0.42	0.65
7	$A_{\mathrm{AP}} + \mathrm{FWHM} + \Delta z$ $+A_{\mathrm{AP}} \times \mathrm{FWHM}$	0.83	cross terms n.s.	0.69
8	$A_{\mathrm{AP}} + \mathrm{FWHM} + \Delta z$ $+A_{\mathrm{AP}} \times \mathrm{FWHM}$ $+\Delta z \times \mathrm{FWHM}$ $+\Delta z \times A_{\mathrm{AP}}$	0.86	cross terms n.s.	0.71

Table 5.4.: Results of the uni- and multivariate analysis of the HI for abdominal compression and the two gating windows. The coefficient of variation, R^2, is tabulated for the univariate (1–4) and the multivariate models (5–8). $p < 0.05$ was considered statistically significant. $|A|$ and A_{AP} denote the length of the motion vector and the AP motion component, respectively.

for both gating models). The addition of cross-terms in the model resulted in further strong increases in R^2 for abdominal compression and the 30 % GW, but not for the 50 % GW. The final models explained 86, 42 and 71 % of the observed variance for abdominal compression, the 50 % and the 30 % GW, respectively, see table 5.4.

Impact of the 4DCT phase sampling

In figure 5.8 the expected advantage of a 30 % over the 50 % GW regarding dose homogeneity was observed only for CTV TG3 (figure 5.8c), which exhibited the largest difference in the estimated motion amplitudes between the two gating windows of about 8 mm. Likewise, the results for the V_{95} and V_{107} have shown no significant benefit of the 30 % GW for most patients. The impact of the 4DCT sampling on the dose distributions was studied for two patients by re-iteration of the dose calculations using 14 instead of eight CT phases. The former provided a more adequate coverage of the GW in 10 % steps of the relative amplitude. Figure 5.1b illustrates the distribution of CT phases in both cases. In figure 5.10 resulting DVH cohorts for patient G2 are compared for 4D dose calculations on the two 4DCT sets. As seen in figure 5.5 before, only small differences between the 50 % and the 30 % GW are observed for the smaller 4DCT set which was used for most patients. For 14 CT phases the DVH curve for the 30 % GW exhibits a significantly increased steepness w.r.t. the larger gating window. Also, less overdose is present for both GWs compared to the 4DCT set with eight phases. Similar results were obtained for the comparison of the two 4DCT sets of patient G3.

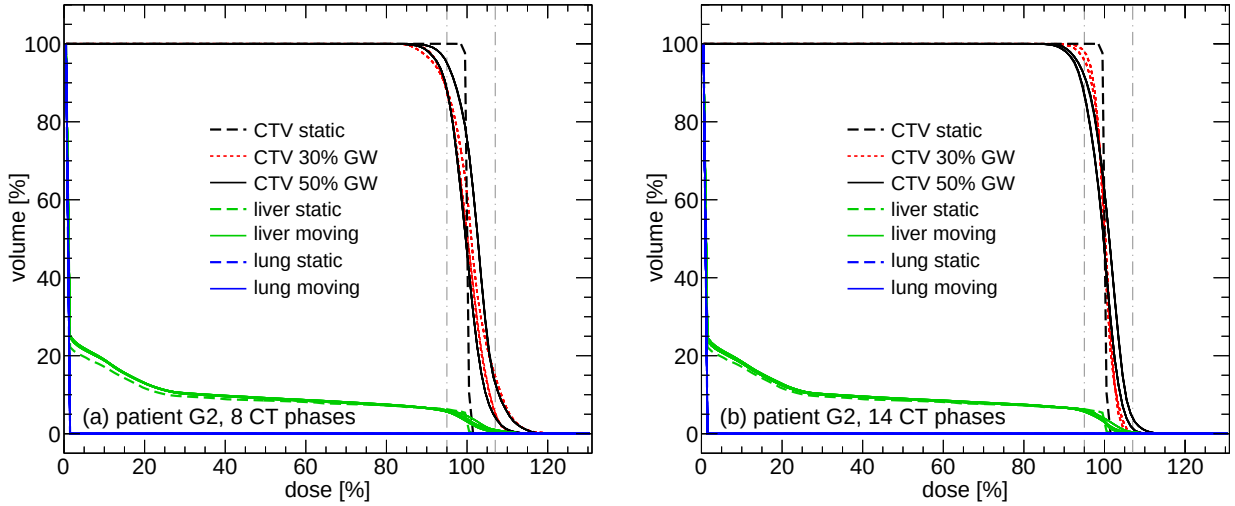

Figure 5.10.: Comparison of DVHs for patient G2. Dose calculations were based on eight **(a)** and 14 4DCT phases **(b)**. Dashed-dotted lines represent ICRU dose thresholds of 95 % and 107 % of the prescribed dose, respectively.

5.3.2.2 Dose conformity

Dose conformity of the treatment plans with and without target motion was evaluated using the CN. The results for a subset of the patients with a single CTV volume are shown in figure 5.11. The data presentation is identical to figures 5.7 including the respective trend lines for target motion (gray dash-dotted line) and the static treatments (black dash-dotted line). The dependence on the gating window was not analyzed, since the dose optimization was done on the same ITV for both gating windows. Static CN values exhibit an approximately linear decrease with the beam spot FWHM. The slopes are different for each tumor volume. Extreme cases are shown in the figure for CTV TA5 and CTV TG5 (figures 5.11b,d) with decays of the CN of about 5 % and 30 % over the studied FWHM range, respectively. In the presented example of CTV TA5 the CN amounts to only 75–80 % of the static conformity at the smallest beam spot size with standard deviations of about 15 %. Reduced standard deviations are observed for all CTVs with increasing beam spot size, especially at 15 mm. For CTVs TA3 and TA5 the average conformity under target motion increases with the beam FWHM and gradually approaches the static values (see figure 5.11b). Differences of more than one standard deviation between different IES spacings are seen for CTVs TA5 and TG4. The lateral raster spacing did not exhibit a relevant impact on the CN. Likewise, a clear dependence of the CN on the tumor motion amplitude was not observed. For instance, despite a comparable amount of tumor motion CTVs TG4 and TG5 have significantly different CN characteristics. For CTV TG4 larger standard deviations and a decreasing average deviation from the static values is observed for increasing FWHM. In contrast, CN values for CTV TG5 are close to the static reference at all FWHM.

5.3.2.3 Normal tissue exposure

The exposure of the liver and lung was analyzed as a function of varying beam parameters for all patients, as far as the respective contours were available. As a representative example,

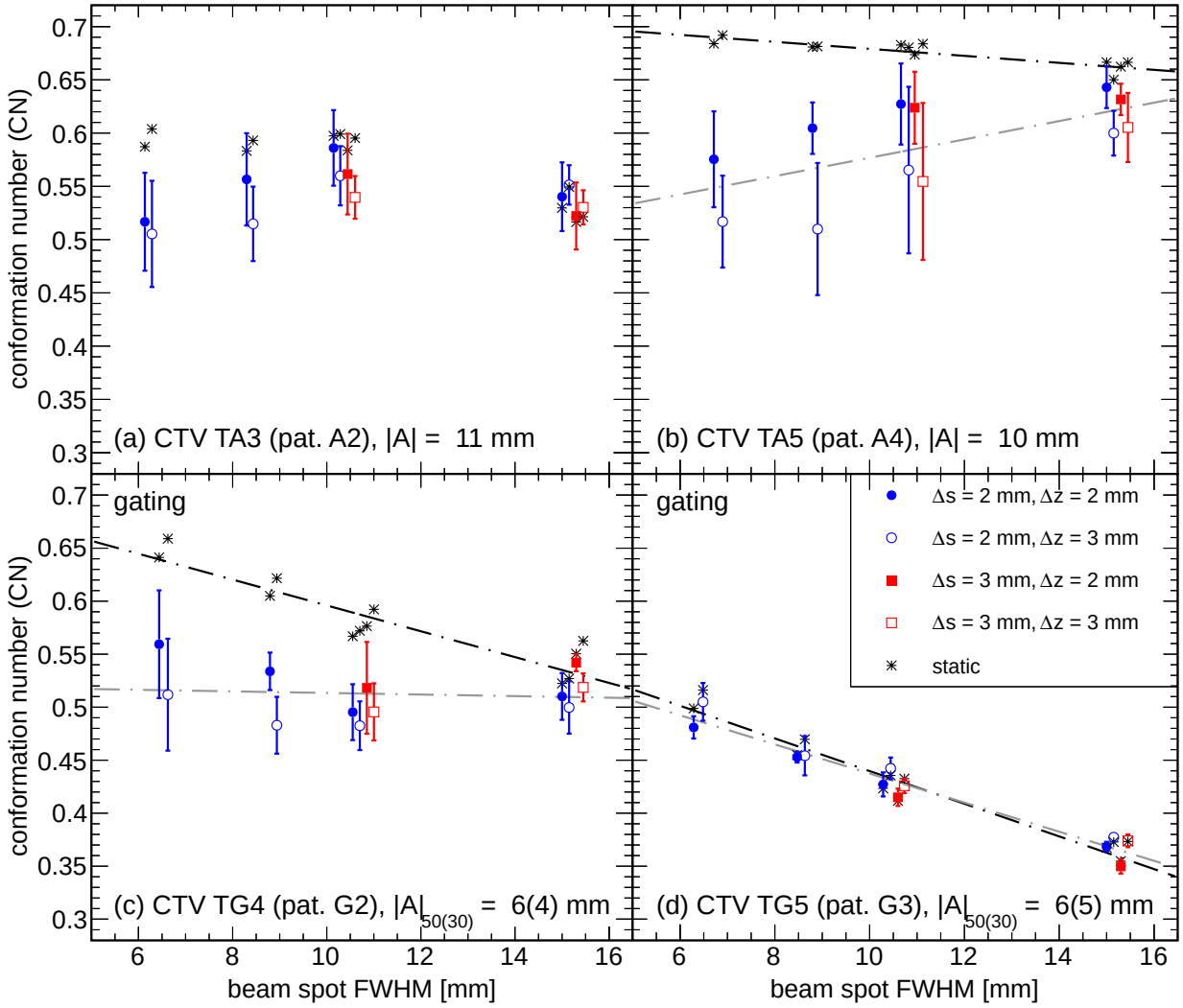

Figure 5.11.: Conformation number as a function of the beam spot FWHM for CTVs TA3 and TA5 with abdominal compression **(a–b)** and CTVs TG4 and TG5 with gating **(c–d)**. The static CN values and trend are drawn for comparison.

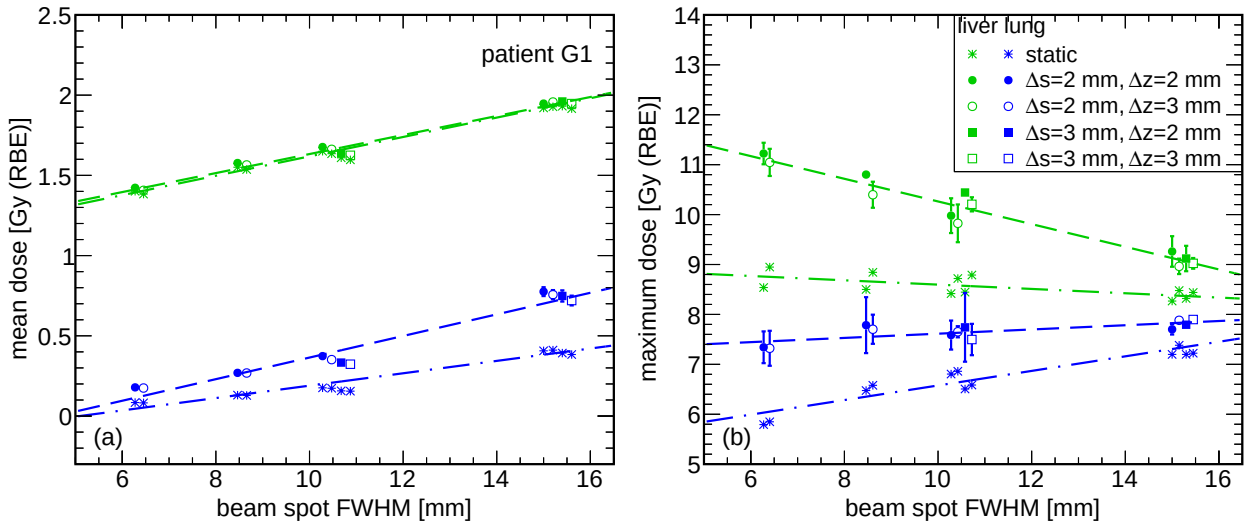

Figure 5.12.: Mean and maximum dose in liver and lung as a function of the beam spot size for patient G1. The data points for static irradiation are drawn for comparison.

figure 5.12 shows the results for the dose to the liver and lung in patient G1. The various raster spacing combinations are visualized by different markers. Mean dose values for both organs increase with the beam spot FWHM. However, only for the lung a difference between static and moving irradiation is observed. The mean dose to the lung in this case increases by about 10 % per millimeter beam spot. The same qualitative behaviour of the mean dose was found for most patients. A gradual decrease of the the maximum dose to the lung and liver relative to the static case is observed with increasing beam spot size, in particular for the liver (figure 5.12b). The decrease in the maximum dose amounts to about 20 % over the studied range of FWHM. Comparable results have also been found for the other patients. Differences from this behaviour were observed for patient A2, in particular. The CTV for this patient is located close to the lung volume boundary. Range overshoots into the lung, due to organ motion, in this case lead to a systematically increased maximum dose w.r.t. the static irradiation (see also figure 5.6). From figure 5.12 it can also be seen that there is no relevant difference in the mean and maximum dose to the two organs with regard to different lateral or longitudinal raster spacings.

Due to different volumes of the lung covered by the CT scans, absolute comparisons of the mean lung dose among different patients could not be made. In summary, maximum lung dose values of 0–10 Gy (RBE) were determined, depending on the individual location of the tumor. For the liver the mean received dose is between 0.7 and 2.0 Gy (RBE) for most patients. Only for patient G3 values up to 3 Gy (RBE) were found. Maximum dose values for the liver range between 9 and 13 Gy (RBE). Detailed results are listed in tables C.6 to C.13 in the appendix.

5.4 Summary and discussion

In this chapter the results of 4D treatment planning studies for eight patients with HCC were presented. A major focus of these studies was to investigate the potential of the concept of enhanced pencil beam overlap, in order to mitigate residual motion interplay effects. Most of the analyzed patients had received treatment with scanned carbon ion therapy at HIT before. During treatment, the patient motion and the beam delivery sequence were monitored. Based on these data, 4D treatment reconstructions were performed with TRiP4D for two of these

patients. The calculations used the 4D treatment simulation functionality developed within the scope of this thesis.

4D treatment reconstructions

The 4D reconstructions were carried out for patient A2 with abdominal compression and patient G2, the first patient treated with respiratory gating at HIT. This also is the world's first patient treated with gating and scanned beam delivery. The reconstructed dose distributions for the two patients were considerably affected by residual motion interplay effects, especially in the case of patient A2. V_{95} values of 76–97 % for patient A2 and of 88–99 % for patient G2 were obtained for the single fractions. The total dose distribution of patient A2, obtained as the sum of all fractions, exhibited an improvement in V_{95} ($V_{95} = 92.8\,\%$) compared to the single fractions. This improvement can be attributed to the averaging rescan effect introduced by dose fractionation (Knopf et al., 2011). Compared to the static reference, a 25 % increase in the mean lung dose was observed for patient A2 for the full treatment. This increase was predominantly caused by range overshoots, due to organ motion, and the close proximity of the tumor to the lung. The dose to the lung for patient G2 was largely unaffected. An 18 % increase of the mean dose to the liver was observed w.r.t. the static dose delivery. For technical reasons, the dose delivered in the first fraction and the resulting cumulative dose for patient G2 could not be calculated. However, a similar averaging effect of the dose is expected. The clinical interpretation of the presented results and the possible implications are left to the physician.

Although 4D treatment reconstructions in TRiP4D have been demonstrated in chapter 4 to be accurate to a few percent for a complex experimental setup, it is important to realize that the sources of uncertainty for patient treatment reconstructions are much more diverse and difficult to assess. The validity of the 4DCT at the time of treatment is a central issue. It has, for instance, been reported by Siebenthal et al. that liver drift and deformations of more than 5 mm can occur on a time-scale of tens of minutes after patient positioning, potentially invalidating prior imaging (von M. Siebenthal et al., 2007). Above that, intra-fractional changes of the breathing pattern can occur (Shirato et al., 2004) which likewise are not covered by the 4DCT. In the presented study, additional uncertainty of the 4DCT arises from deviations from the assumed relation of HU numbers and water-equivalent path length. The analysis of this uncertainty was beyond the scope of this thesis. However, visual inspection of the static dose distributions for the clinical treatment plans of patients A2 and G2 indicate that range differences may be on the order of few millimeters. For a routine clinical application of 4D treatment reconstructions a more accurate estimation of the introduced errors and adequate modification of the HU look-up table or the 4DCT protocol are essential. At the time of writing, research with respect to this issue is under way at HIT.

Apart from the 4DCT, also the correlation of the external surrogate signal to the internal tumor motion carries significant uncertainties. Systematic intra-fractional differences, such as phase shifts, may occur (Hoisak et al., 2004; Ionascu et al., 2007) and will have a significant impact on the dose reconstructions if the phase shift is not corrected for. Furthermore, the technical limitations of the surrogate motion monitoring system and the respective module of TRiP4D are relevant. While patient A2 showed a very regular breathing pattern, patient G2 had notably irregular respiration. Hence, even assuming acceptable correlation to the internal tumor motion, it is to be expected that accurate determination of the respiratory phase from the surrogate motion trace under these conditions is challenging.

Finally, the acquisition of the BDS data during treatment is in principle well controlled and sufficiently accurate. However, due to separate data acquisition systems, temporal correlation of the BDS data and the motion trace is required. At HIT motion monitoring is performed using the ANZAI system (AZ-773V, ANZAI MEDICAL CO., LTD). For technical reasons, the beam status is also acquired with the ANZAI device. The data can in principle be used to guide temporal correlation. However, the fact that the ANZAI system is not a real-time system induces significant timing inaccuracies. In the course of this study, discrepancies of up to 500 ms were found between beam-off signals and the irradiation time of the last point in the respective beam gate. The data indicate that these discrepancies are proportional to the acquisition time. For this reason, manual temporal correlation was performed. To generate the required beam status data from the treatment records, two simplifications had to be made. Firstly, a constant irradiation time of the first raster point in each beam gate and secondly, an instant interruption of the beam were assumed. Since only few raster points are affected, the impact of these approximations is expected to be small compared to the residual effects introduced by the motion trace uncertainties. The timing inaccuracies of the ANZAI system compromise the identification of the motion state for each raster point which is equivalent to a time-dependent phase shift. Data correction is only feasible if the phase shift is linearly increasing with the acquisition time. Further investigation on this issue is required. To investigate the uncertainties due to manual temporal correlation and the ANZAI system timing, phase shifts between the BDS and the motion trace of $\pm$250 ms were studied. As shown in section 5.2.3, the introduced variation in V_{95} is considerable and on the order of $\pm$10 %. The discussed issue can be avoided, if an integrated data acquisition is used for the synchronous monitoring of the BDS and the patient motion at an acquisition rate smaller than 1 ms. For an efficient application of 4D treatment reconstructions in clinical routine such a system is strongly recommended.

4D treatment simulations

The treatment simulations reported in this chapter comprised over 1500 4D dose calculations for gating and abdominal compression in eight patients with HCC. The dose homogeneity, dose coverage and dose conformity were studied as a function of the employed beam parameters, i.e. the beam FWHM, the IES spacing and the lateral raster spacing. Additionally, the correlation of the dose parameters with the CTV motion amplitude was investigated. A statistical analysis was carried out using multivariate linear regression models to investigate the impact of the beam and CTV parameters on the dose homogeneity.

Similar to the results reported in chapter 4, the beam spot FWHM and the motion amplitude exhibited the largest impact on all studied dose parameters. An increase in the beam FWHM from 6 mm to 15 mm resulted in a reduction of the lacking dose coverage (V_{95}) by about 50–60 % for abdominal compression and 36–100 % for gating, depending on the CTV volume. Comparable improvements were obtained for the dose homogeneity index and the V_{107}. Assuming an acceptance threshold for the V_{95} of 95 %, five out of six CTVs could have been treated with a 30 % GW and a 15 mm beam spot. In contrast, only two CTVs with abdominal compression would have passed this threshold. These results suggest that an increase in the beam FWHM yields considerable mitigation of residual motion interplay effects, especially for gating. However, the variability among different patients is large as can, for instance, be seen by comparison of figures 5.5d,e. While the gain in V_{95} for patient G2 in this case is considerable, patient G3 shows little response to the increased beam FWHM. However, the overall motion of the two CTVs is comparable. These observations suggest that a general prediction of the desired effect

on the basis of the CTV motion only is not feasible. The individual anatomy of the patient, tumor location and the tumor motion pattern may be starting points for a better understanding of the observed variability. However, the multivariate analysis has confirmed that there was generally a larger response to the beam FWHM for gated beam delivery, as can be seen from the fraction of the explained variances in table 5.4. In the case of gating, the respective R^2 values were about twice as large as for abdominal compression. Moreover, the statistical analysis also showed a different behavior for gating and abdominal compression w.r.t. the correlation of the HI with the CTV motion amplitude. Only in the case of abdominal compression a large impact ($R^2 > 0.4$) of the SI motion amplitude and the length of the motion vector was found. Instead, a stronger correlation of the HI with the AP motion amplitude was present (see also figure 5.9) ($r < 0.7$ on average). A possible explanation for this behaviour is the relative motion between the beam and the CTV. For the employed treatment plans horizontal line-by-line scanning was used, i.e. parallel to the SI direction for the used beam port configuration (left lateral to medial). Bert et al. (2008) have shown that a perpendicular configuration of scanning and target motion in general leads to more severe interplay patterns. Hence, the AP motion component in this case may predominantly drive the interplay patterns, although absolute motion amplitudes are below 4 mm. In addition, the CT resolution is only 3 mm in the SI direction, thus, absolute uncertainties on this motion component may be larger. On the other hand, the registration accuracy is on the order of 1 mm (Brock, 2010), causing the relative uncertainty of the AP motion to be considerable, as well. Zhang et al. (2012) recently have reported even larger registration errors for the liver of several millimeters, due to low image contrast. It should be noted, however, that the uncertainties of the mean and median motion amplitudes for statistical reasons are subject to less uncertainty than the displacements of individual voxels. Nevertheless, the latter are of interest for 4D dose calculation. In their study Zhang et al. found a considerable impact of the registration accuracy in the liver on the 4D dose distribution of on average 3 %.

The observed differences with regard to the two gating windows in general were smaller than expected. Only for CTV TG3 a consistent advantage of the 30 % GW w.r.t. dose coverage and dose homogeneity was observed. TG3 was the tumor ehibiting the largest motion amplitude and the largest difference in the SI and AP motion components between gating windows. The small improvements for the smaller gating window are most likely due to the fact that the employed 4DCT could not adequately sample the motion in the gating window. As can be seen from figure 5.1b, for the 4DCT with eight phases only few CT phases are located in the gating window and the phase distribution is strongly asymmetrical. For two of the patients a more adequate 4DCT set with 10 % steps was available. It has been shown in figure 5.10 that the 4D dose calculations in the presented case strongly depended on the 4DCT sampling. Hence, the results obtained for gating may in general be considerably affected by the inadequate phase sampling. The same also holds for the estimation of the motion amplitudes from the 4DCT, using deformable registration. Therefore, the disadvantageous phase sampling may also be the reason for the very small influence of the AP and SI motion components on the dose homogeneity in the case of the 50 % GW, as found in the statistical analysis. Although the number of patients in this study is small, the results provide evidence that the 4DCT sampling has a considerable impact on 4D dose calculation. A revision of the 4DCT protocol is recommended. The optimal phase sampling should be determined in further studies.

Variation of the IES spacing only showed notable differences in few cases. CTVs TA1 and TA5 exhibited about 30–50 % larger HI values for the 3 mm IES spacing. The statistical analysis, however, revealed that the impact on the total variance is on average about one order of magnitude

smaller than for the beam FWHM and the motion amplitude (see table 5.4). An explanation for the few cases with larger variation between different IES spacings can be resonance effects between beam and CTV motion, leading to extreme interplay patterns. Comparable effects were observed in chapter 4 for the impact of certain beam delivery sequences on the dose homogeneity (cf. figure 4.14). Since correlations are broken up more frequently by beam pauses for the smaller IES spacing, formation of extreme interplay patterns should be less likely. This argument also holds for gating where even more beam pauses are introduced, depending on the gating window size.

For the lateral raster spacing no significant effect has been found. Hence, also a 3 mm raster spacing seems dosimetrically acceptable. This can potentially be exploited to reduce the treatment time when used in combination with a large enough beam spot.

The results w.r.t. dose conformity demonstrate that a larger beam spot leads to less conformal static dose distributions for all analyzed patients. However, large differences were observed from patient to patient. The magnitude of the conformity decay varied between 5 and 30 % over the full range of studied beam spot sizes. In a first approximation the characteristic loss of conformity can be related to the tumor size. The relative increase of the irradiated volume is larger for smaller tumors, resulting in a steeper decay of the conformity. Large variations in conformity due to interplay are found, especially at small beam FWHM. Scattering of the CN amounts to 15–30 % around the mean in many cases (see figure 5.11). This is comparable to the results obtained for the water phantom simulation study in section 4.3.2.2. Standard deviations gradually decrease for increasing beam FWHM and approach the static reference. In general, a larger beam FWHM decreases the static conformity, while on average increasing the dynamic conformity. Application of an increased beam spot size may be feasible for those patients for which the static conformity is not already unacceptable, e.g. due to normal tissue constraints. It should be noted that, based on the results presented here, a smaller beam FWHM in most cases does not yield an advantage in conformity for target motion, due to the variability introduced by interplay effects. An exception to this, however, has been found for CTV 10 (see figure 5.11d).

Conclusion

The results of the 4D treatment reconstructions for two patients demonstrate considerable dose degradation due to interplay effects, in particular in the case of abdominal compression. The discussed 4D treatment planning study reveals that an increased beam FWHM can significantly mitigate residual motion interplay effects. Based on the available data, a beam FWHM of at least 15 mm is recommended for treatments under abdominal compression. The findings of this study also suggest that a revised 4DCT protocol with adequate phase sampling is essential for future treatment planning studies and dose reconstructions.

6 Discussion

In 2011, the Heidelberg Ion-Beam Therapy Center (HIT) has commenced the treatment of liver cancer patients with mobile tumors with a scanned carbon ion beam. To compensate for motion-induced dose inhomogeneities, the treatments are delivered under abdominal compression or using respiratory gating. However, both techniques can only establish partial compensation of interplay effects. Therefore, further mitigation has been attempted using optimized treatment plan parameters.

In the course of this thesis, a 4D treatment planning system (4DTPS) was developed, allowing detailed 4D treatment simulations in a clinical environment and for various motion mitigation techniques, including gating. The 4D dose calculation capabilities of the program were tested in dedicated experiments, showing good agreement with the measurements. The 4DTPS enabled extensive experiments, simulations and treatment planning studies for liver cancer patients, addressing the mitigation of residual motion interplay effects using enhanced beam overlap. The results demonstrate that an enlarged beam spot size (FWHM) can considerably reduce dose heterogeneities caused by residual motion interplay effects. TRiP4D further allowed 4D dose reconstructions of the first liver cancer patients treated with a scanned carbon ion beam at HIT.

Experiments and simulation studies

Bert et al. (2009) have proposed a concept of an enlarged overlap of individual pencil beams to increase the robustness with regard to motion-induced dose heterogeneities. Their initial studies indicated that a mitigation effect can likewise be reached by a decreased lateral raster spacing or by an increased beam spot size. The findings in this work, however, suggest that the ratio of the beam FWHM and the lateral raster spacing is not the crucial variable. In fact, the presented studies revealed an impact of the beam spot size only. A systematic impact of the lateral raster spacing on the dose homogeneity was not observed.

Comparing the two studies, the different preconditions have to be taken into account. Bert et al. have performed experiments and simulations with gated irradiation of radiographic films in two separate setups to independently study the effect of lateral and longitudinal pencil beam overlap. In contrast, in this work absolute dose measurements and simulations were performed for ungated beam delivery in a more complex water phantom setup with three dimensional target motion. In general, radiographic film response is not directly comparable to the absorbed physical dose (Spielberger et al., 2003). Hence, a quantitative comparison of the results of the two studies is difficult. Bert et al. have aimed at the separation of lateral and longitudinal overlap effects. In the presented study, both effects were studied in parallel. The observed differences between the two studies may partially result from interaction of the lateral and longitudinal beam overlap. Indeed, the results in chapter 4 suggest that lateral and longitudinal overlap may not be fully independent, since a combined lateral and longitudinal overlap did not always yield a better result than an increased lateral overlap only. Additional differences are to be expected from the fact that for gated beam delivery only the dip-like motion characteristic around the exhale minimum is of relevance. The impact of different motion characteristics has

not been studied in the presented work. However, it seems unlikely that qualitative differences are introduced by this fact.

Steidl (2011) has performed simulation studies for gated beam delivery which are very similar to those discussed in chapter 4. He used the same water phantom setup and simulation environment and reports comparable results with regard to the effect of an increased beam FWHM. In agreement with the findings in this work, he also did not observe a significant impact of the lateral raster spacing on the target dose homogeneity. He further reports a mitigation effect of a decreased IES spacing. Although a smaller IES spacing in the presented study did not show the same results in all cases, the general tendency was the same.

The observed differences between the two simulation studies may at least partially originate from the different beam delivery sequences (BDSs) used. While Steidl employed simulated BDSs, the study described in this thesis is based on measured sequences. Since the former were generated using simplifications, they may not describe the beam delivery at HIT with sufficient accuracy. The impact of the BDS on the 4D dose distribution was investigated in chapter 4, revealing that a variation in the BDS translates into considerable variability of the 4D dose distribution. The reason for this seems to be a modulation of the temporal structure of the beam delivery and the extracted intensity pattern. In some cases, very large dose differences were observed which may be caused by disadvantageous synchronization between beam delivery and target motion and provoke resonance-like interplay patterns. There is reason to believe that irregular target volume shapes and frequent beam interruptions, e.g., due to beam gating, lower the probability for these synchronization effects. For the patient treatment studies carried out in this work, similar effects were observed at a much smaller magnitude for patients with abdominal compression. However, in the presented case only simulated BDSs could be studied.

So far, interplay patterns have been studied in the literature mostly with a focus on the target motion component rather than the beam motion. This is due to the fact that the target motion is usually better defined and simpler to control in experiments. Nevertheless, considering the results of the discussed study, future research on the variability of BDSs and its dosimetric impact is recommended. The large number of measured beam delivery sequences obtained in the course of this study may serve as a starting point for these investigations. A better understanding of the crucial variables affecting the dosimetric influence of the beam delivery structure may open up possibilities for a directed modification of the beam delivery. In a first approach, robustness considerations could be included into the choice of the particle intensity level. In a more elaborate concept, real-time beam intensity control could be used to modulate the extracted beam intensity as needed. Dynamic intensity control for synchrotron accelerators has been developed at NIRS (Sato et al., 2007) and is currently under investigation at HIT and GSI (Schömers et al., 2011).

Treatment planning studies

The potential of the mitigation of interplay effects using an enlarged beam spot size has been confirmed in treatment planning studies for eight patients with liver cancer. For the analyzed patients with abdominal compression an enlarged beam FWHM of up to 15 mm could not definitely establish V_{95} values larger than 95 %, except for very small tumor motion amplitudes below 2 mm. In general, a larger mitigation effect of the beam FWHM has been observed for gating. For three of the analyzed target volumes, V_{95} values larger than 95 % were obtained if the FWHM of the beam was increased to 15 mm. While a decreased IES spacing only had a

small impact on the dose distributions, considerable differences were found between different patients.

In particular for gating, the CTV motion amplitude did not show a clear correlation with the resulting level of dose heterogeneity due to residual motion interplay. Furthermore, apart from one patient, no significant dosimetric differences were observed between the two selected gating windows. A comparison of 4D dose calculations on two 4DCT sets with a different number of CT phases inside the gating window was carried out for a sub-set of the patients. The results suggest that the 4DCT protocol currently used at HIT is not well suited to study residual motion interplay effects inside the gating window. Hence, quantitative interpretation of the obtained results for gated beam delivery may be limited. Since also the tumor motion amplitudes were estimated from the 4DCT, these may be subject to considerable uncertainties. Considering the findings in this work, future studies to determine the optimal 4DCT sampling, especially in the gating window, are recommended.

Apart from an increased pencil beam overlap, other approaches for the mitigation of tumor motion have been published. Furukawa et al. (2010a) from NIRS have proposed to mitigate residual tumor motion in the gating window by combining gating with rescanning. PSI plans to use a similar approach (Knopf et al., 2011). Rescanning also can be used independently from gating. It aims at an statistical averaging of the dose heterogeneities by performing multiple scans of the target volume (Phillips et al., 1992). Rescanning is inherently robust, however, large margins encompassing the full tumor motion have to be used. A similar effect to rescanning can be achieved by the use of multiple fields. Knopf et al. (2011) have reported on the effectiveness of rescanning for liver cancer using single and multiple fields. However, they have only considered rigid liver motion and did not take into account range changes. An alternative approach to rescanning is to compensate the tumor motion by adapting the beam position to the changing tumor position, so-called beam tracking. GSI has implemented beam tracking into the therapy control system and has demonstrated the technical feasibility (Bert and Rietzel, 2007; Saito et al., 2009). While lateral beam adaptation is controlled via the scanner magnets, range adaptation is facilitated using a fast double wedge absorber system. From a clinical point of view, the application of beam tracking is currently limited by the precision of 4D treatment planning routines and motion monitoring. Apart from modification of the beam delivery, direct reduction of the tumor motion is also possible. RPTC routinely performs treatments of lung and liver tumors in apnea under general anesthesia (RPTC, 2011). However, this produces a heavy clinical workload. All of the above treatment modalities are subject to uncertainties which may compromise the precision of the respective technique. The concept of enlarged beam overlap might not only be of advantage to increase the robustness of treatments using gating or abdominal compression. Also, a combination of this approach with beam tracking or rescanning inside the gating window, as proposed by Furukawa et al., can be thought of.

4D treatment planning system

The parameter study of chapter 4 and the treatment planning study discussed above both were enabled by the availability of the 4D treatment planning system, TRiP4D, which was developed in the course of this work (chapter 3). The 4D treatment planning functionality incorporates the current state of research in the field. That is, the treatment planning workflow is based on 4DCT and deformable image registration data. Basic concepts and algorithms developed earlier by other authors (Bert and Rietzel, 2007; Gemmel et al., 2011) have been integrated into the GSI in-house treatment planning system TRiP98 (Krämer et al., 2000). Dedicated tests have shown

that the program is capable of performing 4D dose calculations for a complex experimental setup with an accuracy of on average $(-1 \pm 4)\,\%$ for the typical beam configuration (section 4.3.1). A major enhancement of the 4D treatment planning functionality is the integration of deformable image registration data and 4D volume segmentation which are indispensable for patient treatment planning. Furthermore, compatibility to clinically used motion monitoring devices and beam delivery sequence data has been established, thus, enabling 4D treatment simulations and 4D dose reconstructions for irregular patient respiration. Using motion monitoring and beam delivery sequence data measured during treatment, TRiP4D is capable of retrospectively calculating the delivered dose. This functionality has been demonstrated for two patients with liver cancer who were treated at HIT with abdominal compression and gating. The results indicate that the dose delivery was considerably affected by interplay effects and is very sensitive to the relative alignment between the motion trace and the BDS. To the author's best knowledge, 4D dose reconstructions for patients treated with a scanned ion beam are reported here for the first time.

The possibility to perform 4D dose reconstructions based on data acquired during treatment opens up new perspectives for quality assurance and treatment planning. One of the major problems related to interplay patterns is that they are very sensitive to all beam delivery and motion parameters and, therefore, are very difficult to predict. Retrospective 4D treatment simulations enable to assess the magnitude of dose heterogeneities for the individual patient, breathing pattern and beam delivery. Such simulations may provide the possibility to change a treatment course, if necessary. Thus, TRiP4D can be used to facilitate adaptive treatment planning strategies. In a conventional approach, this can include changes to the treatment plan based on repeated imaging. Further adaptive concepts may comprise changes of the motion mitigation technique or modification of treatment parameters, such as the beam spot size. However, of a greater clinical importance is the possibility to perform simulations prior to treatment. Although the exact conditions are unknown, 4D simulations for the individual patient can serve to determine necessary treatment parameters, such as the gating window size or the most suitable motion mitigation technique. In order to determine robust treatment parameters, a large number of simulations can be performed to adequately sample the respective parameter space. The results of such simulations can be exploited in two ways. Firstly, the motion-related uncertainties of a treatment can be assessed for a specific treatment plan and, secondly, alternative treatment options can be investigated on a patient-specific basis. Due to the large parameter space of these simulations, clinical decision making is non-trivial. For this reason, research projects at HIT and GSI currently aim at visualization concepts for the results of such simulations which shall enable the physician to determine the best treatment option in an efficient way.

TRiP4D now also provides the opportunity to systematically investigate the sources of uncertainty entering into the 4D treatment planning process in general and the 4D treatment simulations in particular. Only some of the uncertainties shall be addressed here. All 4D treatment planning attempts so far rely on the validity of 4DCT data. Research in the field has shown that the expected variability is considerable, even over a short period of time (Shirato et al., 2004; von M. Siebenthal et al., 2007). Therefore, a single 4DCT set does not necessarily represent the moving anatomy of the patient accurately enough. Using the new 4DTPS, the variability of the intra-fractional anatomy changes can be studied under controlled conditions, for instance, using serial 4DCT data. The obtained understanding in turn may help to more reliably perform 4D treatment simulations and to interpret their results accordingly.

To take full advantage of 4DCT data, deformable registration is indispensable. Zhang et al. (2012) recently have reported on registration uncertainties in the liver and their impact on the 4D dose distribution. They found considerable variability in 4D dose calculations based on registration results from different algorithms. They conclude that these variations originate from registration uncertainties due to the typically low image contrast in the liver. Using deformable registration data of different software packages for the same 4DCT set, similar studies can be performed with TRiP4D in the future.

Finally, the use of external motion surrogates, for instance to control respiratory gating, usually assumes direct correlation between the external and the internal motion. However, for instance, Hoisak et al. (2004) have reported on phase shifts between the internal motion and the external motion surrogate. For gating these phase shifts can lead to partial irradiation outside the intended gating window. TRiP4D enables simulations which explicitly account for this kind of miscorrelation and allow to study its dosimetric impact.

At the time of writing, TRiP4D is being further developed by colleagues to incorporate 4D dose optimization techniques into the treatment planning process. To date, dose optimization in 4D treatment planning is usually performed on a single reference 4DCT phase only, ignoring most of the available 4DCT data. Recent publications have reported on optimization techniques for intensity-modulated radiation therapy (IMRT) which include the full 4DCT information into dose optimization (Nohadani et al., 2010) or incorporate robustness considerations (Unkelbach et al., 2009). The development of similar approaches for scanned ion beam therapy in the future seems particularly promising.

7 Conclusion

In this work, a 4D treatment planning system (4DTPS) for scanned ion beam therapy was developed and implemented based on the GSI in-house planning system, TRiP98, and previous efforts in the field. The 4D treatment planning functionality integrates state-of-the-art planning tools, such as 4DCT imaging and deformable image registration, allowing therapy planning and time-resolved treatment simulations in a clinical environment. The 4D dose calculation was validated experimentally, reaching an average accuracy of $(-1 \pm 4)\,\%$ for the typical beam configuration. The new 4DTPS is currently used as the basis for further research on 4D treatment planning solutions by several colleagues.

Within this work, the 4DTPS was used for extensive studies addressing the dosimetric influence of residual tumor motion for liver cancer patients. Aiming at optimized treatment plan parameters, it could be shown for an artificial geometry in experiments and simulations that an enlarged beam spot size considerably mitigates residual motion interplay effects. These findings were supported by the results of 4D treatment planning studies based on clinical data. The most appropriate beam parameter settings can be determined on a patient specific basis, using individual treatment simulations or adaptive treatment planning concepts.

The 4DTPS contributed to the world's first treatments of patients with mobile liver tumors with a scanned carbon ion beam at HIT. 4D dose reconstructions of patients treated with gating and abdominal compression demonstrated a considerable impact of tumor motion on the delivered dose distribution and indicate a need for further motion mitigation efforts. To the author's best knowledge, these are the first retrospective treatment simulations of this kind.

A Developed software and used materials

A.1 dcm2ctx — DICOM CT and contour converter software

The **dcm2ctx** program is capable of converting DICOM-CT and DICOM-RT data into the native file format of the DKFZ-grown treatment planning system VOXELPLAN (Schlegel et al., 1992). This file format also is used by TRiP98/TRiP4D. The software is command line-based, written in C++ programming language and natively runs on LINUX operating systems. It depends on the open source DCMTK (DICOM toolkit) libraries provided by OFFIS e.V. (Eichelberg et al., 2004). dcm2ctx reads and manipulates DICOM-CT data sets and corresponding contour data in DICOM-RT format. Various data manipulation options are provided. The input syntax and available options are given in the following.

synopsis:

usage: dcm2ctx [-vdhsuyoim][-p <prefix>][-z < z_{min},z_{max} >][-c <voi_file>]
[-t <threshold>][<ct_file1> <ct_file2> ...]

mandatory arguments:

<ct_file1>, <ct_file2>, ...	input DICOM files. These must be individual slices of the same CT (in no particular order)

general options:

-h, --help	print help text
-v, --verbose	dcm2ctx is talkative (info messages)
-d, --debug	turn on debug mode (loads of output)

output options:

-s, --write-separate-files	write one .hed/.ctx set for each input file, per default all files are combined into one .hed/.ctx file set
-p, --prefix <prefix>	output files are named in the scheme: <prefix>[index][suffix]
-z, --z-range < z_{min},z_{max} >	manually select slice range in mm ($z_{min} \leq z \leq z_{max}$)
-u, --unsorted	do not sort the slices according to their z-position and keep the order in which they were given as input
-y, --flip-y	flip CT/VOI data in y direction
-o, --use-original-hu	use original Hounsfield units of CT and do not attempt to correct for a rescale intercept or rescale slope
-c, --contours <voi_file>	convert corresponding contours along with CT. The input file has to be a DICOM-RT file
-i, --interactive	interactively handle multiple contours in a slice
-m, --multi-cont	do not connect any multiple contours in a slice
-t, --th-multi-cont <num>	set threshold to remove a multiple contour in a slice number of points less than <num> will be removed (default num = 0)

example:

dcm2ctx --verbose -p my_prefix -y --contours voi_file ct_file1 ct_file2

A.2 extract+ — dose extraction software

The **extract+** program is a software to extract dose values at defined positions of a dose cube. Extraction point geometries like dosimeter arrays can be defined using a dedicated text file. Image format output is also available to overlay the extraction geometry with a CT or dose distribution. The program is command line-based, written in C programming language and natively runs on AIX and LINUX operating systems. extract+ depends on the TRiP98 libraries. The input syntax and options are given in the following.

synopsis:

extract+ [OPTIONS...] -p x,y,z <dose cube> (<ct cube>)

arguments:
mandatory arguments:

-p, --extraction-point <x,y,z>	dose extraction point, usually the center of the dosimeter geometry in CT coordinates.
<dose cube>	dose cube file (.dos) w/ or w/o file extension

optional arguments:

<CT cube>	CT cube file (.ctx) w/ file extension

options (no long options on AIX):
general options:

-d, --debug	switch on debug mode (a lot of output)
-q, --quiet	switch on quiet mode (no output on screen)
-h, --help	print help text
-H, --home-path	extract+ home (installation) path
-e, --export-gd	switch on gd image export. If <ct cube> is specified, also triggers ct image export

output options:

-o, --output-directory <dir>	output directory (default is current directory)
-f, --output-file <file>	output file (.xtr) name

extraction options:

-g, --geometry <geo>	detector geometry, default is 'waterB'
-c, --couch-angle <angle>	couch angle in deg., default is 0 deg.
-a, --gantry-angle <angle>	gantry angle in deg., default is 0 deg.
-v, --voi <voi>	VOI file w/ file extension
-i, --interpolation-method <alg>	dose interpolation algorithm, available are: (i) 'ckarger' or 'ck', as used in old extract tool (ii) 'trilinear' or 'tl', equivalent to ckarger, default (iii) 'none' or 'no', nearest neighbour only
-k, --ckarger-mode	switch on simulation of C. Karger's classic extract tool, equivalent to option chain: '-g waterB -c 90 -a 0 -i ck'
-s, --single-point	dose extraction at a single point as given by the -p option, equivalent to option chain: '-g point -i trilinear'
-r, --reference-dose	reference (planned) dose, needed for correct gd color wash

example:

extract+ -d -g waterB -c 90 -i trilinear -f output.xtr -p 10,20,15 -e dosefile.dos

A.3 mbr2lmdout — beam delivery sequence generation software

The **mbr2lmdout** program is capable of generating TRiP4D beam delivery sequence input data (.lmdout format) based on HIT treatment records (machine beam records) and beam status data (ANZAI or EtherCAT format). Time alignment either is performed by using beam status data of different formats or interpolation methods. mbr2lmdout is a command line tool and written in C++. It natively runs on LINUX operating systems and depends on GSI and HIT in-house libraries. The input syntax and options are given in the following.

synopsis:

usage: mbr2lmdout -[dvhmrbi] <machine beam record> <lmdout log file>

mandatory arguments:

<machine beam record>	input HIT MBR file (.xml)
<lmdout log file>	output lmdout log file (.lmdout)

options:
general options:

-h, --help	print help text
-d, --debug	switch on debug mode (a lot of output)
-v, --verbose	switch on verbose mode (a lot of output)
-m, --monitor	write ROOT file (.root) with monitoring information
-r, --try-repair	try to repair scan log event sequence defects

output options:

One of these options needs to be defined:

-b, --beam-status <ID>:<file>	use defined beam status log file, ANZAI (ID = az) format (.daf) and Beckhoff EtherCAT (ID = ec) format (.dat) are supported
-i, --interpolation-method <method>:<arg>	use specific beam status interpolation method 1) 'fixed': use fixed irradiation times for the first and last raster point in a beam gate 2) 'linear': linear fit of the irradiation time of the first raster point in a beam gate, not yet implemented

example:

mbr2lmdout --debug -b az:beamstatus.daf mbr.xml record.lmdout

B Water phantom measurements and simulations

B.1 Gating simulations

Table B.1.: Agreement of 4D simulations with the respective measurements for all 52 gated and the 18 static reference irradiations. The table is sorted by the plan parameters: RiFi (effective Bragg peak width), Δs (lateral raster spacing), Δz (IES spacing) and $\overline{\text{FWHM}}$ (average beam FWHM). A_{LR} and $A_{\perp}$ name the motion amplitudes in left-right BEV and the remaining dimensions, respectively. The mean relative dose deviation $\overline{\Delta D}$ and standard deviation σ^D were calculated from the 22 measured and calculated dose values per experiment.

No.	plan parameters [mm]				amplitude [mm]		agreement [%]	
	RiFi	Δs	Δz	$\overline{\text{FWHM}}$	A_{LR}	$A_{\perp}$	$\overline{\Delta D}$	σ^D
(S01)	3.0	2.0	2.0	6.1	static ref.		−1.62	1.91
(S02)	3.0	2.0	2.0	8.3	static ref.		−2.17	1.70
(S03)	3.0	2.0	2.0	10.1	static ref.		−2.43	1.64
(S04)	3.0	2.0	3.0	6.1	static ref.		−1.68	1.95
(S05)	3.0	2.0	3.0	8.3	static ref.		−2.30	1.75
(S06)	3.0	2.0	3.0	10.1	static ref.		−2.76	1.65
(S07)	3.0	3.0	1.0	10.1	static ref.		−2.33	1.80
(S08)	3.0	3.0	2.0	10.1	static ref.		−2.28	1.75
(S09)	3.0	3.0	3.0	10.1	static ref.		−2.61	1.87
(S10)	4.0	2.0	2.0	6.1	static ref.		−3.07	1.38
(S11)	4.0	2.0	2.0	8.2	static ref.		−3.41	1.25
(S12)	4.0	2.0	2.0	10.1	static ref.		−3.40	1.20
(S13)	4.0	2.0	3.0	6.1	static ref.		−3.11	1.41
(S14)	4.0	2.0	3.0	8.2	static ref.		−3.30	1.29
(S15)	4.0	2.0	3.0	10.1	static ref.		−3.58	1.24
(S16)	4.0	2.0	4.0	10.1	static ref.		−3.80	1.37
(S17)	4.0	3.0	2.0	10.1	static ref.		−3.77	1.12
(S18)	4.0	3.0	3.0	10.1	static ref.		−3.75	1.22
(01)	3.0	2.0	2.0	6.1	2.0	1.0	−0.39	4.17
(02)	3.0	2.0	2.0	6.1	4.0	2.0	−0.90	5.10

continued on next page

No.	plan parameters [mm]				amplitude [mm]		agreement [%]	
	RiFi	Δs	Δz	$\overline{\text{FWHM}}$	A_{LR}	$A_{\perp}$	$\overline{\Delta D}$	σ^D
(03)	3.0	2.0	2.0	6.1	10.0	5.0	−1.51	5.49
(04)	3.0	2.0	2.0	8.3	2.0	1.0	−2.51	3.08
(05)	3.0	2.0	2.0	8.3	4.0	2.0	−1.13	4.88
(06)	3.0	2.0	2.0	8.3	6.0	3.0	−1.80	4.15
(07)	3.0	2.0	2.0	8.3	9.0	4.5	−1.12	5.09
(08)	3.0	2.0	2.0	8.3	10.0	5.0	−2.46	5.22
(09)	3.0	2.0	2.0	10.1	4.0	2.0	−1.94	2.32
(10)	3.0	2.0	2.0	10.1	5.0	2.5	−1.31	3.81
(11)	3.0	2.0	2.0	10.1	6.0	3.0	−1.88	3.30
(12)	3.0	2.0	2.0	10.1	10.0	5.0	−2.02	3.94
(13)	3.0	2.0	3.0	6.1	2.0	1.0	−1.90	4.11
(14)	3.0	2.0	3.0	6.1	4.0	2.0	−1.18	4.24
(15)	3.0	2.0	3.0	6.1	10.0	5.0	−0.27	7.81
(16)	3.0	2.0	3.0	8.3	4.0	2.0	−1.51	3.06
(17)	3.0	2.0	3.0	8.3	6.0	3.0	−1.72	3.98
(18)	3.0	2.0	3.0	8.3	10.0	5.0	−1.90	4.60
(19)	3.0	2.0	3.0	8.3	10.0	5.0	−1.90	4.60
(20)	3.0	2.0	3.0	10.1	4.0	2.0	−0.97	3.19
(21)	3.0	2.0	3.0	10.1	4.0	2.0	−2.13	2.66
(22)	3.0	2.0	3.0	10.1	6.0	3.0	0.16	5.76
(23)	3.0	2.0	3.0	10.1	6.0	3.0	−1.85	3.37
(24)	3.0	2.0	3.0	10.1	10.0	5.0	−0.36	5.28
(25)	3.0	2.0	3.0	10.1	10.0	5.0	−1.51	3.25
(26)	3.0	3.0	1.0	10.1	4.0	2.0	−1.59	2.72
(27)	3.0	3.0	1.0	10.1	10.0	5.0	−1.49	3.37
(28)	3.0	3.0	2.0	10.1	4.0	2.0	−1.37	2.76
(29)	3.0	3.0	2.0	10.1	10.0	5.0	−1.05	4.71
(30)	3.0	3.0	3.0	10.1	4.0	2.0	−1.58	3.08
(31)	3.0	3.0	3.0	10.1	6.0	3.0	−1.54	3.69
(32)	3.0	3.0	3.0	10.1	10.0	5.0	−2.45	4.34
(33)	4.0	2.0	2.0	6.1	2.0	1.0	−2.02	3.93
(34)	4.0	2.0	2.0	6.1	10.0	5.0	−1.57	5.35
(35)	4.0	2.0	2.0	8.2	4.0	2.0	−2.88	5.93
(36)	4.0	2.0	2.0	10.1	4.0	2.0	−3.12	2.89
(37)	4.0	2.0	2.0	10.1	6.0	3.0	−2.59	2.49
(38)	4.0	2.0	2.0	10.1	10.0	5.0	−2.32	3.01
(39)	4.0	2.0	3.0	6.1	2.0	1.0	−3.26	4.24
(40)	4.0	2.0	3.0	8.2	4.0	2.0	−2.69	3.49
(41)	4.0	2.0	3.0	8.2	6.0	3.0	−2.97	3.29
(42)	4.0	2.0	3.0	8.2	10.0	5.0	−2.80	5.04

continued on next page

No.	plan parameters [mm]				amplitude [mm]		agreement [%]	
	RiFi	Δs	Δz	$\overline{\text{FWHM}}$	A_{LR}	$A_{\perp}$	$\overline{\Delta D}$	σ^D
(43)	4.0	2.0	3.0	10.1	10.0	5.0	−3.49	6.35
(44)	4.0	2.0	4.0	10.1	4.0	2.0	−3.21	3.06
(45)	4.0	2.0	4.0	10.1	6.0	3.0	−3.03	1.91
(46)	4.0	2.0	4.0	10.1	8.0	4.0	−3.99	3.18
(47)	4.0	2.0	4.0	10.1	10.0	5.0	−2.88	3.41
(48)	4.0	3.0	2.0	10.1	6.0	3.0	−3.46	3.39
(49)	4.0	3.0	2.0	10.1	10.0	5.0	−3.58	3.85
(50)	4.0	3.0	3.0	10.1	4.0	2.0	−3.03	2.43
(51)	4.0	3.0	3.0	10.1	6.0	3.0	−2.43	3.67
(52)	4.0	3.0	3.0	10.1	10.0	5.0	−3.26	4.22

B.2 Residual motion simulations

Table B.2.: Agreement of 4D simulations with the respective measurements for all 74 interplay cases and the 19 static reference irradiations of the first and second measurement series. The table is sorted by the plan parameters: RiFi (effective Bragg peak width), Δs (lateral raster spacing), Δz (IES spacing) and $\overline{\text{FWHM}}$ (average beam FWHM). A_{LR} and $A_{\perp}$ name the motion amplitudes in left-right BEV and the remaining dimensions, respectively. The mean relative dose deviation $\overline{\Delta D}$ and standard deviation σ^D were calculated from the 22 measured and calculated dose values per experiment.

No.	plan parameters [mm]				amplitude [mm]		agreement [%]	
	RiFi	Δs	Δz	$\overline{\text{FWHM}}$	A_{LR}	$A_{\perp}$	$\overline{\Delta D}$	σ^D
(S01)	3.0	2.0	2.0	6.1	static ref.		−1.20	1.18
(S02)	3.0	2.0	2.0	8.3	static ref.		−1.43	1.12
(S03)	3.0	2.0	2.0	10.1	static ref.		−1.45	0.89
(S04)	3.0	2.0	3.0	6.1	static ref.		−1.27	1.17
(S05)	3.0	2.0	3.0	8.3	static ref.		−1.46	1.15
(S06)	3.0	2.0	3.0	10.1	static ref.		−1.95	1.13
(S07)	3.0	2.0	3.0	10.1	static ref.		−2.35	1.52
(S08)	3.0	3.0	1.0	10.1	static ref.		−1.50	0.91
(S09)	3.0	3.0	2.0	10.1	static ref.		−1.89	0.88
(S10)	3.0	3.0	3.0	10.1	static ref.		−1.53	0.97
(S11)	4.0	2.0	2.0	6.1	static ref.		−2.97	1.18
(S12)	4.0	2.0	2.0	8.2	static ref.		−3.45	1.16
(S13)	4.0	2.0	2.0	10.1	static ref.		−3.97	1.14
(S14)	4.0	2.0	3.0	6.1	static ref.		−2.98	1.36
(S15)	4.0	2.0	3.0	8.2	static ref.		−3.38	1.16

continued on next page

No.	plan parameters [mm]				amplitude [mm]		agreement [%]	
	RiFi	Δs	Δz	$\overline{\text{FWHM}}$	A_{LR}	$A_{\perp}$	$\overline{\Delta D}$	σ^D
(S16)	4.0	2.0	3.0	10.1	static ref.		−3.82	1.15
(S17)	4.0	2.0	4.0	10.1	static ref.		−3.73	0.95
(S18)	4.0	3.0	2.0	10.1	static ref.		−3.67	1.07
(S19)	4.0	3.0	3.0	10.1	static ref.		−3.79	1.04
(01)	3.0	2.0	2.0	6.1	2.0	1.0	−1.06	1.68
(02)	3.0	2.0	2.0	6.1	4.0	2.0	−1.53	3.79
(03)	3.0	2.0	2.0	6.1	8.0	4.0	0.49	6.93
(04)	3.0	2.0	2.0	6.1	10.0	5.0	1.65	10.10
(05)	3.0	2.0	2.0	8.3	3.0	1.5	−1.60	2.31
(06)	3.0	2.0	2.0	8.3	5.0	2.5	−2.02	4.04
(07)	3.0	2.0	2.0	8.3	7.0	3.5	−1.68	5.77
(08)	3.0	2.0	2.0	8.3	10.0	5.0	−1.35	8.15
(09)	3.0	2.0	2.0	10.1	3.0	1.5	−1.33	1.77
(10)	3.0	2.0	2.0	10.1	5.0	2.5	−1.70	3.68
(11)	3.0	2.0	2.0	10.1	7.0	3.5	−0.72	5.61
(12)	3.0	2.0	2.0	10.1	10.0	5.0	−1.50	6.24
(13)	3.0	2.0	3.0	6.1	2.0	1.0	−1.58	2.25
(14)	3.0	2.0	3.0	6.1	4.0	2.0	−0.66	3.61
(15)	3.0	2.0	3.0	6.1	6.0	3.0	−1.71	5.69
(16)	3.0	2.0	3.0	6.1	8.0	4.0	−2.56	6.74
(17)	3.0	2.0	3.0	8.3	3.0	1.5	−1.42	3.22
(18)	3.0	2.0	3.0	8.3	5.0	2.5	−0.38	3.68
(19)	3.0	2.0	3.0	8.3	7.0	3.5	−2.06	4.89
(20)	3.0	2.0	3.0	8.3	10.0	5.0	−1.80	7.03
(21)	3.0	2.0	3.0	10.1	3.0	1.5	−2.32	2.19
(22)	3.0	2.0	3.0	10.1	3.0	1.5	−1.99	2.31
(23)	3.0	2.0	3.0	10.1	4.0	2.0	−3.44	2.85
(24)	3.0	2.0	3.0	10.1	5.0	2.5	−1.58	3.96
(25)	3.0	2.0	3.0	10.1	7.0	3.5	−1.23	5.38
(26)	3.0	2.0	3.0	10.1	7.0	3.5	−1.37	2.75
(27)	3.0	2.0	3.0	10.1	10.0	5.0	−2.96	8.23
(28)	3.0	2.0	3.0	10.1	10.0	5.0	−1.08	5.40
(29)	3.0	3.0	1.0	10.1	3.0	1.5	−1.79	2.72
(30)	3.0	3.0	1.0	10.1	5.0	2.5	−1.90	4.67
(31)	3.0	3.0	1.0	10.1	7.0	3.5	0.48	6.18
(32)	3.0	3.0	1.0	10.1	10.0	5.0	−0.95	6.49
(33)	3.0	3.0	2.0	10.1	5.0	2.5	−0.70	3.72
(34)	3.0	3.0	2.0	10.1	7.0	3.5	−2.14	4.47
(35)	3.0	3.0	3.0	10.1	3.0	1.5	−2.22	2.22
(36)	3.0	3.0	3.0	10.1	5.0	2.5	−1.42	3.03

continued on next page

No.	plan parameters [mm]				amplitude [mm]		agreement [%]	
	RiFi	Δs	Δz	$\overline{\text{FWHM}}$	A_{LR}	$A_{\perp}$	$\overline{\Delta D}$	σ^D
(37)	3.0	3.0	3.0	10.1	7.0	3.5	−0.76	4.47
(38)	3.0	3.0	3.0	10.1	10.0	5.0	−1.38	6.19
(39)	4.0	2.0	2.0	6.1	2.0	1.0	−3.17	1.53
(40)	4.0	2.0	2.0	6.1	4.0	2.0	−2.88	4.78
(41)	4.0	2.0	2.0	6.1	6.0	3.0	−3.25	5.87
(42)	4.0	2.0	2.0	6.1	10.0	5.0	−2.65	9.64
(43)	4.0	2.0	2.0	8.2	3.0	1.5	−3.59	1.95
(44)	4.0	2.0	2.0	8.2	5.0	2.5	−3.59	4.48
(45)	4.0	2.0	2.0	8.2	7.0	3.5	−4.37	6.27
(46)	4.0	2.0	2.0	8.2	10.0	5.0	−3.57	7.53
(47)	4.0	2.0	2.0	10.1	3.0	1.5	−3.87	2.16
(48)	4.0	2.0	2.0	10.1	5.0	2.5	−3.78	3.70
(49)	4.0	2.0	2.0	10.1	7.0	3.5	−3.51	5.20
(50)	4.0	2.0	2.0	10.1	10.0	5.0	−3.34	5.36
(51)	4.0	2.0	3.0	6.1	2.0	1.0	−3.06	1.88
(52)	4.0	2.0	3.0	6.1	4.0	2.0	−3.02	3.38
(53)	4.0	2.0	3.0	6.1	6.0	3.0	−2.88	6.16
(54)	4.0	2.0	3.0	6.1	10.0	5.0	−2.84	7.69
(55)	4.0	2.0	3.0	8.2	3.0	1.5	−3.63	2.51
(56)	4.0	2.0	3.0	8.2	5.0	2.5	−3.26	3.91
(57)	4.0	2.0	3.0	8.2	7.0	3.5	−3.33	5.74
(58)	4.0	2.0	3.0	8.2	10.0	5.0	−2.83	7.16
(59)	4.0	2.0	3.0	10.1	3.0	1.5	−3.51	2.14
(60)	4.0	2.0	3.0	10.1	5.0	2.5	−4.26	3.93
(61)	4.0	2.0	3.0	10.1	6.0	3.0	−3.86	4.18
(62)	4.0	2.0	3.0	10.1	10.0	5.0	−4.72	6.70
(63)	4.0	2.0	4.0	10.1	3.0	1.5	−3.20	2.32
(64)	4.0	2.0	4.0	10.1	5.0	2.5	−3.43	3.37
(65)	4.0	2.0	4.0	10.1	7.0	3.5	−2.40	5.25
(66)	4.0	2.0	4.0	10.1	10.0	5.0	−5.39	7.12
(67)	4.0	3.0	2.0	10.1	3.0	1.5	−3.45	1.79
(68)	4.0	3.0	2.0	10.1	5.0	2.5	−3.39	3.44
(69)	4.0	3.0	2.0	10.1	7.0	3.5	−3.18	4.13
(70)	4.0	3.0	2.0	10.1	10.0	5.0	−2.99	4.49
(71)	4.0	3.0	3.0	10.1	3.0	1.5	−3.66	1.89
(72)	4.0	3.0	3.0	10.1	5.0	2.5	−3.66	3.76
(73)	4.0	3.0	3.0	10.1	7.0	3.5	−3.60	4.41
(74)	4.0	3.0	3.0	10.1	10.0	5.0	−3.75	6.22

Table B.3.: Agreement of 4D simulations with the respective measurements for all 19 interplay cases and the 10 static reference irradiations of the third measurement series. See table B.2 on the previous page for details on the listed parameters.

No.	plan parameters [mm]				amplitude [mm]		agreement [%]	
	RiFi	Δs	Δz	$\overline{\text{FWHM}}$	A_{LR}	$A_{\perp}$	$\overline{\Delta D}$	σ^D
(S01)	3.0	2.0	2.0	6.1	static ref.		−1.31	0.74
(S02)	3.0	2.0	2.0	8.3	static ref.		−1.53	0.77
(S03)	3.0	2.0	2.0	10.1	static ref.		−2.08	0.85
(S04)	3.0	2.0	3.0	6.1	static ref.		−1.23	0.77
(S05)	3.0	2.0	3.0	8.3	static ref.		−1.56	0.79
(S06)	3.0	2.0	3.0	10.1	static ref.		−2.00	0.86
(S07)	3.0	3.0	2.0	10.1	static ref.		−1.79	0.74
(S08)	3.0	3.0	3.0	10.1	static ref.		−1.89	0.75
(S09)	4.0	2.0	2.0	10.1	static ref.		−3.30	0.66
(S10)	4.0	2.0	3.0	10.1	static ref.		−3.33	0.65
(01)	3.0	2.0	2.0	6.1	5.0	2.5	−1.89	2.25
(02)	3.0	2.0	2.0	6.1	10.0	5.0	−2.49	4.96
(03)	3.0	2.0	2.0	8.3	5.0	2.5	−1.47	1.68
(04)	3.0	2.0	2.0	8.3	10.0	5.0	−1.66	1.88
(05)	3.0	2.0	2.0	10.1	5.0	2.5	−1.34	1.44
(06)	3.0	2.0	2.0	10.1	10.0	5.0	−0.33	1.65
(07)	3.0	2.0	3.0	6.1	5.0	2.5	−2.11	2.81
(08)	3.0	2.0	3.0	6.1	10.0	5.0	−2.57	3.84
(09)	3.0	2.0	3.0	8.3	5.0	2.5	−1.52	1.02
(10)	3.0	2.0	3.0	8.3	10.0	5.0	−1.41	2.61
(11)	3.0	2.0	3.0	10.1	5.0	2.5	−2.45	2.22
(12)	3.0	3.0	2.0	10.1	5.0	2.5	−0.87	1.39
(13)	3.0	3.0	2.0	10.1	10.0	5.0	−2.10	2.33
(14)	3.0	3.0	3.0	10.1	5.0	2.5	−2.87	2.42
(15)	3.0	3.0	3.0	10.1	10.0	5.0	−1.57	2.37
(16)	4.0	2.0	2.0	10.1	5.0	2.5	−2.93	1.63
(17)	4.0	2.0	2.0	10.1	10.0	5.0	−4.62	2.11
(18)	4.0	2.0	3.0	10.1	5.0	2.5	−3.43	1.56
(19)	4.0	2.0	3.0	10.1	10.0	5.0	−4.64	2.65

C Detailed results of 4D treatment planning studies

C.1 Patient motion analysis

The 4DCT sets of the patients were used to estimate the amount of motion expected in the target volume and the surrounding organs. A statistical analysis of the tumor motion in the CTVs was performed for the full respiratory cycle and the two gating windows (patients G1–G4). To assess the impact of the 4DCT phase sampling, the analysis was repeated for the 14 phase 4DCT (patients G2–G3). Additionally, the deformation fields were analyzed by visual inspection of cross sections through the CTV.

In figure C.1 the organ motion is visualized for the individual patients in axial CT slices through the CTV centers. It can be seen that for the analyzed patients the organ motion is in general more pronounced for the posterior than for the anterior region of the liver and lung. For patient A3 the overall motion is significantly smaller than for the other patients. For the gated patients (figures C.1e–h) the motion near the skin and in the anterior part of the liver is larger compared to most patients with abdominal compression (figures C.1a–d), with the exception of patient A4. The motion amplitudes for the gated patients as a function of the GW are listed in table C.1. The motion vectors were determined using the registration of the CT phase with the largest motion inside the gating window to the end-exhale phase. For a 50 % GW, the SI motion amplitudes are reduced below 8 mm for seven out of eight volumes. For the same volumes and a 30 % GW, SI amplitudes are smaller than 5 mm in seven out of eight cases and smaller than 4 mm for 50 % of the volumes. The starred values for patients G2 and G3 represent the amplitudes obtained with the 4DCT with 14 phases. In the latter, CT phases matching the GW limits more adequately were available. For both patients and gating windows the observed changes, predominantly in the SI direction, are on the order of 1 mm or less, thus, they are of the same magnitude as the expected registration accuracy.

C.2 Validation of static dose calculations with TRiP4D

To validate the treatment planning procedure and the 3D biological dose calculation with TRiP4D, the static dose distributions of TRiP4D were compared to those obtained with the commercial TPS used at HIT. The clinical treatment plans optimized at HIT for the patients A1–A4 and G1 were converted for use with TRiP4D and the physical and biological dose distributions were re-calculated on the corresponding planning CTs. The differences of the dose distributions were assessed by statistical analysis of the differential dose distributions. For a direct comparison, the TRiP4D dose distributions were sampled to the same dose voxel spacing as used in the HIT TPS ($2 \times 2 \times 2$ mm).

Figure C.2 displays an axial cross section through the differential biologically effective dose distribution obtained for the clinical treatment plan of patient A1. Dose differences between the

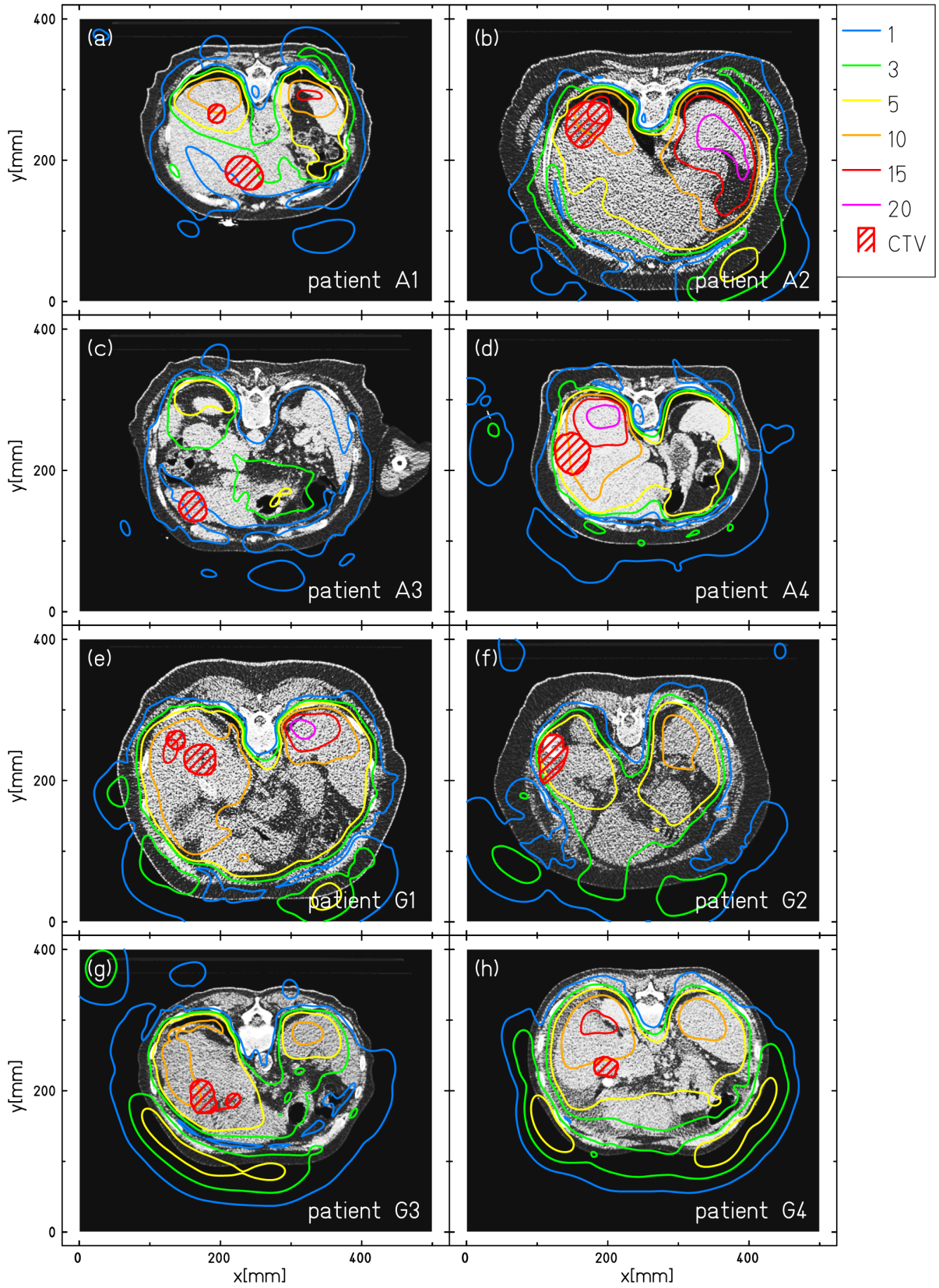

Figure C.1.: Visualization of organ motion for the patients with abdominal compression **(a–d)** and the gated patients **(e–h)**. The contour map represents the length of the motion vector for the transition from the end-inhale to the end-exhale CT phase (scale in mm). Contours are overlayed on the axial CT slices through the CTV centers.

			mean motion amplitude and SD [mm]			
GW	patient	CTV	|A|	SI	AP	LR
		TG1	7.4 ± 0.7	-7.4 ± 0.7	-1.0 ± 0.3	0.0 ± 0.0
	G1	TG2	7.6 ± 1.4	-7.1 ± 1.3	-2.5 ± 0.9	-0.9 ± 0.5
		TG3	11.7 ± 1.2	-10.8 ± 1.3	-3.7 ± 0.7	-2.4 ± 0.6
50 %	G2	TG4	6.1 ± 1.5	-5.5 ± 1.4	-2.5 ± 0.6	-0.5 ± 0.5
			$5.2 \pm 1.4^*$	$-4.7 \pm 1.3^*$	$-2.3 \pm 0.6^*$	$-0.3 \pm 0.3^*$
	G3	TG5	5.5 ± 0.9	-5.4 ± 0.9	-1.0 ± 0.3	-0.1 ± 0.3
			$5.5 \pm 1.0^*$	$-5.4 \pm 1.0^*$	$-1.1 \pm 0.2^*$	$-0.1 \pm 0.4^*$
	G4	TG6	7.2 ± 0.9	-6.4 ± 0.9	-3.2 ± 0.3	0.0 ± 0.1
		TG1	4.7 ± 0.8	-4.7 ± 0.7	-0.2 ± 0.3	0.0 ± 0.0
	G1	TG2	3.8 ± 0.9	-3.5 ± 0.8	-1.1 ± 0.9	-0.3 ± 0.3
		TG3	5.1 ± 1.0	-5.1 ± 1.0	-0.2 ± 0.3	-0.1 ± 0.2
30 %	G2	TG4	4.2 ± 1.5	-3.6 ± 1.4	-1.9 ± 0.7	-0.2 ± 0.3
			$3.2 \pm 0.9^*$	$-2.3 \pm 0.8^*$	$-1.9 \pm 0.6^*$	$-0.7 \pm 0.4^*$
	G3	TG5	4.7 ± 0.8	-4.6 ± 0.9	-0.9 ± 0.2	0.2 ± 0.2
			$4.1 \pm 1.0^*$	$-4.0 \pm 1.0^*$	$-0.6 \pm 0.2^*$	$-0.1 \pm 0.3^*$
	G4	TG6	3.2 ± 0.4	-2.9 ± 0.4	-1.2 ± 0.2	0.0 ± 0.1

Table C.1.: Statistical analysis of the CTV motion in the two gating windows of 50 % and 30 % of the relative amplitude range. The mean motion amplitude and standard deviation (SD) have been determined over all CT voxels inside the CTV for the SI, AP and LR direction, as well as for the length of the motion vector, $|A|$. Starred values were obtained from analysis of the 10 % step 4DCT and deformation maps.

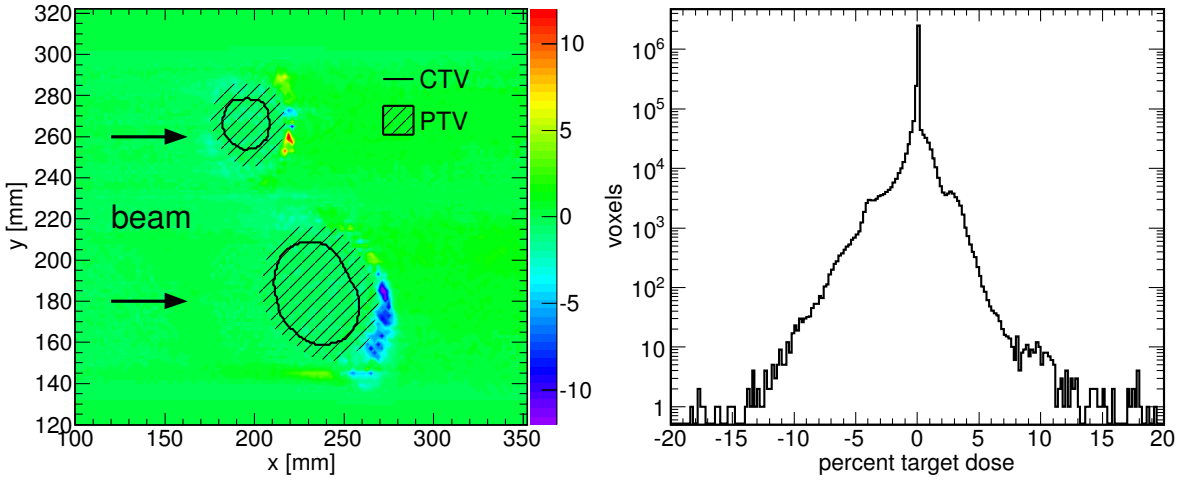

Figure C.2.: Analysis of the differential biologically effective dose distribution for TRiP4D and the commercial treatment planning system used at HIT. **(Left)** Axial cross section of the differential dose for the clinical treatment plan of patient A1 (dose in percent of the target dose). **(Right)** Histogram of the relative dose differences inside the patient's skin contour. Note the logarithmic scale.

	dose differences in % of the prescribed dose					
patient	$\overline{\Delta D}^{\text{phys}} \pm \text{SD}$	$\Delta D^{\text{phys}}_{\text{min}}$	$\Delta D^{\text{phys}}_{\text{max}}$	$\overline{\Delta D}^{\text{biol}} \pm \text{SD}$	$\Delta D^{\text{biol}}_{\text{min}}$	$\Delta D^{\text{biol}}_{\text{max}}$
1	0.0 ± 0.4	-16.5	47.4	0.0 ± 0.8	-33.4	77.5
2	0.0 ± 0.3	-9.5	48.6	0.0 ± 0.6	-17.4	80.5
3	0.0 ± 0.3	-15.2	44.4	0.0 ± 0.5	-28.5	79.1
4	0.0 ± 0.3	-17.8	45.4	0.0 ± 0.5	-34.9	76.5
5	0.0 ± 0.5	-7.9	40.8	0.1 ± 1.0	-15.3	73.0

Table C.2.: Comparison of static dose distributions calculated with the HIT treatment planning system and TRiP4D using the clinical treatment plans for patients A1–A4 & G1. Mean deviations ($\overline{\Delta D}$) and respective standard deviations, as well as minimum and maximum deviations are listed for the physical and biologically effective dose, respectively.

HIT TPS and TRiP4D are shown as a color map. A histogram of the relative dose differences is given on the right. Negative values indicate that the dose was overestimated by TRiP4D w.r.t. the clinical TPS. The dose differences exceed 10 % only in the fragment tail regions near the distal edges of the field. The mean, minimum and maximum deviations determined between dose distributions for the clinical treatment plans of patients A1–A4 and G1 are given in table C.2. While standard deviations of the mean differences are smaller than 1 % in most cases, maximum deviations can range up to 80 % of the prescribed dose. However, most of these extreme deviations occur in few voxels located near the patient skin contour, to which the dose calculation was confined. These can be attributed to artifacts introduced by the re-sampling of the TRiP4D dose distributions to the HIT TPS voxel spacing.

C.3 Normal tissue exposure — treatment reconstructions

dose distr.	Δt [ms]	liver dose [Gy (RBE)] mean	liver dose [Gy (RBE)] max	lung dose [Gy (RBE)] mean	lung dose [Gy (RBE)] max
static	—	0.9	8.7	1.6	8.6
fraction 1	−250	0.9	10.2	2.0	10.0
	+0	0.9	10.5	2.0	10.3
	+250	0.9	10.4	2.0	9.7
fraction 2	−250	0.9	10.4	2.0	9.3
	+0	0.9	10.3	2.0	8.9
	+250	0.9	10.3	2.0	8.9
fraction 3	−250	0.9	10.9	2.0	9.6
	+0	0.9	10.0	2.0	9.6
	+250	0.9	9.5	2.0	9.3
fraction 4	−250	0.9	10.4	2.0	9.5
	+0	0.9	10.4	2.0	9.5
	+250	0.9	10.5	2.0	9.6
total	—	3.7	37.3	8.1	35.2

Table C.3.: Reconstructed mean and maximum dose to lung and liver for patient A2. For each fraction three simulations were performed with varying temporal shifts (Δt) of the beam delivery sequence w.r.t. the motion trace.

dose distr.	Δt [ms]	liver dose [Gy (RBE)] mean	liver dose [Gy (RBE)] max	lung dose [Gy (RBE)] mean	lung dose [Gy (RBE)] max
static	+0	1.1	9.4	0.0	0.0
fraction 2	−250	1.3	10.6	0.0	0.4
	+0	1.3	10.5	0.0	0.4
	+250	1.3	10.5	0.0	0.3
fraction 3	−250	1.3	10.4	0.0	0.3
	+0	1.3	10.6	0.0	0.3
	+250	1.3	10.1	0.0	0.3
fraction 4	−250	1.4	10.5	0.0	0.8
	+0	1.4	10.2	0.0	0.7
	+250	1.4	11.1	0.0	0.7

Table C.4.: Reconstructed mean and maximum dose to lung and liver for patient G2. For each fraction three simulations were performed with varying temporal shifts (Δt) of the beam delivery sequence w.r.t. the motion trace. For technical reasons, the data of the missing first fraction could not be analyzed.

C.4 Target overdose

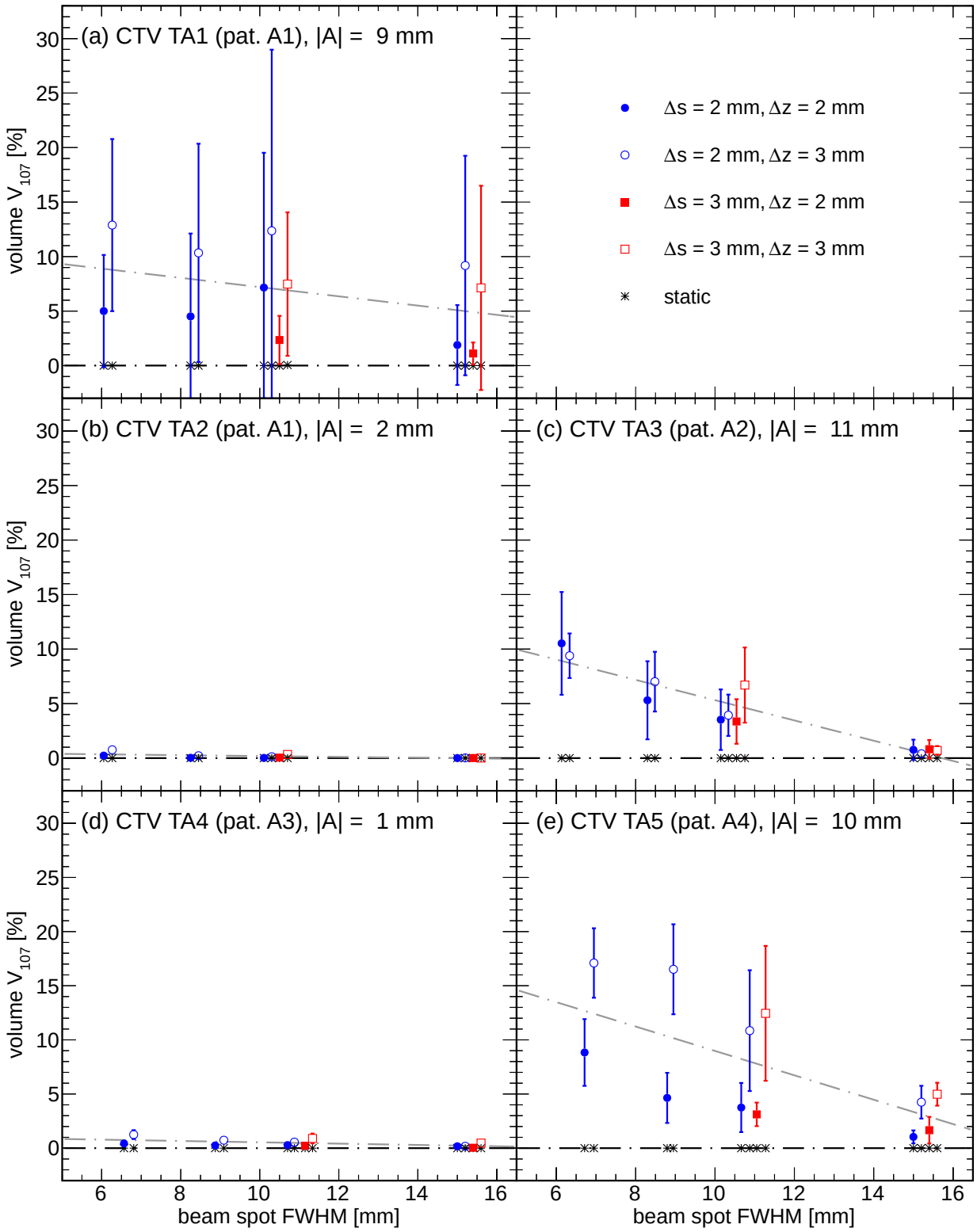

Figure C.3.: V_{107} as a function of the beam spot FWHM for the five CTVs in patients A1–A4 with abdominal compression. $|A|$ denotes the motion amplitude for each CTV volume. The dash-dotted lines are linear fits to the data.

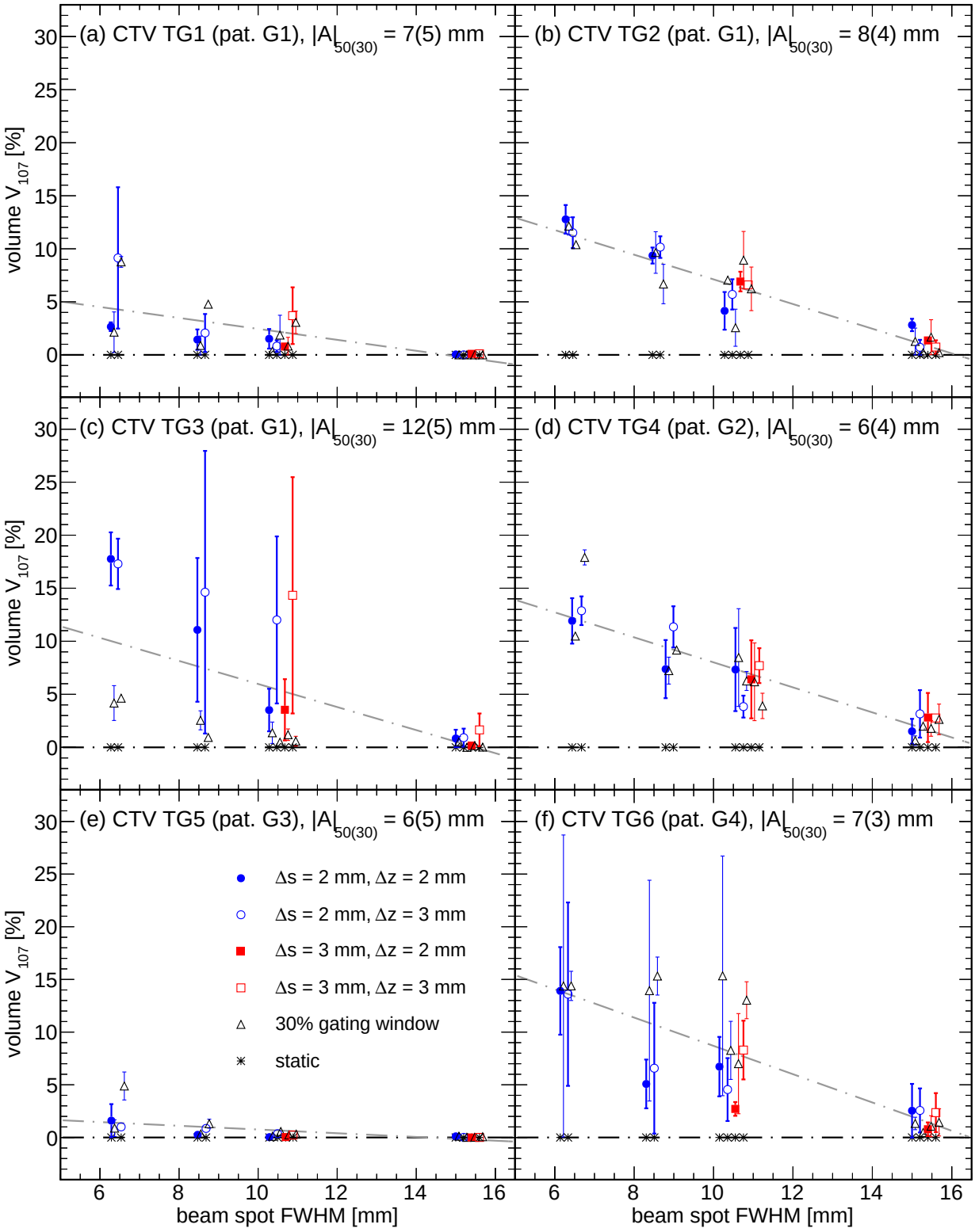

Figure C.4.: V_{107} as a function of the beam spot FWHM for the six CTVs in patients G1–G4 with gating. $|A|_{50(30)}$ denote the motion amplitude in the 50 % and 30 % GW, respectively.

amplitude-dependence of HI and V_{95} — correlation coefficient r						
[mm]		focus level	HI		V_{95}	
Δs	Δz		**SI**	**AP**	**SI**	**AP**
2	2	2	0.56	0.66	-0.59	-0.47
2	2	3	0.49	0.61	-0.48	-0.40
2	2	4	0.37	0.55	-0.35	-0.33
2	2	5	0.45	0.67	-0.36	-0.34
2	3	2	0.47	0.67	-0.55	-0.57
2	3	3	0.52	0.73	-0.52	-0.58
2	3	4	0.52	0.70	-0.40	-0.47
2	3	5	0.49	0.69	-0.38	-0.35
3	2	4	0.45	0.62	-0.46	-0.41
3	2	5	0.58	0.72	-0.55	-0.47
3	3	4	0.58	0.74	-0.53	-0.57
3	3	5	0.47	0.76	-0.35	-0.38
mean ± SD			$\mathbf{0.50 \pm 0.06}$	$\mathbf{0.68 \pm 0.06}$	$\mathbf{-0.46 \pm 0.08}$	$\mathbf{-0.45 \pm 0.09}$

Table C.5.: Pearson correlation coefficients, r, for the relationship of HI and V_{95} to the motion amplitudes in the superior-inferior (SI) and anterior-posterior (AP) direction. The focus levels 2, 3, 4 and 5 approximately correspond to beam FWHM of 6, 8, 10 and 15 mm.

C.5 Normal tissue exposure — treatment simulations

plan par. in mm			liver dose [Gy (RBE)]		lung dose [Gy (RBE)]	
Δs	Δz	$\overline{\text{FWHM}}$	mean	max	mean	max
2	2	6.1	1.3 (1.3)	10.4 (9.2)	0.0 (0.0)	6.0 (5.7)
2	2	8.2	1.5 (1.5)	10.0 (8.9)	0.0 (0.0)	6.0 (5.7)
2	2	10.1	1.6 (1.6)	9.8 (8.7)	0.1 (0.0)	6.0 (5.7)
2	2	15.0	1.9 (1.9)	9.2 (8.8)	0.1 (0.1)	5.9 (5.8)
2	3	6.1	1.3 (1.3)	11.1 (9.8)	0.0 (0.0)	6.0 (5.8)
2	3	8.2	1.5 (1.5)	10.2 (9.3)	0.0 (0.0)	6.1 (5.8)
2	3	10.1	1.6 (1.6)	10.1 (9.0)	0.1 (0.0)	5.9 (5.8)
2	3	15.0	1.9 (1.9)	9.9 (8.9)	0.1 (0.1)	6.0 (5.8)
3	2	10.1	1.6 (1.6)	10.0 (9.0)	0.0 (0.0)	5.9 (5.8)
3	2	15.0	1.9 (1.9)	9.4 (8.8)	0.1 (0.1)	5.9 (5.8)
3	3	10.1	1.6 (1.6)	10.7 (9.2)	0.0 (0.0)	6.2 (5.7)
3	3	15.0	2.1 (2.1)	10.1 (8.7)	0.1 (0.1)	6.2 (5.8)

Table C.6.: Mean and maximum dose received by liver and lung in patient A1 for varying plan parameters. Listed are the maximum and minimum values (in brackets) found over all simulations with different motion parameters.

plan par. in mm			liver dose [Gy (RBE)]		lung dose [Gy (RBE)]	
Δs	Δz	$\overline{\text{FWHM}}$	mean	max	mean	max
2	2	6.1	0.6 (0.6)	10.5 (9.8)	0.8 (0.7)	9.4 (8.2)
2	2	8.3	0.7 (0.7)	10.4 (9.5)	0.9 (0.9)	9.1 (8.3)
2	2	10.1	0.7 (0.7)	9.9 (9.2)	1.0 (0.9)	8.8 (8.2)
2	2	15.0	0.9 (0.8)	9.4 (8.9)	1.5 (1.4)	9.1 (8.3)
2	3	6.1	0.6 (0.6)	12.0 (10.1)	0.8 (0.7)	10.0 (8.2)
2	3	8.3	0.6 (0.6)	10.8 (9.7)	0.9 (0.8)	9.6 (8.8)
2	3	10.1	0.7 (0.7)	10.5 (9.4)	1.0 (0.9)	9.4 (8.6)
2	3	15.0	0.8 (0.8)	9.4 (9.0)	1.5 (1.4)	9.4 (8.3)
3	2	10.1	0.7 (0.7)	9.8 (9.3)	1.1 (1.0)	9.1 (8.4)
3	2	15.0	0.8 (0.8)	9.5 (8.8)	1.6 (1.6)	9.4 (8.5)
3	3	10.2	0.7 (0.7)	10.4 (9.7)	1.0 (1.0)	10.0 (8.4)
3	3	15.0	0.8 (0.8)	9.6 (8.9)	1.6 (1.5)	9.3 (8.6)

Table C.7.: Mean and maximum dose received by liver and lung in patient A2 for varying plan parameters. Listed are the maximum and minimum values (in brackets) found over all simulations with different motion parameters.

plan par. in mm			liver dose [Gy (RBE)]		lung dose [Gy (RBE)]	
Δs	Δz	$\overline{\text{FWHM}}$	mean	max	mean	max
2	2	6.6	0.8 (0.8)	9.9 (9.0)	0.0 (0.0)	0.6 (0.1)
2	2	8.9	0.8 (0.8)	9.5 (8.9)	0.0 (0.0)	1.5 (0.7)
2	2	10.7	0.9 (0.9)	9.4 (8.8)	0.0 (0.0)	1.8 (1.3)
2	2	15.0	1.0 (1.0)	9.4 (8.8)	0.0 (0.0)	2.8 (2.6)
2	3	6.6	0.8 (0.8)	9.9 (9.1)	0.0 (0.0)	0.5 (0.3)
2	3	8.9	0.8 (0.8)	9.7 (9.1)	0.0 (0.0)	1.4 (1.2)
2	3	10.7	0.9 (0.8)	9.5 (8.9)	0.0 (0.0)	1.7 (1.5)
2	3	15.0	1.0 (1.0)	9.1 (8.7)	0.0 (0.0)	3.0 (2.8)
3	2	10.7	0.9 (0.9)	9.4 (8.9)	0.0 (0.0)	1.7 (1.5)
3	2	15.0	1.0 (1.0)	9.0 (8.7)	0.0 (0.0)	2.8 (2.5)
3	3	10.7	0.9 (0.8)	9.7 (9.0)	0.0 (0.0)	1.7 (1.5)
3	3	15.0	1.0 (0.9)	9.5 (8.8)	0.0 (0.0)	2.7 (2.6)

Table C.8.: Mean and maximum dose received by liver and lung in patient A3 for varying plan parameters. Listed are the maximum and minimum values (in brackets) found over all simulations with different motion parameters.

plan par. in mm			liver dose [Gy (RBE)]		lung dose [Gy (RBE)]	
Δs	Δz	$\overline{\text{FWHM}}$	mean	max	mean	max
2	2	6.7	1.5 (1.5)	11.3 (10.1)	0.2 (0.2)	9.9 (8.6)
2	2	8.8	1.6 (1.5)	10.8 (9.6)	0.3 (0.2)	9.0 (8.4)
2	2	10.7	1.6 (1.6)	10.5 (9.5)	0.3 (0.3)	9.1 (8.3)
2	2	15.0	1.8 (1.8)	9.5 (9.1)	0.6 (0.5)	8.7 (8.3)
2	3	6.7	1.4 (1.4)	12.5 (10.4)	0.2 (0.2)	10.0 (8.9)
2	3	8.8	1.5 (1.5)	11.9 (10.3)	0.3 (0.2)	10.0 (8.7)
2	3	10.7	1.6 (1.6)	11.1 (9.7)	0.3 (0.2)	9.3 (8.5)
2	3	15.0	1.8 (1.8)	10.6 (9.2)	0.6 (0.5)	9.0 (8.4)
3	2	10.7	1.6 (1.6)	10.2 (9.4)	0.4 (0.3)	9.1 (8.4)
3	2	15.0	1.8 (1.8)	9.5 (9.0)	0.6 (0.5)	8.8 (8.4)
3	3	10.7	1.6 (1.6)	11.6 (9.9)	0.4 (0.3)	9.6 (8.8)
3	3	15.0	1.7 (1.7)	10.3 (9.4)	0.6 (0.5)	9.0 (8.4)

Table C.9.: Mean and maximum dose received by liver and lung in patient A4 for varying plan parameters. Listed are the maximum and minimum values (in brackets) found over all simulations with different motion parameters.

plan par. in mm			liver dose [Gy (RBE)]		lung dose [Gy (RBE)]	
Δs	Δz	$\overline{\text{FWHM}}$	mean	max	mean	max
2	2	6.3	1.4 (1.4)	11.5 (11.0)	0.2 (0.2)	7.7 (6.9)
2	2	8.5	1.6 (1.6)	10.9 (10.7)	0.3 (0.3)	8.5 (6.9)
2	2	10.3	1.7 (1.7)	10.5 (9.6)	0.4 (0.3)	7.9 (7.1)
2	2	15.0	1.9 (1.9)	9.7 (8.9)	0.8 (0.7)	7.8 (7.5)
2	3	6.3	1.4 (1.4)	11.5 (10.8)	0.2 (0.2)	7.6 (6.7)
2	3	8.5	1.6 (1.6)	10.8 (10.1)	0.3 (0.3)	8.1 (7.3)
2	3	10.3	1.7 (1.7)	10.3 (9.2)	0.4 (0.3)	7.8 (7.5)
2	3	15.0	2.0 (2.0)	9.2 (8.7)	0.8 (0.7)	7.9 (7.8)
3	2	10.3	1.6 (1.6)	10.5 (10.4)	0.4 (0.3)	8.6 (6.8)
3	2	15.0	2.0 (2.0)	9.5 (8.8)	0.8 (0.7)	7.9 (7.7)
3	3	10.3	1.6 (1.6)	10.3 (10.0)	0.4 (0.3)	7.8 (7.0)
3	3	15.0	1.9 (1.9)	9.1 (8.8)	0.8 (0.7)	8.0 (7.8)

Table C.10.: Mean and maximum dose received by liver and lung in patient G1 for varying plan parameters. Listed are the maximum and minimum values (in brackets) found over all simulations with different motion parameters.

plan par. in mm			liver dose [Gy (RBE)]		lung dose [Gy (RBE)]	
Δs	Δz	$\overline{\text{FWHM}}$	mean	max	mean	max
2	2	6.4	0.8 (0.7)	10.7 (10.5)	0.0 (0.0)	0.0 (0.0)
2	2	8.8	0.8 (0.8)	10.3 (9.9)	0.0 (0.0)	0.0 (0.0)
2	2	10.6	0.9 (0.9)	10.2 (9.9)	0.0 (0.0)	0.0 (0.0)
2	2	15.0	1.0 (1.0)	9.8 (9.1)	0.0 (0.0)	0.1 (0.1)
2	3	6.5	0.7 (0.7)	12.7 (12.3)	0.0 (0.0)	0.0 (0.0)
2	3	8.8	0.8 (0.8)	11.3 (10.5)	0.0 (0.0)	0.0 (0.0)
2	3	10.6	0.9 (0.8)	10.6 (9.6)	0.0 (0.0)	0.0 (0.0)
2	3	15.0	1.0 (1.0)	9.9 (9.3)	0.0 (0.0)	0.1 (0.0)
3	2	10.6	0.9 (0.9)	10.4 (10.0)	0.0 (0.0)	0.0 (0.0)
3	2	15.0	1.0 (0.9)	9.8 (9.2)	0.0 (0.0)	0.1 (0.1)
3	3	10.6	0.9 (0.8)	10.6 (9.7)	0.0 (0.0)	0.0 (0.0)
3	3	15.0	0.9 (0.9)	9.6 (9.1)	0.0 (0.0)	0.1 (0.0)

Table C.11.: Mean and maximum dose received by liver and lung in patient G2 for varying plan parameters. Listed are the maximum and minimum values (in brackets) found over all simulations with different motion parameters.

plan par. in mm			liver dose [Gy (RBE)]		lung dose [Gy (RBE)]	
Δs	Δz	$\overline{\text{FWHM}}$	mean	max	mean	max
2	2	6.3	1.7 (1.7)	9.8 (8.8)	0.0 (0.0)	6.6 (6.5)
2	2	8.5	2.0 (1.9)	9.3 (8.8)	0.0 (0.0)	6.6 (6.6)
2	2	10.3	2.2 (2.2)	9.1 (8.8)	0.0 (0.0)	6.7 (6.5)
2	2	15.0	2.9 (2.9)	9.0 (8.7)	0.0 (0.0)	6.8 (6.6)
2	3	6.3	1.7 (1.6)	9.7 (9.4)	0.0 (0.0)	6.7 (6.4)
2	3	8.5	1.9 (1.9)	9.3 (9.1)	0.0 (0.0)	6.7 (6.4)
2	3	10.3	2.2 (2.2)	9.2 (9.1)	0.0 (0.0)	6.8 (6.4)
2	3	15.0	2.8 (2.8)	8.9 (8.6)	0.0 (0.0)	6.7 (6.5)
3	2	10.3	2.2 (2.2)	9.0 (8.6)	0.0 (0.0)	6.8 (6.6)
3	2	15.0	2.9 (2.9)	8.8 (8.6)	0.0 (0.0)	6.8 (6.7)
3	3	10.3	2.2 (2.2)	9.1 (8.8)	0.0 (0.0)	6.8 (6.7)
3	3	15.0	2.9 (2.8)	8.8 (8.7)	0.0 (0.0)	6.8 (6.6)

Table C.12.: Mean and maximum dose received by liver and lung in patient G3 for varying plan parameters. Listed are the maximum and minimum values (in brackets) found over all simulations with different motion parameters.

plan par. in mm			liver dose [Gy (RBE)]		lung dose [Gy (RBE)]	
Δs	Δz	$\overline{\text{FWHM}}$	mean	max	mean	max
2	2	6.1	0.7 (0.7)	9.9 (9.2)	n/a	n/a
2	2	8.3	0.9 (0.8)	9.3 (9.0)	n/a	n/a
2	2	10.1	1.0 (1.0)	9.2 (9.0)	n/a	n/a
2	2	15.0	1.3 (1.3)	9.2 (8.9)	n/a	n/a
2	3	6.1	0.7 (0.7)	10.2 (9.7)	n/a	n/a
2	3	8.3	0.9 (0.8)	9.7 (9.3)	n/a	n/a
2	3	10.2	1.0 (1.0)	9.8 (8.9)	n/a	n/a
2	3	15.0	1.3 (1.2)	9.1 (8.9)	n/a	n/a
3	2	10.1	1.0 (1.0)	9.2 (9.1)	n/a	n/a
3	2	15.0	1.3 (1.3)	8.9 (8.8)	n/a	n/a
3	3	10.2	1.0 (1.0)	9.6 (9.2)	n/a	n/a
3	3	15.0	1.3 (1.2)	9.1 (8.9)	n/a	n/a

Table C.13.: Mean and maximum dose received by liver and lung in patient G4 for varying plan parameters. Listed are the maximum and minimum values (in brackets) found over all simulations with different motion parameters.

Bibliography

Accuray (2011). CyberKnife VSI treatment planning. Official Accuray CyberKnife website.

Ahlen, S. P. (1980). Theoretical and experimental aspects of the energy loss of relativistic heavily ionizing particles. *Rev. Mod. Phys.*, 52(1):121.

Alpen, E. L. (1998). *Radiation biophysics*. Academic Press.

Amaldi, H. and Kraft, G. (2005). Recent applications of synchrotrons in cancer therapy with carbon ions. *europhysics news*, 36(4):114–118.

Balter, J. M., Wright, J. N., Newell, L. J., Friemel, B., Dimmer, S., Cheng, Y., Wong, J., Vertatschitsch, E., and Mate, T. P. (2005). Accuracy of a wireless localization system for radiotherapy. *Int. J. Radiat. Oncol. Biol. Phys.*, 61(3):933–937.

Barkas, W. H. and Berger, M. J. (1964). Tables of energy losses and ranges of heavy charged particles. *National Aeronautics and Space Administration*, (NASA-SP-3013):131.

Belderbos, J., Heemsbergen, W., Hoogeman, M., Pengel, K., Rossi, M., and Lebesque, J. (2005). Acute esophageal toxicity in non-small cell lung cancer patients after high dose conformal radiotherapy. *Radiother. Oncol.*, 75:157–164.

Berbeco, R. I., Jiang, S. B., Sharp, G. C., Chen, G. T. Y., Mostafavi, H., and Shirato, H. (2004). Integrated radiotherapy imaging system (iris): design considerations of tumour tracking with linac gantry-mounted diagnostic x-ray systems with flat-panel detectors. *Phys. Med. Biol.*, 49(2):243–255.

Berbeco, R. I., Mostafavi, H., Sharp, G. C., and Jiang, S. B. (2005). Towards fluoroscopic respiratory gating for lung tumours without radiopaque markers. *Phys. Med. Biol.*, 50(19):4481–4490.

Berbeco, R. I., Nishioka, S., Shirato, H., and Jiang, S. B. (2006). Residual motion of lung tumors in end-of-inhale respiratory gated radiotherapy based on external surrogates. *Med. Phys.*, 33(11):4149.

Bert, C. (2006). *Bestrahlungsplanung fuer bewegte Zielvolumina in der Tumortherapie mit gescanntem Kohlenstoffstrahl*. Thesis/dissertation, TU Darmstadt.

Bert, C. and Durante, M. (2011). Motion in radiotherapy: particle therapy. *Phys. Med. Biol.*, 56:R113–R144.

Bert, C., Gemmel, A., Chaudhri, N., Lüchtenborg, R., Saito, N., Durante, M., and Rietzel, E. (2009). Rescanning to mitigate the impact of motion in scanned particle therapy. Report.

Bert, C., Gemmel, A., Saito, N., Chaudhri, N., Schardt, D., Durante, M., Kraft, G., and Rietzel, E. (2010). Dosimetric precision of an ion beam tracking system. *Radiat. Oncol.*, 5(1):61.

Bert, C., Groezinger, S. O., and Rietzel, E. (2008). Quantification of interplay effects of scanned particle beams and moving targets. *Phys. Med. Biol.*, 53(9):2253–2265.

Bert, C., Richter, D., Durante, M., and Rietzel, E. (2012). Scanned carbon beam irradiation of moving films: comparison of measured and calculated response. *Radiat. Oncol.*, 7(1):55.

Bert, C. and Rietzel, E. (2007). 4D treatment planning for scanned ion beams. *Radiat. Oncol.*, 2(24).

Bethe, H. (1930). Zur Theorie des Durchgangs schneller Korpuskularstrahlung durch Materie. *Annalen der Physik*, 5(5):325–400.

Bloch, F. (1933a). Bremsvermögen von Atomen mit mehreren Elektronen. *Zeitschrift für Physik A Hadrons and Nuclei*, 81(5):363–376.

Bloch, F. (1933b). Zur Bremsung rasch bewegter Teilchen beim Durchgang durch Materie. *Annalen der Physik*, 5(16):285–321.

Bohr, N. (1940). Scattering and stopping of fission fragments. *Phys. Rev.*, 58(7):654–655.

Bortfeld, T., Jiang, S. B., and Rietzel, E. (2004). Effects of motion on the total dose distribution. *Semin. Radiat. Oncol.*, 14(1):41–51.

Bragg, W. (1905). On the a-particles of radium and their loss of range in passing through various atoms and molecules. *Philos. Mag.*, 10:318–340.

Britton, K. R., Starkschall, G., Tucker, S. L., Pan, T., Nelson, C., Chang, J. Y., Cox, J. D., Mohan, R., and Komaki, R. (2007). Assessment of gross tumor volume regression and motion changes during radiotherapy for non-small-cell lung cancer as measured by four-dimensional computed tomography. *Int. J. Radiat. Oncol. Biol. Phys.*, 68(4):1036–1046.

Brock, K. K. (2010). Results of a multi-institution deformable registration accuracy study (midras). *Int. J. Radiat. Oncol. Biol. Phys.*, 76(2):583–596.

Brock, K. K. and Dawson, L. A. (2010). Adaptive management of liver cancer radiotherapy. *Semin. Radiat. Oncol.*, 20(2):107–115.

Brock, K. K., Dawson, L. A., Sharpe, M. B., Moseley, D. J., and Jaffray, D. A. (2006). Feasibility of a novel deformable image registration technique to facilitate classification, targeting, and monitoring of tumor and normal tissue. *Int. J. Radiat. Oncol. Biol. Phys.*, 64(4):1245–1254.

Brown, W. T., Wu, X., Fayad, F., Fowler, J. F., Amendola, B. E., Garcia, S., Han, H., de la, Z. A., Bossart, E., Huang, Z., and Schwade, J. G. (2007). Cyberknife radiosurgery for stage I lung cancer: results at 36 months. *Clin. Lung Cancer.*, 8(8):488–492.

Case, R. B., Moseley, D. J., Sonke, J. J., Eccles, C. L., Dinniwell, R. E., Kim, J., Bezjak, A., Milosevic, M., Brock, K. K., and Dawson, L. A. (2010). Interfraction and intrafraction changes in amplitude of breathing motion in stereotactic liver radiotherapy. *Int. J. Radiat. Oncol. Biol. Phys.*, 77(3):918–925.

Chatterjee, A. and Schaefer, H. J. (1976). Microdosimetric structure of heavy ion tracks in tissue. *Radiat. Environ. Biophys.*, 13:215–227.

Chen, G. T., Kung, J. H., and Rietzel, E. (2007). Four-dimensional imaging and treatment planning of moving targets. *Front. Radiat. Ther. Oncol.*, 40:59–71.

Chiba, T., Tokuuye, K., Matsuzaki, Y., Sugahara, S., Chuganji, Y., Kagei, K., Shoda, J., Hata, M., Abei, M., Igaki, H., Tanaka, N., and Akine, Y. (2005). Proton beam therapy for hepatocellular carcinoma: a retrospective review of 162 patients. *Clin. Cancer Res.*, 11(10):3799–3805.

Chu, W. T., Ludewigt, B. A., and Renner, T. R. (1993). Instrumentation for treatment of cancer using proton and light-ion beams. *Rev. Sci. Instrum.*, 64(8):2055–2122.

Combs, S. E., Jäkel, O., Haberer, T., and Debus, J. (2010). Particle therapy at the Heidelberg Ion Therapy Center (HIT) - Integrated research-driven university-hospital-based radiation oncology service in Heidelberg, Germany. *Radiother. Oncol.*, 95(1):41–44.

Dawson, L. A., McGinn, C. J., Normolle, D., Ten Haken, R. K., Walker, S., Ensminger, W., and Lawrence, T. S. (2000). Escalated focal liver radiation and concurrent hepatic artery fluorodeoxyuridine for unresectable intrahepatic malignancies. *J. Clin. Oncol.*, 18(11):2210–2218.

de Orban, X., Janssens, G., Bosmans, G., De, C. M., Dekker, A., Buijsen, J., van, B. A., De, R. D., Macq, B., and Lambin, P. (2007). Tumour delineation and cumulative dose computation in radiotherapy based on deformable registration of respiratory correlated CT images of lung cancer patients. *Radiother. Oncol.*, 85(2):232–238.

Durante, M. and Loeffler, J. S. (2010). Charged particles in radiation oncology. *Nat. Rev. Clin. Oncol.*, 7(1):37–43.

Eccles, C. L., Patel, R., Simeonov, A. K., Lockwood, G., Haider, M., and Dawson, L. A. (2011). Comparison of liver tumor motion with and without abdominal compression using cine-magnetic resonance imaging. *Int. J. Radiat. Oncol. Biol. Phys.*, 79(2):602–608.

Eichelberg, M., Riesmeier, J., Wilkens, T., Hewett, A. J., Barth, A., and Jensch, P. (2004). Ten years of medical imaging standardization and prototypical implementation: the DICOM standard and the OFFIS DICOM Toolkit (DCMTK). In Ratib, O. M. and Huang, H. K., editors, *Medical Imaging 2004: PACS and Imaging Informatics*, volume 5371, pages 57 – 68.

Elsaesser, T., Brons, S., Psonka, K., Scholz, M., Gudowska-Nowak, E., and Taucher-Scholz, G. (2008). Biophysical modeling of fragment length distributions of DNA plasmids after x and heavy-ion irradiation analyzed by atomic force microscopy. *Radiat. Res.*, 169(6):649–659.

Elsaesser, T., Gemmel, A., Scholz, M., Schardt, D., and Krämer, M. (2009). Relevance of very low energy ions for heavy ion therapy. *Phys. Med. Biol.*, 54(7):N101–N106.

Elsaesser, T. and Scholz, M. (2006). Improvement of the local effect model (LEM)–implications of clustered DNA damage. *Radiat. Prot. Dosimetry.*, 122(1-4):475–477.

Elsaesser, T. and Scholz, M. (2007). Cluster effects within the local effect model. *Radiat. Res.*, 167(3):319–329.

Engelsman, M., Rietzel, E., and Kooy, H. M. (2006). Four-dimensional proton treatment planning for lung tumors. *Int. J. Radiat. Oncol. Biol. Phys.*, 64(5):1589–1595.

Faggiano, E., Fiorino, C., Scalco, E., Broggi, S., Cattaneo, M., Maggiulli, E., Dell'Oca, I., Di Muzio, N., Calandrino, R., and Rizzo, G. (2011). An automatic contour propagation method to follow parotid gland deformation during head-and-neck cancer tomotherapy. *Phys. Med. Biol.*, 56(3):775–791.

Fano, U. (1963). Penetration of protons, alpha particles, and mesons. *Ann. Rev. Nucl. Sci.*, 13(1):1–66.

Feuvret, L., Noël, G., Mazeron, J., and Bey, P. (2006). Conformity index: a review. *Int. J. Radiat. Oncol. Biol. Phys.*, 64(2):333–342.

Fokas, E., Kraft, G., An, H., and Engenhart-Cabillic, R. (2009). Ion beam radiobiology and cancer: Time to update ourselves. *BBA-Rev. Cancer*, 1796(2):216–229.

Fokdal, L., Honoré, H., Høyer, M., Meldgaard, P., Fode, K., and von der Maase, H. (2004). Impact of changes in bladder and rectal filling volume on organ motion and dose distribution of the bladder in radiotherapy for urinary bladder cancer. *Int. J. Radiat. Oncol. Biol. Phys.*, 59(2):436–444.

Ford, E. C., Mageras, G. S., Yorke, E., and Ling, C. C. (2003). Respiration-correlated spiral CT: A method of measuring respiratory-induced anatomic motion for radiation treatment planning. *Med. Phys.*, 30(1):88–97.

Fowler, J. F. (1989). The Linear-Quadratic Formula and Progress in Fractionated Radiotherapy. *Brit. J. Radiol.*, 62(740):679–694.

Freeman, H. and Davis, L. S. (1977). A Corner-Finding algorithm for Chain-Coded curves. *IEEE Transactions on Computers*, C-26(3):297–303.

Frigo, M. and Johnson, S. G. (2005). The design and implementation of FFTW3. *Proceedings of the IEEE*, 93(2):216–231.

Fuji, H., Asada, Y., Numano, M., Yamashita, H., Nishimura, T., Hashimoto, T., Harada, H., Asakura, H., and Murayama, S. (2009). Residual motion and duty time in respiratory gating radiotherapy using individualized or population-based windows. *Int. J. Radiat. Oncol. Biol. Phys.*, 75(2):564–570.

Furukawa, T., Inaniwa, T., Sato, S., Shirai, T., Mori, S., Takeshita, E., Mizushima, K., Himukai, T., and Noda, K. (2010a). Moving target irradiation with fast rescanning and gating in particle therapy. *Med. Phys.*, 37(9):4874–4879.

Furukawa, T., Inaniwa, T., Sato, S., Shirai, T., Takei, Y., Takeshita, E., Mizushima, K., Iwata, Y., Himukai, T., Mori, S., Fukuda, S., Minohara, S., Takada, E., Murakami, T., and Noda, K. (2010b). Performance of the NIRS fast scanning system for heavy-ion radiotherapy. *Med. Phys.*, 37(11):5672–5682.

Furukawa, T., Inaniwa, T., Sato, S., Tomitani, T., Minohara, S., Noda, K., and Kanai, T. (2007). Design study of a raster scanning system for moving target irradiation in heavy-ion radiotherapy. *Med. Phys.*, 34(3):1085–1097.

Furukawa, T., Noda, K., Uesugi, T. H., Naruse, T., and Shibuya, S. (2005). Intensity control in RF-knockout extraction for scanning irradiation. *Nucl. Instrum. Meth. B*, 240:32–35.

Gaede, S., Olsthoorn, J., Louie, A. V., Palma, D., Yu, E., Yaremko, B., Ahmad, B., Chen, J., Bzdusek, K., and Rodrigues, G. (2011). An evaluation of an automated 4D-CT contour propagation tool to define an internal gross tumour volume for lung cancer radiotherapy. *Radiother. Oncol.*, 101(2):322–328.

Geiss, O. B., Schardt, D., Voss, B., Krämer, M., and Kraft, G. (1999). Correlation between CT number and water equivalent thickness. Report.

Gemmel, A., Bert, C., Saito, N., Chaudhri, N., Iancu, G., Schardt, D., and Rietzel, E. (2008). Biological dosimetry for motion compensated targets. Report.

Gemmel, A., Rietzel, E., Kraft, G., Durante, M., and Bert, C. (2011). Calculation and experimental verification of the RBE-weighted dose for scanned ion beams in the presence of target motion. *Phys. Med. Biol.*, 56:7337–7351.

German Federal Statistical Office (2012). Jeder Vierte starb 2010 an Krebs. Official Destatis press release No. 041.

Ghilezan, M., Yan, D., and Martinez, A. (2010). Adaptive radiation therapy for prostate cancer. *Semin. Radiat. Oncol.*, 20(2):130–137.

Glassner, A. S. (1989). *An Introduction to Ray Tracing*. Academic Pr Inc.

Goldhaber, A. S. and Heckman, H. H. (1978). High energy interactions of nuclei. *Ann. Rev. Nucl. Part. Sci.*, 28(1):161–205.

Gottschalk, B., Koehler, A. M., Schneider, R. J., Sisterson, J. M., and Wagner, M. S. (1993). Multiple coulomb scattering of 160 MeV protons. *Nucl. Instrum. Meth. B*, 74(4):467–490.

Gottschalk, B. and Pedroni, E. (2008). Treatment delivery systems. In DeLaney, T. F. and Kooy, H. M., editors, *Proton and charged particle radiotherapy*, book chapter 5, pages 33–49. Lippincott Williams and Wilkins.

Graeff, C., Durante, M., and Bert, C. (2012). Motion mitigation in intensity modulated particle therapy by internal target volumes covering range changes. *Med. Phys.* Submitted.

Groezinger, S. O., Rietzel, E., Li, Q., Bert, C., Haberer, T., and Kraft, G. (2006). Simulations to design an online motion compensation system for scanned particle beams. *Phys. Med. Biol.*, 51(14):3517–3531.

Haberer, T., Becher, W., Schardt, D., and Kraft, G. (1993). Magnetic scanning system for heavy ion therapy. *Nucl. Instrum. Meth. A*, 330:296–305.

Haberer, T., Debus, J., Eickhoff, H., Jäkel, O., Schulz-Ertner, D., and Weber, U. (2004). The Heidelberg Ion Therapy Center. *Radiother. Oncol.*, 73 Suppl 2:S186–S190.

Hales, T. C. (2007). The Jordan Curve Theorem, Formally and Informally. *Am. Math. Mon.*, 114(10):882–894.

Hartkens, T. (1993). *Measuring, analysing, and visualizing brain deformation using non-rigid registration*. Thesis/dissertation, King's College London.

Hashimoto, T., Tokuuye, K., Fukumitsu, N., Igaki, H., Hata, M., Kagei, K., Sugahara, S., Ohara, K., Matsuzaki, Y., and Akine, Y. (2006). Repeated proton beam therapy for hepatocellular carcinoma. *Int. J. Radiat. Oncol. Biol. Phys.*, 65(1):196–202.

Hättner, E., Iwase, H., and Schardt, D. (2006). Experimental fragmentation studies with 12C therapy beams. *Radiat. Prot. Dosimetry.*, 122(1-4):485–487.

Heeg, P., Eickhoff, H., and Haberer, T. (2004). Conception of heavy ion beam therapy at Heidelberg University (HICAT). *Z. Med. Phys.*, 14(1):17–24.

Hill, D. L., Batchelor, P. G., Holden, M., and Hawkes, D. J. (2001). Medical image registration. *Phys. Med. Biol.*, 46(3):R1–45.

Hirao, Y., Ogawa, H., Yamada, S., Sato, Y., Yamada, T., Sato, K., Itano, A., Kanazawa, M., Noda, K., Kawachi, K., Endo, M., Kanai, T., Kohno, T., Sudou, M., Minohara, S., Kitagawa, A., Soga, F., Takada, E., Watanabe, S., Endo, K., Kumada, M., and Matsumoto, S. (1992). Heavy ion synchrotron for medical use –HIMAC project at NIRS-Japan–. *Nuclear Physics A*, 538:541–550.

Hof, H., Herfarth, K. K., Muenter, M. W., Hoess, A., Motsch, J., Wannenmacher, M., and Debus, J. (2003). Stereotactic single-dose radiotherapy of stage I non-small-cell lung cancer (nsclc). *Int. J. Radiat. Oncol. Biol. Phys.*, 56(2):335–341.

Hoisak, J. D. P., Sixel, K. E., Tirona, R., Cheung, P. C. F., and Pignol, J. P. (2004). Correlation of lung tumor motion with external surrogate indicators of respiration. *Int. J. Radiat. Oncol. Biol. Phys.*, 60(4):1298–1306.

Hüfner, J. (1985). Heavy fragments produced in proton-nucleus and nucleus-nucleus collisions at relativistic energies. *Phys. Rep.*, 125(4):129–185.

ICRU (1984). Stopping powers for electrons and positrons. ICRU report no. 37.

ICRU (1993a). Prescribing, recording and reporting photon beam therapy. ICRU report no. 50.

ICRU (1993b). Quantities and units in radiation protection dosimetry. ICRU report no. 51.

ICRU (1993). Stopping powers and ranges for protons and alpha particles. ICRU report no. 49.

ICRU (1999). Prescribing, recording and reporting photon beam therapy, supplement to ICRU report 50. ICRU report no. 62.

ICRU (2007). Prescribing, recording, and reporting proton-beam therapy. ICRU report no. 78.

Inaniwa, T., Furukawa, T., Kase, Y., Matsufuji, N., Toshito, T., Matsumoto, Y., Furusawa, Y., and Noda, K. (2010). Treatment planning for a scanned carbon beam with a modified microdosimetric kinetic model. *Phys. Med. Biol.*, 55(22):6721–6737.

Inaniwa, T., Kohno, T., Tomitani, T., and Sato, S. (2008). Monitoring the irradiation field of 12C and 16O SOBP beams using positron emitters produced through projectile fragmentation reactions. *Phys. Med. Biol.*, 53(3):529–542.

Ionascu, D., Jiang, S. B., Nishioka, S., Shirato, H., and Berbeco, R. I. (2007). Internal-external correlation investigations of respiratory induced motion of lung tumors. *Med. Phys.*, 34(10):3893–3903.

Iwata, H., Murakami, M., Demizu, Y., Miyawaki, D., Terashima, K., Niwa, Y., Mima, M., Akagi, T., Hishikawa, Y., and Shibamoto, Y. (2010). High-dose proton therapy and carbon-ion therapy for stage I nonsmall cell lung cancer. *Cancer*, 116(10):2476–2485.

Jäkel, O., Jacob, C., Schardt, D., Karger, C. P., and Hartmann, G. H. (2001a). Relation between carbon ion ranges and x-ray CT numbers. *Med. Phys.*, 28:701–703.

Jäkel, O., Krämer, M., Karger, C. P., and Debus, J. (2001b). Treatment planning for heavy ion radiotherapy: clinical implementation and application. *Phys. Med. Biol.*, 46(4):1101–1116.

Kang, J. H., Wilkens, J. J., and Oelfke, U. (2007). Demonstration of scan path optimization in proton therapy. *Med. Phys.*, 34(9):3457–3464.

Karger, C. P., Jäkel, O., and Hartmann, G. H. (1999). A system for three-dimensional dosimetric verification of treatment plans in intensity-modulated radiotherapy with heavy ions. *Med. Phys.*, 26(10):2125–2132.

Karger, C. P., Jäkel, O., Palmans, H., and Kanai, T. (2010). Dosimetry for ion beam radiotherapy. *Phys. Med. Biol.*, 55(21):R193–R234.

Kato, H., Tsujii, H., Miyamoto, T., Mizoe, J. E., Kamada, T., Tsuji, H., Yamada, S., Kandatsu, S., Yoshikawa, K., Obata, T., Ezawa, H., Morita, S., Tomizawa, M., Morimoto, N., Fujita, J., and Ohto, M. (2004). Results of the first prospective study of carbon ion radiotherapy for hepatocellular carcinoma with liver cirrhosis. *Int. J. Radiat. Oncol. Biol. Phys.*, 59(5):1468–1476.

Katz, R. and Cucinotta, F. (1999). Tracks to therapy. *Radiat. Meas.*, 31(1-6):379–388.

Keall, P. J. (2004). 4-dimensional computed tomography imaging and treatment planning. *Semin. Radiat. Oncol.*, 14(1):81–90.

Keall, P. J., Joshi, S., Vedam, S. S., Siebers, J. V., Kini, V. R., and Mohan, R. (2005). Four-dimensional radiotherapy planning for dmlc-based respiratory motion tracking. *Med. Phys.*, 32(4):942–951.

Keall, P. J., Kini, V. R., Vedam, S. S., and Mohan, R. (2001). Motion adaptive x-ray therapy: a feasibility study. *Phys. Med. Biol.*, 46(1):1–10.

Kessler, M. L. (2006). Image registration and data fusion in radiation therapy. *Br. J. Radiol.*, 79 Spec No 1:S99-108.:S99–108.

Kiefer, J. and Straaten, H. (1986). A model of ion track structure based on classical collision dynamics. *Phys. Med. Biol.*, 31(11):1201–1209.

Kilby, W., Dooley, J. R., Kuduvalli, G., Sayeh, S., and C. R. Maurer, J. (2010). The cyberknife robotic radiosurgery system in 2010. *Technol. Cancer Res. Treat.*, 9(5):433–452.

Knopf, A., Boye, D., Zhang, Y., and Lomax, A. J. (2010a). Current status of the 4D treatment planning approach at PSI.

Knopf, A., Hong, T. S., and Lomax, A. (2011). Scanned proton radiotherapy for mobile targets-the effectiveness of re-scanning in the context of different treatment planning approaches and for different motion characteristics. *Phys. Med. Biol.*, 56(22):7257–7271.

Knopf, A., Hug, E., and Lomax, A. (2010b). Scanned proton radiotherapy for mobile targets - which plan characteristics require rescanning, which maybe not?

Kong, F. M., Haken, R. T., Eisbruch, A., and Lawrence, T. S. (2005). Non-small cell lung cancer therapy-related pulmonary toxicity: An update on radiation pneumonitis and fibrosis. *Semin. Oncol.*, 32(S3):42.

Koto, M., Miyamoto, T., Yamamoto, N., Nishimura, H., Yamada, S., and Tsujii, H. (2004). Local control and recurrence of stage I non-small cell lung cancer after carbon ion radiotherapy. *Radiother. Oncol.*, 71(2):147–156.

Kraft, G. (2000). Tumor therapy with heavy charged particles. *Prog. Part. Nucl. Phys.*, 45(s2):s473–s544.

Kraft, G. and Kraft, S. D. (2009). Research needed for improving heavy-ion therapy. *New J. Phys.*, 11:025001.

Krämer, M. (1995). Calculation of heavy-ion track structure. *Nucl. Instrum. Meth. B*, 105(1-4):14–20.

Krämer, M. (2009). Swift ions in radiotherapy – treatment planning with TRiP98. *Nucl. Instrum. Meth. B*, 267(6):989–992.

Krämer, M. and Durante, M. (2010). Ion beam transport calculations and treatment plans in particle therapy. *Eur. Phys. J. D*, 60:8 pages.

Krämer, M., Jäkel, O., Haberer, T., Kraft, G., Schardt, D., and Weber, U. (2000). Treatment planning for heavy-ion radiotherapy: physical beam model and dose optimization. *Phys. Med. Biol.*, 45(11):3299–3317.

Krämer, M. and Scholz, M. (2000). Treatment planning for heavy-ion radiotherapy: calculation and optimization of biologically effective dose. *Phys. Med. Biol.*, 45(11):3319–3330.

Krämer, M., Wang, J. F., and Weyrather, W. (2003). Biological dosimetry of complex ion radiation fields. *Phys. Med. Biol.*, 48(14):2063–2070.

Kumazaki, Y., Akagi, T., Yanou, T., Suga, D., Hishikawa, Y., and Teshima, T. (2007). Determination of the mean excitation energy of water from proton beam ranges. *Radiat. Meas.*, 42(10):1683–1691.

Lambert, J., Suchowerska, N., McKenzie, D. R., and Jackson, M. (2005). Intrafractional motion during proton beam scanning. *Phys. Med. Biol.*, 50(20):4853–4862.

Langen, K. M. and Jones, D. T. L. (2001). Organ motion and its management. *Int. J. Radiat. Oncol. Biol. Phys.*, 50(1):265–278.

Li, Q., Groezinger, S. O., Haberer, T., Rietzel, E., and Kraft, G. (2004). Online compensation of target motion with scanned particle beams: simulation environment. *Phys. Med. Biol.*, 49(14):3029–3046.

Li, T., Thorndyke, B., Schreibmann, E., Yang, Y., and Xing, L. (2006). Model-based image reconstruction for four-dimensional PET. *Med. Phys.*, 33(5):1288–1298.

Liu, H. H., Balter, P., Tutt, T., Choi, B., Zhang, J., Wang, C., Chi, M., Luo, D., Pan, T., Hunjan, S., Starkschall, G., Rosen, I., Prado, K., Liao, Z., Chang, J., Komaki, R., Cox, J. D., Mohan, R., and Dong, L. (2007). Assessing respiration-induced tumor motion and internal target volume using four-dimensional computed tomography for radiotherapy of lung cancer. *Int. J. Radiat. Oncol. Biol. Phys.*, 68(2):531–540.

Llacer, J., Tobias, C. A., Holley, W. R., and Kanai, T. (1984). On-line characterization of heavy-ion beams with semiconductor detectors. *Med. Phys.*, 11(3):266–278.

Lu, H. M., Brett, R., Sharp, G., Safai, S., Jiang, S., Flanz, J., and Kooy, H. (2007). A respiratory-gated treatment system for proton therapy. *Med. Phys.*, 34(8):3273–3278.

Lu, H. M., Safai, S., Schneider, R., Adams, J. A., Chen, Y. L., Wolfgang, J. A., Sharp, G. C., Brett, R. C., Kirch, D. G., Hong, T. S., Delaney, T. F., Jiang, S. B., Kooy, H. M., and Chen, G. T. Y. (2006a). Respiratory-gated proton therapy treatment. In *Abstract Book PTCOG 44*.

Lu, W., Olivera, G. H., Chen, Q., Chen, M. L., and Ruchala, K. J. (2006b). Automatic re-contouring in 4D radiotherapy. *Phys. Med. Biol.*, 51(5):1077–1099.

Lu, W., Parikh, P. J., Hubenschmidt, J. P., Bradley, J. D., and Low, D. A. (2006c). A comparison between amplitude sorting and phase-angle sorting using external respiratory measurement for 4D CT. *Med. Phys.*, 33(8):2964–2974.

Lüchtenborg, R., Saito, N., Durante, M., and Bert, C. (2011). Experimental verification of a real-time compensation functionality for dose changes due to target motion in scanned particle therapy. *Med. Phys.*, 38(10):5448–5458.

Lujan, A. E., Larsen, E. W., Balter, J. M., and Haken, R. K. T. (1999). A method for incorporating organ motion due to breathing into 3D dose calculations. *Med. Phys.*, 26(5):715–720.

Lynch, W. G. (1987). Nuclear fragmentation in proton- and heavy-ion-induced reactions. *Ann. Rev. Nucl. Part. Sci.*, 37(1):493–535.

Lyons, R. G. (2010). *Understanding Digital Signal Processing*. Addison Wesley Pub Co Inc, 0003 edition.

Maccabee, H. D. and Ritter, M. A. (1974). Fragmentation of high-energy oxygen-ion beams in water. *Radiat. Res.*, 60:409–421.

McInerney, T. and Terzopoulos, D. (1996). Deformable models in medical image analysis: a survey. *Med. Image Anal.*, 1(2):91–108.

Minohara, S., Kanai, T., Endo, M., Noda, K., and Kanazawa, M. (2000). Respiratory gated irradiation system for heavy-ion radiotherapy. *Int. J. Radiat. Oncol. Biol. Phys.*, 47(4):1097–1103.

Mitaroff, A., Kraft-Weyrather, W., Geiss, O. B., and Kraft, G. (1998). Biological verification of heavy ion treatment planning. *Radiat. Environ. Biophys.*, 37(1):47–51.

Molière (1948). Theorie der Streuung schneller geladener Teilchen II, Mehrfach- und Vielfach-streuung. *Zeitschrift für Naturforschung*, 3a:78–97.

Montagnat, J. and Delingette, H. (2005). 4D deformable models with temporal constraints: application to 4D cardiac image segmentation. *Med. Image Anal.*, 9(1):87–100.

Mori, S., Lu, H., Wolfgang, J. A., Choi, N. C., and Chen, G. T. Y. (2009). Effects of interfractional anatomical changes on Water-Equivalent pathlength in Charged-Particle radiotherapy of lung cancer. *J. Radiat. Res.*, 50(6):513–519.

Moyers, M. F., Miller, D. W., Bush, D. A., and Slater, J. D. (2001). Methodologies and tools for proton beam design for lung tumors. *Int. J. Radiat. Oncol. Biol. Phys.*, 49(5):1429–1438.

Munro, T. R. (1970). The relative radiosensitivity of the nucleus and cytoplasm of chinese hamster fibroblasts. *Radiat. Res.*, 42(3):451–470.

Nakamura, K. and Particle Data Group (2010). Review of particle physics. *J. Phys. G: Nucl. Part. Phys.*, 37(7A):075021.

Naumann, J. (2011). personal communication.

Negoro, Y., Nagata, Y., Aoki, T., Mizowaki, T., Araki, N., Takayama, K., Kokubo, M., Yano, S., Koga, S., and Sasai, K. (2001). The effectiveness of an immobilization device in conformal radiotherapy for lung tumor: reduction of respiratory tumor movement and evaluation of the daily setup accuracy. *Int. J. Radiat. Oncol. Biol. Phys.*, 50(4):889–898.

Nihei, K., Ogino, T., Ishikura, S., and Nishimura, H. (2006). High-dose proton beam therapy for stage I non-small-cell lung cancer. *Int. J. Radiat. Oncol. Biol. Phys.*, 65(1):107–111.

Noda, K., Kanazawa, M., Itano, A., Takada, E., Torikoshi, M., Araki, N., Yoshizawa, J., Sato, K., Yamada, S., Ogawa, H., Itoh, H., and Noda, A. (1996). Slow beam extraction by a transverse RF field with AM and FM. *Nucl. Instrum. Meth. A*, 374:269–277.

Nohadani, O., Seco, J., and Bortfeld, T. (2010). Motion management with phase-adapted 4d-optimization. *Phys. Med. Biol.*, 55(17):5189–5202.

Paganetti, H., Jiang, H., Adams, J. A., Chen, G. T., and Rietzel, E. (2004). Monte carlo simulations with time-dependent geometries to investigate effects of organ motion with high temporal resolution. *Int. J. Radiat. Oncol. Biol. Phys.*, 60(3):942–950.

Paganetti, H., Jiang, H., and Trofimov, A. (2005). 4D monte carlo simulation of proton beam scanning: modelling of variations in time and space to study the interplay between scanning pattern and time-dependent patient geometry. *Phys. Med. Biol.*, 50(5):983–990.

Paganetti, H., Niemierko, A., Ancukiewicz, M., Gerweck, L. E., Goitein, M., Loeffler, J. S., and Suit, H. D. (2002). Relative biological effectiveness (RBE) values for proton beam therapy. *Int. J. Radiat. Oncol. Biol. Phys.*, 53(2):407–421.

Paretzke, H. G. (1986). Physical events of heavy ion interactions with matter. *Adv. Space Res.*, 6(11):67–73.

Paul, H. (2007). The mean ionization potential of water, and its connection to the range of energetic carbon ions in water. *Nucl. Instrum. Meth. B*, 255(2):435–437.

Pedroni, E., Bacher, R., Blattmann, H., Bohringer, T., Coray, A., Lomax, A., Lin, S., Munkel, G., Scheib, S., Schneider, U., and Tourovsky, A. (1995). The 200-MeV proton therapy project at the Paul Scherrer Institute: Conceptual design and practical realization. *Med. Phys.*, 22(1):37–53.

Phillips, M. H., Pedroni, E., Blattmann, H., Boehringer, T., Coray, A., and Scheib, S. (1992). Effects of respiratory motion on dose uniformity with a charged particle scanning method. *Phys. Med. Biol.*, 37(1):223–233.

PTCOG (2011). Particle therapy cooperative group. Internet Communication.

Puck, T. T. and Marcus, P. I. (1955). A rapid method for viable cell titration and clone production with hela cells in tissue culture: The use of x-irradiated cells to supply conditioning factors. *Proc. Natl. Acad. Sci. USA*, 41(7):432–437.

Ragan, D., Starkschall, G., McNutt, T., Kaus, M., Guerrero, T., and Stevens, C. W. (2005). Semi-automated four-dimensional computed tomography segmentation using deformable models. *Med. Phys.*, 32(7):2254.

Rengan, R., Rosenzweig, K., Venkatraman, E., Koutcher, L., Fox, J., Nayak, R., Amols, H., Yorke, E., Jackson, A., and Ling, C. (2004). Improved local control with higher doses of radiation in large-volume stage III non–small-cell lung cancer. *Int. J. Radiat. Oncol. Biol. Phys.*, 60(3):741–747.

Rietzel, E. and Bert, C. (2010). Respiratory motion management in particle therapy. *Med. Phys.*, 37(2):449–460.

Rietzel, E. and Chen, G. T. (2006a). Improving retrospective sorting of 4D computed tomography data. *Med. Phys.*, 33(2):377–379.

Rietzel, E. and Chen, G. T. Y. (2006b). Deformable registration of 4D computed tomography data. *Med. Phys.*, 33(11):4423–4430.

Rietzel, E., Chen, G. T. Y., Choi, N. C., and Willet, C. G. (2005a). Four-dimensional image-based treatment planning: Target volume segmentation and dose calculation in the presence of respiratory motion. *Int. J. Radiat. Oncol. Biol. Phys.*, 61(5):1535–1550.

Rietzel, E., Liu, A. K., Doppke, K. P., Wolfgang, J. A., Chen, A. B., Chen, G. T., and Choi, N. C. (2006). Design of 4D treatment planning target volumes. *Int. J. Radiat. Oncol. Biol. Phys.*, 66(1):287–295.

Rietzel, E., Pan, T., and Chen, G. T. Y. (2005b). Four-dimensional computed tomography: Image formation and clinical protocol. *Med. Phys.*, 32(4):874–889.

Rietzel, E., Schardt, D., and Haberer, T. (2007). Range accuracy in carbon ion treatment planning based on CT-calibration with real tissue samples. *Radiat. Oncol.*, 2:14.

Robert Koch Institute (2012). Krebs in Deutschland 2007/2008. Official website.

Rosenzweig, K. E., Fox, J. L., Yorke, E., Amols, H., Jackson, A., Rusch, V., Kris, M. G., Ling, C. C., and Leibel, S. A. (2005). Results of a phase I study using three-dimensional conformal radiotherapy in the treatment of inoperable nonsmall cell lung carcinoma. *Cancer*, 103(10):2118–2127.

RPTC (2011). Erfahrungsbericht zweiter Monat klinischer Betrieb RPTC, Mai 2009. Internet Communication.

Ruan, D. and Keall, P. (2010). Online prediction of respiratory motion: multidimensional processing with low-dimensional feature learning. *Phys. Med. Biol.*, 55(11):3011–3025.

Saito, N., Bert, C., Chaudhri, N., Durante, M., Gemmel, A., Lüchtenborg, R., Schardt, D., and Rietzel, E. (2009). Technical status of the real-time beam tracking system. Report.

Sancar, A., Lindsey-Boltz, L. A., Unsal-Kacmaz, K., and Linn, S. (2004). Molecular mechanisms of mammalian DNA repair and the DNA damage checkpoints. *Annu. Rev. Biochem.*, 73:39-85.:39–85.

Sarfaraz, M., West, J. B., Skaryak, L., Mone, P., Coleman, C. M., Aliyar, A., and Brenner, M. (2009). Four-dimensional CT-based treatment planning with CyberKnife respiratory tracking system. In *8th Annual CyberKnife Users' Meeting*.

Sato, S., Furukawa, T., and Noda, K. (2007). Dynamic intensity control system with RF-knockout slow-extraction in the HIMAC synchrotron. *Nucl. Instrum. Meth. A*, 574(2):226–231.

Schall, I., Schardt, D., Geissel, H., Irnich, H., Kankeleit, E., Kraft, G., Magel, A., Mohar, M. F., Muenzenberg, G., Nickel, F., Scheidenberger, C., and Schwab, W. (1996). Charge-changing nuclear reactions of relativistic light-ion beams (5 <= z <= 10) passing through thick absorbers. *Nucl. Instrum. Meth. B*, 117:221–234.

Schardt, D., Elsaesser, T., and Schulz-Ertner, D. (2010). Heavy-ion tumor therapy: Physical and radiobiological benefits. *Rev. Mod. Phys.*, 82(1):383.

Schardt, D., Steidl, P., Krämer, M., Weber, U., Parodi, K., and Brons, S. (2008). Precision bragg-curve measurements for light-ion beams in water. Report.

Scheib, S. G. (1993). *Spotscanning mit Protonen: Experimentelle Resultate und Therapieplanung*. PhD thesis, ETH Zürich.

Schimmerling, W., Subramanian, T. S., McDonald, W. J., Kaplan, S. N., Sadoff, A., and Gabor, G. (1983). Beam analysis spectrometer for relativistic heavy ions. *Nucl. Instrum. Meth.*, 205(3):531–543.

Schlegel, W., Pastyr, O., Bortfeld, T., Becker, G., Schad, L., Gademann, G., and Lorenz, W. J. (1992). Computer systems and mechanical tools for stereotactically guided conformation therapy with linear accelerators. *Int. J. Radiat. Oncol. Biol. Phys.*, 24(4):781–787.

Scholz, M. (2003). Effects of ion radiation on cells and tissues. In Kausch, H., Anjum, N., Chevolot, Y., Gupta, B., Léonard, D., Mathieu, H. J., Pruitt, L. A., Ruiz-Taylor, L., and Scholz, M., editors, *Radiation Effects on Polymers for Biological Use*, volume 162, pages 95–155. Springer Berlin Heidelberg, Berlin, Heidelberg.

Scholz, M. and Kraft, G. (1994). Calculation of heavy ion inactivation probabilities based on track structure, x ray sensitivity and target size. *Radiat. Prot. Dosim.*, 52(1–4):29–33.

Scholz, M. and Kraft, G. (1996). Track structure and the calculation of biological effects of heavy charged particles. *Adv. Space Res.*, 18:5–14.

Schömers, C., Feldmeier, E., Haberer, T., Naumann, J., Panse, R., and Peters, A. (2011). Implementation of an intensity feedback-loop for an ion-therapy sychrotron. In *Proceedings of IPAC2011*.

Schulz-Ertner, D., Karger, C. P., Feuerhake, A., Nikoghosyan, A., Combs, S. E., Jäkel, O., Edler, L., Scholz, M., and Debus, J. (2007). Effectiveness of carbon ion radiotherapy in the treatment of skull-base chordomas. *Int. J. Radiat. Oncol. Biol. Phys.*, 68(2):449–457.

Seco, J., Robertson, D., Trofimov, A., and Paganetti, H. (2009). Breathing interplay effects during proton beam scanning: simulation and statistical analysis. *Phys. Med. Biol.*, 54(14):N283–N294.

Seong, J., Park, H. C., Han, K. H., and Chon, C. Y. (2003). Clinical results and prognostic factors in radiotherapy for unresectable hepatocellular carcinoma: a retrospective study of 158 patients. *Int. J. Radiat. Oncol. Biol. Phys.*, 55(2):329–336.

Seppenwoolde, Y., Shirato, H., Kitamura, K., Shimizu, S., Lebesque, J. V., and Miyasaka, K. (2002). Precise and real-time measurement of 3D tumor motion in lung due to breathing and heartbeat, measured during radiotherapy. *Int. J. Radiat. Oncol. Biol. Phys.*, 53(4):822–834.

Sharp, G. C., Jiang, S. B., Shimizu, S., and Shirato, H. (2004). Prediction of respiratory tumour motion for real-time image-guided radiotherapy. *Phys. Med. Biol.*, 49(3):425–440.

Sharp, G. C., Kandasamy, N., Singh, H., and Folkert, M. (2007). GPU-based streaming architectures for fast cone-beam CT image reconstruction and demons deformable registration. *Phys. Med. Biol.*, 52(19):5771–5783.

Shekhar, R., Lei, P., Castro-Pareja, C. R., Plishker, W. L., and D'Souza, W. D. (2007). Automatic segmentation of phase-correlated CT scans through nonrigid image registration using geometrically regularized free-form deformation. *Med. Phys.*, 34(7):3054.

Shirato, H., Oita, M., Fujita, K., Watanabe, Y., and Miyasaka, K. (2004). Feasibility of synchronization of real-time tumor-tracking radiotherapy and intensity-modulated radiotherapy from viewpoint of excessive dose from fluoroscopy. *Int. J. Radiat. Oncol. Biol. Phys.*, 60(1):335–341.

Shirato, H., Shimizu, S., Kunieda, T., Kitamura, K., Kagei, K., Nishioka, T., Hashimoto, S., Fujita, K., and Aoyama, H. (2000). Physical aspects of a real-time tumor-tracking system for gated radiotherapy. *Int. J. Radiat. Oncol. Biol. Phys.*, 48(4):1187–1195.

Skinner, H. D., Hong, T. S., and Krishnan, S. (2011). Charged-Particle Therapy for Hepatocellular Carcinoma. *Semin. Radiat. Oncol.*, 21(4):278–286.

Sonke, J. J., Lebesque, J., and van, H. M. (2008). Variability of four-dimensional computed tomography patient models. *Int. J. Radiat. Oncol. Biol. Phys.*, 70(2):590–598.

Spielberger, B., Krämer, M., Scholz, M., and Kraft, G. (2003). Three-dimensional dose verification in complex particle radiation fields based on x-ray films. *Nucl. Instrum. Meth. B*, 209:277–282.

Steidl, P. (2011). *Gating for scanned ion beam therapy*. PhD thesis.

Steidl, P., Richter, D., Schuy, C., Schubert, E., Haberer, T., Durante, M., and Bert, C. (2012). A breathing thorax phantom with independently programmable 6D tumour motion for dosimetric measurements in radiation therapy. *Phys. Med. Biol.*, 57(8):2235–2250.

Suh, Y., Sawant, A., Venkat, R., and Keall, P. J. (2009). Four-dimensional IMRT treatment planning using a dmlc motion-tracking algorithm. *Phys. Med. Biol.*, 54(12):3821–3835.

Tobias, C. A., Lawrence, J. H., Born, J. L., McCombs, R. K., Roberts, J. E., Anger, H. O., Low-Beer, B. V., and Huggins, C. B. (1958). Pituitary irradiation with high-energy proton beams: a preliminary report. *Cancer Res.*, 18(2):121–134.

Tsujii, H., Kamada, T., Baba, M., Tsuji, H., Kato, H., Kato, S., Yamada, S., Yasuda, S., Yanagi, T., Kato, H., Hara, R., Yamamoto, N., and Mizoe, J. (2008). Clinical advantages of carbon-ion radiotherapy. *New J. Phys.*, 10(7):075009.

Tsujii, H., Mizoe, J., Kamada, T., Baba, M., Kato, S., Kato, H., Tsuji, H., Yamada, S., Yasuda, S., and et a. Ohno (2004). Overview of clinical experiences on carbon ion radiotherapy at NIRS. *Radiother. Oncol.*, 73(S2):41.

Tsujii, H., Mizoe, J., Kamada, T., Baba, M., Tsuji, H., Kato, H., Kato, S., Yamada, S., Yasuda, S., Ohno, T., Yanagi, T., Imai, R., Kagei, K., Kato, H., Hara, R., Hasegawa, A., Nakajima, M., Sugane, N., Tamaki, N., Takagi, R., Kandatsu, S., Yoshikawa, K., Kishimoto, R., and Miyamoto, T. (2007). Clinical results of carbon ion radiotherapy at NIRS. *J. Radiat. Res. (Tokyo).*, 48 Suppl A:A1-A13.:A1–A13.

Tsunashima, Y., Vedam, S., Dong, L., Umezawa, M., Sakae, T., Bues, M., Balter, P., Smith, A., and Mohan, R. (2008). Efficiency of respiratory-gated delivery of synchrotron-based pulsed proton irradiation. *Phys. Med. Biol.*, 53(7):1947–1959.

Unkelbach, J., Bortfeld, T., Martin, B. C., and Soukup, M. (2009). Reducing the sensitivity of IMPT treatment plans to setup errors and range uncertainties via probabilistic treatment planning. *Med. Phys.*, 36(1):149–163.

van de Water, S., Kreuger, R., Zenklusen, S., Hug, E., and Lomax, A. J. (2009). Tumour tracking with scanned proton beams: assessing the accuracy and practicalities. *Phys. Med. Biol.*, 54(21):6549–6563.

van't Riet, A., Mak, A. C., Moerland, M. A., Elders, L. H., and van der Zee, W. (1997). A conformation number to quantify the degree of conformality in brachytherapy and external beam irradiation: application to the prostate. *Int. J. Radiat. Oncol. Biol. Phys.*, 37(3):731–736.

Varma, M. N., Baum, J. W., and Kuehner, A. V. (1977). Radial dose, LET, and W for 160 ions in N2 and tissue-equivalent gases. *Radiat. Res.*, 70(3):511–518.

Veblen, O. and Young, J. W. (2005). *Projective geometry*.

von M. Siebenthal, Szekely, G., Lomax, A. J., and Cattin, P. C. (2007). Systematic errors in respiratory gating due to intrafraction deformations of the liver. *Med. Phys.*, 34(9):3620–3629.

Weber, U., Becher, W., and Kraft, G. (2000). Depth scanning for a conformal ion beam treatment of deep seated tumours. *Phys. Med. Biol.*, 45(12):3627–3641.

Weber, U. and Kraft, G. (1999). Design and construction of a ripple filter for a smoothed depth dose distribution in conformal particle therapy. *Phys. Med. Biol.*, 44(11):2765–2775.

Weber, U. and Kraft, G. (2009). Comparison of carbon ions versus protons. *Cancer J.*, 15(4):325–332.

Wilson, R. R. (1946). Radiological use of fast protons. *Radiology*, 47:487–491.

Wolthaus, J. W., Sonke, J. J., van, H. M., Belderbos, J. S., Rossi, M. M., Lebesque, J. V., and Damen, E. M. (2008). Comparison of different strategies to use four-dimensional computed tomography in treatment planning for lung cancer patients. *Int. J. Radiat. Oncol. Biol. Phys.*, 70(4):1229–1238.

Wunderink, W., Méndez Romero, A., de Kruijf, W., de Boer, H., Levendag, P., and Heijmen, B. (2008). Reduction of respiratory liver tumor motion by abdominal compression in stereotactic body frame, analyzed by tracking fiducial markers implanted in liver. *Int. J. Radiat. Oncol. Biol. Phys.*, 71(3):907–915.

Xing, L., Siebers, J., and Keall, P. (2007). Computational challenges for image-guided radiation therapy: framework and current research. *Semin. Radiat. Oncol.*, 17(4):245–257.

Yang, D., Lu, W., Low, D. A., Deasy, J. O., Hope, A. J., and Naqa El, I. (2008). 4D-CT motion estimation using deformable image registration and 5d respiratory motion modeling. *Med. Phys.*, 35(10):4577–4590.

Zenklusen, S. M., Pedroni, E., and Meer, D. (2010). A study on repainting strategies for treating moderately moving targets with proton pencil beam scanning at the new gantry 2 at PSI. *Phys. Med. Biol.*, 55(17):5103–5121.

Zhang, P., Hugo, G. D., and Yan, D. (2008). Planning study comparison of real-time target tracking and four-dimensional inverse planning for managing patient respiratory motion. *Int. J. Radiat. Oncol. Biol. Phys.*, 72(4):1221–1227.

Zhang, Y., Boye, D., Tanner, C., Lomax, A. J., and Knopf, A. (2012). Respiratory liver motion estimation and its effect on scanned proton beam therapy. *Phys. Med. Biol.*, 57(7):1779–1795.

Ziegler, J. F. (1999). Stopping of energetic light ions in elemental matter. *J. Appl. Phys.*, 85:1249.

Danksagungen

An dieser Stelle möchte ich gerne all jenen Menschen und Institutionen danken, die ihren Anteil am Gelingen dieser Doktorarbeit hatten. Dabei gilt mein Dank zunächst der Deutschen Forschungsgemeinschaft für die Finanzierung dieser Forschungsarbeit im Rahmen der Klinischen Forschergruppe 214 und der Helmholtz Graduate School for Hadron and Ion Research (HGS-HIRe) für die finanzielle Unterstützung bei diversen Konferenzteilnahmen.

Ganz besonders möchte ich mich bei Prof. Marco Durante bedanken, der es mir ermöglicht hat, dieses spannende Promotionsthema in seiner Arbeitsgruppe zu bearbeiten. Für die Betreuung dieser Arbeit danke ich sehr herzlich Dr. Christoph Bert. Von seinen vielen Ideen, seinem organisatorischen Talent und seinen unzähligen Hilfestellungen hat diese Arbeit entscheidend profitiert. Trotz wachsender Arbeitsgruppe und seinen vielfältigen Aufgaben war er für mich während und neben der Arbeitszeit jederzeit ansprechbar. Ebenfalls dankbar bin Prof. Gerhard Kraft für seine bereitwillige Übernahme des Korreferats. Er unterstützt die Arbeit der Moving-Targets-Gruppe stets mit großem Interesse und wertvollen Ratschlägen.

Besonderen Anteil am Gelingen dieser Arbeit hatte Peter Steidl, mit dem ich viele nächtliche Strahlzeiten in Heidelberg verbracht habe. Für die sehr gute Zusammenarbeit, vor allem bei der Planung, Durchführung und Auswertung der Experimente, möchte ich ihm hiermit danken. Auch Andreas von Knobloch, Stephan Brons und Ralf Panse gebührt an dieser Stelle mein Dank für die wertvolle Unterstützung während der Strahlzeiten. Für die Bereitstellung der Basisdaten für die entsprechenden Rechnungen möchte ich mich außerdem bei Katia Parodi und Florian Sommerer bedanken. Entscheidende Teile der Entwicklung von TRiP4D verdanke ich der intensiven Zusammenarbeit mit Jan Trautmann und Andreas Schwarzkopf. Ohne diese wertvolle Hilfe wären auch die hier vorgestellten Rechnungen nicht möglich gewesen. TRiP4D wäre ebenfalls undenkbar ohne die unermüdliche und langjährige Arbeit von Michael Krämer. Sein mehr denn je genutztes Programm stellt eine hervorragende und unverzichtbare Basis für TRiP4D dar. Darüber hinaus möchte ich mich bei Alexander Gemmel für seine jederzeit bereitwillige Hilfe bei allen Fragen der biologischen Dosisberechnung bedanken, sowie für die wertvolle Hilfe bei den Strahlzeiten. Für die vielen fruchtbaren Diskussionen, die gute Schreibtischnachbarschaft und die Durchsicht von Teilen dieser Arbeit danke ich insbesondere Robert Lüchtenborg und Christian Graeff. Christian verdanke ich ausserdem eine tatkräftige Unterstützung bei den statistischen Auswertungen, sowie viele wertvolle Anregungen. Auch John Eley danke ich herzlich für die bereitwillige Durchsicht von Teilen des Manuskriptes. Bei Nami Saito möchte ich mich vor allem für das zuverlässige Bereitstellen der Bildregistrierung bedanken, die eine wesentliche Voraussetzung für die durchgeführten Patientenrechnungen darstellte, sowie für viele anregende Diskussion. Des Weiteren danke ich Martin Härtig und Naved Chaudhri für die intensive Unterstützung bei der Vorbereitung der Patientenstudien. Das Bereitstellen der Patientendaten und die Aufnahme der Bestrahlungsdaten waren für diese Arbeit von großem Wert. Dankbar bin ich auch Jens Wölfelschneider für seine Hilfe bei der Vorbereitung der Dosisrekonstruktionen. Letztlich möchte ich nicht versäumen, mich auch bei all denjenigen zu bedanken, deren vielfältige Unterstützung und Hilfestellung für diese Arbeit hier nicht ausdrücklich erwähnt werden konnte. Mein Dank gilt insbesondere an dieser Stelle allen ehemaligen und derzeitigen Mit-

gliedern der Moving-Targets-Gruppe für die schöne gemeinsame Zeit, die sich nicht nur auf die Arbeitszeit beschränkte. Eine angenehmere Arbeitsatmosphäre ist für mich schwer vorstellbar. Auch allen anderen Mitgliedern der ständig wachsenden GSI Biophysik danke ich für die immer freundliche Arbeitsatmosphäre.

Einen ganz besonderen Dank möchte ich meinen derzeitigen und ehemaligen Mitbewohnern, sowie allen Mitgliedern der Kochgruppe aussprechen. Sie alle hatten einen ganz wesentlichen Anteil daran, dass ich mich sehr schnell in Darmstadt heimisch und wohl gefühlt habe. Die gewonnenen Freundschaften und gemeinsamen Unternehmungen schätze ich außerordentlich. In diesem Zusammenhang habe ich auch das Bedürfnis einen speziellen Dank an Sebastian Hild, Christoph Schuy und Simon Seibert zu richten. Die uns verbindende Kletterleidenschaft, mit der ich mich in Darmstadt unheilbar infiziert habe, hat mir mehr als nur einen Ausgleich zur Arbeit beschert. Für ihr unermüdliches Bemühen, gerade in der Endphase dieser Arbeit, mich zum Einhalten der empfohlenen Pausenzeiten an der Boulderwand zu bewegen, sei Ihnen hiermit vielmals gedankt.

Diese Arbeit wäre in keiner Weise möglich gewesen ohne die uneingeschränkte Unterstützung meiner Eltern. Sei es bei der Durchsicht dieser Arbeit, während meines Studiums oder in anderen Lebenslagen; für ihre stets verlässliche Hilfe schätze ich mich glücklich und bin Ihnen dafür außerordentlich dankbar.

Mein ganz besonderer Dank gilt Katharina für ihre Unterstützung während dieser Arbeit und ihr großes Verständnis für alle damit manchmal verbundenen Entbehrungen. Die gemeinsame Zeit mit ihr macht mich sehr glücklich.

Lebenslauf

Persönliche Daten

Name	Daniel Richter
Geburtstag	11. Juli 1981
Geburtsort	Aachen

Ausbildung und Werdegang

seit 05/2009	Mitglied der **Helmholtz Graduate School for Hadron and Ion Research (HGS-HIRe)**
04/2009–04/2010	**Universität Heidelberg** Fortbildung: *Medizinphysik für Physiker*
seit 01/2009	**TU Darmstadt, GSI Helmholtzzentrum für Schwerionenforschung** Promotion
02/2008–01/2009	**Humboldt-Universität zu Berlin** Wissenschaftlicher Mitarbeiter am Institut für Physik im Bereich experimentelle Elementarteilchenphysik. Forschungsaufenthalt am Europäischen Kernforschungszentrum (CERN) in Genf (Schweiz)
02/2008	**Humboldt-Universität zu Berlin** Diplomabschluss in Physik Titel der Diplomarbeit: *Energy Loss Measurements with the ATLAS Transition Radiation Tracker using Test Beam Data*
10/2002–02/2008	**Humboldt-Universität zu Berlin** Physikstudium
10/2001–06/2002	Wehrdienst
08/1995–05/2001	**Humboldt-Gymnasium**, Eichwalde
08/1991–07/1995	**Christian-Wirth-Schule** (Gymnasium), Usingen
08/1987–06/1991	**Jürgen Schumann Schule** (Grundschule), Arnoldshain

Nebentätigkeiten

12/2004–05/2007	**Deutsches Zentrum für Luft und Raumfahrt (DLR)** studentische Tutortätigkeit

Erklärung zur Dissertation

Hiermit versichere ich, die vorliegende Dissertation ohne Hilfe Dritter nur mit den angegebenen Quellen und Hilfsmitteln angefertigt zu haben. Alle Stellen, die aus Quellen entnommen wurden, sind als solche kenntlich gemacht. Diese Arbeit hat in gleicher oder ähnlicher Form noch keiner Prüfungsbehörde vorgelegen.

Darmstadt, den 29. Juli 2012

(Daniel Richter)